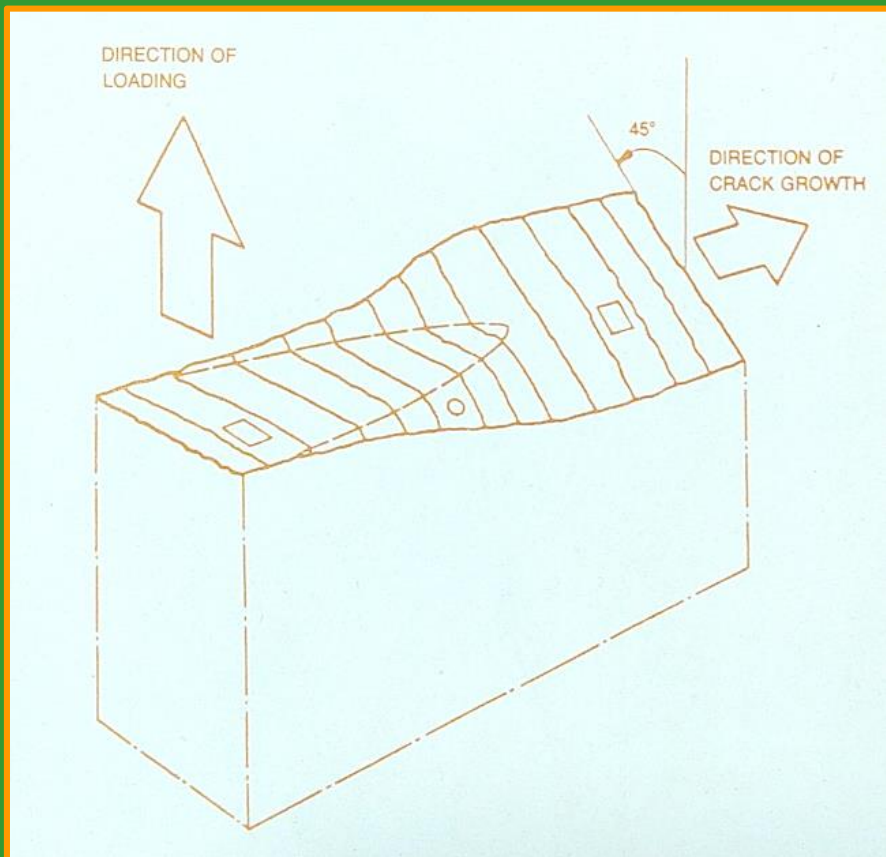


FRACTURE MECHANICS

Öktem Vardar



FRACTURE MECHANICS

Öktem Vardar

**Professor of Mechanical Engineering
Bogazigi University**

ERRATA SHEET (some corrected in the pdf file)

- page 29 Center (Δ) should be (ΔU)
- page 31 4th equation – in the bracket should be +
- page 40 Fig. 3.13 top scale $\pi/2$ should be $(\pi/2)^2$
- page 40 5th line from bottom M_R should be M_K
- page 49 Prob.5 : polynomial 41.99 should be 41.19
- page 68 Eq. 5.1 : b should be B
- page 70 Fig. 5.2 caption (*Eq. 4.2*) should be (*Eq. 5.2*)
- page 78 Fig. 5.12 caption $\alpha = K_{ic} / K_{max}$ should be $\alpha = K_{max} / K_{ic}$
- page 87 Fig. 5.24 X_o should be ΔX_o
- page 98 Eq. 5.21 last line $-\frac{1+v}{[\]^{0.5}} + v$
- page 104 Prob 2 ADD “...steel of yield strength 90 kgf/mm²”
- page 111 Eq. 6.1b $250 S_y <$ should be $250 < S_y <$
- page 138 4th line from bottom II should be $[II]$
- page 142 7th line from bottom $-\infty$ should be $+\infty$
- page 226 Fig. 9.6 R scale $-I$ should be $+I$
- page 227 Fig. 9.7 R scale $-I$ should move to the right
- page 235 17th line 2000 should be 200
- page 258 2nd line $2I$ should be $[2I]$
- page 260 8th line *accurance* should be “*occurrence*”

TABLE OF CONTENTS

1. INTRODUCTION	1
2. SOLUTIONS THAT ARE USEFUL IN FRACTURE PREDICTIONS	5
2.1 Stresses Around a Circular Hole	5
2.2 Stresses Around an Elliptical Crack	9
2.3 Stresses At a Sharp Crack (Westergaard's Solution)	12
2.3.1 Mode I loading	15
2.3.2 Mode II loading	20
2.3.3 Mode III loading	22
3. LINEAR ELASTIC FRACTURE MECHANICS	26
3.1 The Energy Approach	26
3.1.1 Griffith's Idea	26
3.1.2 The Energy Balance	28
3.1.3 Compliance Calibration	30
3.2 The Stress Intensity Factor Approach	34
3.2.1 Some Useful and Common Cases	36
3.3 The Equivalence of Energy and Stress Intensity Approaches	45
4. SMALL SCALE YIELDING	50
4.1 Estimation of Plastic Zones Based on Elastic Fields	50
4.2 Irwin Plastic Zone Correction for Plane Stress	53
4.3 The Dugdale Model	56
4.4 Plane Stress versus Plane Strain	59
4.5 Limitations on Plastic Zone Size	63
5. FRACTURE TOUGHNESS TESTING	68
5.1 The Standard Tests of Plane Strain Fracture Toughness	68
5.1.1 The Standard Specimens	68
5.1.2 Fatigue Precracking	75
5.1.3 Test Procedure	75
5.1.4 Further Details	80
5.1.5 Chevron Round Double Beam Specimen	83
5.2 Plane Stress Behavior	89
5.2.1 The R-Curve Concept	92
5.2.2 The Standard Procedure for R-Curve Determination	97

6. TRANSITION TEMPERATURE APPROACH	106
6.1 Introduction	106
6.2 Micromechanisms	106
6.3 Charpy Based DBTT Definitions	107
6.4 Additional Fracture Test Methods	111
6.4.1 DT and DWTT Methods	111
6.4.2 CAT Tests	112
6.4.3 NDT Test	115
6.5 Fracture Analysis Diagram	116
6.6 Impact Tests vs. LEFM	118
7. ELASTIC-PLASTIC FRACTURE MECHANICS	128
7.1 The J-Integral	128
7.1.1 Path Independence	130
7.1.2 Alternative Definition of J	132
7.1.3 Crack Tip Fields	135
7.1.4 Limitations	136
7.2 Determination of J-Integral	142
7.2.1 Direct Integration	142
7.2.2 The Potential Energy Route	143
7.2.3 The Superposition Technique	152
7.3 Evaluation of J_{IC}	157
7.3.1 Experimental Details	158
7.3.2 Estimation of Crack Growth	160
7.3.3 The Significance of J_{IC}	167
7.3.4 Examples of J_{IC} Results	168
7.4 The Crack Opening Displacement	173
8. FURTHER TOPICS OF EPFM	184
8.1 Crack Growth and Instability	184
8.1.1 Theoretical Justification for the Use of J-Integral	184
8.1.2 Modified $J:J_M$	188
8.1.3 The R-Curve	191
8.1.4 Instability	194
8.1.5 The Crack Tip Opening Angle	202
8.2 The Failure Assessment Diagram	204
8.2.1 The R-6 Failure Diagram	204
8.2.2 Deformation Plasticity Based Failure Diagram	206

9. FATIGUE CRACK PROPAGATION UNDER CONSTANT AMPLITUDE LOADING	219
9.1 Introduction	219
9.2.1 Crack Propagation Laws	224
9.2.2 Constant Amplitude Testing	229
9.3 Short Crack Behavior	234
9.3.1 Observed Trends	234
9.3.2 Difficulties Associated with short cracks	235
9.4 Propagation Beyond Yield	241
10. FATIGUE CRACK PROPAGATION UNDER VARIABLE AMPLITUDE LOADING	250
10.1 Single Overloads	254
10.2 Intermittent Overloads	259
10.3 Random Loading	265
10.4 Flight Simulation Loading	270
10.4.1 Standard Load Sequences	272
10.4.2 Planning Flight Simulation Tests	279
10.5 Prediction Models	284
10.5.1 Non-interaction Models	286
10.5.2 Yield zone Models	286
10.5.3 Crack Closure Models	292
10.5.4 Strip Yield Models	297
10.5.5 Empirical Models	298
11. TIME DEPENDENT FRACTURE MECHANICS	305
11.1 Introduction	305
11.2 Steady State Creep	306
11.2.1 Creep Tests	308
11.2.2 Determination of C^*	309
11.2.3 C^* Based Correlations	312
11.2.4 Other Correlations	316
11.3 Transient Creep	317
11.3.1 Growth Rate Correlations	318
APPENDIX	325

No: 453
Boğaziçi University Publication
1988

PREFACE

The text is intended to be a guide in one-semester graduate courses emphasizing the macro-aspects of fracture and addressing design. It is the outgrowth of lecture notes of the "Fracture" course given at Boğaziçi University for more than a decade.

Special thanks are due to Prof. I. Finnie of University of California at Berkeley who inspired in me the joy of fracture. The early chapters—which are establishing the foundations of fracture—are inevitably heavily influenced by his class notes of 1972.

Fracture is a very rapidly expanding field. Emphasis is placed in this work on recent developments rather than the "by now traditional" aspects of fracture. Elastic plastic fracture mechanics and variable amplitude fatigue crack propagation takes the major portion of the book.

Problems and answers to these problems are provided at the end of each chapter to promote the understanding. References are kept minimum on well developed topics and abundant on developing ones.

Istanbul, May 1988

Öktem VARDAR

1. INTRODUCTION

In the classical sense failure is predicted when stress reaches the relevant strength value. As far as fracture is concerned this relevant strength is the breaking strength. Its theoretical value, that is the cohesive strength in an ideally perfect crystal, may be estimated if the interatomic forces are known in detail. But a crude estimate is obtained by considering an isolated pair of atoms as Orowan did. Assuming that there is no interaction between neighboring atoms, the force necessary to displace atoms may be represented by a sine-function (Fig.1.1).

$$\sigma = S_t \sin \frac{2\pi}{\lambda} x \tag{1.1}$$

where σ denotes the force per unit area, S_t the theoretical breaking strength, x the displacement around the equilibrium point and $\lambda/2$ the range of the interatomic forces. For small displacements, linear elastic behavior is observed. Thus

$$\sigma = E \cdot \epsilon = E \frac{x}{b_0} = S_t \frac{2\pi}{\lambda} x \tag{1.2}$$

where E is the elastic modulus, ϵ the strain, b_0 the interatomic distance at equilibrium. The energy necessary to break the solid may be assumed to be equal to the surface energy for creating two fresh surfaces:

$$\int_0^{\lambda/2} \sigma dx = 2\gamma$$

where γ represents the surface energy (tension) per unit area, usually considered as a thermodynamic property of the material. Using equation 1.1 it becomes

$$S_t \int_0^{\lambda/2} \sin \frac{2\pi}{\lambda} x dx = 2 \gamma \tag{1.3}$$

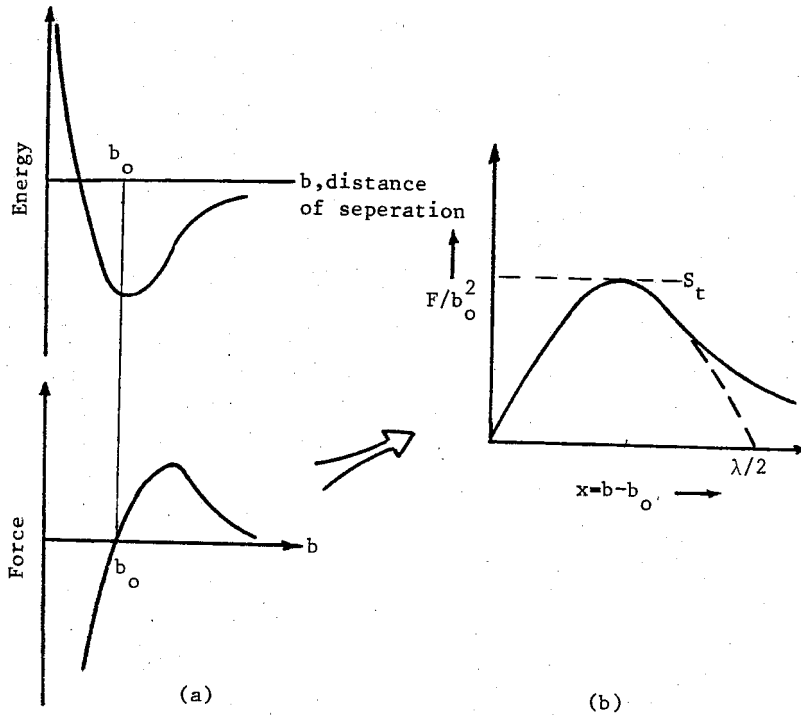


Fig.1.1- (a) Interatomic energy and force variation and
(b) its idealization

Combining equations 1.1 and 1.2 to eliminate the unknown λ and substituting it into equation 1.3 leads to

$$S_t = \sqrt{E\gamma/b_0} \quad (1.4)$$

Crude approximation of $\lambda/2 \approx b_0$ results in $S_t = E/\pi$. More accurate predictions [1] lead to the conclusion

$$S_t = \sqrt{E\gamma/b_0} \approx E/10 \quad (1.5)$$

which implies that the theoretical breaking strength is almost two orders of magnitude higher than the observed breaking strength of real engineering materials.

The discrepancy between the theoretical and observed strength can be explained by hypothesizing that real materials contain flaws which locally increase the stress. This is not unrealistic since defects such as pores, slag particles, inclusions, brittle particles, scratches of all sorts due to manufacturing and intentionally introduced discontinuities such as fillets, holes, groves are very common. These stress concentration sites not only raise the local stresses but they also induce multiaxial loading. A simple model would be that of figure 1.2 which indicates that high tensile stresses exist in the link AB but also in AC and BB, which in the absence of the notch would not exist. This effect of inducing transverse

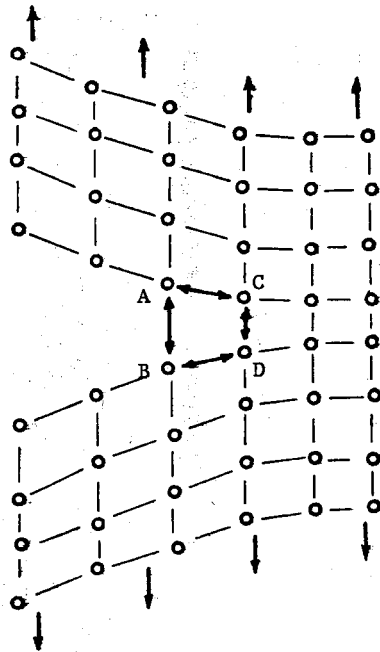


Fig.1.2- A simple sketch of the notch effect at the atomic level.

stresses-biaxiality or triaxiality-has important consequences on yielding. Since dislocation motion leading to plastic deformation is governed by shear stresses, i.e. by the difference of normal stresses, as triaxiality increases yielding is prevented and the tendency towards brittle behavior increases.

The idea that stress concentrators are responsible for the observed low strength of engineering materials is supported by the fact that

extremely thin-fibers of materials are exceptionally strong since they can hardly contain any defects. The observed strength of such whiskers reach almost the theoretical strength (Table 1.1). Having established the major role of "notches" it is worthwhile to consider the stress states in the neighborhood of some practical notched geometries.

Table 1.1- Tensile strength of whiskers at room temperature [1]

Material	Elastic Modulus(GPa)	Strength(GPa)
Graphite	675	19.3
Al ₂ O ₃	524	15.2
Al ₂ O ₃ large crystal	524	6.9
Iron	193	12.4
Si ₃ N ₄	380	13.8
Si C	690	20.7
Si	180	6.9
Si large crystal	180	3.6

References

- 1- Kelly, A, "Strong Solids" Clarendon Press, Oxford 1966

2. SOLUTIONS THAT ARE USEFUL IN FRACTURE PREDICTIONS

2.1 STRESSES AROUND A CIRCULAR HOLE

The most common stress concentration type is that of a circular cavity and luckily the solution is quite simple. Thus, it will be presented here as a typical case.

Consider an infinite plate with a hole, subject to a uniform tensile stress σ in the y-direction (Fig.2.1). The solution is obtained through Airy stress function [1]. If there is no hole in the plate, the state

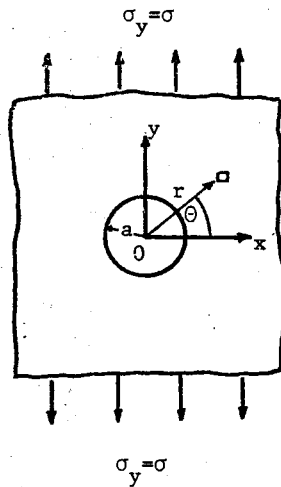


Fig. 2.1- The geometry in the circular hole problem

of stress will be given by:

$$\left. \begin{aligned} \sigma_y &= \sigma \\ \sigma_x &= 0 \\ \tau_{xy} &= 0 \end{aligned} \right\} \quad (2.1)$$

This state of stress can be derived from the stress function

$$\phi = \frac{1}{2} \sigma x^2$$

or through polar coordinates

$$\phi = \frac{\sigma}{4} r^2 (1 + \cos 2\theta) \quad (2.2)$$

and the corresponding stress components are

$$\left. \begin{aligned} \sigma_r &= \frac{1}{2} \sigma (1 - \cos 2\theta) \\ \sigma_\theta &= \frac{1}{2} \sigma (1 + \cos 2\theta) \\ \tau_{r\theta} &= -\frac{1}{2} \sigma \sin 2\theta \end{aligned} \right\} \quad (2.3)$$

Now if a hole of radius a is introduced at the origin O , the stress state will be disturbed. The new stress state must satisfy the boundary conditions

$$\left. \begin{aligned} \text{at } r = a & \quad \sigma_r = \tau_{r\theta} = 0 \\ \text{at } r \rightarrow \infty & \quad \sigma_r, \sigma_\theta \text{ and } \tau_{r\theta} \text{ coincide} \\ & \quad \text{with eq. (2.3)} \end{aligned} \right\} \quad (2.4)$$

and will be derived from a stress function ϕ which must satisfy $\nabla^4 \phi$ in polar coordinates

$$\left[\frac{\partial^2}{\partial r^2} + \frac{1}{r} \frac{\partial}{\partial r} + \frac{1}{r^2} \frac{\partial^2}{\partial \theta^2} \right] \left[\frac{\partial^2 \phi}{\partial r^2} + \frac{1}{r} \frac{\partial \phi}{\partial r} + \frac{1}{r^2} \frac{\partial^2 \phi}{\partial \theta^2} \right] = 0 \quad (2.5)$$

If it is assumed that the stress function, with hole present, is of the same form as the stress function given by eq.(2.2), i.e., composed of a function $f_1(r)$ plus another function $f_2(r)$ multiplied by $\cos 2\theta$,

$$\phi(r,\theta) = f_1(r) + f_2(r) \cos 2\theta$$

then the compatibility equation, eq.(2.5), yields

$$\left[\frac{d^2}{dr^2} + \frac{1}{r} \frac{d}{dr} \right] \left[\frac{d^2 f_1}{dr^2} + \frac{1}{r} \frac{df_1}{dr} \right] + \left[\frac{d^2}{dr^2} + \frac{1}{r} \frac{d}{dr} - \frac{4}{r^2} \right] \left[\frac{d^2 f_2}{dr^2} + \frac{1}{r} \frac{df_2}{dr} - \frac{4f_2}{r^2} \right] \cos 2\theta = 0$$

or

$$\left. \begin{aligned} \left[\frac{d^2}{dr^2} + \frac{1}{r} \frac{d}{dr} \right] \left[\frac{d^2 f_1}{dr^2} + \frac{1}{r} \frac{df_1}{dr} \right] &= 0 \\ \left[\frac{d^2}{dr^2} + \frac{1}{r} \frac{d}{dr} - \frac{4}{r^2} \right] \left[\frac{d^2 f_2}{dr^2} + \frac{1}{r} \frac{df_2}{dr} - \frac{4f_2}{r^2} \right] &= 0 \end{aligned} \right\} \quad (2.6)$$

These equations reduce to linear differential equations with constant coefficients through the substitution $r = e^x$, and give the general solution

$$f_1(r) = C_1 r^2 \log r + C_2 r^2 + C_3 \log r + C_4$$

$$f_2(r) = C_5 r^2 + C_6 r^4 + \frac{C_7}{r^2} + C_8$$

and the stress function $\phi(r,\theta)$ is

$$\phi = \left[C_1 r^2 \log r + C_2 r^2 + C_3 \log r + C_4 \right] + \left[C_5 r^2 + C_6 r^4 + \frac{C_7}{r^2} + C_8 \right] \cos 2\theta$$

which corresponds to the following system of stresses:

$$\sigma_r = C_1 (1+2 \log r) + 2C_2 + \frac{C_3}{r^2} - \left[2C_5 + \frac{6C_7}{r^4} + \frac{4C_8}{r^2} \right] \cos 2\theta$$

Thus, the stress components are obtained as:

$$\left. \begin{aligned} \sigma_r &= \frac{\sigma}{2} \left[1 - \frac{a^2}{r^2} \right] - \frac{\sigma}{2} \left[1 + \frac{3a^4}{r^4} - \frac{4a^2}{r^2} \right] \cos 2\theta \\ \sigma_\theta &= \frac{\sigma}{2} \left[1 + \frac{a^2}{r^2} \right] + \frac{\sigma}{2} \left[1 + \frac{3a^4}{r^4} \right] \cos 2\theta \\ \tau_{r\theta} &= -\frac{\sigma}{2} \left[1 - \frac{3a^4}{r^4} + \frac{2a^2}{r^2} \right] \sin 2\theta \end{aligned} \right\} \quad (2.7)$$

There are several features worth noting. These are sketched in Fig.2.2 and summarized below.

- i, Due to the presence of the hole one has at the two points A and A' a stress concentration of three.
- ii, The elevation of stress at these stress concentration sites is very localized. At one hole diameter away from the stress concentration point the stress is only about 7% higher than the nominal value.
- iii, For applied tensile stresses, compressive ones are induced at point C and C' and vice versa.
- iv, The same stress distribution is obtained for both plane stress and plane strain conditions.

2.2 STRESSES AROUND AN ELLIPTICAL CRACK

Consider an elliptical hole in an infinite plate loaded by biaxial tensile stresses σ (Fig.2.3). Elliptical coordinates ξ and η are particularly well suited for this geometry. These are defined through

$$\left. \begin{aligned} x &= c \cosh \xi \cos \eta \\ y &= c \sinh \xi \sin \eta \end{aligned} \right\} \quad (2.8)$$

Thus, $\xi = \text{constant}$ curves are ellipses given by

$$\frac{x^2}{c^2 \cosh^2 \xi} + \frac{y^2}{c^2 \sinh^2 \xi} = 1$$

and $\eta = \text{constant}$ curves are hyperbolas expressed by

$$\frac{x^2}{c^2 \cos^2 \eta} - \frac{y^2}{c^2 \sin^2 \eta} = 1$$

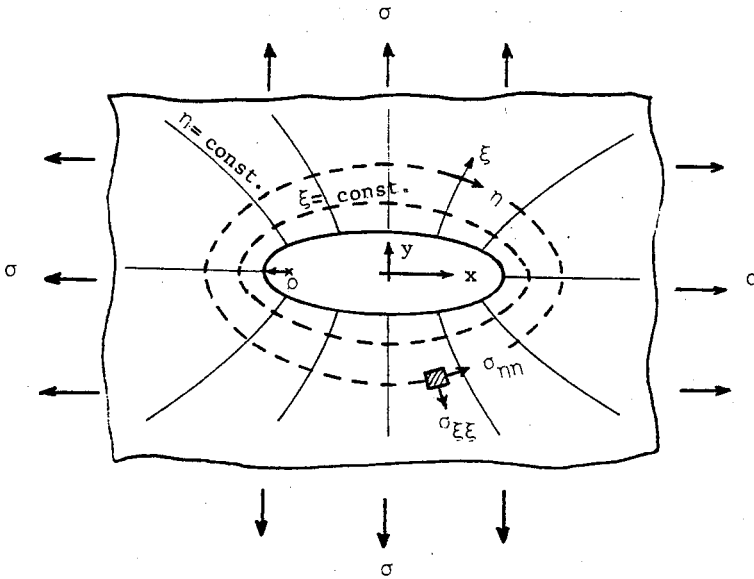


Fig. 2.3- The geometry of the elliptical hole problem.

Inglis obtained the stress field in 1913 [2] :

$$\left. \begin{aligned} \sigma_{\xi\xi} &= \frac{\sigma \sinh 2\xi (\cosh 2\xi - \cosh 2\xi_0)}{(\cosh 2\xi - \cos 2\eta)^2} \\ \sigma_{\eta\eta} &= \frac{\sigma \sinh 2\xi (\cosh 2\xi + \cosh 2\xi_0 - 2\cos 2\eta)}{(\cosh 2\xi - \cos 2\eta)^2} \\ \tau_{\xi\eta} &= \frac{\sigma \sin 2\eta (\cosh 2\xi - \cosh 2\xi_0)}{(\cosh 2\xi - \cos 2\eta)^2} \end{aligned} \right\} \quad (2.9)$$

The boundary of the crack is expressed by ξ_0 while $\eta = 0, \pi$ represent the ends of the major axis. The focii of the ellipse are $x = \pm c$ and

the semi-major and semi-minor axes are given by

$$a = c \cosh \xi_0$$

$$b = c \sinh \xi_0$$

As $\xi_0 \rightarrow \infty$ the ellipse becomes a circle, while as $\xi_0 \rightarrow 0$ the ellipse becomes a sharp crack of length $2a = 2c$.

If we examine the stresses along the x-axis, we find $\sin 2\eta = 0$, $\cos 2\eta = 1$, $\tau_{\xi\eta} = 0$ and

$$\left. \begin{aligned} \sigma_x = \sigma_{\xi\xi} &= \frac{\sigma \sinh 2\xi (\cosh 2\xi - \cosh 2\xi_0)}{(\cosh 2\xi - 1)^2} \\ \sigma_y = \sigma_{\eta\eta} &= \frac{\sigma \sinh 2\xi (\cosh 2\xi + \cosh 2\xi_0 - 2)}{(\cosh 2\xi - 1)^2} \end{aligned} \right\} \quad (2.10)$$

In particular, at the ends of the major axis, i.e. at $\xi = \xi_0$, $\eta = 0, \pi$

$$\sigma_y = \frac{\sigma (\sinh 2\xi_0) (2)}{\cosh 2\xi_0 - 1} = \sigma \frac{2a}{b} = 2\sigma \sqrt{\frac{a}{\rho}}$$

where $\rho =$ root radius $= b^2/a$. Letting $\xi_0 \rightarrow 0$ in eq.(2.10) we obtain a very slender ellipse which in the limit is a sharp crack

$$\sigma_y = \sigma_{yy} = \frac{\sigma \sinh 2\xi}{\cosh 2\xi - 1} \quad (2.11)$$

Since $c \rightarrow a$ as $\xi_0 \rightarrow 0$, we have $x = a \cosh \xi$ along the x-axis and σ_y in eq (2.11) can be rearranged to read

$$\sigma_y = \frac{\sigma 2 \sinh \xi \cosh \xi}{2 \sinh^2 \xi} = \frac{\sigma \cosh \xi}{\sqrt{\cosh^2 \xi - 1}} = \frac{\sigma (x/a)}{\sqrt{(x/a)^2 - 1}}$$

Making a coordinate transformation $a + r = x$, i.e. moving the coordinate axes to the crack tip yields

$$\sigma_y = \sigma \sqrt{\frac{a}{2r}} \cdot \frac{1+r/a}{\sqrt{1+r/2a}} \quad (2.12)$$

Thus, for points very close to the tip, i.e. $r/a \ll 1$

$$\sigma_y \approx \sigma \sqrt{\frac{a}{2r}} = \frac{\sigma \sqrt{\pi a}}{(2\pi r)^{1/2}} \quad (2.13)$$

This is an interesting result, showing that stresses go to infinity as the tip is approached, for a mathematically sharp crack.

Similarly, σ_x stress along the x-axis can be obtained for a sharp crack using eq.(2.10).

$$\sigma_x = \sigma_{\xi\xi} = \sigma \frac{\sinh 2\xi}{\cosh 2\xi - 1}$$

Hence, for sharp cracks $\sigma_x = \sigma_y$ at the tip. The solutions for σ_x along x-axis for the line crack and the ellipse differ greatly if we consider sharp ellipses other than the extreme case $\xi_0 = 0$. For ellipses with $\xi_0 \neq 0$, we see in Fig.2.4 that $\sigma_x = 0$ at the tip and rises to a value less than that of the peak σ_y stress at a small distance ahead of the crack tip.

If uniaxial loading of the elliptical hole is considered, the solution "becomes too lengthy" as Inglis states. Stress concentration at the tip of the ellipse turns out to be

$$\sigma_y = \sigma \left(1 + \frac{2a}{b}\right) = \sigma \left(1 + 2\sqrt{\frac{a}{\rho}}\right)$$

as opposed to $\sigma(2a/b)$ in biaxial loading, which is very close for elongated ellipses. For sharp cracks parallel stressing does not have any effect.

2.3 STRESSES AT A SHARP CRACK (WESTERGAARD'S SOLUTION)

There is no reason why Airy's stress function cannot be a complex function of two variables x and y . In fact, Westergaard presented a simple solution of cracked geometries using complex functions [3], which is reproduced here as an exemplary solution to sharp crack problems.

If $f(z)$ is an analytic function (i.e. it is single-valued and has a derivative at every point in the region of interest) then $z = x+iy$ implies

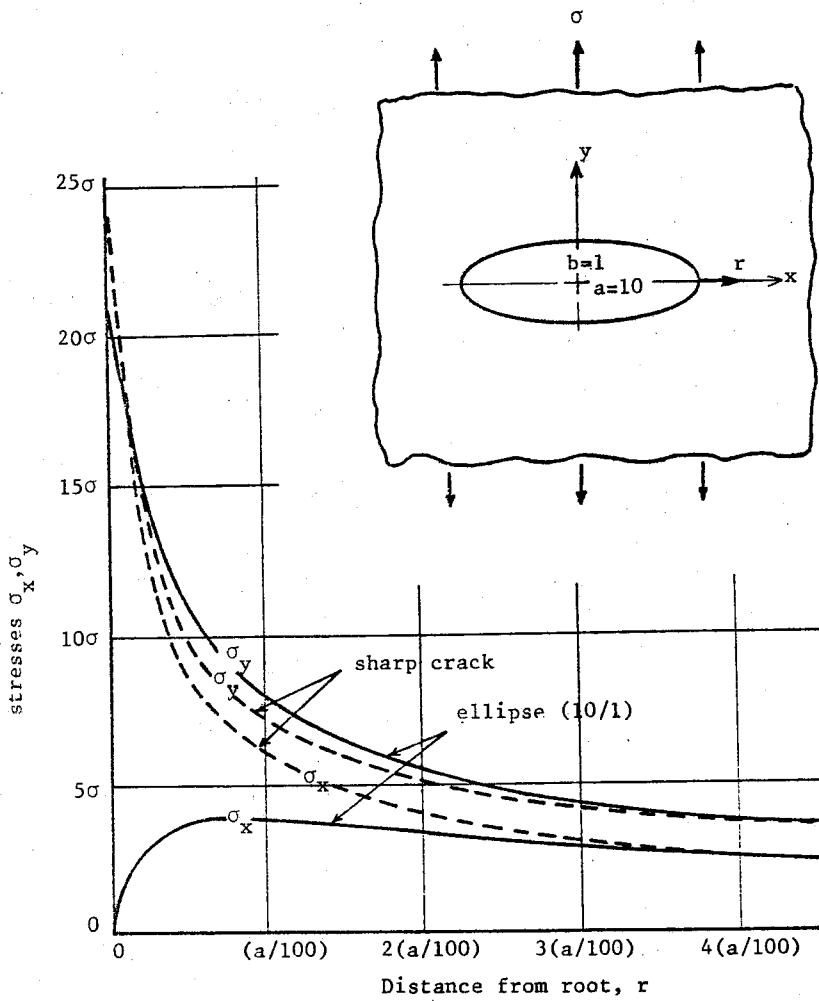


Fig.2.4- Stress distribution for an elliptical cavity.

$$\left. \begin{aligned} f'(z) &= \partial f / \partial x \\ i f'(z) &= \partial f / \partial y \end{aligned} \right\} \quad (2.14)$$

In general, the complex function will have its real and imaginary parts

$$f(z) = \alpha(x,y) + i \beta(x,y)$$

which yields through equations 2.14

$$\frac{\partial f}{\partial x} = \frac{\partial \alpha}{\partial x} + i \frac{\partial \beta}{\partial x} = f'$$

$$\frac{\partial f}{\partial y} = \frac{\partial \alpha}{\partial y} + i \frac{\partial \beta}{\partial y} = i f'$$

Thus

$$i \left(\frac{\partial \alpha}{\partial x} + i \frac{\partial \beta}{\partial x} \right) = \left(\frac{\partial \alpha}{\partial y} + i \frac{\partial \beta}{\partial y} \right)$$

yielding

$$\frac{\partial \alpha}{\partial x} = \frac{\partial \beta}{\partial y}$$

$$\frac{\partial \alpha}{\partial y} = - \frac{\partial \beta}{\partial x}$$

(2.15)

which are known as Cauchy-Riemann conditions. Taking the derivatives of the first Cauchy-Riemann condition with respect to x and of the second with respect to y (and vice versa) and combining them leads to

$$\left(\frac{\partial^2}{\partial x^2} + \frac{\partial^2}{\partial y^2} \right) \alpha = 0$$

and

$$\left(\frac{\partial^2}{\partial x^2} + \frac{\partial^2}{\partial y^2}\right) \beta = 0.$$

Thus, both the real and the imaginary parts of any analytic function are candidates for Airy's stress function since a harmonic function is also bi-harmonic. In fact, if ψ is a harmonic function, it is easy to show that $x\psi$, $y\psi$ or $(x^2 + y^2)\psi$ are all bi-harmonic. For example:

$$\left(\frac{\partial^2}{\partial x^2} + \frac{\partial^2}{\partial y^2}\right) x\psi = \frac{\partial}{\partial x} \left(\frac{\partial}{\partial x} x\psi\right) + \frac{\partial}{\partial y} \left(\frac{\partial}{\partial y} x\psi\right) =$$

$$\frac{\partial}{\partial x} (x \frac{\partial \psi}{\partial x} + \psi) + \frac{\partial}{\partial y} (x \frac{\partial \psi}{\partial y}) = x \left(\frac{\partial^2}{\partial x^2} + \frac{\partial^2}{\partial y^2}\right) \psi + 2 \frac{\partial \psi}{\partial x}$$

$$\nabla^4 (x\psi) = \left(\frac{\partial^2}{\partial x^2} + \frac{\partial^2}{\partial y^2}\right) \left(0 + 2 \frac{\partial \psi}{\partial x}\right) = 2 \frac{\partial}{\partial x} \left(\frac{\partial^2}{\partial x^2} + \frac{\partial^2}{\partial y^2}\right) \psi = 0$$

2.3.1. Mode I loading: The opening mode of a cracked panel is characterized by displacements in which the crack surfaces move directly apart (Fig.2.5). The boundary conditions for this loading are:

$$\left. \begin{aligned} \sigma_y &= 0 && \text{for } |x| < a, y = 0 \\ \sigma_y &> \sigma && \text{for } |x| > a + \epsilon, y = 0 \\ \sigma_y &\rightarrow \sigma && \text{as } x, y \rightarrow \infty \\ \tau_{xy} &= 0 && \text{along } y = 0 \\ v &= 0 && \text{along } y = 0, |x| > a \end{aligned} \right\} \quad (2.16)$$

where a is the half of the crack length and ϵ is a small number.

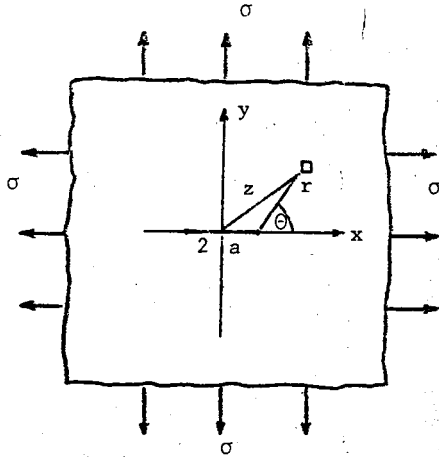


Fig.2.5- Mode I loading discussed by Westergaard

Consider

$$\phi = \operatorname{Re} \bar{\bar{\phi}} + y \operatorname{Im} \bar{\phi} \quad (2.17)$$

where $\bar{\bar{\phi}}$ and $\bar{\phi}$ are the second and first integrals of ϕ , respectively.

If $\bar{\bar{\phi}}$ is analytic, $\bar{\phi}$ is analytic and all the further derivatives ϕ' , ϕ'' , etc. are analytic. Thus, $\operatorname{Re} \bar{\bar{\phi}}$ and $\operatorname{Im} \bar{\phi}$ are harmonic and eq.2.17 is biharmonic.

Then

$$\begin{aligned} \sigma_y &= \frac{\partial^2 \phi}{\partial x^2} = \frac{\partial}{\partial x} \left(\frac{\partial}{\partial x} (\operatorname{Re} \bar{\bar{\phi}} + y \operatorname{Im} \bar{\phi}) \right) \\ &= \frac{\partial}{\partial x} (\operatorname{Re} \bar{\phi} + y \operatorname{Im} \phi) \\ &= \operatorname{Re} \phi + y \operatorname{Im} \phi' \end{aligned} \quad (2.18)$$

$$\sigma_x = \frac{\partial^2 \phi}{\partial y^2} = \frac{\partial}{\partial y} \left(\frac{\partial}{\partial y} (\operatorname{Re} \bar{\bar{\phi}}) + y \frac{\partial}{\partial y} (\operatorname{Im} \bar{\phi}) + \operatorname{Im} \bar{\phi} \right)$$

$$\begin{aligned}
&= \frac{\partial}{\partial y} \left(-\frac{\partial}{\partial x} (\text{Im}\bar{\phi}) + y \frac{\partial}{\partial x} (\text{Re}\bar{\phi}) + \text{Im}\bar{\phi} \right) \\
&= \frac{\partial}{\partial y} (-\text{Im}\bar{\phi} + y\text{Re}\bar{\phi} + \text{Im}\bar{\phi}) \\
&= y \frac{\partial}{\partial x} (\text{Im}\bar{\phi}) + \text{Re}\bar{\phi} \\
&= \text{Re}\phi - y\text{Im}\phi' \tag{2.19}
\end{aligned}$$

$$\begin{aligned}
\tau_{xy} &= -\frac{\partial^2 \phi}{\partial x \partial y} = -\frac{\partial}{\partial x} \left(\frac{\partial}{\partial y} (\text{Re}\bar{\phi}) + y \frac{\partial}{\partial y} (\text{Im}\bar{\phi}) + \text{Im}\bar{\phi} \right) \\
&= -\frac{\partial}{\partial x} (-\text{Im}\bar{\phi} + y \text{Re}\bar{\phi} + \text{Im}\bar{\phi}) \\
&= -y \text{Re}\phi' \tag{2.20}
\end{aligned}$$

The simplest function ϕ satisfying the boundary conditions 2.16 would be

$$\phi(z) = \frac{\sigma}{\sqrt{1-a^2/z^2}} \tag{2.21}$$

Along the x-axis, $y = 0$ and $\sigma_y = \sigma / \sqrt{1-a^2/x^2}$, in complete agreement with the boundary conditions. If the coordinate system is changed to one originating at the crack tip, $z-a = \eta = r e^{i\theta}$, eq.2.21 becomes

$$\begin{aligned}
\phi(\eta) &= \frac{\sigma(\eta+a)}{\sqrt{\eta(\eta+2a)}} = \frac{\sigma a}{\sqrt{2a\eta}} \frac{1+\eta/a}{\sqrt{1+\eta/2a}} \\
&= \sigma \sqrt{\frac{a}{2re^{i\theta}}} \left[\frac{1+(r/a)e^{i\theta}}{\sqrt{1+(r/2a)e^{i\theta}}} \right] \tag{2.22}
\end{aligned}$$

For points close to the crack tip, $r/a \ll 1$ and

$$\phi(\eta) \approx \sigma \sqrt{a/2\eta} \quad , \quad \phi'(\eta) \approx -\frac{\sigma}{2} \sqrt{a/2\eta^3} \quad (2.23)$$

Thus, using eq.2.18,

$$\begin{aligned} \sigma_y &= \operatorname{Re} (\sigma \sqrt{a/2r} e^{-i\theta/2}) + r \sin\theta \operatorname{Im} \left(-\frac{\sigma}{2} \sqrt{a/2r^3} e^{-i3\theta/2} \right) \\ &= \sigma \sqrt{a/2r} \cos \frac{\theta}{2} + \frac{\sigma}{2} \sqrt{a/2r} \sin\theta \sin \frac{3\theta}{2} \\ &= \sigma \sqrt{\frac{\pi a}{2\pi r}} \cos \frac{\theta}{2} \left(1 + \sin \frac{\theta}{2} \sin \frac{3\theta}{2} \right) \end{aligned} \quad (2.24)$$

Similarly, using eq.2.19,

$$\begin{aligned} \sigma_x &= \operatorname{Re} (\sigma \sqrt{a/2r} e^{-i\theta/2}) - r \sin\theta \operatorname{Im} \left(-\frac{\sigma}{2} \sqrt{a/2r^3} e^{-i3\theta/2} \right) \\ &= \sigma \sqrt{\frac{\pi a}{2\pi r}} \cos \frac{\theta}{2} \left(1 - \sin \frac{\theta}{2} \sin \frac{3\theta}{2} \right) \end{aligned} \quad (2.25)$$

And using eq.2.20,

$$\begin{aligned} \tau_{xy} &= -r \sin\theta \operatorname{Re} \left(-\frac{\sigma}{2} \sqrt{a/2r^3} e^{-i3\theta/2} \right) \\ &= \sigma \sqrt{\frac{\pi a}{2\pi r}} \cos \frac{\theta}{2} \sin \frac{\theta}{2} \cos \frac{3\theta}{2} \end{aligned} \quad (2.26)$$

Note that equations 2.24 through 2.26 are just the first terms in a series expansion the higher terms of which are neglected since we only consider points close to the crack tip and use eq. 2.23 instead of eq.2.22 in obtaining the stress field. The singular behavior predicted by eq.2.13 is rediscovered here.

To obtain the displacement field in plane strain, the stress-strain relationship is used

$$2\tilde{G}\epsilon_x = \sigma_x - \nu(\sigma_x + \sigma_y) = (1-2\nu) \operatorname{Re}\phi - \nu \operatorname{Im}\phi'$$

where $\tilde{G} = E/2(1+\nu)$ is the shear modulus and ν the Poisson's ratio. Integrating the strain expression, x-directional displacement u becomes

$$2\tilde{G}u = (1-2\nu) \operatorname{Re} \bar{\phi} - y \operatorname{Im} \phi + g(y)$$

where $g(y)$ is an arbitrary function of y . Similarly,

$$2\tilde{G}v_y = (1-2\nu) \operatorname{Re} \phi + y \operatorname{Im} \phi'$$

leads to y-directional displacement v

$$2\tilde{G}v = (2-2\nu) \operatorname{Im} \bar{\phi} - y \operatorname{Re} \phi + f(x)$$

where $f(x)$ is an arbitrary function of x . Using the shear stress-shear strain relationship and the displacement expressions above

$$\begin{aligned} 2\tilde{G}\gamma_{xy} &= -2y \operatorname{Re} \phi' = 2\tilde{G} \frac{\partial u}{\partial y} + 2\tilde{G} \frac{\partial v}{\partial x} \\ &= -2y \operatorname{Re} \phi' + g' + f' \end{aligned}$$

Thus

$$g' + f' = 0$$

which leads to

$$g = Ay + D$$

$$f = -Ax + C$$

with A , C and D being just constants. Since the boundary condition dictates that v be zero for $|x| > a$ along the symmetry axis $A = 0$. The constants C and D just give rigid body displacements, hence may be omitted. Thus,

$$2\tilde{G}u = (1-2\nu) \operatorname{Re} \bar{\phi} - y \operatorname{Im} \phi$$

$$2\tilde{G}v = (2-2\nu) \operatorname{Im} \bar{\phi} - y \operatorname{Re} \phi$$

Through the use of $\bar{\phi}(\eta) = \sigma \sqrt{2a\eta}$, $\phi(\eta) = \sigma \sqrt{a/2\eta}$ one obtains

$$2\tilde{G}u = (1-2\nu) \sigma \sqrt{2ar} \cos \frac{\theta}{2} + \sigma r \sin \theta \sqrt{a/2r} \sin \frac{\theta}{2}$$

$$u = \sigma \frac{\sqrt{\pi a}}{\tilde{G}} \sqrt{\frac{r}{2\pi}} \cos \frac{\theta}{2} (1-2\nu + \sin^2 \frac{\theta}{2}) \quad (2.27)$$

and

$$2\tilde{G}v = (2-2\nu) \sigma \sqrt{2ar} \sin \frac{\theta}{2} - \sigma r \sin \theta \sqrt{a/2r} \cos \frac{\theta}{2}$$

$$v = \sigma \frac{\sqrt{\pi a}}{\tilde{G}} \sqrt{\frac{r}{2\pi}} \sin \frac{\theta}{2} (2-2\nu - \cos^2 \frac{\theta}{2}) \quad (2.28)$$

To obtain the displacements in plane stress, it is sufficient to replace ν by $\nu/1+\nu$.

The shape of the open crack can be obtained if $\phi(z) = \sigma z / \sqrt{a^2 - z^2}$ is used without any simplification. In this case

$$2\tilde{G}v(x,0) = 2(1-\nu) \operatorname{Im}\bar{\phi} = 2(1-\nu) \sigma \sqrt{a^2 - x^2} \quad (2.29)$$

which shows that the line crack opens up to form an ellipse.

2.3.2 Mode II loading: The forward sliding mode is characterized by displacements in which the crack surfaces slide over one another normal to the crack front. This in-plane shear loading is depicted in figure 2.6. The boundary conditions are:

$$\begin{aligned} \sigma_y = 0, \quad \tau_{xy} = 0 & \quad \text{for } |x| < a, y = 0 \\ \sigma_y = 0 & \quad \text{along } x\text{-axis} \\ \tau_{xy} \rightarrow \tau & \quad \text{as } x, y \rightarrow \infty \\ \tau_{xy} > \tau & \quad \text{for } |x| > a + \epsilon, y = 0 \\ u = 0 & \quad \text{for } y = 0 \text{ and } |x| > a \end{aligned} \quad (2.30)$$

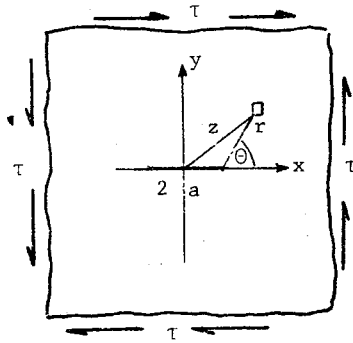


Fig.2.6- Mode II loading discussed by Westergaard .

Consider

$$\phi = -y \operatorname{Re} \bar{\phi} \quad (2.31)$$

Similar to mode I analysis.

$$\sigma_y = \frac{\partial^2 \phi}{\partial x^2} = -y \operatorname{Re} \phi' \quad (2.32)$$

$$\sigma_x = \frac{\partial^2 \phi}{\partial y^2} = 2 \operatorname{Im} \phi + y \operatorname{Re} \phi' \quad (2.33)$$

$$\tau_{xy} = \frac{-\partial^2 \phi}{\partial x \partial y} = \operatorname{Re} \phi - y \operatorname{Im} \phi' \quad (2.34)$$

The simplest function satisfying the boundary conditions 2.30 is

$$\phi(z) = \frac{\tau}{\sqrt{1-a^2/z^2}} \quad (2.35)$$

which for points close to the tip becomes

$$\phi(\eta) \approx \tau \sqrt{\frac{a}{2\eta}} \quad (2.36)$$

Thus, using this simplified expression in eq.2.32 through 2.34 yields

$$\sigma_y = \frac{\tau \sqrt{\pi a}}{\sqrt{2\pi r}} \sin \frac{\theta}{2} \cos \frac{\theta}{2} \cos \frac{3\theta}{2} \quad (2.37)$$

$$\sigma_x = \frac{-\tau\sqrt{\pi a}}{\sqrt{2\pi r}} \sin \frac{\theta}{2} \left(2 + \cos \frac{\theta}{2} \cos \frac{3\theta}{2}\right) \quad (2.38)$$

$$\tau_{xy} = \frac{\tau\sqrt{\pi a}}{\sqrt{2\pi r}} \cos \frac{\theta}{2} \left(1 - \sin \frac{\theta}{2} \sin \frac{3\theta}{2}\right) \quad (2.39)$$

The displacements (for plane strain) are obtained as follows:

$$2\tilde{G}\epsilon_x = 2(1-\nu) \operatorname{Im}\bar{\phi} + y \operatorname{Re}\phi'$$

$$2\tilde{G}u = 2(1-\nu) \operatorname{Im}\bar{\phi} + y \operatorname{Re}\phi$$

$$u = \tau \frac{\sqrt{\pi a}}{\tilde{G}} \sqrt{\frac{r}{2\pi}} \sin \frac{\theta}{2} \left(2 - 2\nu + \cos^2 \frac{\theta}{2}\right) \quad (2.40)$$

$$2\tilde{G}v = (-1 + 2\nu) \operatorname{Re}\bar{\phi} - y \operatorname{Im}\phi$$

$$v = \tau \frac{\sqrt{\pi a}}{\tilde{G}} \sqrt{\frac{r}{2\pi}} \cos \frac{\theta}{2} \left(-1 + 2\nu + \sin^2 \frac{\theta}{2}\right) \quad (2.41)$$

2.3.3. Mode III loading: In the parallel shear (or anti-plane shear) mode the crack surfaces slide with respect to one another parallel to the crack front (Fig.2.7). This is the type of loading experienced in circumferentially notched rods subject to torsion. The boundary conditions are:

$$\left. \begin{aligned} \tau_{yz} &= 0 && \text{for } |x| < a \\ \tau_{yz} &\rightarrow \tau && \text{as } y \rightarrow \infty \\ w &= 0 && \text{for } y = 0 \text{ and } |x| > a \end{aligned} \right\} \quad (2.42)$$

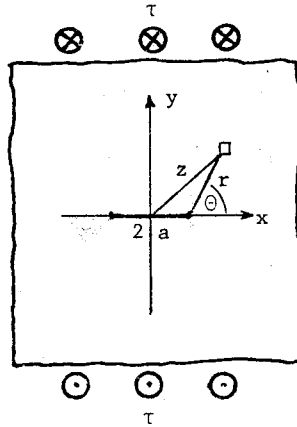


Fig.2.7- Mode III loading discussed by Westergaard

Since $u = v = 0$ for this case, the equilibrium equation in terms of the displacement w simply reduces to

$$\nabla^2 w = 0 \quad (2.43)$$

Choosing

$$w = \frac{1}{G} \operatorname{Im} \bar{\phi} \quad (2.44)$$

yields

$$\tau_{xz} = \operatorname{Im} \phi \quad (2.45)$$

$$\tau_{yz} = \operatorname{Re} \phi \quad (2.46)$$

Again, a simple function will be

$$\phi(z) = \frac{\tau}{\sqrt{1 - a^2/z^2}} \quad (2.47)$$

which for $r/a \ll 1$ leads to

$$\tau_{xz} = \frac{-\tau \sqrt{\pi a}}{\sqrt{2\pi r}} \sin \frac{\theta}{2} \quad (2.48)$$

$$\tau_{yz} = \frac{\tau \sqrt{\pi a}}{\sqrt{2\pi r}} \cos \frac{\theta}{2} \quad (2.49)$$

and

$$w = \frac{\tau \sqrt{\pi a}}{\tilde{G}} \sqrt{\frac{2r}{\pi}} \sin \frac{\theta}{2} \quad (2.50)$$

Westergaard solutions reveal that all stresses have a $1/\sqrt{r}$ singularity. Stresses tend to infinity as the crack tip is approached. Given the loading mode (i.e. Mode I, II or III) the stress expressions have the same form for all geometry and loadings except the numerator of the singular term. This term, the numerator of the singular term, indicates the strength or the intensity of singularity, that is, how fast the stresses go to infinity. Hence it is called the stress intensity factor and is shown by K_1, K_2 or K_3 for modes 1, 2 or 3, respectively. For plane strain conditions K_I, K_{II} and K_{III} , i.e. the roman numerals are used, to signify the important consequences of plane strain condition in fracture. These K expressions for different loading and geometry are listed in handbooks.

References

1- Volterra, E. and Gaines, J.H. "Advanced Strength of Materials, Prentice-Hall, Inc. New Jersey, 1971.

2- Inglis, C.E. "Stresses In a Plate Due to the Presence of Cracks and Sharp Corners" Proceedings, Institution of Naval Architects, 55, 1913, pp 219-230.

3- Westergaard, H.M. "Bearing Pressures and Cracks" Journal of Applied Mechanics, Transactions ASME, 6, (1939) pp. A49-53.

Problems:

1- For mode I loading, obtain expressions for the two principal stresses in the x,y plane. What value of θ gives the maximum value of principal stress? What is the direction of this principal stress relative to the x,y axes

Answer: $\pm 60^\circ$; coincident with x and y axes.

2- For the infinite plate subjected to uniform stress σ and containing a crack of length $2a$, calculate the stress σ_y along the x-axis both from Westergaard's solution and from Inglis' solution. By comparing these, determine the distance ahead of the crack at which Westergaard's solution is in error by 10%.

Answer: $r/a = 15\%$

3- Knowing the solutions for the stress concentrations at cylindrical and spherical holes, sketch the "failure envelope" for materials containing these type of flaws.

3. LINEAR ELASTIC FRACTURE MECHANICS

Chapter One presented the dilemma between the theoretical and observed strength. Engineering materials are not as strong as they should be. As a possible explanation to this, it is shown in Chapter Two that stresses increase appreciably at a discontinuity—in fact stresses go to infinity at a mathematically sharp crack, which implies zero strength. Engineering materials are not as weak, however, even if they contain sharp cracks. The balance is realized considering either the energy requirements at the crack tip or the applied stresses at the tip in conjunction with cohesive forces acting at the tip.

3.1 THE ENERGY APPROACH

3.1.1 Griffith's Idea: Griffith [1] introduced the idea that fracture could only occur if the solid can pass from the unbroken to broken condition by a process involving a continuous decrease in energy.

He considered an infinite plate of unit thickness containing a crack of length $2a$ (Fig.3.1). The loading is taken as equi-biaxial to simplify the strain energy calculations. As Griffith pointed out the loading parallel to the sharp crack does not change the strain energy value since

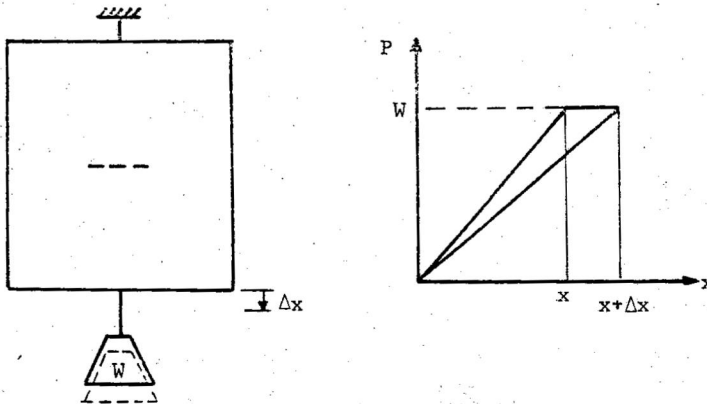


Fig.3.1: Center cracked panel subject to dead load

only changes in energy are of importance as the solid passes from the unbroken to broken condition.

change in potential

$$\text{energy of the weight} = \Delta \text{ P.E.} = - W \Delta x$$

change in strain

$$\text{energy of the plate} = \Delta U = + \frac{1}{2} W(x+\Delta x) - \frac{1}{2} Wx = \frac{1}{2} W\Delta x$$

Thus,

$$\Delta \text{ P.E.} = -2\Delta U$$

Griffith found from Inglis' solution that the strain energy of the cracked plate exceeded that of the uncracked plate by $\pi a^2 \sigma^2 / E$ for plane stress and by $\pi(1-\nu^2)a^2 \sigma^2 / E$ for plane strain. Including the energy dissipation by the newly created surface, total energy change becomes

$$\Delta \text{ energy} = -2 \frac{\pi a^2 \sigma^2}{E} + \frac{\pi a^2 \sigma^2}{E} + 4 a \gamma = - \frac{\pi a^2 \sigma^2}{E} + 4 a \gamma$$

where γ is the surface energy per unit fresh area.

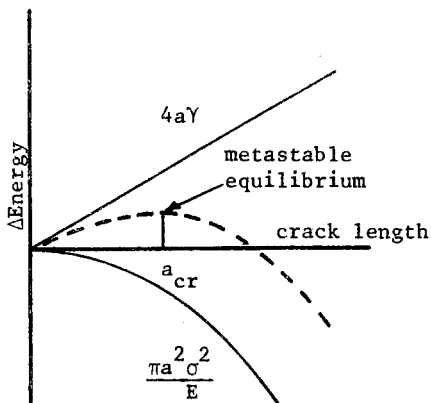


Fig.3.2- Variation of various energy components with crack length.

The maximum in the energy curve represents the metastable equilibrium (Fig.3.2).

$$\frac{\partial}{\partial a} \left(-\frac{\pi a^2 \sigma^2}{E} + 4a\gamma \right) = 0$$

Leading to

$$a_{cr} = \frac{2\gamma E}{\pi \sigma^2} \quad (3.1)$$

or

$$\sigma = \sqrt{\frac{2\gamma E}{\pi a}} \quad \text{in plane stress} \quad (3.2a)$$

$$\sigma = \sqrt{\frac{2\gamma E}{\pi a(1-\nu^2)}} \quad \text{in plane strain} \quad (3.2b)$$

This implies that fracture is imminent the moment you introduce a crack of size larger than critical (a_{cr}).

Tests on glass show that γ is 10-times the thermodynamic value; even for Al_2O_3 , at $-193^\circ C$, γ is 15-times higher than the thermodynamic value. Usually γ from fracture and γ from thermodynamics differ by one or more orders of magnitude. Thus, Orowan proposed to include an additional dissipation term to account for plastic deformation.

$$\sigma = \left\{ \frac{2(\gamma + \gamma_p) E}{\pi a} \right\}^{1/2}$$

Irwin [2] extended the formulation by replacing 2γ by G_c which is left as a material property to be determined from a fracture test.

$$\sigma = (G_c E / \pi a)^{1/2} \quad (3.3)$$

There is no a priori reason to accept G_c as a material property. It was Irwin's insight to postulate it as such initially which later turned out to be correct within certain limitations and formed the basis of linear elastic fracture mechanics (LEFM).

3.1.2 The Energy Balance: In the most general case, the thermodynamic equilibrium of the body requires that [3]

$$\dot{W} + Q = \dot{U} + \dot{K} + \dot{\Gamma} \quad (3.4)$$

where \dot{W} = rate of work done by the external loads = $\int_{S_T} t_i \dot{u}_i ds$ with t_i, u_i, S_T being the traction, displacement vectors and the portion of the boundary where tractions are specified, respectively.

$$Q = \text{total rate of heat supply} = - \int_S q_i n_i ds + \int_V oh dV$$

with q_i being the heat conduction vector per unit time per unit area and h being the heat source per unit time per unit mass.

$$\dot{U} = \text{rate of the recoverable stored energy} = \frac{d}{dt} \int_V \rho \epsilon dV$$

with ϵ being the internal energy density.

$$\dot{K} = \text{the kinetic energy rate} = \frac{d}{dt} \left(\frac{1}{2} \int_V \rho \dot{u}_i \dot{u}_i dV \right)$$

$$\dot{\Gamma} = \text{rate of all the irreversible energies} = G_c (\dot{a})$$

with G_c being the fracture energy per unit crack area, in agreement with the definition in the previous section.

In the quasi-static case, excluding the heat supply, the work done by external agents (ΔW) increases the energy level. Some of this increase goes to strain energy elevation (ΔU). The remaining energy is there for fracture process to occur, and just balances $G_c \Delta a$ under equilibrium conditions.

$$\Delta W - \Delta U = G_c \Delta a$$

which in the limit, for fixed load point displacement ($\Delta = \text{constant}$, $PE = PE(a)$), gives

$$\frac{1}{B} \frac{d}{da} (W-U) = G_c \quad (3.5)$$

The term $W-U$ is by definition negative of the potential energy (P.E) of the system, and represents the energy available for release. Thus, calling

$$-\frac{1}{B} \frac{d}{da} (P.E) = G = \text{energy release rate} \tag{3.6}$$

the equilibrium condition at fracture becomes

$$G = G_c \tag{3.7}$$

where G_c assumes the name critical energy release rate, or simply, fracture toughness. Energy release rate is commonly thought of as a "crack driving force" due to units of force/length or energy/area. Energy release rate is a "stress-like" quantity, governed by geometry and loading whereas its critical value is a "strength-like" quantity, depending very much on the material.

The stability of fracture propagation may be determined from

$$\frac{d}{da} (G - G_c) \left\{ \begin{array}{l} > 0 : \text{unstable fracture} \\ < 0 : \text{stable fracture} \\ = 0 : \text{neutral equilibrium} \end{array} \right. \tag{3.8}$$

3.1.3 Compliance Calibration: In general the total displacement is specified during loading (Fig.3.3). Thus, it is more appropriate

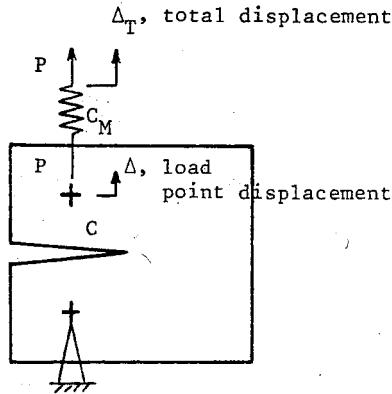


Fig.3.3- Cracked body under compliant conditions.

to write the potential energy as a function of the total displacement and the crack length.

$$\frac{d P.E}{dt} = \left(\frac{\partial P.E}{\partial \Delta_T} \right)_a \frac{d\Delta_T}{dt} + \left(\frac{\partial P.E}{\partial a} \right)_{\Delta_T} \frac{da}{dt}$$

which yields from the energy balance equation 3.4 for quasistatic, athermal systems [4]

$$G = - \frac{1}{B} \left(\frac{\partial P.E}{\partial a} \right)_{\Delta_T} \quad (3.9)$$

The compliance of the testing machine (C_M) determines conditions varying from fixed grips ($C_M = 0$) to fixed load ($C_M = \infty$). Consider the general situation, $0 < C_M < \infty$, depicted in figure 3.3.

$$P.E = \frac{1}{2} \frac{\Delta^2}{C} + \frac{1}{2} \frac{(\Delta_T - \Delta)^2}{C_M}$$

$$G = - \frac{1}{B} \left\{ \frac{\partial P.E}{\partial \Delta} \left(\frac{\partial \Delta}{\partial a} \right)_{\Delta_T} + \frac{\partial P.E}{\partial C} \left(\frac{\partial C}{\partial a} \right)_{\Delta_T} \right\}$$

$$G = - \frac{1}{B} \left\{ \left(\frac{\Delta}{C} - \frac{\Delta_T - \Delta}{C_M} \right) \left(\frac{\partial \Delta}{\partial a} \right)_{\Delta_T} - \frac{\Delta^2}{2C^2} \frac{dC}{da} \right\}$$

since $C = C(a)$ only. Both Δ/C and $(\Delta_T - \Delta)/C_M$ are equal to P , yielding

$$G = \frac{1}{2B} \frac{\Delta^2}{C^2} \frac{dC}{da} = \frac{P^2}{2B} \frac{dC}{da} \quad (3.10)$$

Thus, the energy release rate does not depend on the nature of the loading system. This result is also arrived at through the graphical interpretation of G . The shaded area in figure 3.4 corresponds to the energy available for fracture, i.e. $G da B$. The trapezoidal area ABCD corresponds to the work done as crack grows by da and the difference in the triangular areas OBD and OAC gives the change in strain energy. Thus, the triangular region OAB is nothing but $-dP.E$. If different loading conditions are compared (Fig.3.5) it is observed that

$$(G da B)_{\text{fixed load}} = (G da B)_{\text{fixed grips}} + \frac{1}{2} dP d\Delta$$

which in the limit as $da \rightarrow 0$ tends to

$$G_{\text{fixed load}} = G_{\text{fixed grips}}$$

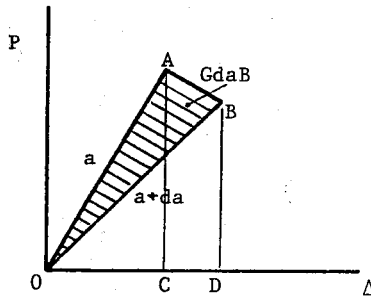


Fig.3.4- Graphical interpretation of the energy release rate

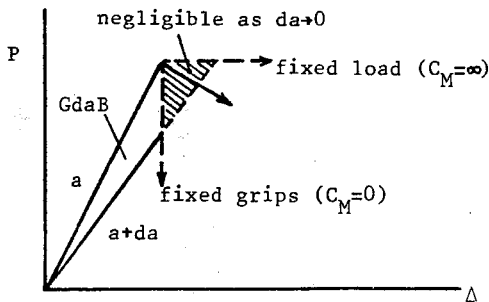


Fig.3.5- Schematic of different loading conditions

This indicates that the rate at which energy is released is the same at the moment of crack growth. However, as the crack grows, more energy will be released for fixed load than for fixed grips.

The expression 3.10 opens up the possibility of estimating G by experiment. For a given specimen, the crack length may be increased by carefully sawing, and the compliance recorded at each step by simply loading to a low value of load not to get fracture. The method, called the

compliance calibration, is applicable to any shape. Once dC/da is obtained for one material, it can be applied to other materials by adjusting for the different elastic moduli E .

In displacement controlled testing (usually with side grooving to control the direction of crack propagation) crack arrest may occur which yields several dC/da values as depicted in figure 3.6.

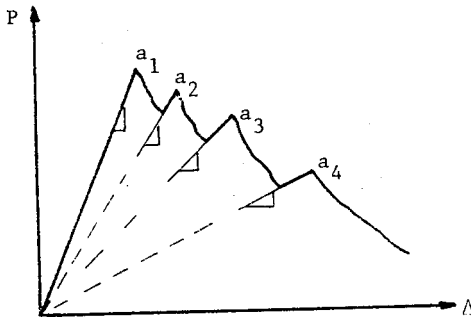


Fig.3.6- Possible crack arrest phenomena in fixed grip conditions

Compliance information about simple geometry and loadings can be obtained through a strength of materials approach. The so called double (cantilever) beam specimen (Fig.3.7) subject to concentrated end loads may be analyzed as simple beams built-in at the crack tip. Ignoring shear deflections

$$\Delta = 2 \frac{Pa^3}{3EI} \quad , \quad I = \frac{1}{12} B h^3$$

$$C = \Delta/P = 2a^3/3EI$$

$$G = \frac{P^2 a^2}{B EI}$$

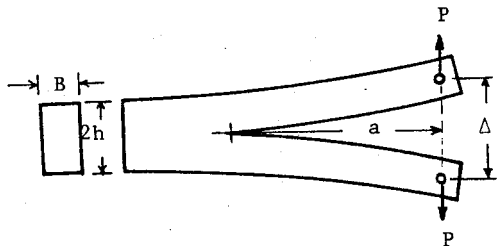


Fig.3.7: Double (Cantilever) Beam, DB(T)

Using Castigliano's theorem and including the shear deflections

$$\Delta = 2 \frac{Pa^3}{3EI} + \frac{12}{5} \frac{Pa}{GA} \quad , \quad A = h \cdot B$$

$$C = \frac{2}{3EI} \left(a^3 + \frac{3(1+\nu)}{5} a h^2 \right)$$

$$G = \frac{P^2}{B} \frac{a^2}{EI} \left(1 + \frac{1+\nu}{5} \frac{h^2}{a^2} \right)$$

In practice the beams of length a are not really clamped to have zero slope where they meet. An empirical correction for the rotation at the built-in end is given as [5]

$$G = \frac{P^2}{B} \frac{a^2}{EI} \left(1 + 1.2 \frac{h}{a} + 0.69 \frac{h^2}{a^2} \right)$$

for beams with heights from 100 mm to 10 mm and Poisson's ratio of 1/3. A detailed analytical solution of the problem yields [6]

$$G = \frac{P^2 a^2}{B EI} \left(1 + 1.35 \frac{h}{a} + 0.45 \frac{h^2}{a^2} + 0.075 \frac{h^3}{a^3} + 0.051 \frac{h^4}{a^4} + 0.0014 \frac{h^6}{a^6} \right)$$

3.2 THE STRESS-INTENSITY FACTOR APPROACH

Since the stresses go to infinity at the crack tip one cannot compare these with the theoretical strength to predict failure. Hence, Griffith looked in a small neighborhood rather than the tip. On the other hand, Barenblatt [7] considered the cohesive forces to overcome this difficulty. The intense cohesive forces are assumed to act on the smoothly closing crack end (Fig.3.8) leading to infinitely large compressive stresses at the tip just as the external loads are causing infinitely large tensile stresses.

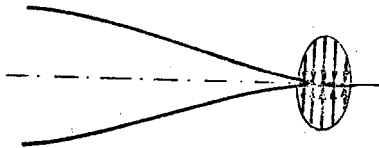


Fig.3.8- Smoothly closing crack of Barenblatt resembling a zipper with the intense cohesive forces around the tip

Since

$$\sigma_{ij} = \frac{K}{\sqrt{2\pi r}} f_{ij}(\theta)$$

total stress is obtained by superposing both effects

$$\sigma_{ij}(\text{total}) = \sigma_{ij}(\text{due to applied loads}) + \sigma_{ij}(\text{due to cohesive forces})$$

$$= \frac{K_{\text{applied}} + K_{\text{cohesive}}}{\sqrt{2\pi r}} f_{ij}(\theta)$$

Not to end up with infinite stresses, the only possibility for metastable equilibrium is

$$K_{\text{applied}} + K_{\text{cohesive}} = 0 \quad (3.11)$$

Now, to develop the concept further, two additional simplifying assumptions are made:

- (i) The region of cohesive forces is much smaller than the crack length
- (ii) The shape of the crack near the edges, thus the local distribution of cohesive forces, does not depend on the shape of the part or applied loads; that is, the same profile translates in the direction of crack growth.

The first assumption means that K_{cohesive} can be calculated by treating the crack as a semi-infinite cut in an infinite body loaded by stresses $g(t)$, for $0 < t < d$. For such a case,

$$K = -\sqrt{\frac{2}{\pi}} \int_0^d \frac{g(t)}{\sqrt{t}} dt \quad (3.12)$$

assuming that the crack faces cannot touch each other to transmit compression. The second assumption means that the above integral (eq.3.12) will have a constant value whatever the shape of the part and magnitude of the loads are. Thus, eq.3.11 reduces to

$$K_{\text{applied}} = -K_{\text{cohesive}} = \text{constant} \quad (3.13)$$

This constant is denoted by K_c and is considered to be a material property.

It cannot be obtained from bond strengths but determined as the critical value of the applied stress intensity factor. Hence the failure criterion becomes

$$K = K_c \quad (3.14)$$

Having established a new failure criterion in terms of K it is worthwhile to consider available stress intensity factors for several geometry and loadings.

3.2.1 Some Useful and Common Cases: Simplest situations are combined in figure 3.9 most of which involve infinite plates.

Extensive compilations of stress intensity factors are available in literature [8,9,10]. Some interesting cases are reproduced here.

Superposition is a simple technique in use for obtaining stress intensity factors. Complex configurations are considered to be a combination of a number of separate simpler configurations with separate boundary conditions and which have known stress intensity factors. As a generalization of this technique, the stress intensity factor for a crack in a loaded body may be determined by considering the crack to be in an unloaded body with applied tractions on the crack surface only (Fig.3.10). These surface tractions are equal in magnitude but opposite in sign to those evaluated along the line of the crack site in the uncracked configuration. Thus, for the pressurized fluid entering the crack, for example, the stress intensity factor is

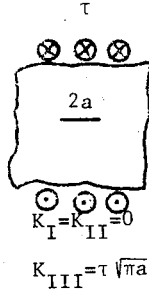
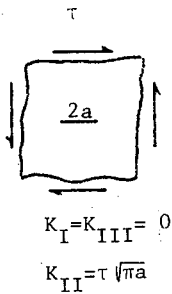
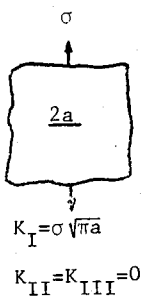
$$K_I = p \sqrt{\pi a}$$

where p denotes the pressure.

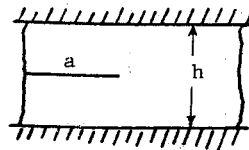
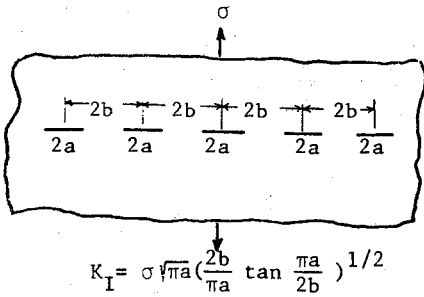
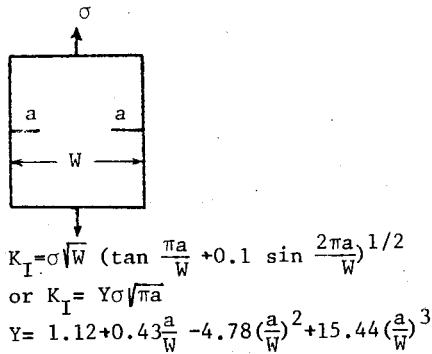
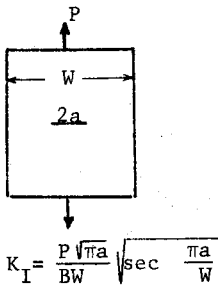
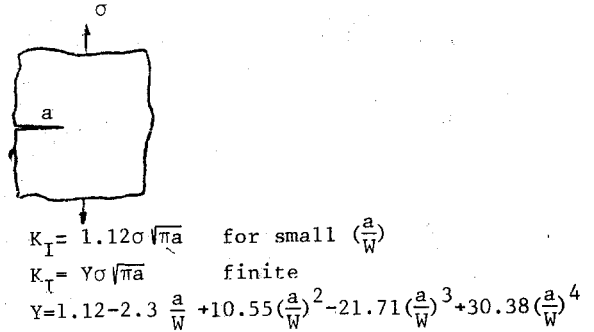
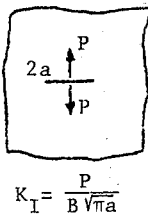
To calculate the stress intensity factors for cracks in residual stress fields, Green's functions are utilized. If the stresses along the crack site in the uncracked body are $\sigma_y(x)$ Fig.(3.11a)

$$K_I = 2 \sqrt{\frac{a}{\pi}} \int_0^a \sigma_y(x) \frac{1}{\sqrt{a^2-x^2}} dx \quad (3.15)$$

for symmetrical loadings at either crack tips, and



as obtained by Westergaard solutions



fixed grip conditions:
 $K_I = \sigma \left(\frac{h}{2} \right)^{1/2}$

Fig.3.9: K expressions for some simple geometry and loadings

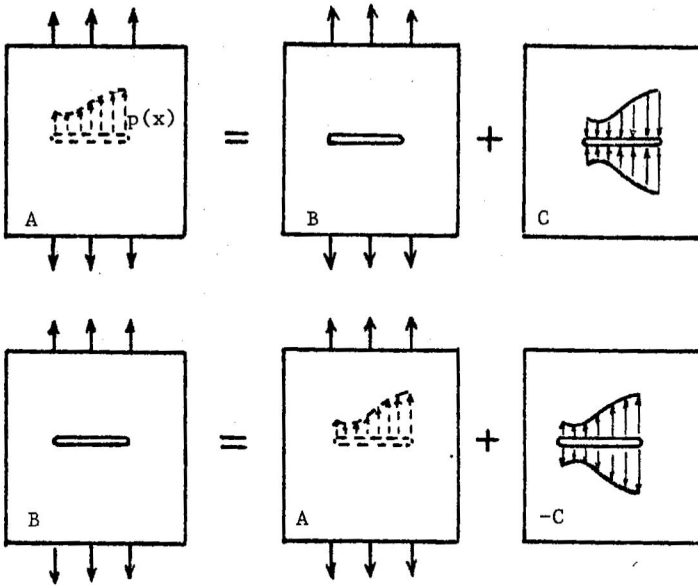


Fig.3.10- Method of superposition implies $K_{(B)} = K_{(-C)}$ since $K_A = 0$

$$K_I = \frac{1}{\sqrt{2\pi c}} \int_0^c \sigma_y(x) \frac{\sqrt{x}}{\sqrt{c-x}} dx \quad (3.16)$$

for unsymmetrical loading at $x = c$ (Fig.3.11b) [7]. These expressions

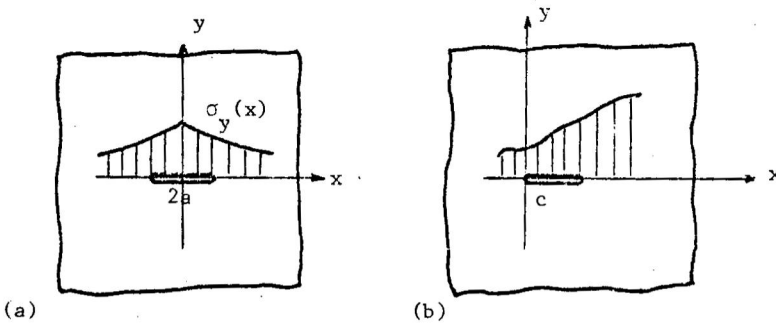


Fig.3.11- Stresses in the plane of the crack in the uncracked body
 (a) symmetrical (b) unsymmetrical

are particularly useful in welding problems where the stress intensity factor due to external loads is added to that due to residual stresses.

As the thickness of the component increases, possibility of finding through cracks decreases. Embedded internal flaws are more appropriate to consider, especially in welded structures. Flat elliptical crack in an infinite solid with its plane normal to applied stress σ is an idealized flaw geometry. The stress intensity factor varies along the periphery as a function of the angular coordinate ϕ : (Fig.3.12) [11]

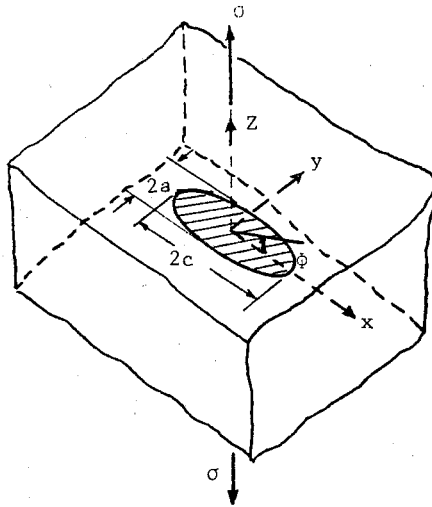


Fig.3.12- Elliptical Crack in an Infinite body subject to uniform tension

$$K(\phi) = \frac{\sqrt{\pi a}}{q} \left[\left(\frac{a}{c}\right)^2 \cos^2 \phi + \sin^2 \phi \right]^{1/4} \quad (3.17)$$

where a = semiminor, c = semi major axes

q = complete elliptical integral of the second kind

$$= \int_0^{\pi/2} \left[1 - (1 - a^2/c^2) \sin^2 \alpha \right]^{1/2} d\alpha, \text{ plotted in figure 3.13}$$

Series expansion of the elliptical integral shows that

$$q \approx \frac{3\pi}{8} + \frac{\pi}{8} \frac{a^2}{c^2}$$

for $a/2c$ between 0.3 and 0.5 which technically is the most important range. Maximum stress intensity factor is reached at $\phi=\pi/2$ and $K = \sigma \sqrt{\pi a/q^2} = \sigma \sqrt{\frac{\pi a}{Q}}$

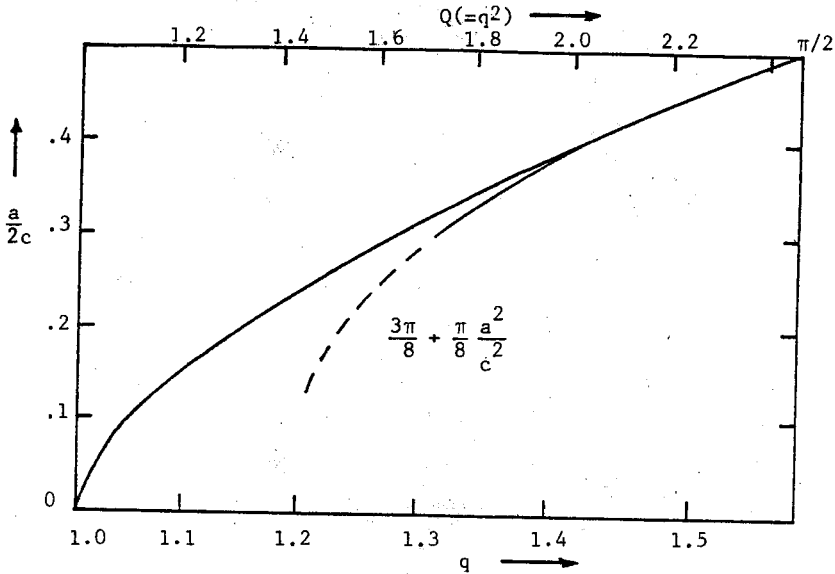


Fig.3.13: Elliptical flaw parameter q and $Q(= q^2)$ [12] .

Thus elliptical flaw grows fastest along the minor axis until the crack assumes a circular configuration. The circular crack is also called a "penny-shaped" crack with the stress intensity factor being

$$K = 2\sigma\sqrt{a/\pi} \tag{3.18}$$

A special case of the elliptical crack is the semi-elliptical surface flaw, thumbnail crack (Fig.3.14). The stress intensity factor is the same as the elliptical flaw (eq.3.17) corrected for the free surface effect. The free surface correction factors range from 1.12 for $a/c = 0$ to 1.03 for $a/c = 1$. If the crack protrudes deeply inward, the proximity of the back free surface also requires a correction to the stress intensity factor. This back-free-surface correction, M_R , is plotted in figure 3.15.

So far, the discussion centered on in-plane loading only. A practical problem arises in pressure vessels where bulging due to lateral forces of the pressure may lead to much higher stress intensity factors than that of flat plate solution. Due to this bulging (Fig.3.16a) not only the membrane(in-plane)

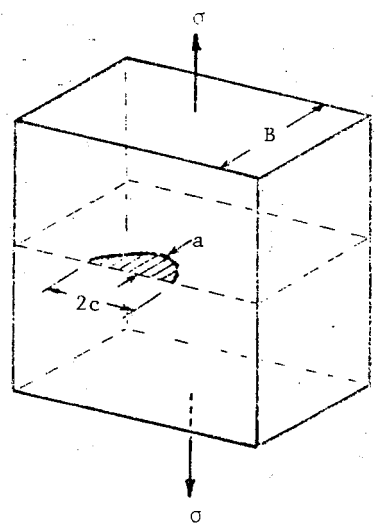


Fig.3.14- Part-through surface crack

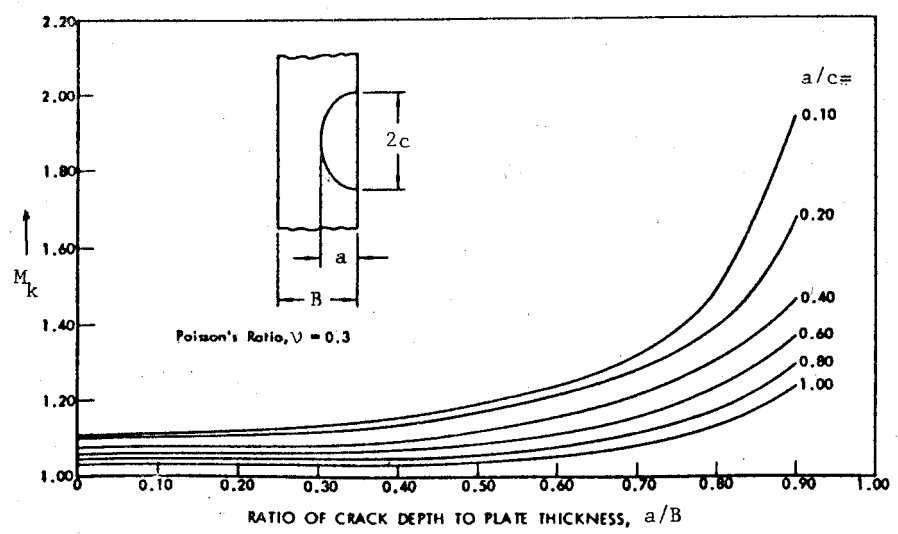


Fig.3.15- Stress Intensity Magnification M_k for surface cracks in tension [13]

loading increases but also a bending loading is introduced. The shell correction factors for longitudinal through cracks in shells can be empirically expressed by the approximations [14]

$$\frac{K}{K_{\text{flat plate}}} = \begin{cases} (1+1.25\lambda^2)^{1/2} & \text{for } 0 \leq \lambda < 1 \\ (0.6+0.9\lambda) & \text{for } 1 \leq \lambda \leq 5 \end{cases} \quad (3.19)$$

where $\lambda = a/\sqrt{Rt}$, R being the radius, t the wall thickness and a the half crack length. Similar expressions are developed for circumferential cracks but are of lesser interest since the applied longitudinal stresses are half of the hoop stresses. Closed form stress intensity factor expressions for various cracks in cylindrical vessels (Fig.3.16) are reported by Zahoor [15].

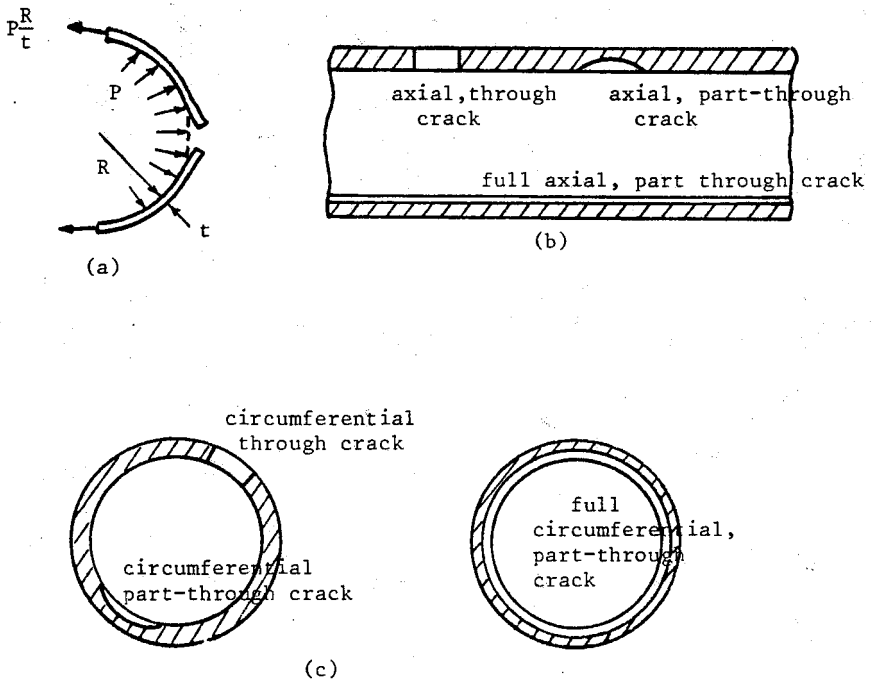


Fig.3.16- Various cracks in cylindrical vessels covered in [15]
 (a) bulging of axial through crack, (b) axial cracks
 (c) circumferential cracks.

Cracks emanating from a round hole is a common situation in riveted structures. As discussed in chapter two, the stress concentration associated with a circular hole is three. Thus, short cracks may be treated as single

edge-notched cases embedded within the local stress concentration sites (Fig.3.17)

$$K \approx 1.12 (3\sigma) \sqrt{\pi a} \quad a \ll R \quad (3.20)$$

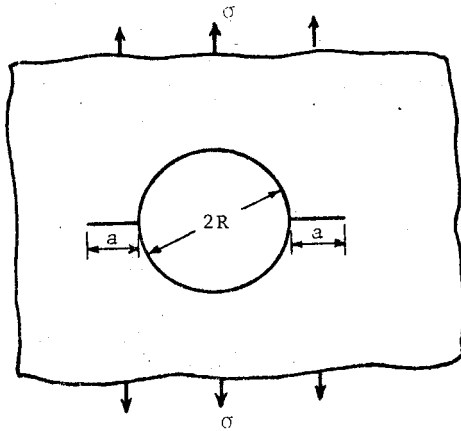


Fig.3.17- Cracks emanating from hole

As cracks grow they move rapidly away from the stress concentration region since concentration is very localized. At the other extreme, $a \gg R$, the crack size may be estimated as $\sqrt{2a+2R}$ for symmetrical cracks, leading to

$$K \approx \sigma \sqrt{\pi(a+R)} \quad (a > R) \quad (3.21)$$

and as $\sqrt{2R+a}$ for asymmetrical (single) crack, leading to

$$K \approx \sigma \sqrt{\pi \frac{(a+2R)}{2}} \quad (a > R) \quad (3.22)$$

The exact solution to the problem due to Bowie is tabulated in handbooks. If the stress intensity factor is written as

$$K = \sigma \sqrt{\pi a} f(a/R) \quad (3.23)$$

the nondimensional function f can be obtained from Table 3.1.

Table 3.1- Correction Factors for Cracks Emanating from a Hole [8]

a/R	One Crack, f(a/R)	Two Cracks, f(a/R)
0.0	3.39	3.39
0.1	2.73	2.73
0.2	2.30	2.41
0.3	2.04	2.15
0.4	1.86	1.96
0.5	1.73	1.83
0.6	1.64	1.71
0.8	1.47	1.58
1.0	1.37	1.45
1.5	1.18	1.29
2.0	1.06	1.21
3.0	0.94	1.14
5.0	0.81	1.07
10.0	0.75	1.03
∞	0.707	1.00

The structure of modern transport aircraft is essentially a thin sheel with stiffening elements. These stiffening elements, provided essentially for static strength, also act as skin crack arrestors by reducing the crack tip stress intensity factor sufficiently. Typically the effect of stiffeners is expressed as [16]

$$K = \beta \sigma \sqrt{\pi a} \quad (3.24)$$

where β is a correction due to all geometry effects, including the stiffener spacing, section properties, elastic-plastic properties, skin thickness, properties etc. The value of β can be less than unity when the crack tip is in the vicinity of an intact stiffener or greater than unity if the stiffener is broken. This is illustrated in figure 3.18 which shows $\beta (= K/\sigma\sqrt{\pi a})$ as a function of crack length for stiffeners spaced 8 in. apart with a cross-sectional area of 0.51 in². It can be seen that when the crack tip is in the vicinity of the broken stiffener, the value of β is high due to load redistribution from the broken stiffener into the cracked area.

This situation is relieved as the crack tip approaches the outer, intact stiffeners.

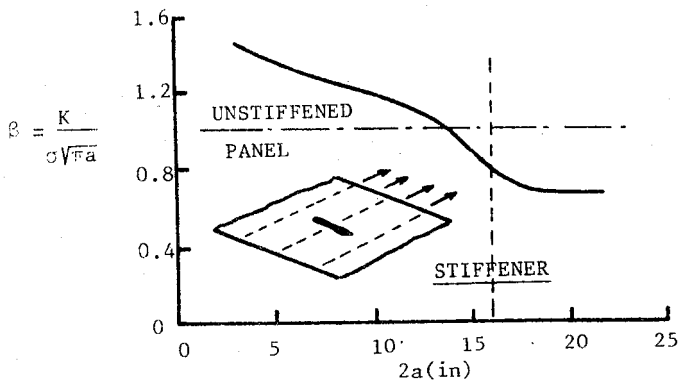


Fig.3.18- Effect of Stiffening on β [16]

3.3 EQUIVALENCE OF THE ENERGY AND THE STRESS INTENSITY FACTOR APPROACHES

The energy approach is physically appealing but the stress intensity approach has a marked advantage. Numerous K solutions are available for practical situations encountered, just as a by-product of elasticity problems. It is a vital step to show that, indeed, both approaches are the same, thus combining the advantages of both.

Irwin [17] considered plane strain conditions with fixed grips. Since it is shown that energy release rate does not depend on the boundary conditions, fixed grips condition can be assumed without loss of generality.

As the crack advances by a small amount da (Fig.3.19), the energy balance is achieved between the energy released ($GBda$) and the change in strain energy ($1/2$ Force displacement)

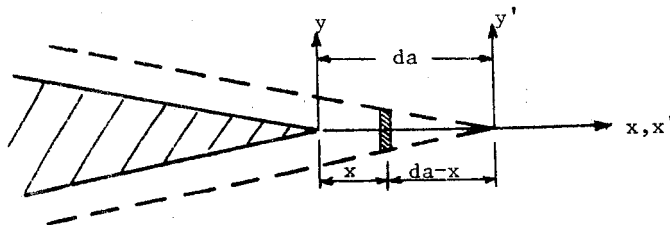


Fig.3.19- Geometry of advancing crack tip

$$\begin{aligned}
 \left. \begin{array}{l} \text{energy released} \\ \text{by crack extension} \end{array} \right\} &= \int \frac{1}{2} \left\{ \begin{array}{l} \text{stresses prior} \\ \text{to crack extension} \end{array} \right\} d\text{Area} \left\{ \begin{array}{l} \text{displacements} \\ \text{after crack ext.} \end{array} \right\} \\
 (\text{GB da}) &= \int_0^{\text{da}} \frac{1}{2} \left\{ \sigma_y \left(\begin{array}{l} \theta = 0 \\ r = x \end{array} \right) \right\} B dx \left\{ 2v \left(\begin{array}{l} \theta = \pi \\ r = \text{da} - x \end{array} \right) \right\} \\
 &= \int_0^{\text{da}} B \left\{ K_I / \sqrt{2\pi x} \right\} \left\{ (K_I / \tilde{G}) \left(\frac{\text{da} - x}{2\pi} \right)^{1/2} (2 - 2\nu) \right\} dx \\
 &= \frac{K_I^2 (1 - \nu) B}{\pi \tilde{G}} \frac{\pi}{2} da
 \end{aligned}$$

Thus,

$$G = \frac{K_I^2}{E} (1 - \nu^2) \quad (3.25)$$

for plane strain conditions and single tip. For central cracks involving two tips, the energy available is twice. For plane stress conditions, using the relevant displacement expressions

$$G = K_I^2 / E \quad (3.26)$$

In a three dimensional body with a crack edge subject to K_I, K_{II} and K_{III} , the energy release rate becomes

$$G = \frac{1 - \nu^2}{E} (K_I^2 + K_{II}^2) + \frac{1}{2\tilde{G}} K_{III}^2 \quad (3.27)$$

References

1- Griffith, A.A. "The Phenomena of Rupture and Flow in Solids"
Phil. Trans., Royal Society of London, 221A, (1920) pp 163-198.

2- Irwin, G.R., "Fracture Dynamics" Fracturing of Metals, ASM,
Cleveland, Ohio (1949) pp 147-166.

3- Eftis, J. and Liebowitz, H. "On Fracture Toughness Evaluation for Semi-brittle Fracture" Engineering Fracture Mechanics, 7, (1975) pp.101-135.

4- Hutchinson, J.W. "A Course on Nonlinear Fracture Mechanics" Tech.Univ. of Denmark (1979) p.7.

5- Mostovoy, S, Crosley P.B. and Ripling E.J., Journal of Materials, Vol.2 No.3 1967, pp.661-681

6- Fichter, W.B. "The Stress Intensity Factor for the Double Cantilever Beam" International Journal of Fracture, 22, (1983), pp 133-143.

7- Barenblatt, G.I. "The Mathematical Theory of Equilibrium Cracks in Brittle Fracture" Advances in Applied Mechanics, Vol.7, Academic Press, New York (1962) pp.55-129.

8- Sih, G. Handbook of Stress Intensity Factors, Lehigh University (1973)

9- Tada, H., Paris, P.C. and Irwin, G.R. The Stress Analysis of Cracks Handbook, Del Research, Hellertown, Pa (1973).

10- Rooke, D.P. and Cartwright, D.J. Compendium of Stress Intensity Factors, Her Majesty's Stationery Office, London (1976).

11- Irwin, G.R. "The Crack Extension Force for a Part Trough Crack in a Plate" Journal of Applied Mechanics, Transactions ASME, 29, (1962) pp.651-654.

12- Broek, D. "Fracture" Agard Lecture Series No.97: Fracture Mechanics Design Methodology, NATO, (1979) p.2.14.

13- Shah, R.C. and Kobayashi, A.S. "Stress Intensity Factors for an Elliptical Crack Approaching the Surface of a Plate in Bending" ASTM STP 513, Amer.Soc.for Testing and Materials (1972) pp.3-21.

14- Paris, P.C. and Johnson, R.E. "A Method of Application of Elastic-Plastic Fracture Mechanics to Nuclear Vessel Analysis" ASTM STP 803, Amer.Soc.for Testing and Materials, (1983) pp.II.5-40.

15- Zahoor, A. "Closed Form Expressions for Fracture Mechanics Analysis of Cracked Pipes" Journal of Pressure Vessel Technology, Transactions ASME, 107, (1985) pp.203-205.

16- Swift, T. "Damage Tolerance Analysis of Redundant Structures" Agard Lecture Series No.97: Fracture Mechanics Design Methodology, NATO, (1979), p.5.2.

17- Irwin, G.R. "Analysis of Stresses and Strains Near the End of a Crack Traversing a Plate" Journal of Applied Mechanics, Transactions ASME, 24, (1957) pl.361-364.

Problems:

1- Obtain an expressions for K_I for double cantilever beam specimen loaded by end moments.

$$\text{Answer: } (M/B) (3/2h^3(1-\nu^2))^{1/2}$$

2- Show that the compliance C of the plate containing a through crack of length $2a$ is related to that of the uncracked plate C_0 by $C/C_0 = 1 + 2\pi a^2/hW$ where W is the width, h is the height of the plate.

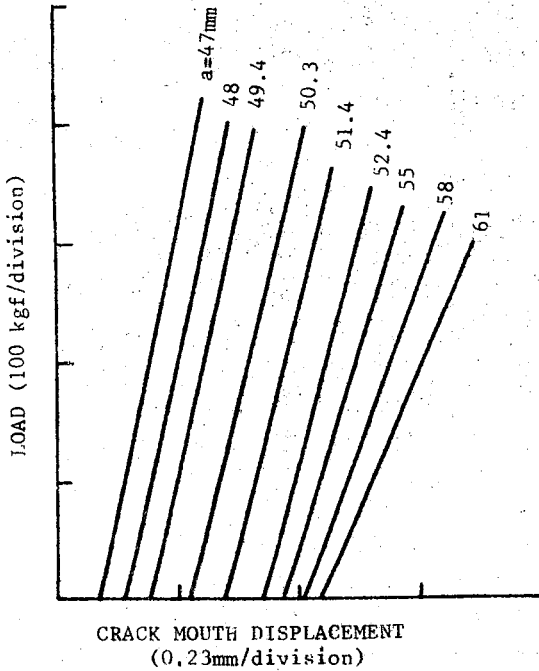
3- A large plate is clamped at the ends but no external loads are applied. Estimate the temperature drop that will cause catastrophic propagation of a 75 mm long through crack if the plate is made of 25mm thick high strength steel having $S_y = 1400$ MPa, $G_{IC} = 0.01$ MPa-m.

$$\text{Answer: } 60^\circ\text{C}$$

4- As an exercise in compliance calibration, the geometry of fig. 5.3 is used and load vs. crack mouth displacement is recorded each time after the crack is extended slightly by sawing. Using the supplied data you are asked to obtain the K value at a crack length of 50 mm.

This geometry happens to be a standard fracture specimen for which an exact K expression is available. Thus, you have the chance of comparing your result with the one obtained through eq.5.3. The material is an Al-

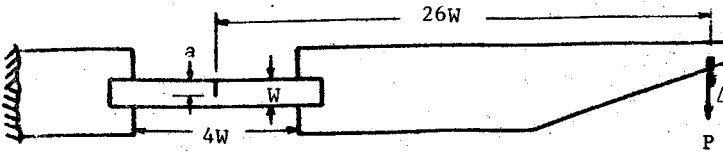
alloy and $W = 100$ mm, $B = 12.5$ mm.



Answer:

$K = 11P/B\sqrt{W}$ versus $9.6 P/B\sqrt{W}$
as obtained from eq.5.3

5- A stress-corrosion study uses single edge cracked specimens in cantilever bending as shown below (Lisagor, STP821, 1984)



Experimental data is fitted with a polynomial expression

$$EBW \frac{\Delta}{M} = \exp \left[6.188 + 12.98 \frac{a}{W} - 41.99 \left(\frac{a}{W}\right)^2 + 54.98 \left(\frac{a}{W}\right)^3 - 22.28 \left(\frac{a}{W}\right)^4 \right]$$

Compute the stress intensity factor for this specimen and compare the results with the ones calculated through K_I expression of three point bend specimen given in eq.5.2. Tabulate $\{K_I BW^2/6M\sqrt{a}\}$ versus $\{a/W\}$ for $0.40 < a/W < 0.70$.

Answer: a/W	.4	.5	.6	.7
Experimental{	1.5	2.3	3.3	4.8
3PB { }	2.2	2.6	3.4	4.9

4. SMALL SCALE YIELDING FRACTURE MECHANICS

Materials have been treated so far as linear elastic independent of the load levels attained. Some amount of yielding is unavoidable in real materials, however, due to the severe elevation of stress at the crack tip. In this chapter, materials and geometries are treated which have limited amount of plastic deformation during loading—up to the point of fracture. High strength steels, aluminum alloys and low-to intermediate-strength steels below the transition temperature range, at sufficiently large sizes, usually fit in this category.

4.1 ESTIMATION OF PLASTIC ZONES BASED ON ELASTIC STRESS DISTRIBUTION

To get a rough feeling about the extent of the plastic zone size, Westergaard solutions may be used together with a yield criterion, say Von Mises criterion. Strictly speaking it is not possible to use the elastic distribution to solve for the growing elastic plastic boundary but an estimate may be obtained. Von Mises criterion reads

$$\bar{\sigma} = \frac{1}{\sqrt{2}} \{ (\sigma_x - \sigma_y)^2 + (\sigma_y - \sigma_z)^2 + (\sigma_z - \sigma_x)^2 + 6\tau_{xy}^2 \}^{1/2} \geq S_y \quad (4.1)$$

where S_y is the yield strength of the material and $\bar{\sigma}$ is the equivalent stress. For plane stress conditions $\sigma_z = 0$. In mode I loading, using eq. 2.25 and 2.26, the yield condition becomes

$$\bar{\sigma} = \frac{1}{\sqrt{2}} \frac{K_I}{\sqrt{\pi r}} \cos \frac{\theta}{2} (1 + 3\sin^2 \theta/2)^{1/2} \geq S_y$$

or

$$r < \frac{1}{2} \left(\frac{K_I}{\sqrt{\pi} S_y} \right)^2 \cos^2 \frac{\theta}{2} \{ 1 + 3\sin^2 \frac{\theta}{2} \} \quad (4.2)$$

For plane strain, $\sigma_z = \nu(\sigma_x + \sigma_y)$. Thus $\bar{\sigma} = S_y$ condition leads to

$$r \leq \frac{1}{2} \left(\frac{K_I}{\sqrt{\pi} S_y} \right)^2 \cos^2 \frac{\theta}{2} \left\{ (1-2\nu)^2 + 3 \sin^2 \frac{\theta}{2} \right\} \quad (4.3)$$

The plastic zones described by eq's 4.2 and 4.3 are shown in figure 4.1. It is evident that plane stress leads to much larger plastic zone than

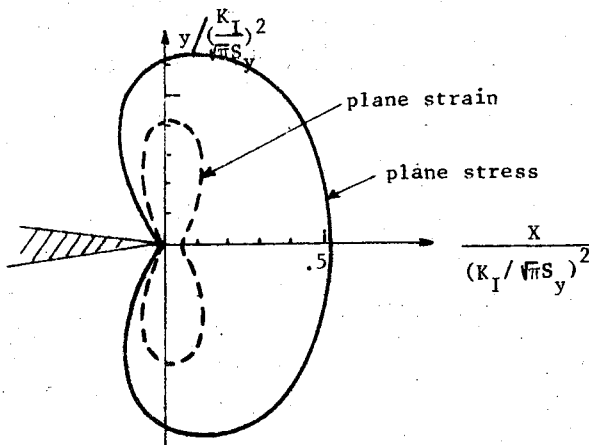


Fig.4.1- Plastic zone shapes in Mode I loading so obtained from elastic solutions [1]

than plane strain condition. Analogous calculations may be performed for mode II loading leading to

$$r \leq \frac{1}{2} \left(\frac{K_{II}}{\sqrt{\pi} S_{sy}} \right)^2 \left\{ 1 + \frac{1}{3} \sin^2 \frac{\theta}{2} - 3 \cos^2 \frac{\theta}{2} \sin^2 \frac{\theta}{2} \right\} \quad (4.4)$$

for plane stress, and to

$$r \leq \frac{1}{2} \left(\frac{K_{II}}{\sqrt{\pi} S_{sy}} \right)^2 \left\{ 1 + \frac{1}{3} \sin^2 \frac{\theta}{2} - \frac{2}{3} \nu(1-\nu) \sin^2 \frac{\theta}{2} - 3 \cos^2 \frac{\theta}{2} \sin^2 \frac{\theta}{2} \right\} \quad (4.5)$$

for plane strain, where S_{sy} denotes the yield strength in shear. These zones are depicted in figure 4.2.

For mode III loading we only have shear components (eq.2.48,2.49) leading to (Fig.4.3)

$$\bar{\sigma} = \sqrt{3} \frac{K_{III}}{\sqrt{2\pi r}} \geq S_y$$

or

$$r < \frac{1}{2} \left(\frac{K_{III}}{\sqrt{\pi} S_{sy}} \right)^2 \quad (4.6)$$

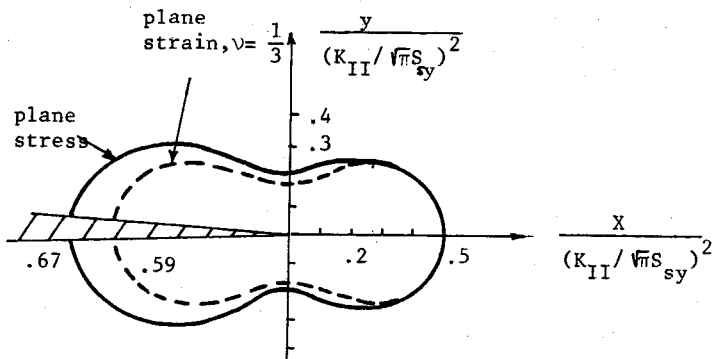


Fig.4.2- Plastic zone shapes in Mode II loading as obtained from elastic solutions

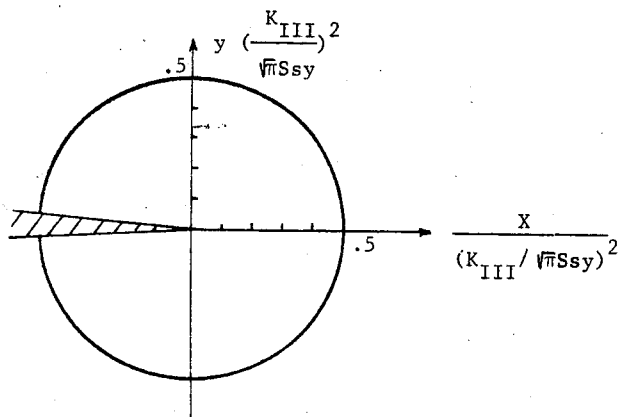


Fig.4.3- Plastic zone shape for mode III loading as obtained from elastic solutions.

4.2 THE IRWIN PLASTIC ZONE CORRECTION FOR PLANE STRESS

Estimates presented in the previous section show that the distance ahead of the mode I crack at which the elastic stresses exceed yield is

$$x_y = \frac{1}{2\pi} \left(\frac{K_I}{S_y} \right)^2$$

This implies for an elastic-perfectly plastic material that $\sigma_y = S_y$ for $0 < x < x_y$ (since $\sigma_x = \sigma_y$ and $\sigma_z = 0$). But such a stress distribution leads to the violation of static force balance, since by truncating the elastic stress distribution at $x = x_y$, the load carrying capacity is decreased (Fig.4.4). In fact, the loss in load carrying capacity is

$$\int_0^{x_y} \frac{K_I}{\sqrt{2\pi x}} dx - S_y \cdot x_y = \frac{K_I}{\sqrt{2\pi}} \cdot 2 \sqrt{x_y} \frac{S_y}{S_y} - S_y x_y = S_y x_y$$

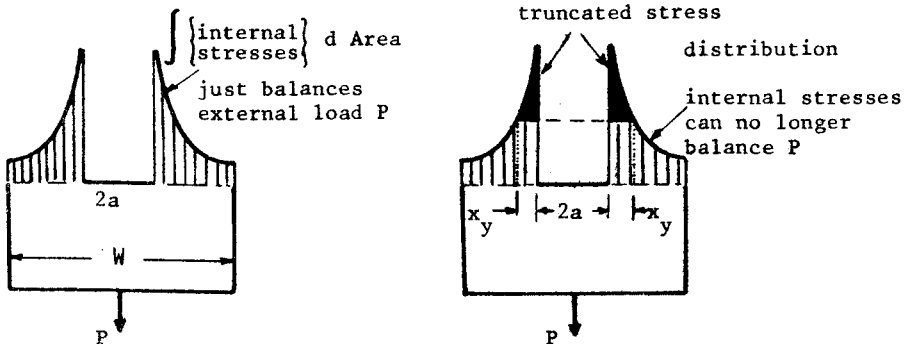


Fig.4.4- Force unbalance due to truncation of elastic stress distribution

It is clear that simple truncation of the elastic distribution at the yield strength does not lead to an acceptable estimate of the plastic zone size. To obtain an elastic plastic stress distribution with the same area under it as the original elastic stress distribution one could move the elastic stress distribution forward by an amount x_y - i.e assume that the plastic zone extends by $2x_y$ (Fig.4.5).

This approach is purely intuitive and is due to Irwin [2]. It is supported by a similar situation in mode III. For mode III loading,

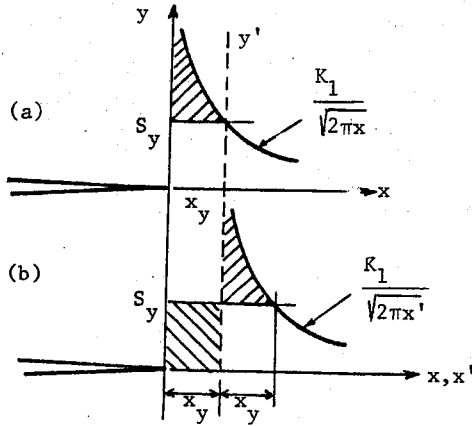


Fig.4.5- Extent of the plastic zone along the x-axis:(a) that of Sec.4.1 (b) more refined one suggested by Irwin

rigorous elastic plastic solution is obtained and this indicates that the plastic zone at the tip is indeed a circle of $r_y = (1/2\pi)(K_{III}/S_{sy})^2$, the center being, however, at $x = r_y$ and not at $x = 0$ (Fig.4.6). In addition to this, the stresses in the elastic region can be calculated from a purely elastic solution by replacing the actual crack length "a" by "a+r_y"

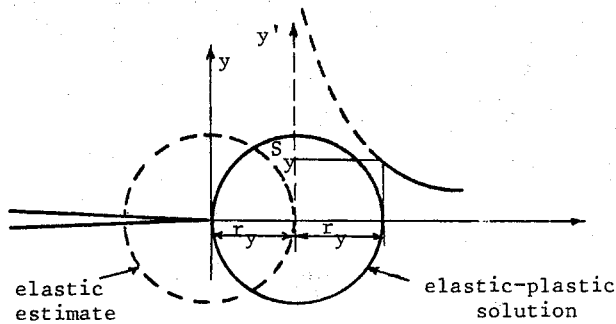


Fig.4.6- Plastic zone size comparisons in mode III-rigorous solution versus the estimation of Sec.4.1.

Since exact solutions of the elastic plastic medium for mode I and II loadings are too complicated, Irwin assumed-based on mode III and the

intuitive argument for the "lost load carrying capacity"- that the plastic zone in mode I extends ahead of the crack by

$$2r_y = \frac{1}{\pi} \left(\frac{K_I}{S_y} \right)^2 \quad (4.7)$$

the exact boundaries being rather vague (Fig.4.7). He also assumed that using $a+r_y$ as the effective crack length the stresses in the elastic region can be calculated through the elastic singularity fields.

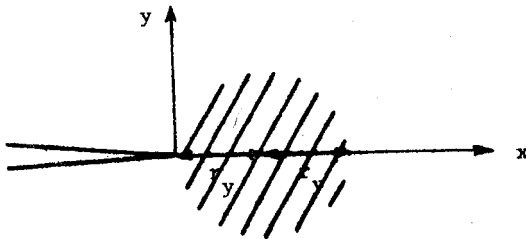


Fig.4.7- The plastic zone of Irwin.

This approach is, of course, empirical and its main justification is that approximately the same fracture toughness is obtained from plane stress fracture toughness tests using varying crack lengths.

For the familiar geometry of infinite plate (Fig.4.8). $K_I = \sigma\sqrt{\pi a}$ and using the effective crack length instead of the physical crack length

$$r_y = \frac{1}{2\pi} \left(\frac{K_I}{S_y} \right)^2 = \frac{1}{2\pi} \frac{\sigma^2 \pi (a+r_y)}{S_y^2}$$

or

$$r_y = \frac{1/2 (\sigma/S_y)^2 a}{1-1/2 (\sigma/S_y)^2} \quad (4.8)$$

which is the "corrected" Irwin plastic zone radius as opposed to the "uncorrected" Irwin plastic zone radius

$$r_y = \frac{1}{2} (\sigma/S_y)^2 a \quad (4.9)$$

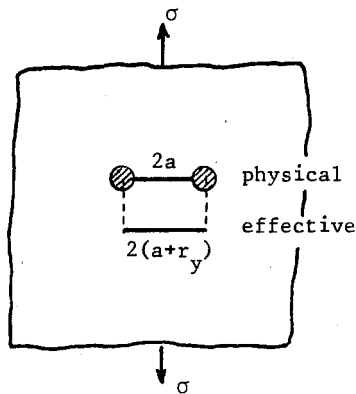


Fig.4.8- Small scale yielding of the center cracked panel.

4.3 THE DUGDALE MODEL

Another estimation model of the plastic zone is the "strip yield model" [3]. It is valid for large plates in plane stress state and for elastic-perfectly plastic materials. Dugdale assumed that the plastic zone forms essentially as an extension of the crack which is verified experimentally for thin mild steel sheets.

Dugdale argued that the crack of length $2a$ plus the plastic zones at both tips of length s can be obtained by the superposition of two separate cases, as discussed in Sec.3.2.1; a crack of length $2\ell = 2a + 2s$ subject to remote stress σ plus a crack of length $2\ell = 2a + 2s$ subject to $\sigma = S_y$ along the crack faces at both tips, representing the strip yield regions (Fig.4.9).

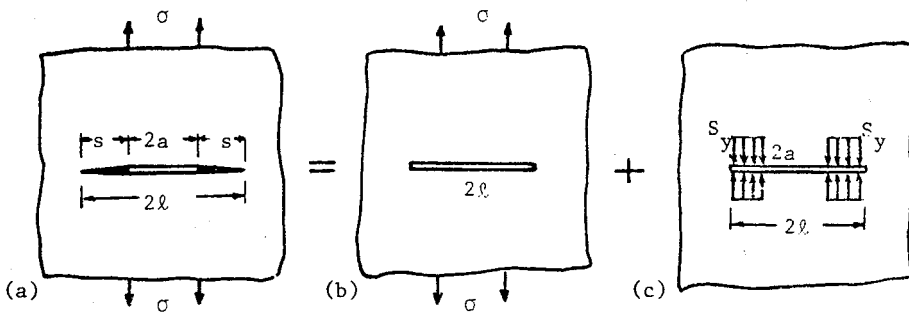


Fig.4.9- The Dugdale model (a) as a superposition of two simple cases (b) and (c).

Following Barenblatt's argument, the stress intensity at the end of the plastic zone must be zero, that is, the plastic zone s must be of such length that K due to remote stress σ equals the K due to S_y on faces of the crack.

$$\text{For Fig.4.9(b) : } K = \sigma\sqrt{\pi\ell}$$

$$\begin{aligned} \text{For Fig.4.9(c) : } K &= 2 \frac{\ell}{\pi} \int_0^{\ell} \frac{\sigma_y dx}{\sqrt{\ell^2-x^2}} = 2 \frac{\ell}{\pi} S_y \int_a^{\ell} \frac{dx}{\sqrt{\ell^2-x^2}} \\ &= 2 \frac{\ell}{\pi} S_y \arccos \frac{a}{\ell} \end{aligned}$$

Thus,

$$\sigma\sqrt{\pi\ell} = 2 \frac{\ell}{\pi} S_y \arccos \left(\frac{a}{\ell} \right)$$

gives

$$\frac{s}{\ell} = 1 - \cos \left(\frac{\sigma}{S_y} \frac{\pi}{2} \right) = 2 \sin^2 \left(\frac{\sigma}{S_y} \frac{\pi}{4} \right)$$

For $\sigma/S_y \ll 1$, $\sin x \approx x$ and

$$s = \frac{\sigma^2 \pi a}{S_y^2} \frac{\pi}{8} = \frac{\pi}{8} \left(\frac{K_1}{S_y} \right)^2 \quad (4.10)$$

which is very close to $2r_y = K_1^2/\pi S_y^2$ as Irwin predicts. For small σ/S_y , values, the extent of the plastic zone along the x -axis is approximately the same in both the Dugdale and Irwin models, but the general shape of the zones is quite different. For large values of σ/S_y ,

$$\frac{s}{a} = \frac{s/\ell}{a/\ell} = \frac{2 \sin^2 \left(\frac{\pi}{4} \frac{\sigma}{S_y} \right)}{1 - 2 \sin^2 \left(\frac{\pi}{4} \frac{\sigma}{S_y} \right)} \quad (4.11)$$

which is compared with the Irwin predictions on figure 4.10.

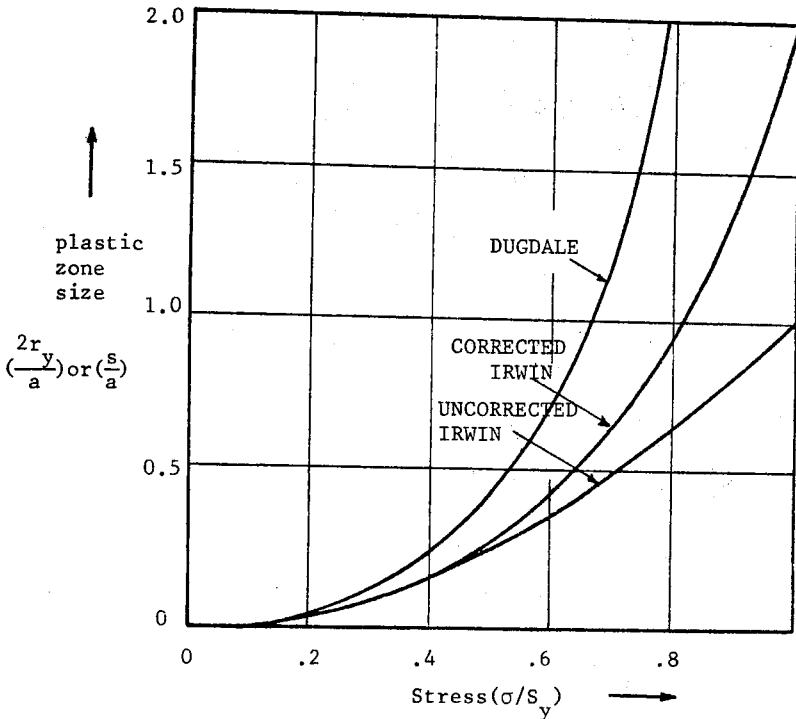


Fig.4.10- Comparison of plastic zone sizes for for center cracked panel.

In rectangular specimens (200mmx360mm) with a central cut the strip yield zones are observed [4]. In mild steel with $S_y \approx 200-250\text{MPa}$ and thickness of 1 and 2mm (Fig.4.11a) a dull spot appears initially at the tips for $\sigma/S_y \approx 0.35$. Narrow wedge-like plastic bands elongate ahead of the cut as loading increases. At about $\sigma/S_y \approx .75-.92$, additional thin plastic bands spread at an angle of 47.5° to 51° (Fig.4.11d).

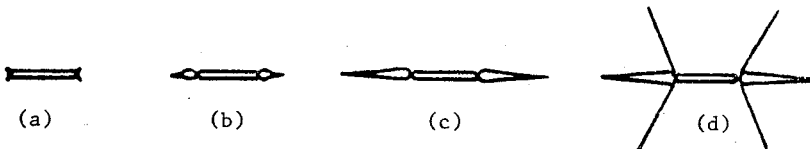


Fig.4.11- Spread of the plastic zone in mild steel sheets [4].

4.4 PLANE STRESS VERSUS PLANE STRAIN

Generally quoted conditions are that

$$\left. \begin{array}{l} r_y > B \quad \text{implies plane stress} \\ r_y \ll B \quad \text{implies plane strain} \end{array} \right\} \quad (4.12)$$

Thus, both the thickness of the component and the applied load play an important role. At low stress levels, even in thin samples, plastic zone size is so small that $B \gg r_y$ and a plane strain condition exists. With increasing stress level, a transition from plane strain to plane stress is observed. This transition takes place at higher stress in thick specimens. Typically for $B = 0.4\text{mm}$ the transition occurred at $\sigma/S_y = 0.4$ while for $B = 5\text{mm}$ at $\sigma/S_y = 0.9$ for a particular alloy [4]. Hahn and Rosenfield [5] have revealed the plastic zones by etch-pitting an iron-silicon alloy which confirms the various stages described above (Fig.4.12).

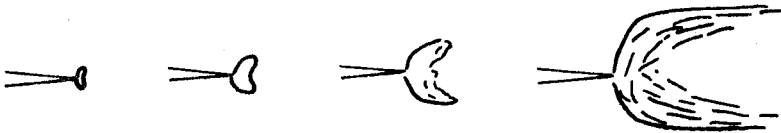


Fig.4.12-Development of the plastic zone as the loading increases.

A simple minded approach considering just the stresses along the crack plane(x-axis) shows that much higher stresses exist in the plastic zone in plane strain conditions and that the plastic zone size is much smaller. In plane stress, $\sigma_y > 0$, $\sigma_x \geq 0$, $\sigma_z = 0$ along the crack plane. Shear stress being zero, $\sigma_y = \sigma_1$ (maximum principal stress), $\sigma_z = \sigma_3$ (minimum principal stress). Hence, yield condition dictates that

$$\sigma_y = S_y$$

in the plastic zone, in plane stress. On the other hand, for plane strain conditions $\sigma_z = \nu(\sigma_x + \sigma_y)$ and as the plastic zone is approached from the

elastic region $\sigma_y = \sigma_x$, $\sigma_z = 2\nu\sigma_y$. Maximum shear criterion gives

$$\sigma_y = \frac{S}{1-2\nu} \approx 3S_y$$

for $\nu = 1/3$. Right at the crack tip blunting occurs and $\sigma_x = 0$ which implies that $\sigma_y = S_y$ in the proximity of the tip. Figure 4.13 indicates the striking differences in the stress levels and the plastic zones. The higher stress and the lower plastic zone size is due to the "thickness constraint" in plane strain—as if the neighboring elastic material does not allow for plastic deformation. For $\theta \neq 0$, $\sigma_y > \sigma_x$, thus $\sigma_z < 2\nu\sigma_y$.

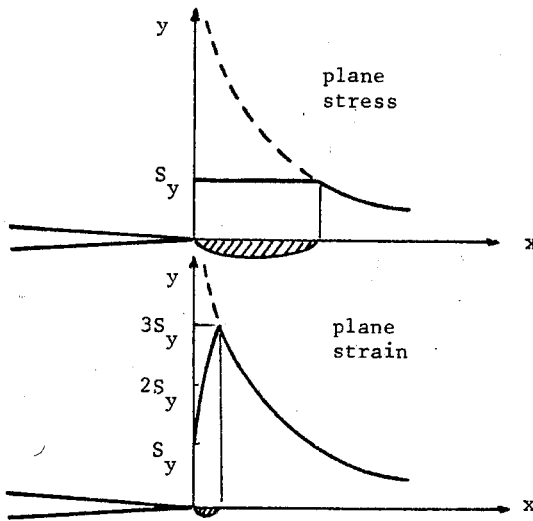


Fig.4.13- Sketch of the stress elevation in plane strain.

This implies that the constraint is less and the plastic zone size is larger off the x-axis, which fully coincides with observed behavior (Fig.4.12).

Another striking difference of plane stress and plane strain behavior is associated with the slip planes. In plane stress, σ_z being zero the maximum shear stress acts in the y-z plane (Fig.4.14a). In plane strain, $\sigma_z \approx 1/2(\sigma_x + \sigma_y)$ in the plastic zone. For $\theta = 0$ $\sigma_x = \sigma_y$, but for $\theta \neq 0$ $\sigma_x < \sigma_y$ and σ_x becomes the minimum principal stress. Thus, the Mohr circle construction shows the maximum shear stress to act in the x-y plane.

(Fig.4.14b) and to be much smaller in magnitude compared to plane stress.

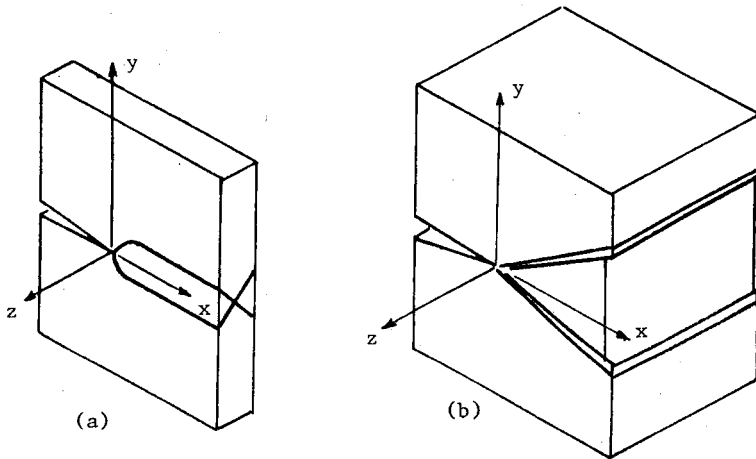


Fig.4.14- Deformation patterns (a) plane stress (b) plane strain.

The size of the plastic zone being large in plane stress implies that more energy is dissipated in thin components than thick ones. Fracture toughness is a strong function of thickness, B (Fig.4.15). Beyond a certain thickness it approaches a minimum value, called plane strain fracture toughness, K_{IC} . For thinner samples toughness value, denoted K_C , rises up to a maximum which can be 3-5 times the minimum value. If the sample were made still thinner, the toughness would gradually decrease because less material would be available for plastic deformation [6]. As thickness changes, a transition in the fracture mode also occurs (Fig.4.15). Slant fracture is observed in thin sheets in agreement with the slip planes discussed above. As thickness increases the fracture surface becomes flat or square. The shear lips signify the plane stress conditions prevailing at the free surfaces and are mostly associated with intermediate thicknesses. In many engineering materials such as aluminum, titanium and steel alloys there is one-to-one correspondence between the fracture mode (flat/slant) and the stress state (plane strain/plane stress). Beryllium, however, exhibits square fracture even under plane stress conditions. For intermediate thicknesses the size of the shear lips roughly coincides with the size of the plastic zone. This enables one to estimate K_I through the expression

$$D = r_y = \frac{1}{2\pi} \left(\frac{K_1}{S_y} \right)^2 \quad (4.13)$$

where D is the depth of shear lips. Ferritic and pearlitic steels tend to exhibit smaller shear lips than that expected through the above expression.

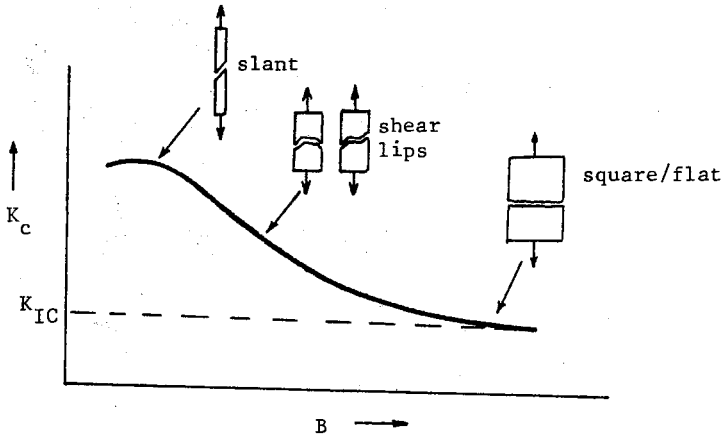


Fig.4.15- Variation of fracture toughness with thickness

The plastic zone size in plane strain state is much smaller than that in plane stress as the heuristic arguments imply. The fact that the normal stress σ_y increases up to $3S_y$ within the plastic zone may be looked upon as if the materials yield strength is elevated to $3S_y$ (Fig.4.13). Due to the absence of constraint on free surfaces, the plastic zone is nonuniform in thickness direction (Fig.4.16). The overall constraint amounts to less than three, leading to an effective yield strength in

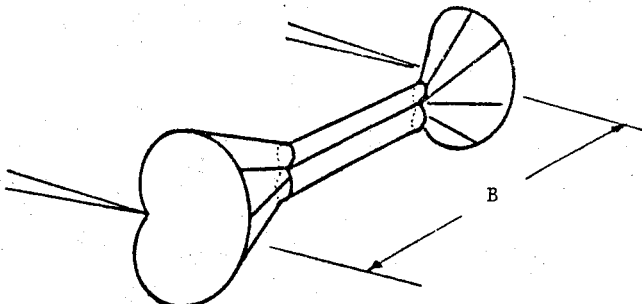


Fig.4.16- Schematic representation of the plastic zone size variation along the thickness

the range of $\sqrt{3}$ to 2 times S_y . Thus, the plastic zone radius in plane strain is assumed to be

$$r_y^{\text{plane strain}} = \frac{1}{2\pi} \left(\frac{K_{IC}}{\sqrt{3} S_y} \right)^2 \quad (4.14)$$

Since K_{IC} is smaller than K_C (Fig.4.15) the plastic zone size in plane strain is much smaller-almost an order of magnitude smaller-than the plastic zone in plane stress. Thus, no plastic zone correction is made for plane strain conditions, in general. The symbol r_y will be reserved for plane stress conditions.

The term S_y represents the yield strength of the material. But the same term in eq.4.7 is also an approximate estimate of the average y direction tensile stress, σ_y , across the crack tip plastic zone. When strain hardening is small, this effective yield strength coincides with the physical (usually 2% offset) yield strength. When strain hardening is large an average of yield and ultimate strengths is more appropriate. Thus, it is more general to define the plane stress zone size as

$$r_y = \frac{1}{2\pi} \left(\frac{K_I}{\sigma_o} \right)^2 \quad (4.15)$$

where σ_o is S_y or $\frac{1}{2} (S_y + S_u)$ for nonstrainhardening or heavily strain hardening materials, respectively.

4.5 LIMITATIONS ON PLASTIC ZONE SIZE

As long as the elastic singularity fields give a good approximation to the actual fields, fracture may be predicted by a single parameter, K or G . And this will be possible only if the plastic zone at the crack tip is sufficiently small-compared to the crack length, remaining ligament and other relevant geometric length quantities; that is, if the small yield zone will act only as a small perturbation on the elastic field and the elastic analysis may be corrected through an effective crack length.

At the crack tip we recognize several regions (Fig.4.17). To continue to use a single parameter in fracture prediction ($K = K_C$ type of a criterion) beyond initial yielding, the plastic zone should be much

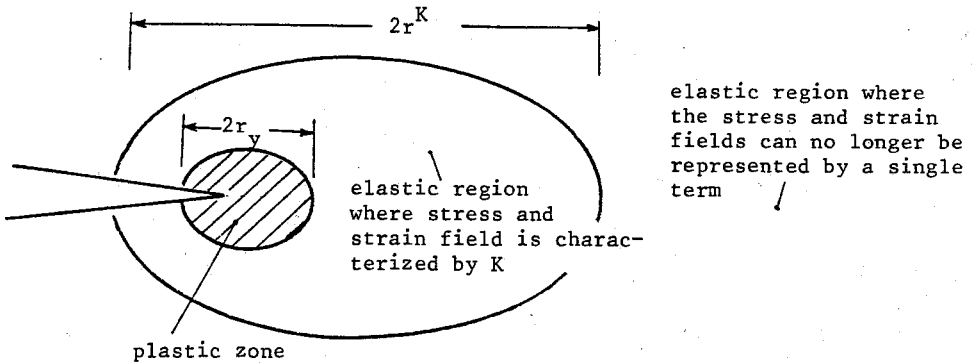


Fig.4.17- Crack tip regions in small scale yielding

smaller than the K-dominated region, such that the elastic singularity fields still give a good approximation to the actual fields in an annular region surrounding the tip. This is an asymptotic condition which is increasingly violated as the load increases.

The K-dominated region can be best viewed through figure 4.18. Here, for widely different cracked body configurations the accuracy of a one term (or K-characterization) of the elastic crack-tip stress components is compared against values obtained using several terms in the series expansion. If (r^K/a) represents the ratio for which singular term gives an acceptable level of approximation for the crack-tip stress field (that is, $r^K =$ radius of K-dominated field), then Irwin's correction procedure will be applied for r/a such that

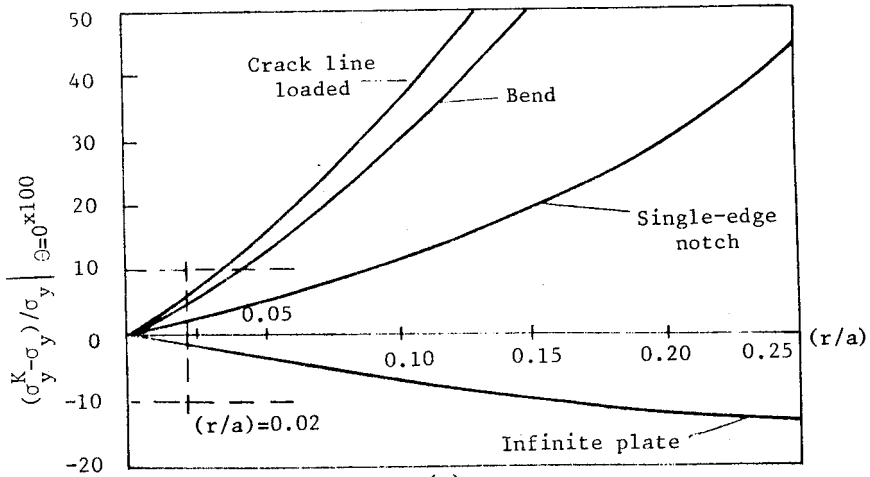
$$\frac{r_y}{a} < \frac{r}{a} < \frac{r^K}{a}$$

After extensive testing, the limiting condition has been set as

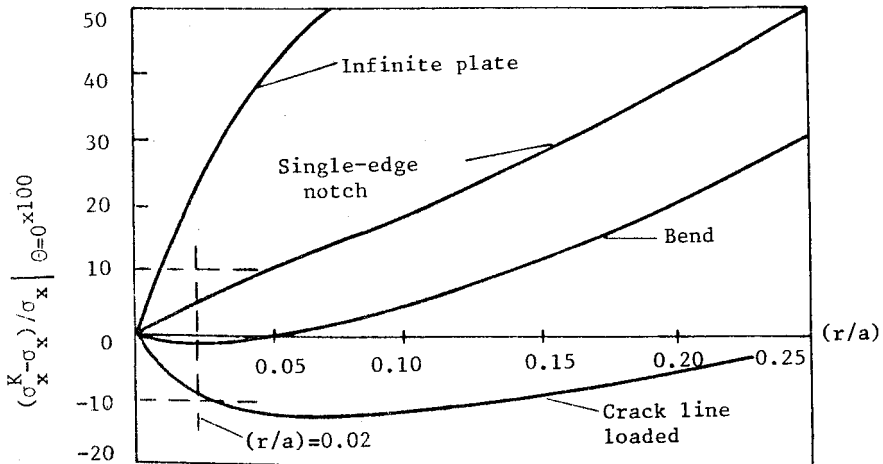
$$\frac{r_y^{\text{plane strain}}}{a} \leq 0.02 \quad (4.16)$$

or

$$\frac{1}{6\pi} \left(\frac{K_{IC}}{S_y} \right)^2 \leq \frac{1}{50} a$$



(a)



(b)

Fig.4.18- Comparison of stresses obtained through K with exact values
 (a) σ_y (b) σ_x [7]

Thus, for the small scale yielding approximation to hold

$$a \geq 2.5 \left(\frac{K_{IC}}{S_y} \right)^2 \quad (4.17)$$

To get repeatability (i.e. for the toughness to be a true material property), plane strain condition should also be met. The limiting condition has been

set as $B \geq 15 r_y$ (or $B \geq 50 r_y$ plane strain), which implies

$$B \geq 2.5 \left(\frac{K_{IC}}{S_y} \right)^2 \quad (4-18)$$

Note that these limitations are empirical, reflecting experience gained over many years.

It is quite difficult to set sharp limits to the range of small scale yielding approach, but roughly speaking, small scale yielding appears to be a reasonable assumption as long as the applied load is below about one half of the load at which full plastic yielding occurs—which corresponds to one half of the limit load for an elastic-perfectly plastic solid.

References

- 1- McClintock, F.A. and Irwin, G.R. "Plasticity Aspects of Fracture Mechanics" ASTM STP 381, Amer.Soc. for Testing and Materials (1965), pp.84-113
- 2- Irwin, G.R. "Plastic Zone Near a Crack and Fracture Toughness" in Proceedings, Seventh Sagamore Ordnance Materials Research Conference, (1960) Syracuse University Press
- 3- Dugdale, D.S. "Yielding of Steel Containing Slits" Journal of the Mechanics and Physics of Solids, 8, (1960) pp.100-104
- 4- Parton, V.Z. and Morozov, E.M. Elastic-Plastic Fracture Mechanics, Mir Publishers, Moscow (1978) p.156
- 5-Hahn, G.T. and Rosenfield, A.R. "Local Yielding and Extension of a Crack Under Plane Stress" Acta Met.13,(1965) pp.263-306
- 6- Hertzberg, R.W., Deformation and Fracture Mechanics of Engineering Materials, John Wiley, New York (1983) p.297
- 7- Wilson, W.K., ASTM STP 410, Amer.Soc. for Testing and Materials, 1966, pp.75-76.

Problems:

1- The failure stress of a component under the presence of cracks is sometimes termed its "residual strength". It is a concept used in aerospace applications where cracks growing due to fatigue are inspected at intervals to evaluate the damage tolerance of the component. For intermediate-strength steel with an ultimate tensile strength of 150 kg/mm^2 , yield strength of 110 kg/mm^2 and fracture toughness of $180 \text{ kg/mm}^{-3/2}$, estimate the residual strength of the plate containing a crack of 32 mm.

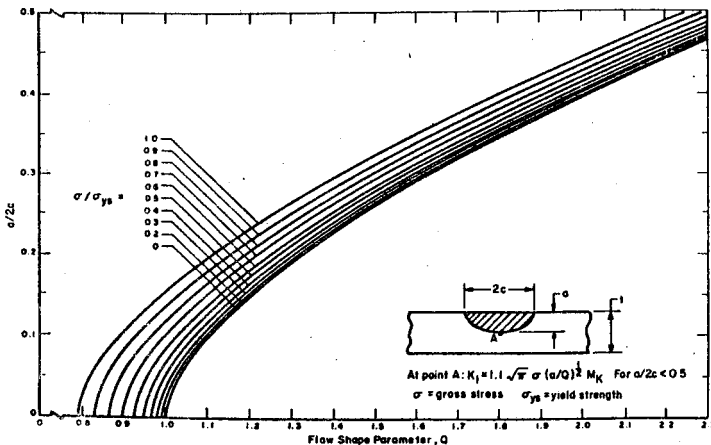
Answer: $\sigma = 25 \text{ kg/mm}^2$

2- Post-mortem analysis on a 1.78cm thick plate revealed a flat fracture surface except the 0.8mm deep shear lips on both sides. Knowing that the applied stress intensity factor was $106 \text{ MPa} \sqrt{\text{m}}$, estimate the yield strength of the material in question.

Answer: $S_y = 1500 \text{ MPa}$.

3- Elliptical flaw parameter Q , plotted in Fig.3.13, is also corrected for small scale yielding, as shown below. Based on this information you are asked to compute the critical crack size for a cylindrical pressure vessel of 20" inside diameter with 1" thick wall. The material is 7079-T6 Aluminum with a yield strength of 65 ksi and a plane strain fracture toughness of $35 \text{ ksi}\sqrt{\text{in}}$. Internal pressure is 4ksi and experience is that crack can be expected on the inside surface of the cylinder. Generally, they are semi-elliptical in shape with length $2c$ about eight times their depth a .

Answer: $a \approx 0.18''$.



5. FRACTURE TOUGHNESS TESTING

5.1 THE STANDARD TESTS OF PLANE STRAIN FRACTURE TOUGHNESS

As discussed in chapter four fracture toughness is a material property only for plane strain situations. In addition to that, the plastic zone size must be small with respect to other linear dimensions to obtain reproducible results. Thus, we have the following limitations on a valid fracture toughness

$$a, b, (W-a) \geq 2.5(K_{IC}/S_y)^2 \quad (5.1)$$

In view of this, fracture toughness evaluation can be at most an iterative procedure. If the chosen specimen size does not satisfy the inequality 5.1 a larger size (usually double of the previous) specimen is used to repeat the experiment-until 5.1 is satisfied.

5.1.1 The Standard Specimens: In principle any geometry, for which accurate stress intensity factor expressions exist, can be used in the evaluation of toughness. Certain specimens are favored, however, since they lead to rather simple test set-ups, are compact (i.e use minimum amount of material to produce specimens) and have accurate K-expressions. Extensive testing on these standard specimens eliminated also any obscured, second order error sources, such as frictions at loading or support pins.

As the ASTM Standard E399-81 describes, three point bend bar, compact specimen and arc shaped specimen are the standard samples as of now.

The three point bend bar, with the standardized nomenclature SE(B), is a single edge notched bar (Fig.5.1) loaded at the center, supported at both ends by simple rollers. The rollers are free to rotate to minimize friction, but attached to each other by rubber bands to minimize support travel. Crack mouth opening displacement is measured via a clip gage; thus the support block is provided with a central recess for the

clip gage to fit.

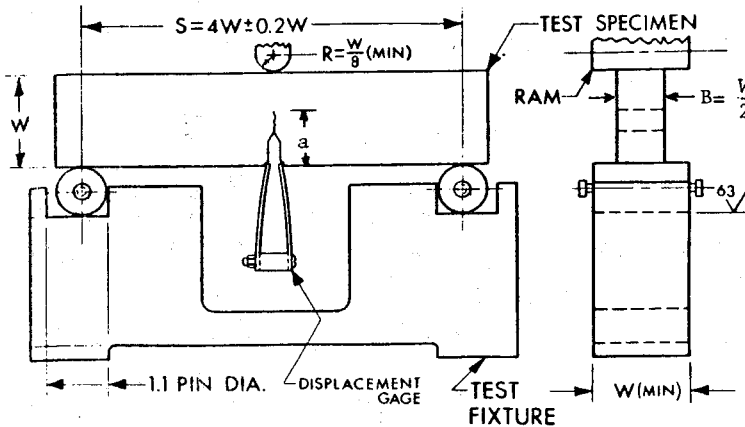


Fig.5.1- ASTM Bend specimen and the loading fixture

The stress intensity factor is given through the expression [1,2] :

$$K = \frac{PS}{B W^{3/2}} f\left(\frac{a}{W}\right) \quad (5.2)$$

where

$$f(\alpha) = \frac{3\sqrt{\alpha} [1.99 - \alpha(1-\alpha)(2.15 - 3.93\alpha + 2.7\alpha^2)]}{2(1+2\alpha)(1-\alpha)^{3/2}}$$

where $\alpha = a/W$, and W, B, S, a are as shown in figure 5.1. The nondimensional factor $f(a/W)$ is plotted in figure 5.2 for convenience.

Compact specimen, C(T), is the compact version of single edge notched sample in tension. In addition to the traditional compact tension specimen (Fig.5.3), a disk shaped version, DC(T), (Fig.5.4) is also standardized, which has reduced specimen preparation job enormously when round stock is used. The stress intensity factor for the compact specimen C(T) is given through [1,2]

$$K = \frac{P}{B\sqrt{W}} f\left(\frac{a}{W}\right) \quad (5.3)$$

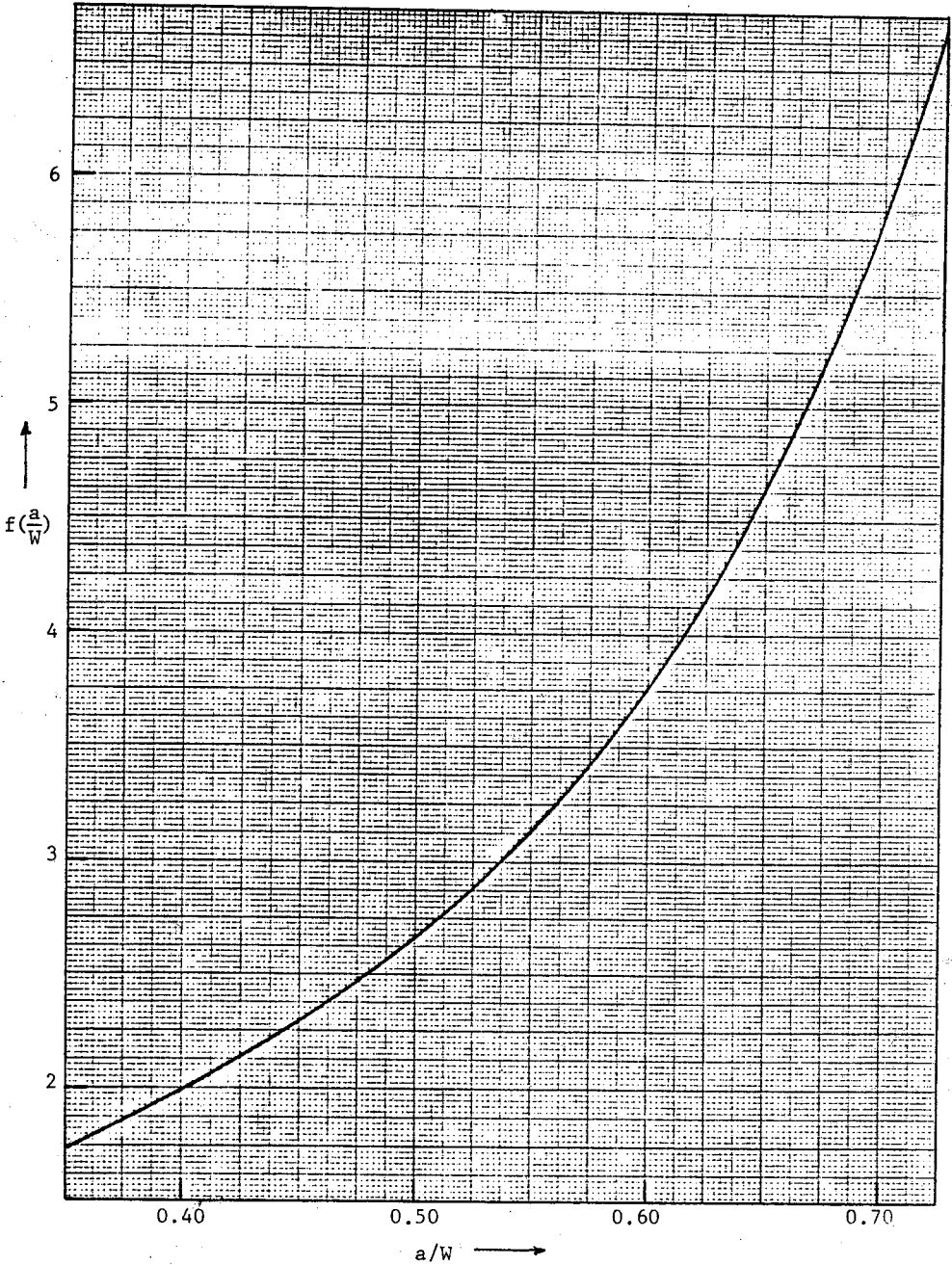


Fig.5.2- Variation of the nondimensional geometry factor $f(a/W)$ for SE(B) specimen (eq.4.2).

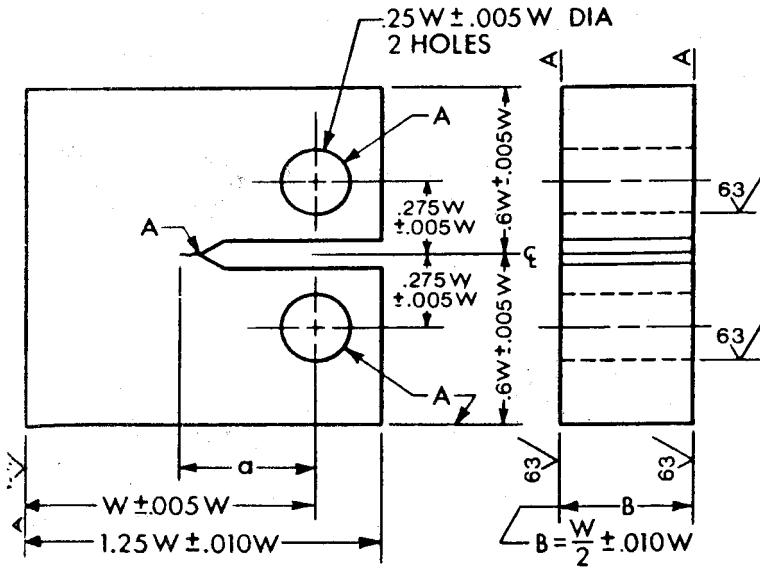


Fig.5.3- ASTM Compact Specimen Proportions

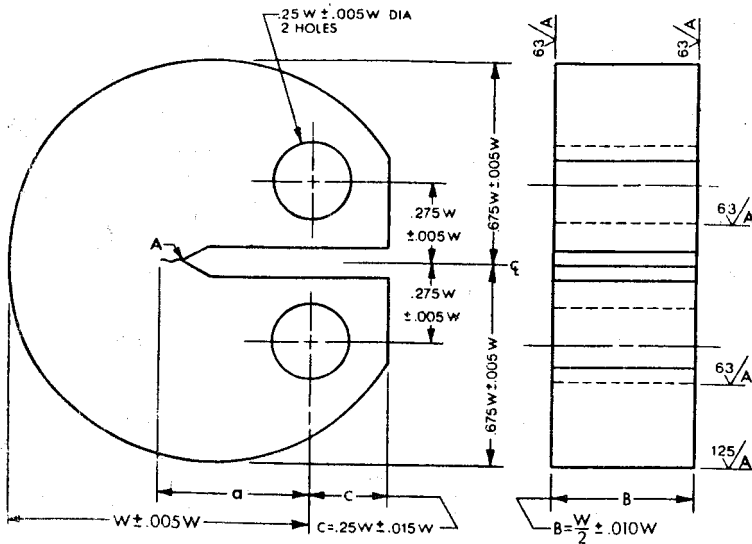


Fig.5.4- ASTM Disk Shaped Compact Specimen DC(T) Proportions

$$\text{where } f(\alpha) = \frac{(2+\alpha)(0.886+4.64\alpha-13.32\alpha^2+14.72\alpha^3-5.6\alpha^4)}{(1-\alpha)^{3/2}}$$

where $\alpha = a/W$, and W, B, a are as shown in figure 5.3. The nondimensional factor $f(a/W)$ is plotted in figure 5.5 for convenience.

The stress intensity factor expression for the disk-shaped compact specimen DC(T) is [1]:

$$K = \frac{P}{B\sqrt{W}} f(a/W) \quad (5.4)$$

where

$$f(\alpha) = \frac{(2+\alpha)(0.76+4.8\alpha-11.58\alpha^2+11.43\alpha^3-4.08\alpha^4)}{(1-\alpha)^{3/2}}$$

where $\alpha = a/W$, and W, B, a are as shown in figure 5.4. The values of $f(a/W)$ are plotted in figure 5.6 for convenience.

The arc shaped specimen A(T) is a single edge notched ring segment loaded in tension (Fig.5.7). It is well suited to hollow cylinder testing. The stress intensity factor expression corresponding this geometry is [1]:

$$K = \frac{P}{B\sqrt{W}} \left[\frac{3X}{W} + 1.9 + 1.1 \frac{a}{W} \right] \left[1 + 0.25 \left(1 - \frac{a}{W} \right)^2 \left(1 - \frac{r_1}{r_2} \right) \right] f\left(\frac{a}{W}\right) \quad (5.5)$$

$$\text{where } f(\alpha) = \left[\sqrt{\alpha} / (1-\alpha)^{3/2} \right] \left[3.74 - 6.30\alpha + 6.32\alpha^2 - 2.43\alpha^3 \right]$$

where $\alpha = a/W$, and B, W, a, X are shown in figure 5.7. The $f(a/W)$ values are plotted in figure 5.8 for convenience.

The crack mouth displacements are measured usually by attaching knife edges above and below the notch mouth which will support the clip gage arms. Crack length measurements are made starting at these knife edges. A special procedure is necessary for crack length determination of arc shaped specimens due to the curvature. As shown in figure 5.9, the true crack length is $a = m - e$, with $e = r_1 - \sqrt{r_1^2 - g^2/4}$.

The loading fixture for the tension-loaded specimens (C(T), DC(T) and A(T)) is developed to minimize friction at the loading pins. These clevises are manufactured according to the specimen size used in testing (Fig.5.10)

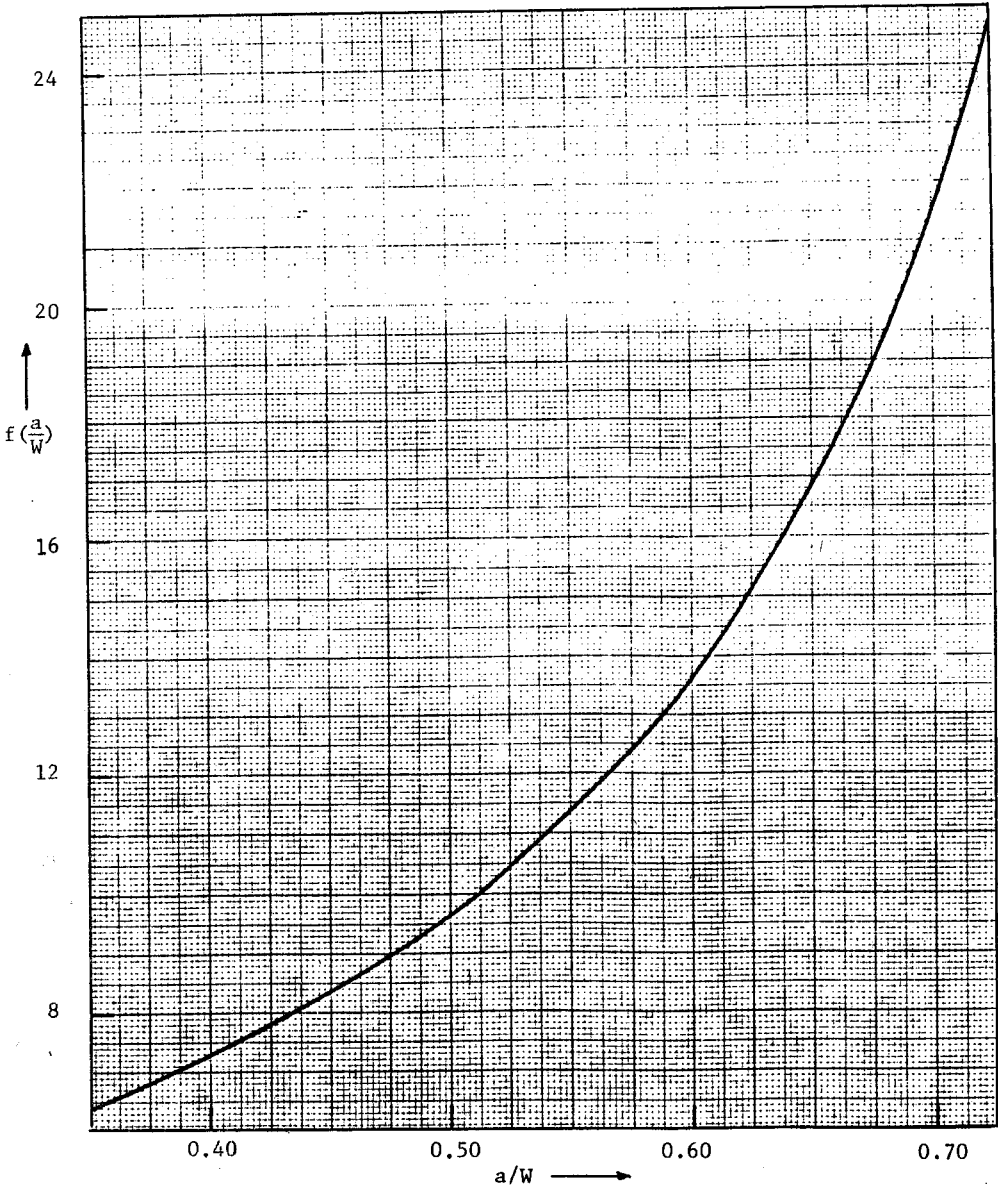


Fig.5.5- Variation of the nondimensional geometry factor $f(a/W)$ for C(T) specimen (eq.5.3).

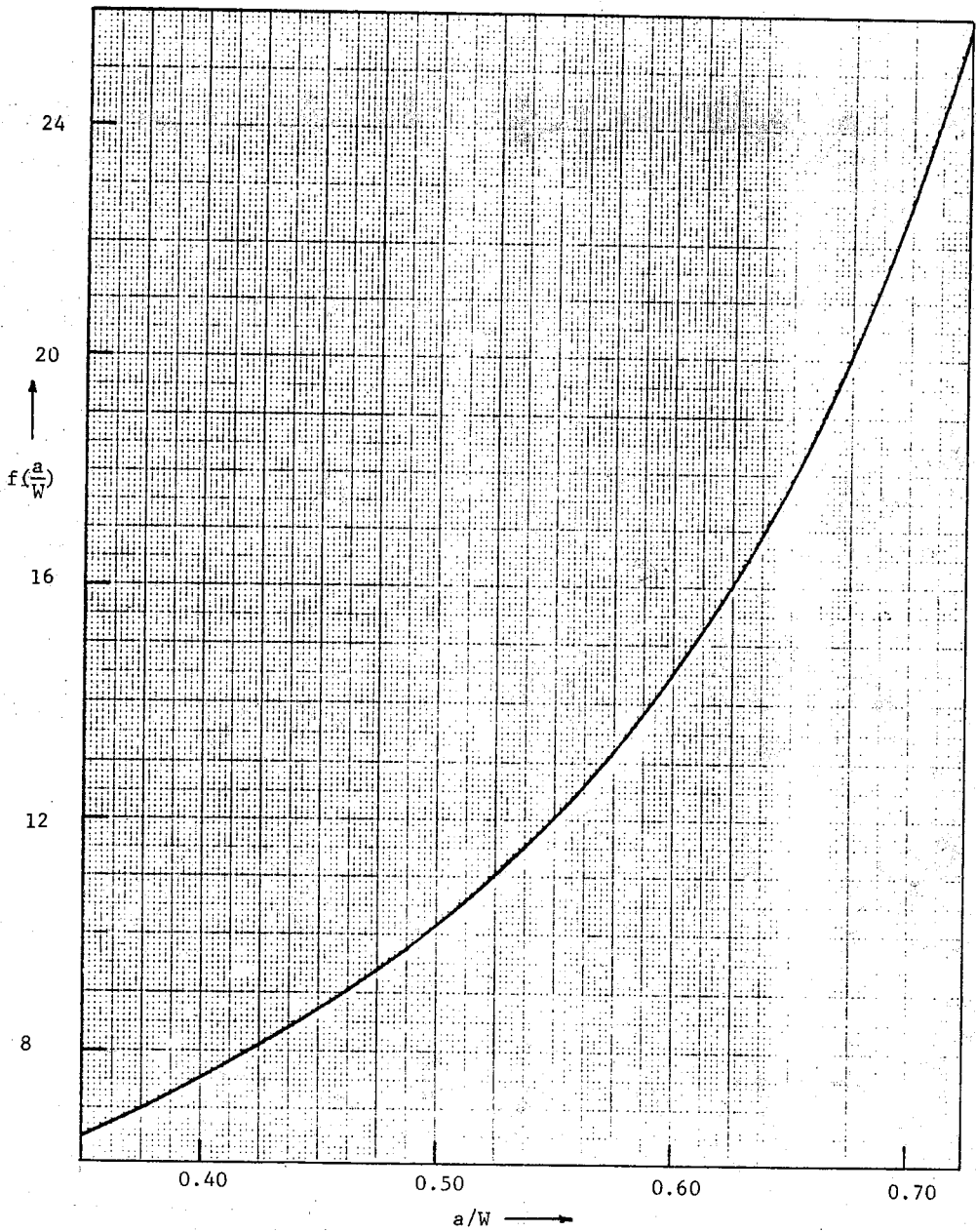


Fig.5.6- Variation of the nondimensional geometry factor $f(a/W)$ for DC(T) specimen (eq.5.4).

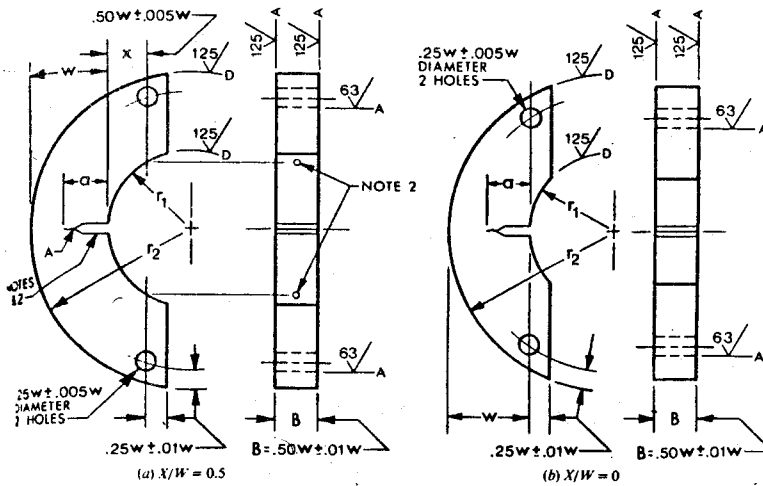


Fig.5.7- ASTM Arc-Shaped Specimen A(T) Proportions

5.1.2 Fatigue Precracking: Once specimens have been made to the recommended design, it is necessary to introduce a sharp crack at the tip of the notch. Fracture toughness values obtained using blunt notches are inflated. As shown in figure 5.11, toughness decreases rapidly with root radius until a limiting "cut-off" radius is obtained [3]. To introduce sharp cracks, fatigue cracking is usually employed. During this "precracking" procedure the maximum value of the stress intensity factor may not exceed 60% of K_{IC} . Higher peaks are reported to lead to unconservative estimates of toughness for both Al-alloys [4] and alloy steels [5] (Fig.5.12).

Fatigue precrack extends for several millimeters, usually. After the fracture toughness test is over, the size and shape of the fatigue crack can be determined easily. Different topographies of the fatigue area and the final fracture area make them easily distinguishable to naked eye.

5.1.3 Test Procedure: Precracked standard specimen is pulled apart quasistatically. A clip gage is placed at crack mouth to measure crack mouth opening displacement as the load is applied. This gage consists of two cantilever beams and a spacer block which are clamped together with a single nut and bolt, as shown in figure 5.13. Electrical resistance strain

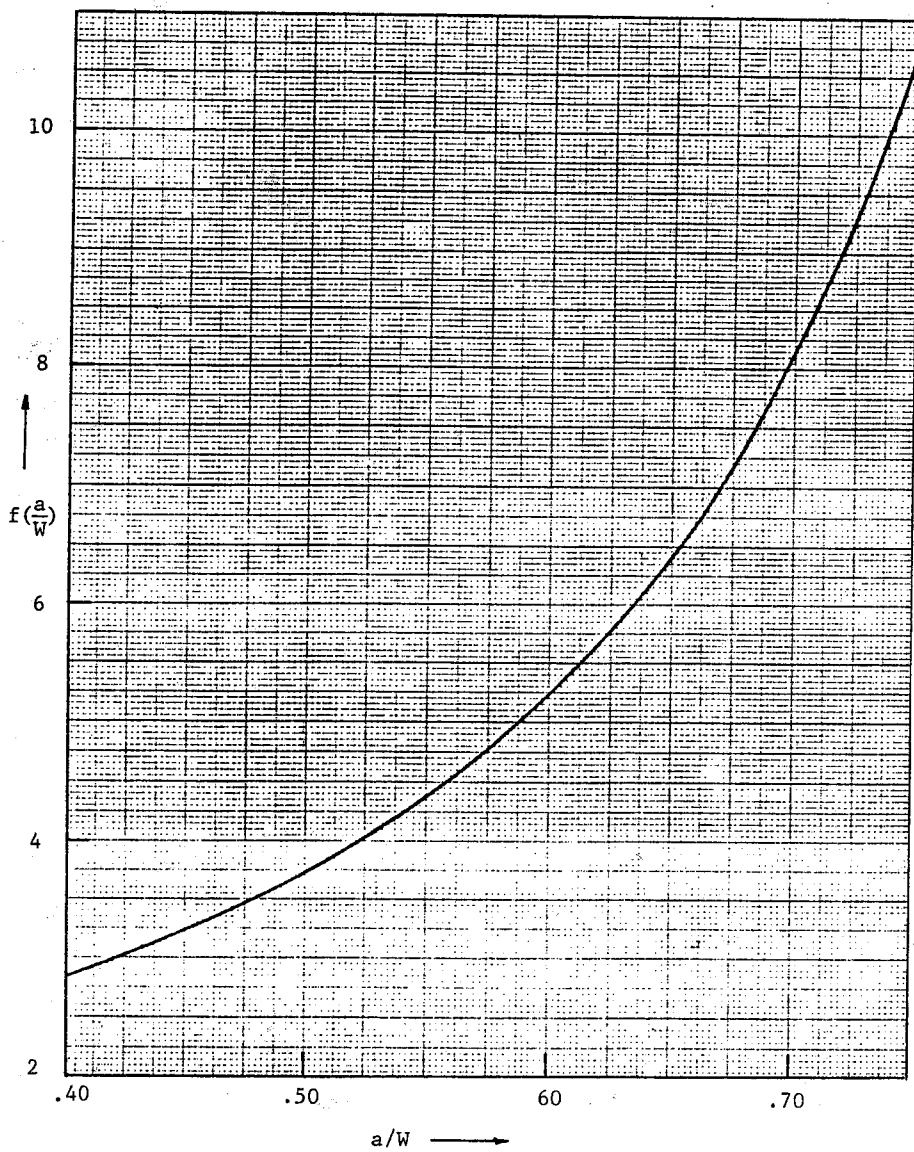


Fig.5.8- Variation of $f(a/W)$ for A(T) specimen used in eq.5.5.

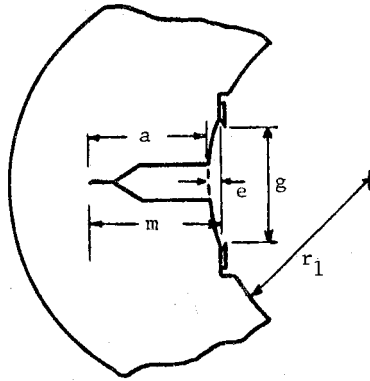


Fig.5.9- Measurement of crack length for the arc-shaped specimen [1]

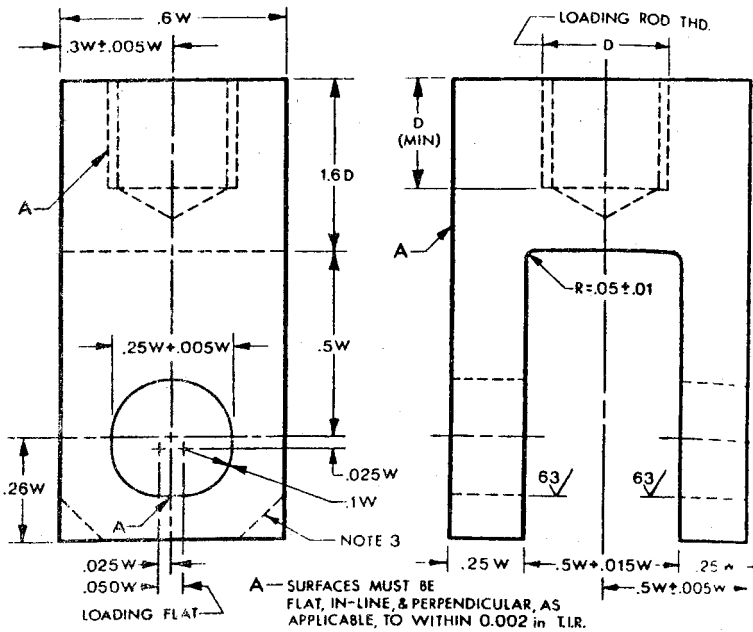


Fig.5.10- Tension Testing Clevis Design [1]

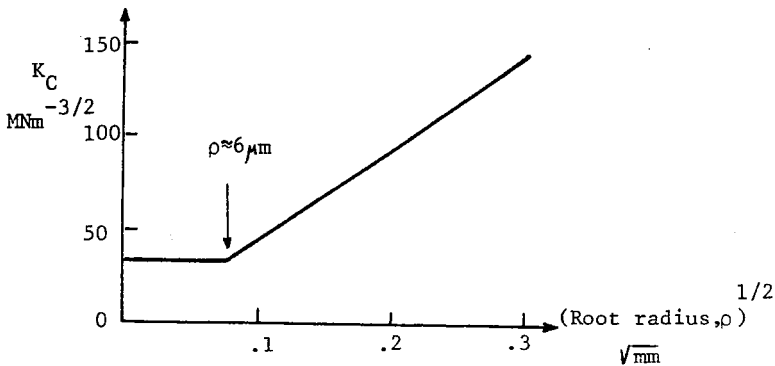


Fig.5.11- Schematic variation of toughness with notch root radius for a high strength steel [3]

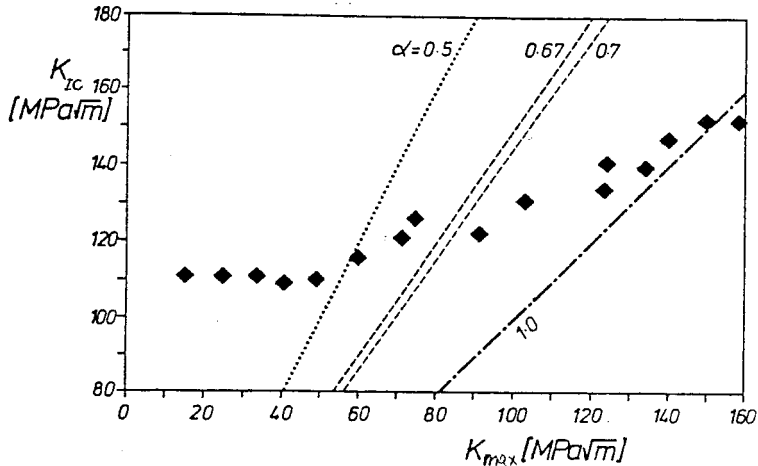


Fig.5.12- The influence of K_{max} during fatigue cracking on tentative fracture toughness K_{IC} , $\alpha = K_{IC}/K_{max}$ [5]

gages are cemented to the tension and compression surfaces of each beam, and are connected as a Wheatstone bridge. The beam material is supposed to have a high yield strength and a low elastic modulus to increase the operating (deflection) range without realizing any plastic deformation. Ti-alloy 13V-11Cr-3Al in the solution treated condition is the preferred beam material. Beryllium copper is another candidate with high S_y/E ratio.

During the use of the clip gage, strain bridge excitation is maintained constant, typically at 10 volts, and the amplified bridge output is

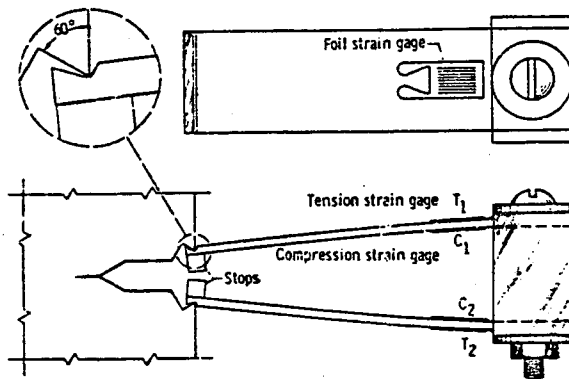


Fig.5.13- Double-Cantilever Clip gage

recorded on one axis of an X-Y recorder. The load cell supplies the signal to the other axis of the recorder. Typical load displacement records, as a result of this procedure, are shown in figure 5.14. To see whether a

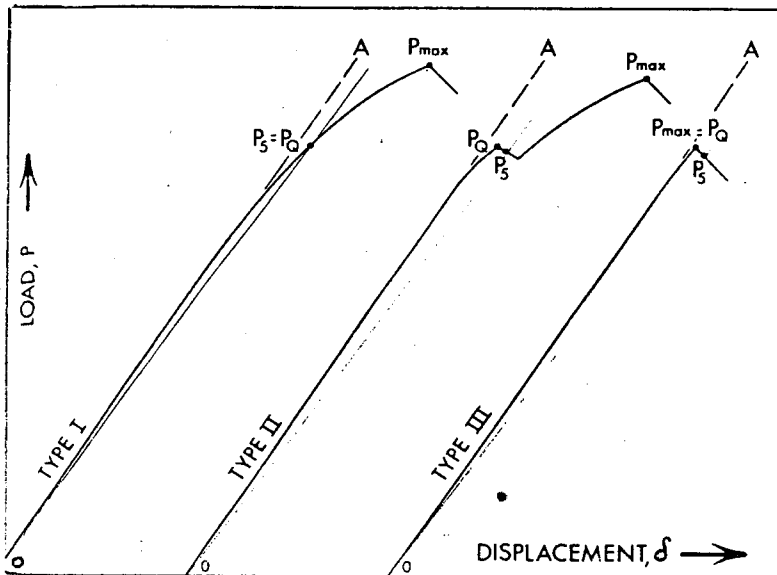


Fig.5.14- Major types of load-displacement records

valid fracture toughness value has been obtained, it is necessary to first calculate a tentative number K_Q , based on a graphical construction on the load-displacement test record. If K_Q satisfies the conditions of eq. 5.1, then $K_Q = K_{IC}$. From ASTM specification E399-81, the graphical construction involves the following procedures [1]. On the load deflection test record, draw a secant line OP_5 (Fig.5.14) through the origin with a slope that is 5% less than the tangent OA to the initial part of the curve. For the $SE(T)$ and $C(T)$ sample, a 5% reduction in slope is approximately equal to a 2% increase in the effective crack length of the sample. P_5 is defined as the load at the intersection of the secant line OP_5 with the original test record. If the load at every point on the record which precedes P_5 is lower than P_5 , then P_5 is labeled as P_Q and used to calculate K_Q (type I in Fig.5.14). If, however, there is a maximum load proceeding P_5 which exceeds it, then this maximum load becomes P_Q (type II or III). It is also required that

$$P_{\max}/P_Q < 1.1 \quad (5.6)$$

to limit the amount of plastic deformation. If the inequality 5.6 on P_Q and the inequality 5.1 on K_Q are satisfied, the procedure is completed.

Altogether there are eight major validity checks in the process of obtaining K_{IC} results. They all should be satisfied to have a "valid" toughness value. Attempts of computerizing materials property data [6] includes information on each validity check, for example. For aluminum alloys, if the departure from validity is small enough (K_Q within 5 to 10% of K_{IC}), the test results are designated invalid but "meaningful" [7].

5.1.4 Further Details: Particularly cold worked materials possess a high degree of directionality. Thus, it is necessary to include the orientation of the toughness specimen when fracture toughness is evaluated. Both the crack plane and the prospective crack propagation directions are to be specified. The standard method [8,9] is to use a hyphenated code with the first letter(s) representing the direction normal to the crack plane and the second letter(s) designating the direction of crack growth. For rectangular sections the reference directions are identified as in figure 5.15 where L shows the direction of principal deformation (maximum grain-flow) and T the direction of least deformation. For specimens that are

tilted in respect to two of the reference axes, the orientation is identified by a three letter code, as illustrated in figure 5.16. For certain

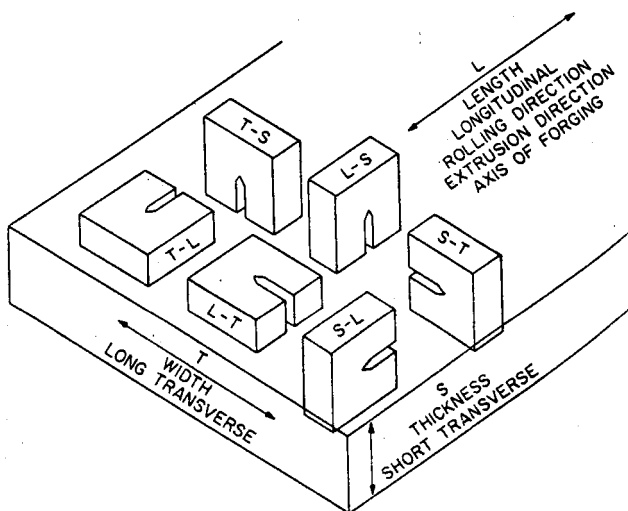


Fig.5.15- Crack Plane Orientation Code for Rectangular Sections [8]

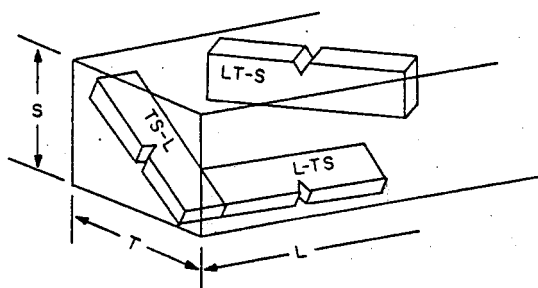


Fig.5.16- Code for Rectangular Sections for Tilted Specimens [8]

cylindrical sections where the direction of maximum grain flow coincides with the axial direction, the reference directions are as shown in figure 5.17.

A systematic code is used in characterizing the various fracture mechanics specimen configurations. This code describes the test specimen in terms of a one, two or three letter code, (in parenthesis) indicating the loading applied to each configuration, followed by two (or three) letter code (in parenthesis) indicating the orientation. Typically, a

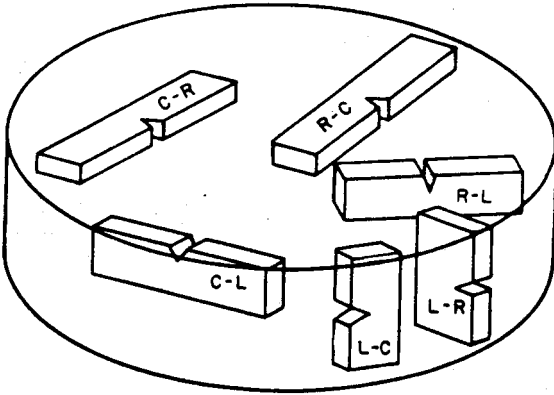


Fig.5.17- Crack plane Orientation Code for round sections [8]

double edge notched specimen tested in tension with the crack plane normal to the longitudinal direction and the expected crack propagation in the short transverse direction would be DE(T) (L-S). The symbols used for specimen configurations are:

M	Middle	MC	Modified Compact
DE	Double Edge	DC	Disk shaped
SE	Single Edge	A	Arc
C	Compact	DB	Double Beam
R-Bar	Round Bar	PS	Part-through Surface

Figure 5.18 shows some examples of the designation Code. The terms "precracked", "notched", "contoured", "chevron" are included as additional descriptions when needed.

Toughness measurements are specific to a particular temperature at which the tests are conducted. For steels, this temperature usually corresponds to lower shelf or, at most, the transition range. Above that, fracture process involves large scale plastic deformation such that LEFM is not applicable.

The loading rate is well known to effect the toughness values. As the rate increases, toughness decreases. To obtain a conservative measure of toughness charpy impact tests have been used traditionally. Plane strain fracture toughness tests are usually carried out quasistatically.

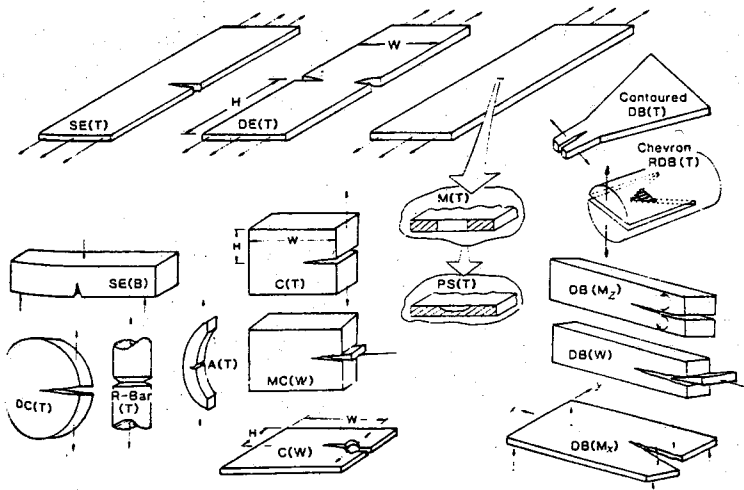


Fig.5.18- Specimen/Loading Codes for various Configurations [9] .

5.1.5 Chevron Notched Specimens: The search for simpler, less expensive methods of measuring the fracture toughness has led to a new test specimen cylindrical in shape, containing a deep, machined notch with a chevron configuration. It is called Chevron Round Double Beam (Chevron RDB(T)) and is shown in figure 5.19. Although this specimen, also called short rod, necessitates the use of special loading fixtures, preparing the specimen itself is simple. Besides that it has the major advantage that the crack initially grows in a stable manner. This makes sure that a sharp crack front exists at the peak load when unstable growth commences. Thus, the time consuming and expensive fatigue precracking procedure is eliminated altogether. Chevron notched specimens are well suited to toughness testing of brittle materials that are difficult to fatigue precrack. The thin chevron slots provide good plane strain constraint at the crack ends, resulting in smaller specimen sizes, for valid fracture toughness values from a given material. A chevron-notched specimen is only about 50% of the thickness and 3% of the weight of specimens required for other fracture toughness tests [10] .

Neither the chevron RDB(T) (short rod) specimen nor its rectangular-shaped counterpart, chevron DB(T) (short bar), have been standardized yet. Tentative dimensions are given by Barker [11,12] and are shown in

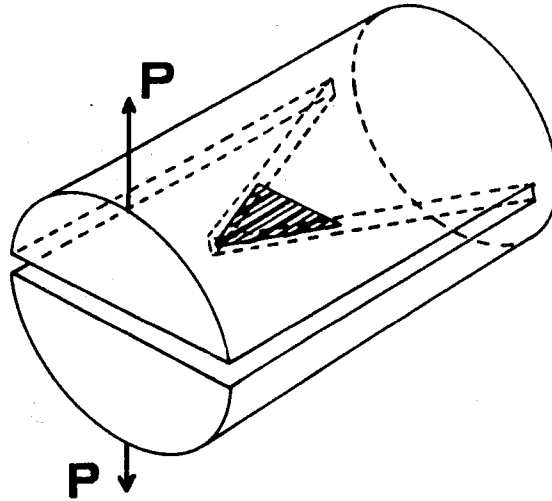
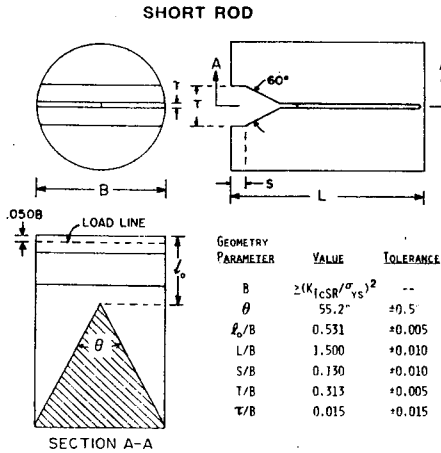


Fig.5.19- Round Double Beam specimen containing a deep chevron notch

figure 5.20. It is worth noting that chevron slots can also be machined



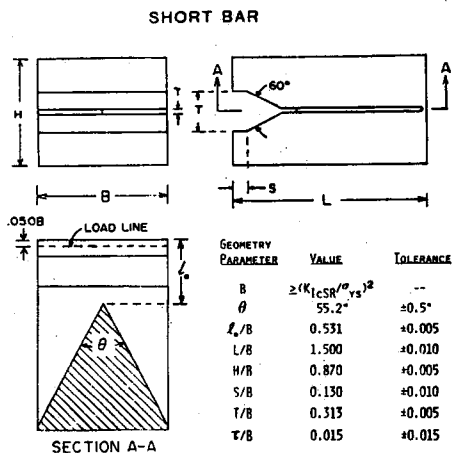


Fig. 5.20- Basic geometries of chevron notched specimens

by feeding the saw blade into the specimen, leading to a curved slot geometry as shown in figure 5.21. A typical setup for testing chevron

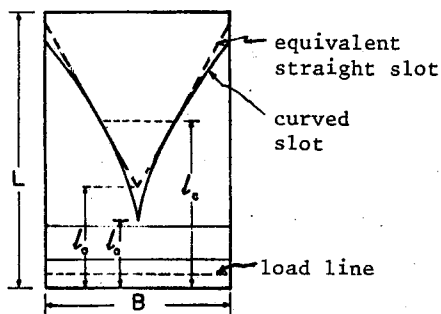


Fig.5.21- Chevron notched specimen with curved slot

notched specimens on a tension testing machine is illustrated in figure 5.22.

Chevron notched specimens made from very hard, brittle materials, such as glass, ceramics, and carbides, exhibit nearly ideal linear elastic behavior. A plot of load versus mouth opening displacement for an ideal elastic material is shown in figure 5.23. Crack initiation occurs at I, where the loading first deviates from linearity. The crack then extends

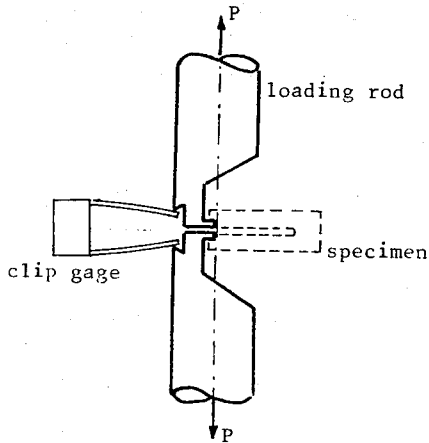


Fig.5.22- Schematic chevron notched specimen testing arrangement

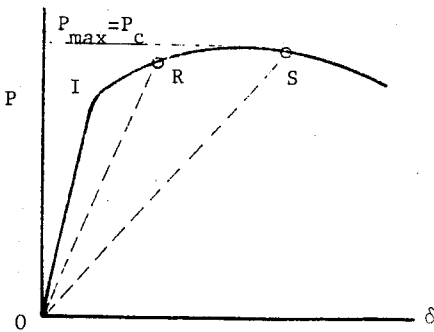


Fig.5.23- Schematic of elastic specimen behavior

in a stable manner throughout the test. The load required to advance the crack increases to a smooth maximum at the critical crack length. The critical crack length is dependent only on specimen geometry and is independent of material. Therefore, there is no need to measure crack length when determining fracture toughness of linear elastic materials. Note that any unloading from R or S (in figure 5.23) goes through the origin for such elastic materials. The fracture toughness is obtained using the expression

$$K_{IC} = A \frac{P_c}{B^{3/2}} \quad (5.7)$$

- where P_c is the critical load (coinciding with the maximum load)
 B is the specimen diameter in short rod (the thickness in short bar)
 A is a dimensionless calibration constant which has a minimum value of 22 for the specimen geometries in fig.5.20 [12,13]

Practical engineering alloys develop sufficient crack tip plastic zone such that the general behavior is elastic-plastic and unloading lines from R and S do not go through the origin (Fig.5.24). In such

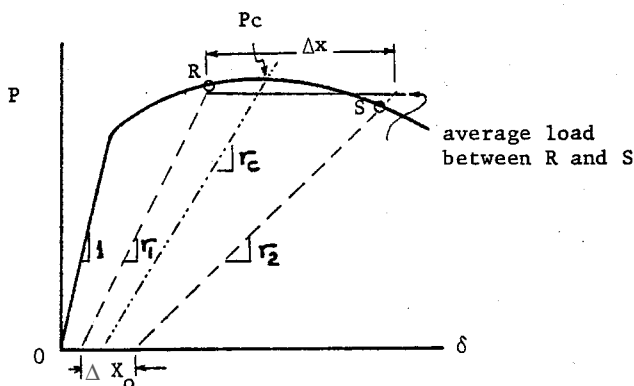


Fig.5.24- Schematic of elastic-plastic specimen behavior

cases an additional parameter called the plasticity, p , is introduced and the toughness is obtained through the expression

$$K_{IC} = A \frac{P_c}{B^{3/2}} (1+p) \quad (5.8)$$

where P_c is the critical load corresponding to critical crack length.
 p is $\Delta x_0 / \Delta x$ as defined in figure 5.24, and
 A and B are as defined in eq.5.7.

The two unloading-reloading cycles (usually one just before and the other just after the peak load) determine p as well as the point on the load-displacement diagram at which the crack passes through the critical crack length a_c . If the unloading slopes normalized by the loading slope are called r_1 and r_2 , an unloading line at the critical slope ratio r_c

corresponding to a_c can be plotted on the load-displacement diagram by interpolating between r_1 and r_2 . The critical slope ratio r_c is known through compliance calibration of chevron notched specimens and is given in figure 5.25. The intersection of the unloading line of slope ratio r_c

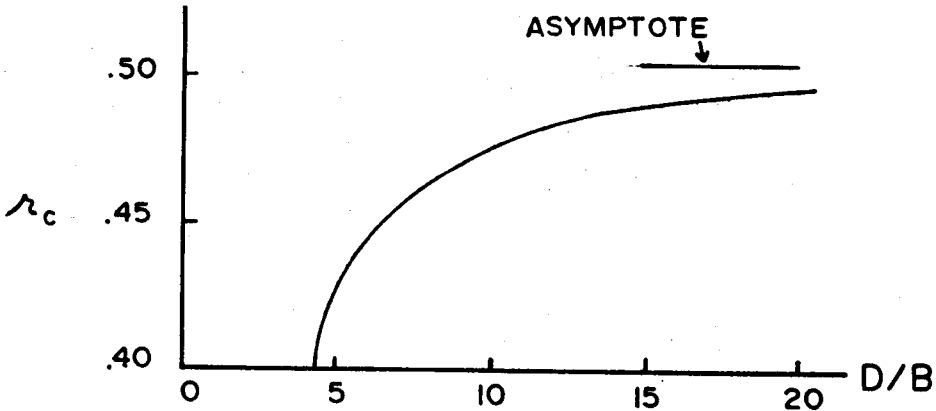


Fig.5.25- Variation of the critical slope ratio r_c with the slot curvature (D = diameter of cutting tool, B = diameter of specimen)

and the smooth curve approximating the P - δ plot defines P_c (Fig.5.24).

A minimum chevron-notched specimen size criterion of

$$B \geq 1.25 (K_{IC}/\sigma_0)^2 \quad (5.9)$$

is suggested based on experimental data. When a chevron-notched specimen is smaller than the minimum size criterion (eq.5.9), it appears that upper and lower bounds can still be found for K_{IC} using the calculated p and $p = 0$ in eq.5.8, respectively [10]. For valid toughness tests the plasticity factor is limited to $p < 0.2$. Non-plane strain effects can become a source of error if chevron slots are not sufficiently thin. Slot thickness is recommended to be less than $0.03 B$ with slot bottoms being sharply pointed and the included angle being 60° or less.

Alternate specimen geometries are proposed by Munz et al. [14]. The equations and the calibration constants for these specimens are given in that particular reference.

5.2 PLANE STRESS BEHAVIOR

Plane stress fracture is of vital importance mainly for aircraft components since the larger part of the primary aircraft structure consists of reinforced thin plates. Plane stress behavior is more difficult to analyze than plane strain behavior and has received relatively little attention in literature. Fracture is more complex and no standardized procedures exist.

Consider a thin plate under plane stress with a central initial crack $2a_i$, loaded in tension (Fig.5.27, insert). Upon reaching a stress σ_i , the crack will begin to extend. However, unlike in plane strain, fracture will not yet occur. In order to maintain crack growth, the stress has to be further increased. This crack growth is stable; the crack will stop growing if the load is kept constant, it will continue to grow upon increasing the load (Fig.5.26). This is believed to be due to the

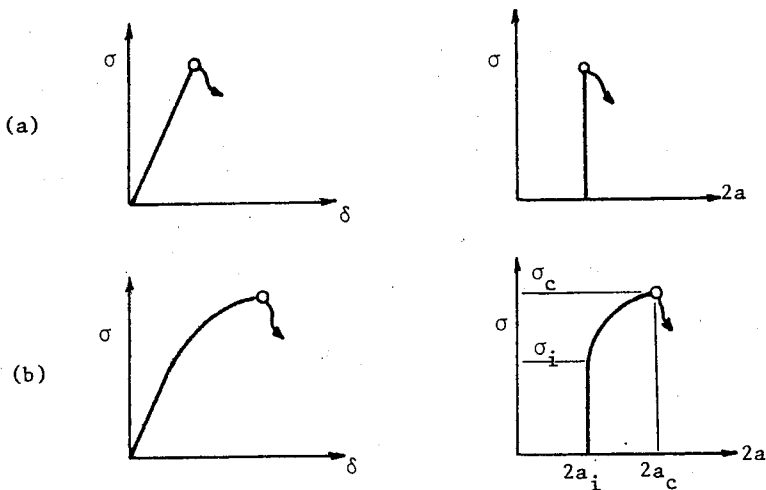


Fig.5.26- Opposing characters of plane strain (a) and plane stress (b) fracture

growth of the plastic zone size with crack length and due to the strain hardening property of the material. Slow stable growth continues until a critical crack size $2a_c$ is reached at a stress σ_c . Then the crack becomes unstable and fracture occurs. If the initial crack is longer, crack growth starts at a lower stress, the amount of sustained crack growth is larger,

but σ_c is lower [15], as shown in figure 5.27. Slow growth may be of the order of 20 to 50 percent of the initial crack size. The initiation of crack growth in figure 5.27 is assumed to be governed by K_i , whereas

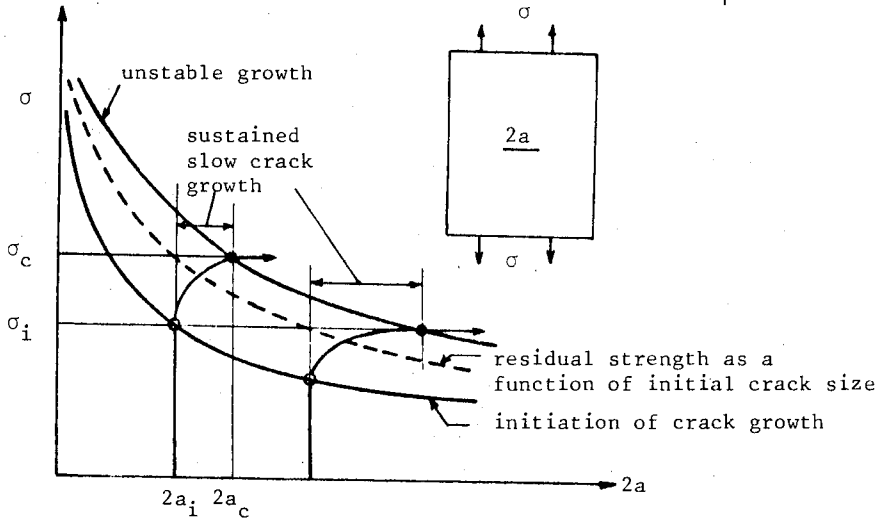


Fig.5.27- Plane stress behavior for different crack sizes

instability by K_c . Thus,

$$K_i = \sigma_i \sqrt{\pi a_i} \tag{5.10}$$

$$K_c = \sigma_c \sqrt{\pi a_c} \tag{5.11}$$

It is sometimes helpful to define an apparent stress intensity K_a which relates the initial crack size to the fracture stress [16]:

$$K_a = \sigma_c \sqrt{\pi a_i} \tag{5.12}$$

K_a is not a physical quantity, but it does have an engineering significance. It gives the residual strength of a plate that contains a (fatigue) crack of a given size. Whether or not this crack shows stable growth before fracture is immaterial from an engineering point of view.

In the center cracked geometry discussed here, the allowable stress value becomes unbounded as the crack size approaches zero. But the residual strength is bounded by the yield strength of the material. To overcome

this discrepancy Feddersen [17] proposed to modify the σ_c versus a_c curves—or the σ_c versus a_i curves based on the above mentioned apparent stress intensity, K_a — as illustrated in figure 5.28. He proposed to

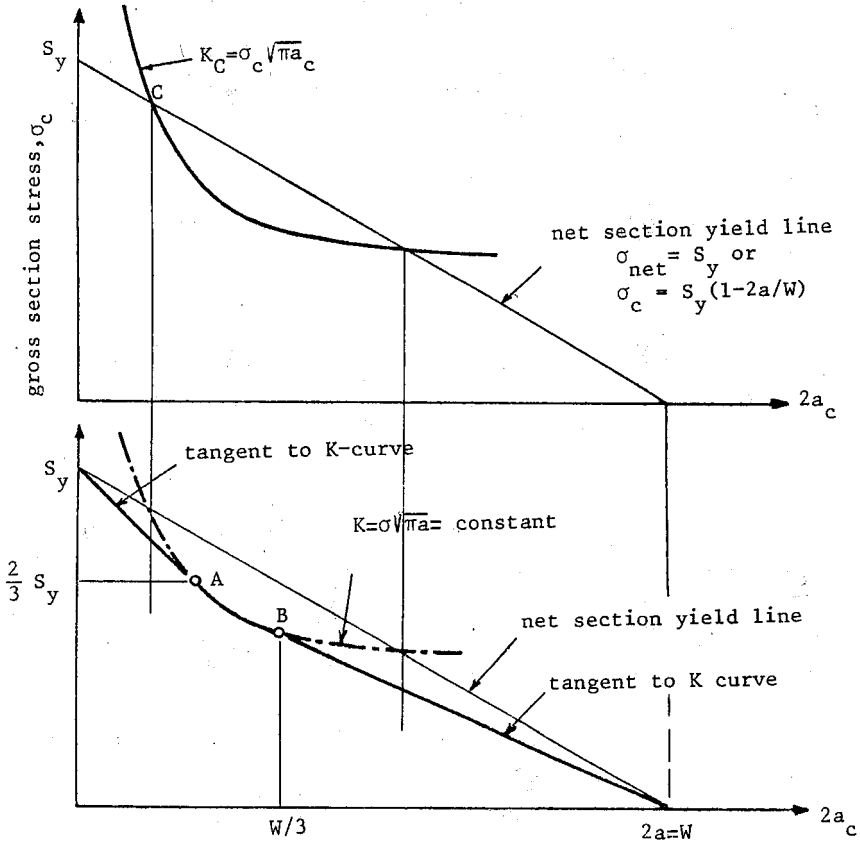


Fig.5.28- Boundaries of stress and crack size for valid K_c results according to Feddersen.

construct two tangents to the curve, one from the stress axis starting at S_y , the other from the crack axis starting at W , the panel width. The tangents to the curve are expressed by

$$\frac{d\sigma}{d(2a)} = \frac{d}{d(2a)} \frac{K}{\sqrt{\pi a}} = -\frac{\sigma}{4a}$$

Hence

$$-\frac{\sigma}{4a} = -\frac{S_y - \sigma}{2a}$$

or

$$\sigma = \frac{2}{3} S_y$$

gives that the left hand tangency point (point A in Fig.5.28) is always at $2S_y/3$, independent of K_c . And

$$-\frac{\sigma}{4a} = -\frac{\sigma}{W-2a}$$

or

$$2a = W/3$$

gives that the right-hand tangency point (point B in Fig.5.28) is always at $W/3$. In the region between the points A and B, K_c is approximately constant. This piece of the curve plus the two tangents constitute the residual strength diagram of Feddersen. The two points of tangency coincide when $\sigma_c = (2/3)S_y$ for $2a_c = W/3$. That is,

$$\frac{2}{3} S_y \sqrt{\pi \frac{W}{6}} = K_c$$

or

$$W = \frac{27}{2\pi} \left(\frac{K_c}{S_y} \right)^2 \quad (5.13)$$

Hence, panels smaller than this will fail by net section yield and cannot be used to measure K_c (Fig.5.29).

5.2.1 The R-Curve Concept: Due to the sustained slow crack growth-observed in high strength materials in plane stress conditions or in intermediate to low strength materials-it is difficult to measure the final crack length and thus to evaluate the maximum stress intensity factor at failure. To overcome this difficulty, an energy based Resistance curve approach has

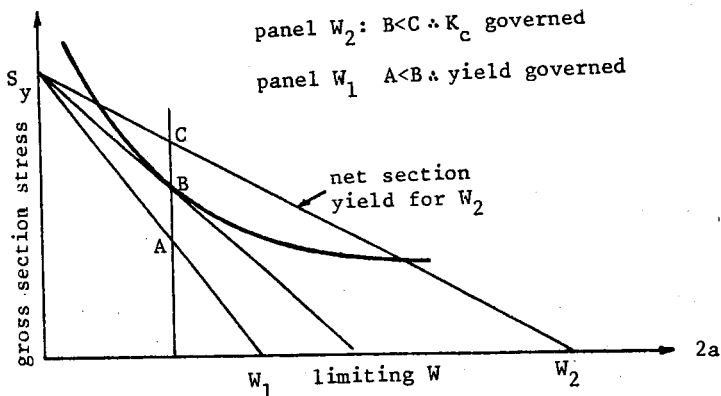


Fig.5.29- Panel size effect in K_c evaluation

been proposed by Irwin and developed by the contenders.

As the stress level increases in a test, the rate of energy available increases; that is, G increases. Opposing this G is a (increasing) rate of resistance to crack extension, designated by G_R . At all stages of slow crack growth energy rate balance must be satisfied, and $G = G_R$ up to the point of instability. As shown in figure 5.30, when the $G(a, \sigma)$ curve is raised sufficiently the increase in energy supplied per unit crack advance exceeds the increase in resistance and unstable crack extension occurs without further increase of the critical applied stress σ_c . Analytically, crack instability is due when

$$G(a, \sigma) = G_R(\Delta a)$$

$$\frac{\partial G}{\partial a} = \frac{dG_R}{d\Delta a}$$

where the partial derivative of G with respect to a is to be taken with the prescribed loading conditions held fixed. The point of tangency between G and G_R curves is the definition of the plane stress fracture toughness G_c (or K_{Ic}) and determines the critical values a_c and σ_c .

The assumption behind the R-curve approach is that the R-curve is a material property for a given thickness B and temperature and is independent of initial crack size, a_i , and specimen configuration [18]. Fracture toughness G_c does vary slightly with the planar dimensions of the specimen, however [19]. It is illustrated in figure 5.31 that for a given material

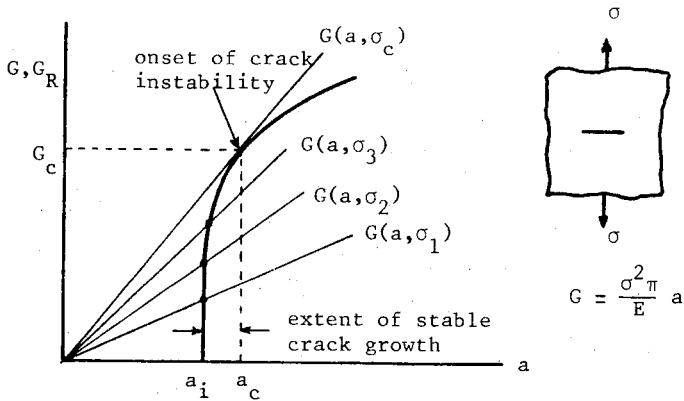


Fig.5.30- Predicting the instability through the Resistance curve

the fracture toughness value will depend on the initial crack length, since the tangency point is displaced slightly when the starting crack

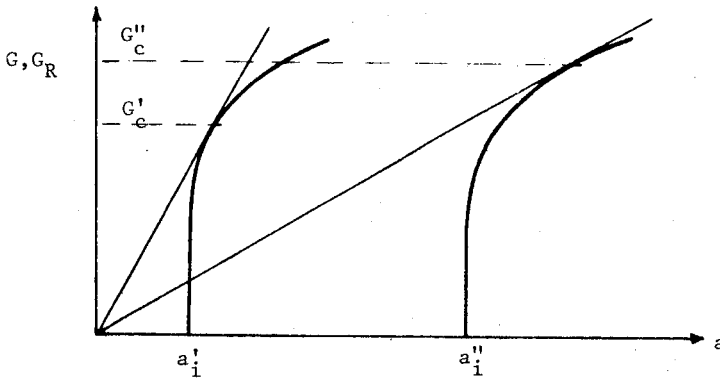


Fig.5.31- Effect of a_i on the predicted G_c

length is changed. A considerably larger change is observed when plates of different width are tested (Fig.5.32). Both of these effects are minimized when large samples are used. Wang and Mc Cabe [20] report that G_c data and R curves were independent of panel width and initial crack size provided the panels do not fail by net-section yielding.

The present analysis can also be carried out in exactly the same way in terms of K rather than G -as is done in ASTM E561 [21].

The compliance of the system-the specimen and the loading frame-plays a major role in the instability phenomena. Consider a specimen

loaded in a compliant machine shown in figure 5.33. Let $C(a)$ denote the compliance of the specimen and let C_M denote the compliance of the

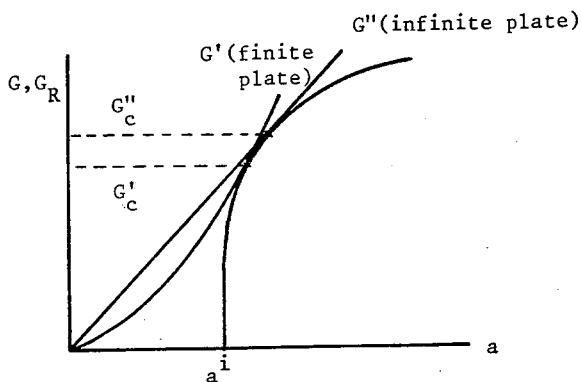


Fig.5.32- Effect of panel width on the predicted G_c

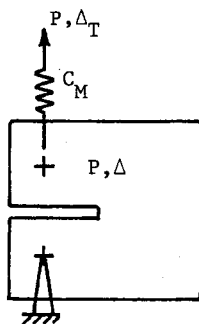


Fig.5.33- The model of specimen and loading frame

loading device [21]. The total displacement Δ_T is taken to be prescribed where

$$\Delta_T = \Delta + C_M P = (C + C_M) P \quad (5.14)$$

The energy release rate can be written as

$$G = P^2 f(a) \quad (5.15)$$

where $f(a)$ is assumed known. Using

$$dG = 2PdP f(a) + P^2 f'(a) da$$

and

$$d\Delta_T = (C+C_M)dP + C'P da = 0$$

one obtains

$$\left(\frac{\partial G}{\partial a}\right)_{\Delta_T} = P^2 f' - \frac{2P^2 f C'}{C+C_M} \quad (5.16)$$

It was shown in section 3.13 that G itself does not depend on the compliance of the loading device. Equation (5.16) proves that stability of growth is, however, strongly dependent on the loading conditions. For dead loads, $C_M \rightarrow \infty$, $P = \text{constant}$ and eq.(5.16) becomes

$$\left(\frac{\partial G}{\partial a}\right)_{\Delta_T} = \left(\frac{\partial G}{\partial a}\right)_P = P^2 f' \quad (5.17)$$

while for fixed grips, $C_M = 0$ and

$$\left(\frac{\partial G}{\partial a}\right)_{\Delta_T} = \left(\frac{\partial G}{\partial a}\right)_{\Delta} = P^2 f' - 2P^2 f C'/C \quad (5.18)$$

Since $C' > 0$ usually, $(\partial G/\partial a)_{\Delta} < (\partial G/\partial a)_P$.

The consequences of eq.(5.16) can be visualized considering the double beam specimen, DB(T), shown in figure 3 7, where

$$C = 2a^3/3EI$$

$$G = P^2 a^2/BEI \quad , \quad f(a) = a^2/BEI$$

Using eq.(5 16)

$$\left(\frac{\partial G}{\partial a}\right)_{\Delta_T} = \frac{2P^2 a}{BEI} \left[1 - \frac{3}{\left(1 + \frac{C_M}{C}\right)} \right]$$

Evaluating this expression for two extreme situations

$$\text{fixed grips: } \left(\frac{\partial G}{\partial a}\right)_{\Delta} = -4P^2 a/BEI$$

$$\text{dead load : } \left(\frac{\partial G}{\partial a}\right)_P = +2P^2 a/BEI$$

indicates that the double beam specimen will always be stable under prescribed displacements whereas the crack becomes unstable at $G = a G'_R/2$ under dead loads, G'_R being the local slope of the R-curve.

5.2.2 The Standard Procedure for R-Curve Determination: ASTM has standardized plane stress testing procedure under E561-81 [20]. The adopted specimens are the center-cracked tension panel, M(T), the compact specimen loaded in tension, C(T), and the crack-line-wedge loaded compact specimen, C(W). The specimen ligaments in the plane of the crack must be predominantly elastic at all values of the applied load. In general, the toughness values obtained are specific to that particular temperature and loading rate. In rate sensitive materials, typically steels with S_y less than 1000 MPa, rapid cleavage fracture may follow small amounts of stable crack extension. Thus, R-curve measurement methods and analysis may be in-appropriate [22].

The center cracked tension panel is the most common geometry (Fig. 5.34). To ensure uniform stress entering the crack plane, the length of

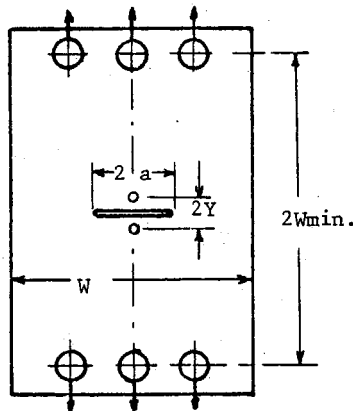


Fig.5.34- The M(T) geometry with clip-on gage locations $2Y$ apart.

the specimen between the innermost loading pins is chosen at least $2W$. If buckling occurs, rigid face plates are used to prevent it. Periodic partial unloading reveals buckling as nonlinear loops in the load-displacement plots. The stress intensity factor expression is:

$$K_I = \frac{P}{WB} \sqrt{a} \left[1.77 - 0.177 \frac{2a}{W} + 1.77 \left(\frac{2a}{W} \right)^2 \right] \quad (5.19)$$

or

$$K_I = \frac{P}{WB} \sqrt{\pi a \sec \left(\frac{\pi a}{W} \right)} \quad (5.20)$$

where the crack length a is the effective crack length, that is, corrected for plastic zone size. It is possible to measure the physical crack size through a microscope or through the electric resistance method or through partial unloading and then to correct for small scale yielding by adding r_y . But more directly, points on the load-displacement curve are joined to the origin (Fig.5.35) and the slopes of these secant lines are used to obtain automatically plastic zone corrected crack lengths. To this end,

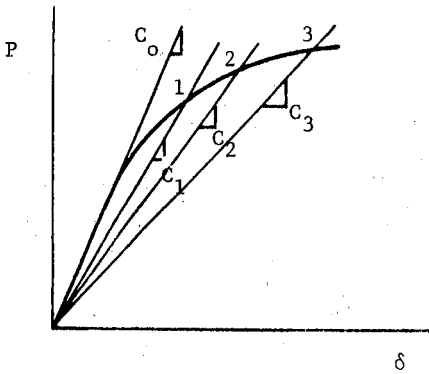


Fig.5.35- Interpretation of test record to obtain crack lengths.

either a compliance versus crack length "calibration curve" is developed experimentally or the analytical expression developed for $M(T)$, eq (5.21), is used.

$$EBC = \frac{2Y}{W} \left\{ \frac{\pi a/W}{\sin(\pi a/W)} \right\}^{1/2} \left\{ \frac{2W}{\pi Y} \cosh^{-1} \left(\frac{\cosh \pi Y/W}{\cos \pi a/W} \right) \right. \\ \left. - \frac{1+\nu}{\left[1 + \left(\frac{\sin(\pi a/W)}{\sinh(\pi Y/W)} \right)^2 \right]^{1/2}} + \nu \right\} \quad (5.21)$$

where C is the compliance at the center hole ($\equiv 2V/P$)

Y is the halfspan of clip gage (Fig.5.34)

a is the effective half crack length

The above compliance expression is valid for $0.2 < \frac{2a}{W} < 0.8$ and $Y/W \leq 0.5$ and is plotted in figure 5.36 for several Y/W ratios. Using the loads

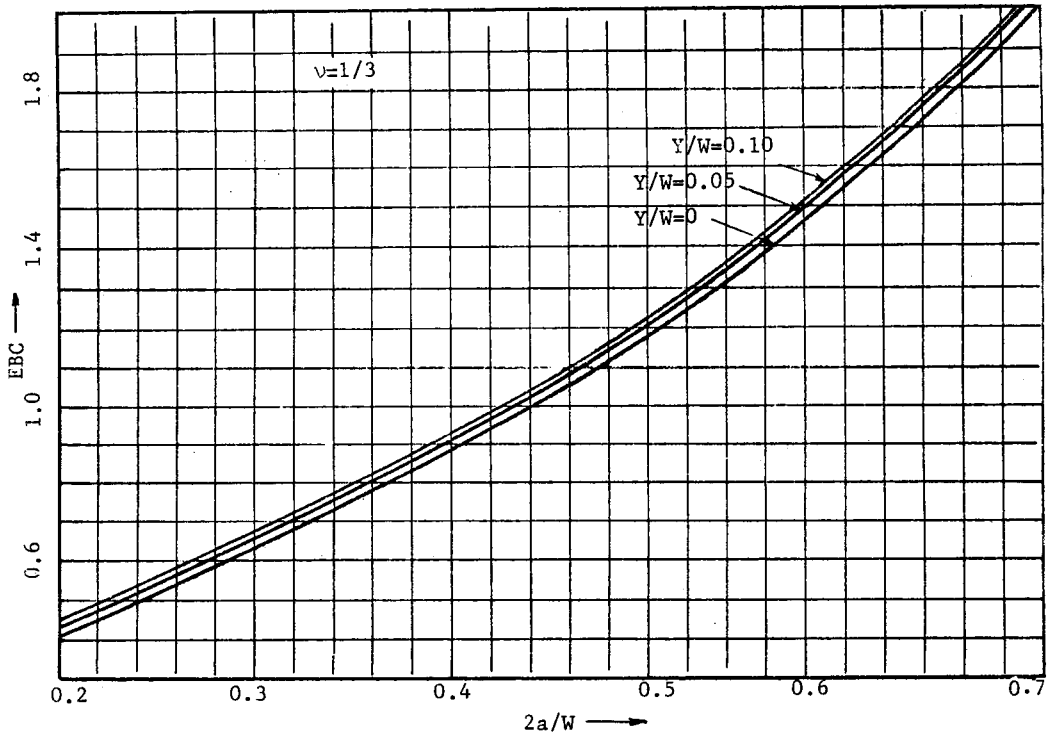


Fig.5.36- Compliance calibration curve for M(T)

at points 1, 2 and 3 in figure 5.35, and the compliance induced effective crack lengths, a_1 , a_2 and a_3 the R-curve is readily plotted.

The alternate specimen in R-curve generation is the compact specimen loaded in tension, which has the same dimensions as its counterpart in K_{IC} testing (Fig.5.3). The stress intensity factor expression is given in eq.(5.3), where a is the effective crack length, now. The compliance is measured at a point 0.1576W in advance of the load line and is given by

$$EBC = 103.8 - 930.4 \frac{a}{W} + 3610 \left(\frac{a}{W}\right)^2 - 5930.5 \left(\frac{a}{W}\right)^3 + 3979 \left(\frac{a}{W}\right)^4 \quad (5.22)$$

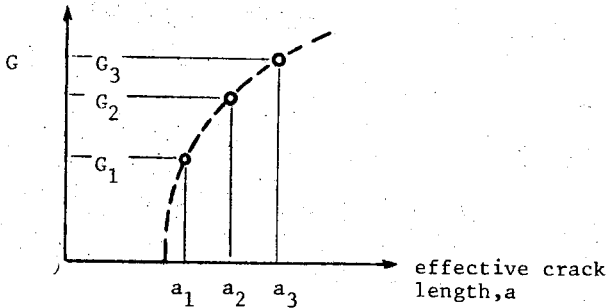


Fig.5.37: Point-by-point evaluation of the resistance curve.

or figure 5.38. Just as in center cracked panel, the secant lines to arbitrary points of $P-\delta$ plot are used to obtain compliance information which is translated into crack lengths. The R-curve is constructed using these effective crack lengths and the corresponding loads directly obtained from the load-displacement record.

The crack-line-wedge-loaded compact specimen, C(W), has the same stress intensity factor as given in K_{IC} testing for C(T) specimen, eq.5.3. The effective crack length (a) is, however, determined through the double compliance technique, that is, by measuring the crack opening displacement at two locations (Fig.5.39) and using tables supplied in E561-81 to infer on a/W . The compliance information δ_1/P may be used to find the load P which cannot be measured directly.

Use of C(W) enables one to obtain the full R curve (until a plateau toughness level is reached) since K is decreasing with crack extension and rapid fracture is suppressed. When a specimen with positive K -gradient characteristics is used the extent of the R-curve is terminated when the crack becomes unstable.

Fatigue pre-cracking procedures of K_{IC} testing (sec.5-1-2) apply equally well to the R-curve determination practice.

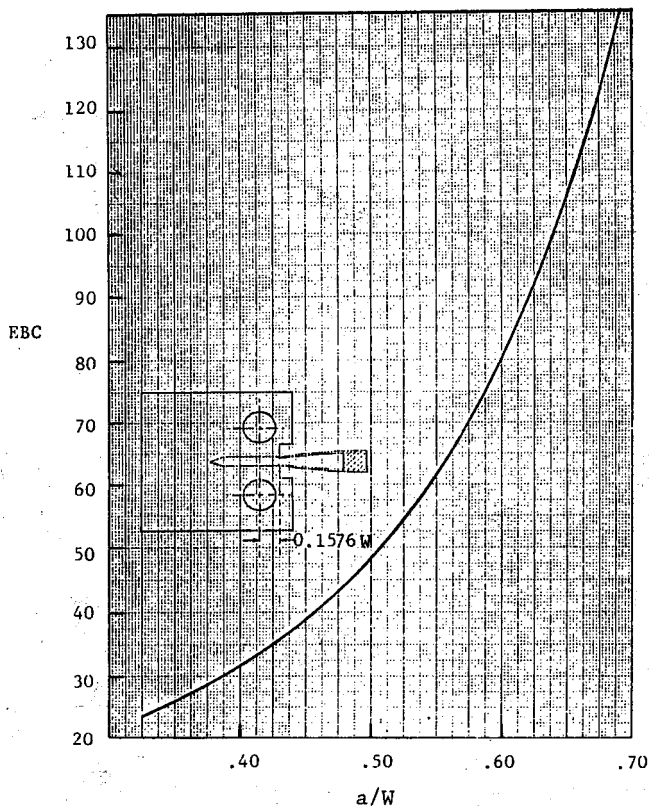


Fig.5.38- Compliance calibration curve for C(T)

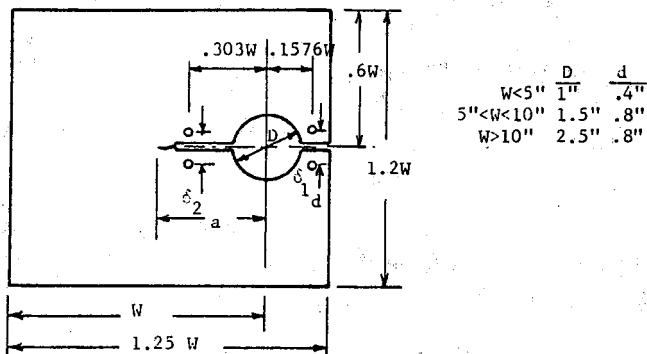


Fig.5.39- The wedge loaded compact specimen, C(W), proportions and the clip gage locations for double compliance technique

References

- 1- ASTM Standards, Annual Book (1985) Vol.03.01, E399-83 "Standard Test Method for Plane Strain Fracture Toughness of Metallic Materials".
- 2- Srawley, J.E. "Wide Range Stress Intensity Factor Expressions for ASTM E399 Standard Fracture Toughness Specimens" International Journal of Fracture, 12 (1976) pp.475-476.
- 3- Knott, J.F., Fundamentals of Fracture Mechanics, Butterworth, London, 1973 p.137.
- 4- Brown, W.F. and Srawley, J.E. "Plane Strain Crack Toughness Testing of high strength metallic materials" ASTM STP 410, (1966) pp
- 5- Clark, G. "Significance of Fatigue Stress Intensity in Fracture Toughness Testing" International Journal of Fracture, 15(1979), pp.R179-R181.
- 6- Kaufmann, J.G. "National Materials Property Data Network" ASTM Standardization News, Febr.86, pp.28-33.
- 7- ASTM Standards, Annual Book (1985) Vol.03.01, E645-84 "Standard Practice for Plane-Strain Fracture Toughness Testing of Aluminum Alloys"
- 8- ASTM Standards, Annual Book (1985) Vol.03.01, E616-82 "Standard Terminology Relating to Fracture Testing".
- 9- Wilhem, D.P. "Standard Designation Code for Fracture Specimens, Loading and Orientation" International Journal of Fracture, 23(1983) pp. R77-R80.
- 10- Barker, L.M. "Specimen Size Effects in Short Rod Fracture Toughness Measurements" ASTM STP 855, Amer.Soc.for Testing and Materials (1984) pp.117-133.
- 11- Barker, L.M. "Short Rod and Short Bar Fracture Toughness Specimen Geometries and Test Methods for Metallic Materials" ASTM STP 743, Amer. Soc.for Testing and Materials, (1981), pp.456-475.

12- Barker, L.M." Compliance Calibration of a Family of Short Rod and Bar Fracture Toughness Specimens" Engineering Fracture Mechanics, 17, (1983), pp.289-312.

13- Barker, L.M. and Baratta, F.I. "Comparison of Fracture Toughness Measurements by the Short Rod and ASTM Standard Method of Test for Plane-Strain Fracture Toughness of Metallic Materials (E399-78)" Journal of Testing and Evaluation, 8, (1980) pp.97-102.

14- Munz, D., Bubsey, R.T. and Srawley, J.E."Compliance and Stress Intensity Coefficients for Short Bar specimens with Chevron Notches" International Journal of Fracture, 16(1980), pp.359-374.

15- Broek, D. "Elementary Engineering Fracture Mechanics", Noordhoff-Leyden, Holland (1974) p.178.

16- Broek, D. "Fracture" in Agard-LS-97 "Fracture Mechanics Design Methodology", NATO, (1979) p.2-2

17- Feddersen, C.E. "Evaluation and Prediction of the Residual strength of Center Cracked Tension Panels" ASTM STP 486 (1971) pp.50-78.

18- Frediani, A. "An Evaluation of the Reliability of Fracture Mechanics Methods" Engineering Fracture Mechanics, 14 (1981), pp.289-322.

19- Hertzberg, R.W. "Deformation and Fracture Mechanics of Engineering Materials" 2nd edition, John Wiley and Sons, New York (1983), p.308.

20- Wang, D.V. and McCabe, D.E. "Investigation of R curve using Comparative Tests with Center Cracked Tension and Crack Line Wedge Loaded Specimens" ASTM STP 590, Amer.Soc.for Testing and Materials (1976) pp.169-193.

21- ASTM Standards, Annual Book (1985) Vol.03.01, E561-81" Standard Practice for R-curve Determination".

22- Hutchinson, J.W. "A Course on Nonlinear Fracture Mechanics" Tech.Univ. of Denmark (1979) pp.20-27.

23- Irwin, G.R. and Roland de Wit "A Summary of Fracture Mechanics Concepts, "Journal of Testing and Evaluation, JTEVA, Vol 11(1983) pp.56-65.

Problems

1- A soft aluminum plate (600 mm wide, 4mm thick) is subjected to uniform stress at infinity. Optical measurements of the thickness made ahead of the crack line give the following values:

Distance from crack tip (mm): 1 2 3 4 5

Decrease in thickness (mm) : 1.2 0.84 0.68 0.60 0.50

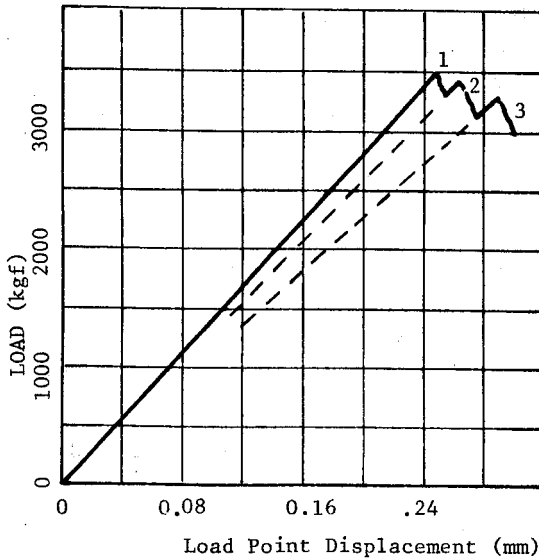
Estimate K_I value and discuss the validity of the assumptions made in the solution if $2a=30\text{mm}$.

Answer: $K_I \approx 14 \text{ kg mm}^{-3/2}$

2- In testing a 1" thick (IT) standard C(T) specimen in a stiff machine occasionally one observes fracture initiation and arrest as sketched below. Assuming that the change in compliance between points 1, 2 and 3 is entirely due to crack growth you are asked to obtain an estimate for the crack length at point 3. $a_1/W = 0.5$.

Steel of yield strength 90 kgf/mm²

Answer: $a_3 \approx 27.4 \text{ mm}$



3- A large 7075-T6 aluminum panel carries a tensile load of 9000 lb/inch of width. You are asked to select a minimum thickness for the panel such that the nominal stress should not exceed $5/8 S_y$ and fast fracture should not occur for cracks 2" or less in length. Yield strength for this material is 72 000 psi and fracture toughness tests have given the following results:

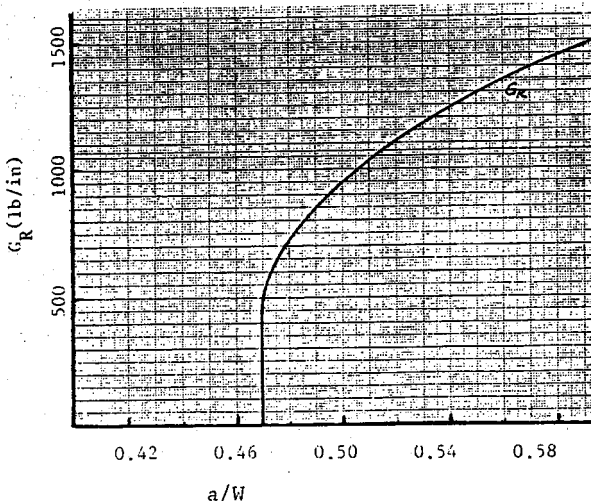
thickness (in):	0.5	.1	.15	.2	.3	.4	.5	.6	.8
K_{Ic} (ksi $\sqrt{\text{in}}$)	75	85	75	60	55	50	45	40	35

What increase in load carrying capacity could be obtained by using two sheets side by side, each half the thickness of the sheet in the above problem.

Answer: $B \approx 0.3''$; $\Delta P = 3000 \text{ lb}$.

4- A clip-on gage will be designed. As a preliminary study, determine the strain induced as a function of displacement for a series of choices. Let the material be beryllium copper ($S_y = 130\,000$ psi, $E = 17 \cdot 10^6$ psi), try thicknesses of 1 and 2 mm and arm lengths of 30, 40 and 50 mm. The strain gages are attached at a distance corresponding to 90% of the arm length from the free end. Discuss both the range of operation and the sensitivity of each candidate clip gage.

5- For the compact tension specimen ($W=8''$, $B=1/8''$) made of high strength steel with the resistance curve supplied below, locate the instability point (a) for $C_M = \infty$ (b) for $EBC_M = 100$.



a/W

Answer: a) at $a/W = .52$ b) at

$a/W = 0.57$

6. TRANSITION TEMPERATURE APPROACH

6.1 INTRODUCTION

Small scale yielding condition requires the plastic zone to be small compared to all linear dimensions of the component. Thus, LEFM is not applicable to lower strength materials which undergo large scale yielding before failure. An elastic-plastic analysis of cracked bodies is necessary to replace the concepts of LEFM. Such analyses are difficult and slow in development. A distinctly different approach to fracture predictions beyond the linear elastic range is the transition temperature approach.

Low strength ferritic steels constitute a major group of construction materials, used extensively in pressure vessel, bridge and ship structures. These ferritic steels, being bcc in crystal structure, are sensitive to temperature and strain rate changes and show a marked change in energy absorption as the ductile to brittle transition temperature (DBTT) is crossed. The transition temperature approach addresses such ferritic steels and can be crudely summarized as "making sure that the material is used above the transition temperature".

6.2 MICRO-MECHANISMS

Excluding intergranular fracture, the two microscopic mechanisms involved in the short-time failure of metals are transgranular cleavage and ductile fracture by void growth. The face centered cubic metals in short time tests at ambient temperature and in the absence of a corrosive environment will fail by a ductile fracture mode. For body centered cubic and hexagonal close packed metals both cleavage and ductile mechanisms may occur. In particular, the material most often studied, low carbon steel, exhibits cleavage fracture at low temperatures. With increasing temperature cleavage becomes more difficult, a rapidly increasing fraction of

the fracture becomes "ductile" until at a high enough temperature ductile fracture modes dominate.

Cleavage fracture occurs by separation along preferred crystallographic planes - (100) planes in steel, for example. As a result of the flat, smooth fracture surface in each grain the surface is quite reflective and has a shiny appearance.

The general features of ductile fracture are the nucleation, growth and coalescence of voids to form a "fibrous" surface on a macroscale and a series of dimples on a microscale. A large amount of evidence indicates that the voids responsible for fracture are formed primarily at hard second-phase particles and inclusions. The nucleation of voids occurs either by fracture of particles or by decohesion of the particle-matrix interface. In some cases such as manganese sulphide particles in steel, decohesion occurs readily while in other cases such as carbides in steel a certain amount of plastic deformation in the matrix is needed to initiate cracking or decohesion. Voids, after being formed, grow by plastic deformation of the matrix. Their growth relative to the overall deformation of the matrix is a very strong function of the triaxiality of stress (hydrostatic stress/effective stress) and the strain hardening rate of the matrix. Final separation results from the coalescence of the growing voids. A limit to the growth process has been taken in analytical studies as that in which the voids contact one another. In practice this is preceded by necking or localized shear between voids. The details of final coalescence, as with initiation, may vary greatly between different alloys.

6.3 CHARPY BASED DBTT DEFINITIONS

It is well known that in testing steels three factors greatly enhance the ductile to brittle transition. These are triaxiality of stress (as around a notch or a crack), high strain rate and low temperature. Various standard tests are used to measure transition temperatures and usually these involve both impact loading and notched specimens. The change from low energy absorption level to upper shelf is not an abrupt one and a range of transition temperatures exists (Fig.6.1). It is not obvious which point to choose as the transition temperature along such gradually changing energy-temperature plots.

The most common impact test is the Charpy test. The V-notch of the Izod specimen is combined with the three point bend geometry of the Charpy

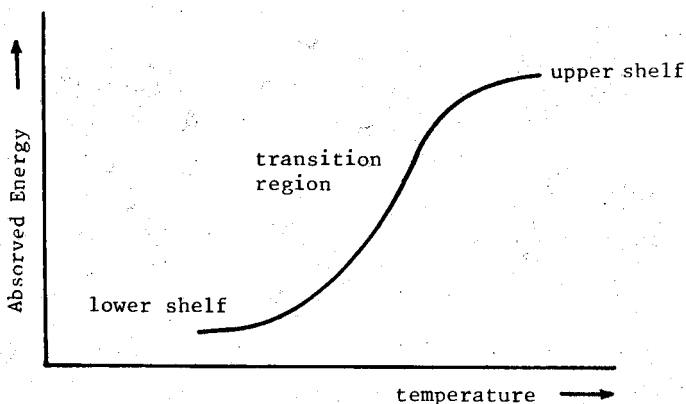


Fig.6.1: Schematic showing the absorbed energy in test of notched specimens at different temperatures

specimen. This Charpy V-notch specimen (CVN) — 50x10x10 mm, V-notch 45° and 2mm deep, described in ASTM specification E23— is broken by a pendulum and the energy absorbed in fracture is obtained from the difference in height of the pendulum mass, before release and when it comes to rest after breaking the specimen. In fact, about one-third of the energy calculated in this manner may be absorbed in the specimen grips, but this is usually not considered in plotting the results of the Charpy test.

One popular approach of defining transition temperature is to study the fracture surface appearance. For a given fraction of shear (fibrous) fracture and a corresponding fraction of cleavage fracture, the temperature is quoted as the Fracture Appearance Transition Temperature (FATT), e.g. FATT 30% shear.

Another approach is to base the transition temperature on some "adequate" level of energy absorbed. Historically, 15 ft-lb(20J) level is used extensively with Liberty Ship steels. 30 ft-lb(41J) and 50 ft-lb(68J) are other quoted energy levels. Midpoint of the energy curve, the point of inflection of the energy curve or 50% of the upper shelf energy level are various definitions of the transition temperature based on energy levels.

The energy level in a Charpy test must be increased for higher strength steels in order to maintain a constant level of resistance to fracture. Energy absorption is controlled by two factors: the strength of the steel, which regulates the force required to deform the Charpy specimen and the

ductility of the steel, which determines the distance through which the force acts during testing. Since loss of fracture toughness is due to loss in ductility rather than strength, a criterion which evaluates notch ductility rather than energy is a more significant and universal index. On this basis, it is recommended that the transition temperature be established by determining the temperature at which a lateral expansion of 15 mils (0.015 in = 0.38mm, thus 3.8%) is obtained on the compression side of a Charpy V-notch impact test specimen. The procedure is described in ASTM Specification A370-68. The average energy absorption corresponding to various lateral expansions is shown in Fig.6.2 [1].

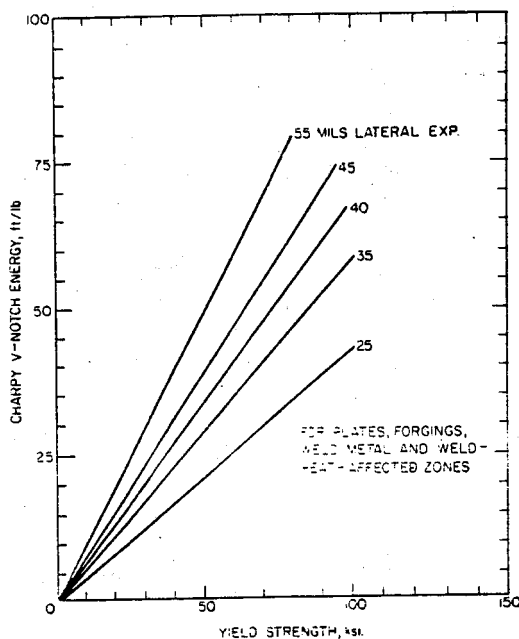


Fig.6.2: Relationship at 25,35,40, 45 and 50 mils lateral expansion between energy and yield strength [1]

Either one of the methods described above appears to be satisfactory for determining the relative transition temperature of pressure vessel or ship steels with yield strengths up to about 700 MPa (100 ksi). But it is not possible to predict an absolute index of safety against brittle fracture for other stress levels and flaw sizes. To complicate the issue further, transition temperatures based on either energy absorption,

ductility or fracture appearance criteria do not agree even for the same material. The following values have been quoted for a 3½ % Ni 0.1%C steel, for example.

$C_V = 15$ ftlb	-105°C
average energy	-55°C
FATT 100% shear	-10°C
FATT 50%	-50°C
FATT 100%cleavage	-118°C

Typical CVN impact curves of absorbed energy versus temperature for various structural materials are presented in Fig.6.3. It should be emphasized that there is no single unique curve for any single composition but that these curves depend also on the thermomechanical processing history. Approximately 15-20 specimens of a single material are tested at various

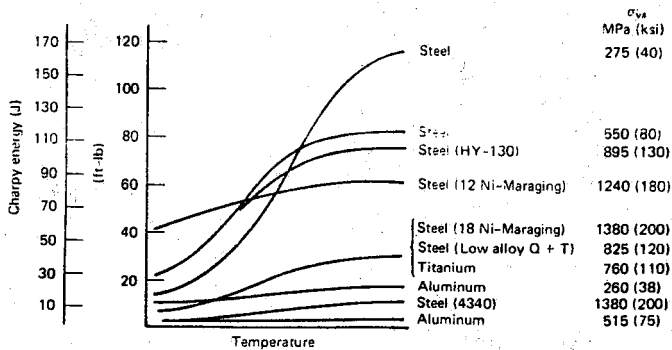


Fig.6.3: Typical Charpy V-notch energy versus temperature behavior of various materials [2].

temperatures, and a smooth curve is fitted to the results. Because of the relative small changes in behavior with temperature of the very high strength steels, the titaniums, and aluminums, the CVN impact specimen is rarely used to evaluate the toughness behavior of these materials.

It is not clear at all how to extend CVN values to different geometries, loading conditions or flaw sizes. CVN specimen has a notch root radius of 0.25mm. As the root radius is increased the triaxiality is reduced and the transition temperature is observed to decrease in the manner shown in Fig.6.4. The strain rate imposed by a striking hammer is in the order of

10 sec^{-1} . For static Charpy tests, where $\dot{\epsilon} \approx 10^{-4} - 10^{-5} \text{ sec}^{-1}$, the transition curve shifts dramatically (Fig.6.5). The greatest strain rate induced shift occurs in the low strength steels and no apparent strain rate sensitivity is observed in alloys with yield strengths in excess of 140 ksi (1000MPa) [3]. The magnitude of the temperature shift in steels of various yield strengths has been related to the room temperature yield strength of the steel and can be approximated by [2]:

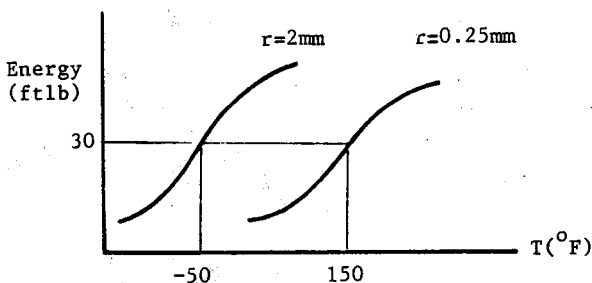


Fig.6.4: Effect of notch radius on absorbed energy in CVN specimens

$$\left. \begin{aligned} T_{\text{shift}} &= 215 - 1.5 S_y && \text{for } 36 \text{ ksi} < S_y < 140 \text{ ksi} \\ &= 0 && \text{for } S_y > 140 \text{ ksi} \end{aligned} \right\} \quad (6.1a)$$

where T_{shift} is in $^{\circ}\text{F}$ and S_y in ksi. In SI (using $^{\circ}\text{C}$ and MPa) it is given through

$$T_{\text{shift}} = 119 - 0.12 S_y \quad \text{for } 250 < S_y < 1000 \text{ MPa} \quad (6.1b)$$

6.4. ADDITIONAL FRACTURE TEST METHODS

6.4.1 DT and DWT Methods: The absolute magnitude of the experimentally determined transition temperature as defined by any of the previously described methods depends on the thickness of the specimen used in the test program. This is due to the potential for a plane strain-plane stress transition when sample thickness is varied. Therefore, laboratory results may bear no direct relation to the transition temperature characteristics of the engineering component if the components thickness is different from

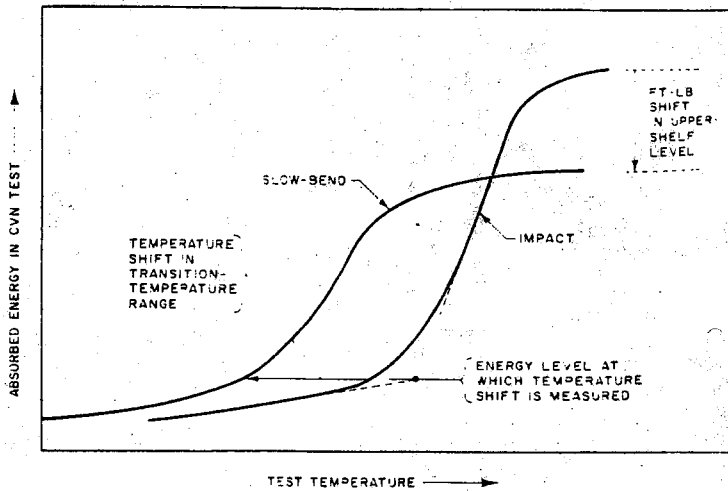


Fig.6.5: Schematic representation of shift in CVN transition temperature and upper shelf level due to strain rate

that of the test bar. To overcome this difficulty, the dynamic tear test (DT) and drop weight tear test (DWTT) were developed. DT and DWTT specimens may be considered to be oversize Charpy samples (Fig.6.6). Again single edge notched beams are impact loaded in three point bending in a drop weight or pendulum type machine but these specimens have very sharp pressed notches. The details of DT and DWTT are covered in ASTM specifications E 604-83 and E 436-74, respectively.

A complete transition curve is usually obtained with DT and DWTT specimens similar to that obtained for CVN specimens. Because the DT and DWTT specimens are thicker than the CVN specimen and have sharper notches (additional constraint) the transition behavior occurs at higher temperatures compared with impact CVN results. The plastic deformation caused by the pressed knife and the resulting tensile residual stresses are also effective in reducing the ductility of the specimen and shifting the transition curves to higher temperatures (Fig.6.7).

6.4.2. CAT Tests: The crack arrest temperature (CAT) test is developed by Robertson and aims at determining the stress temperature pair at which a large running crack arrests. A crack is initiated at the cold side of a

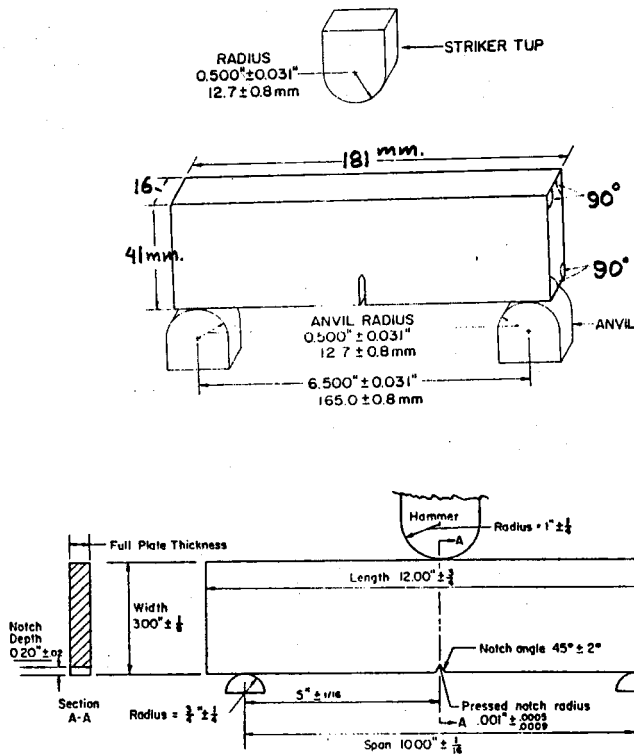


Fig.6.6: (a) Dynamic tear and (b) Drop Weight Tear Test specimens

plate. The plate has a temperature gradient and is subject to a uniform tensile stress (Fig.6.8). The crack is initiated by an impact from a bolt gun. It propagates rapidly driven by the applied stress and assisted by the low toughness of the material at the colder side of the plate, but eventually encounters material at a higher temperature sufficiently tough to arrest it. Unfortunately, at low temperatures the stress values are so low (5-8 ksi, 35-50 MPa) that absolute safety through crack arrest is not economical. At higher temperatures fracture arrest protection may be practical at realistic stress levels (Fig.6.9).

Crack arrest tests such as the Robertson test or the double tension test, the ESSO test (shown in Fig.6.10) are expensive to carry out. A somewhat simpler alternative was developed at the U.S. Naval Research Laboratory, known as the Explosion Bulge test (Fig.6.11). Tests were made at different temperatures and the temperature above which full plastic

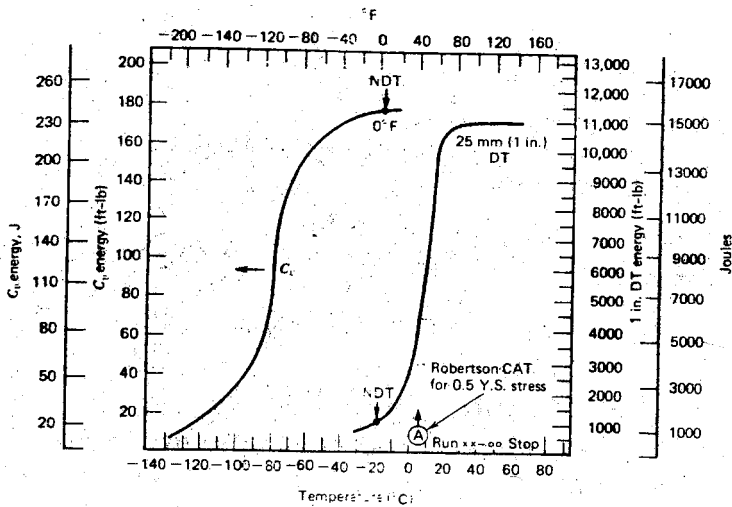


Fig.6.7: Comparison of Charpy V-notch, dynamic tear, drop weight NDT and CAT test results for A541 [4]

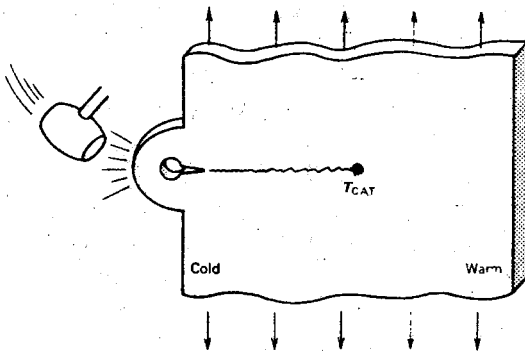


Fig.6.8: Robertson crack arrest test specimen.

bulging occurs without cracking is referred to as the Fracture Transition Plastic (FTP) temperature. The temperature above which cracks will not extend into material which is only elastically deformed, although they do extend into plastically deformed material is called the Fracture Transition Elastic (FTE) temperature. Hence at temperatures below FTE cracks propagate in material in which the nominal stress is below yield. Thus, in terms of the crack

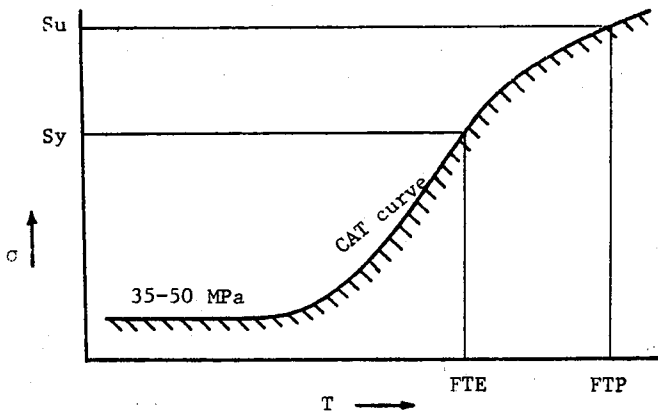


Fig.6.9: The stress and temperature combinations leading to arrest

arrest curve shown earlier, the FTE and FTP temperatures correspond to intersection of the CAT curve with the yield and ultimate curves shown in Fig.6.9.

6.4.3 NDT Test: Another test to investigate the conditions required for initiation of brittle fractures in structural steels is the drop-weight test which determines the nil ductility transition (NDT) temperature. The specimen used contains a notched brittle weld bead. It is loaded in three point bending by a falling weight at various temperatures. As the weight first hits the specimen the brittle weld bead cracks creating a small

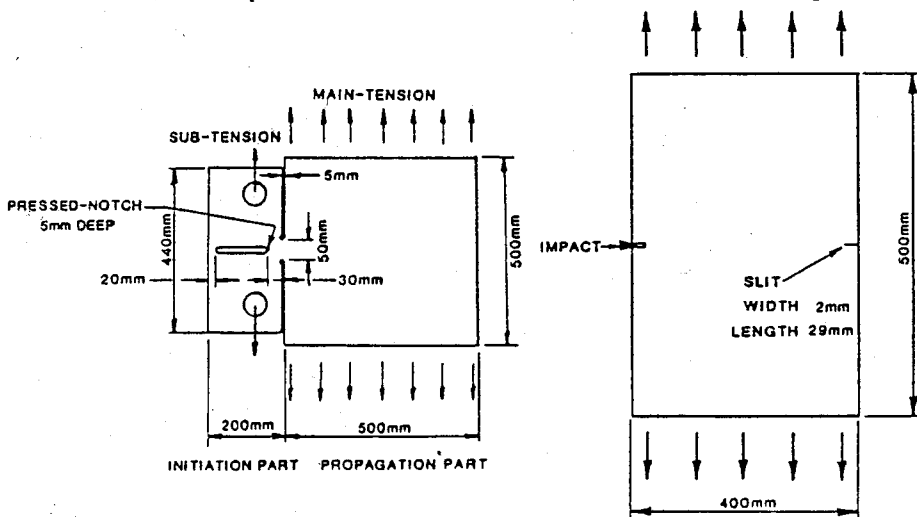


Fig.6.10: The double tension and ESSO wide plate test specimens.

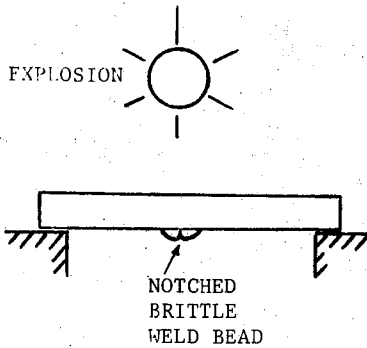


Fig.6.11: The explosion bulge test set-up

very sharp semicircular surface crack. As the weight continues to fall the material being tested is loaded dynamically in the presence of the small weld crack. A mechanical stop placed under the center of the specimen limits the amount of deformation to onset of yielding (Fig.6.12). The NDT temperature, is defined as the highest temperature at which a standard specimen breaks in a brittle manner; that is the temperature at which a small crack propagates at the yield stress. This test is standardized by ASTM and described in specification E208-84a. It has been widely used for quality control of structural steels and since it appears to give a reproducible transition temperature, it has been used as the basis of design and operating procedure in certain codes.

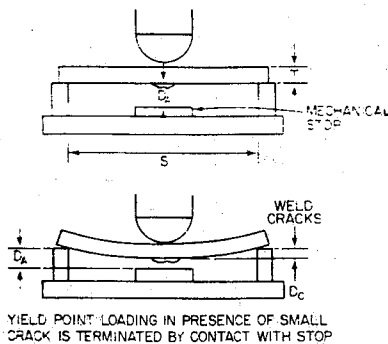


Fig.6.12: NDT temperature test specimen

6.5 FRACTURE ANALYSIS DIAGRAM

The fracture analysis diagram (FAD) was developed by Pellini of the

Naval Research Laboratory to provide design guidelines or criteria for structural steels that exhibit a transition temperature. The general diagram is presented in Fig.6.13. Flaw size and stress level is related in this diagram to the initiation and propagation of brittle fractures with respect to NDT, FTE and FTP temperatures:

1- Below NDT, small flaws initiate brittle fracture only in the presence of yield point stresses. At lower stresses, the flaw size required to initiate brittle fracture increases rapidly so that a flaw size of about 24" is required to initiate brittle fracture at one-fourth the yield stress. Below NDT, cracks will propagate in a brittle manner at very low stress levels down to 35-50 MPa (5-8ksi). Thus, structures must be designed and fabricated such that initiation criterion is not met. That is, crack length must be kept smaller than that required to initiate fracture at specified stress level (e.g. if $\sigma = S_y/2$, keep $a < 12"$ to avoid initiation)

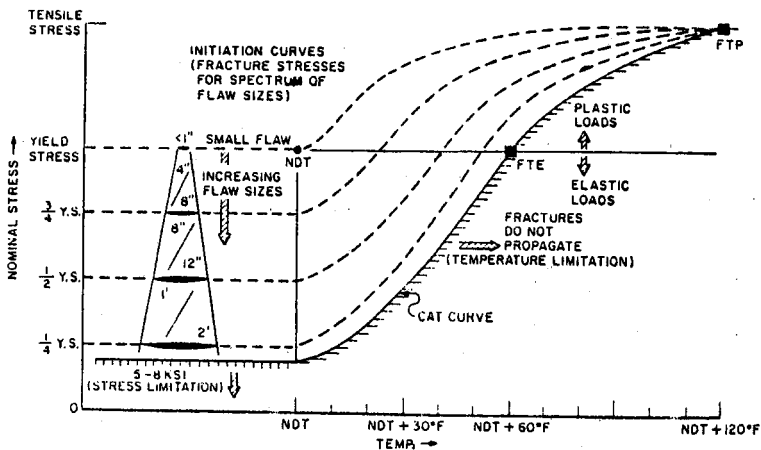


Fig.6.13: The fracture analysis diagram of Pellini [5]

2- Above NDT, the stress level required to initiate or propagate brittle fractures rises rapidly. Typically, for one inch thick ship plates:

(i) At $NDT + 17^{\circ}C$ ($30^{\circ}F$), fractures do not propagate for stresses less than one half the yield stress, regardless of the flaw size.

(ii) At $NDT + 33^{\circ}C$ ($60^{\circ}F$), fractures do not propagate for stresses less than the yield stress.

3- At temperatures above FTE, cracks propagate only in plastically deformed regions and the fracture surface contains heavy shear lips.

4- At $NDT + 67^{\circ}C$ ($120^{\circ}F$), FTP temperature is reached and above FTP, brittle fracture no longer occurs and failure occurs by shear tears under local stresses exceeding the ultimate tensile strength of the material.

Since stress concentrations are likely to exist in structures, local stresses may easily reach S_y , even if the nominal stresses are low. Particularly in nonstress-relieved welded structures an unacceptable high risk of brittle fracture exists if $T < NDT$. If a small crack initiates and grows, it may move away from the discontinuity; but a large running crack, as it is now, will not arrest at nominal stress since this nominal design stress is $(5/8) S_y$ or $S_u/4$ and not 35-50 MPa.

Pellini has noted that the FAD transition temperature range is expanded significantly by an increase in mechanical constraint such as the thickness. Particularly the crack arrest curve shifts starting at the NDT temperature. At six inches plate thicknesses the temperature span between the NDT and FTE is expanded to $67^{\circ}C$ ($120^{\circ}F$), which implies that thick walled structures need more attention. There is no effect of section size for the small flaw curve of the FAD, though. The instability conditions for small flaws are controlled by the flaw size and not the section size. For example, a small flaw of a few millimeters does not recognize that it is located in a 25mm or 250 mm thick section - both are semi-infinite with respect to the flaw size. Larger flaws are affected more by section size increases since relative constraint changes.

6.6 IMPACT TESTS vs. LEFM

Precracked Charpy specimens are used with the hope of correlating CVN values with fracture toughness results. Infact, to provide more information about the load-time history of the sample, the impact hammer is instrumented with strain gages whose output is recorded with an oscilloscope. Having load versus time plots, the total energy can be separated into initiation and propagation energies and values of dynamic fracture toughness (K_{Id}) are hoped to be determined. The specimen size used, however, rarely meets the plane strain fracture toughness requirements presented in chapter five.

Conventional fracture toughness tests leading to K_{IC} values are:

performed at loading rates about $1 \text{ MPa} \sqrt{\text{m}} / \text{sec}$. At rapidly applied loading rates (typically $\dot{K} \approx 10^4 - 10^5 \text{ MPa} \sqrt{\text{m}} / \text{sec}$) the resistance to fracture initiation is designated as K_{I_d} (ASTM favors to designate $K_{I_C}(t)$ where t is the loading time to reach P_Q in milliseconds). On the other hand, the value of K_I under conditions where a rapidly propagating fracture is arrested within a test specimen is called crack arrest fracture toughness and is designated by K_{I_a} .

In structural steels, experimental evidence shows that K_{I_d} and K_{I_a} are usually less than K_{I_C} . Analogous to Charpy tests, K_{I_C} , K_{I_d} and K_{I_a} all exhibit a sharp increase with temperature over a relatively small temperature range. It is virtually impossible to get upper shelf valid K_{I_C} and K_{I_d} values, but lower shelf and transition range values are available. As illustrated in Fig. 6.14, the shift in K_{I_C} behavior as a function of loading rate is the same as the shift in CVN test values presented in sec. 6.3. This enables one to predict the dynamic K_{I_d} values from slow bend K_{I_C} values or vice versa.

The most popular upper shelf K_{I_C} -CVN correlation is

$$\left(\frac{K_{I_C}}{S_y}\right)^2 = \frac{5}{S_y} \left(\text{CVN} - \frac{S_y}{20}\right) \quad (6.2a)$$

where K_{I_C} is in $\text{ksi} \sqrt{\text{in}}$, S_y in ksi and the standard Charpy V-notch impact test value at upper shelf is in $\text{ft-lb} [2]$.

Or in SI

$$\left(\frac{K_{I_C}}{S_y}\right)^2 = 0.64 \left(\frac{\text{CVN}}{S_y} - 0.01\right) \quad (6.2b)$$

where K_{I_C} is in $\text{MPa} \sqrt{\text{m}}$, S_y in MPa and CVN in Joules. These results were obtained on eleven steels having S_y in the range 110-246 ksi . The K_{I_C} values for these steels ranged from 87 to 246 $\text{ksi} \sqrt{\text{in}}$ and the CVN impact values ranged from 16 to 89 ft-lb .

At the upper shelf, the effects of loading rate and notch acuity are not so critical as in the transition temperature region. Thus, the differences in the K_{I_C} and CVN test specimens (namely, loading rate and notch acuity) are not that significant and a reasonable correlation would be expected [2]. In addition to that, the relationship presented in eq. 6.2

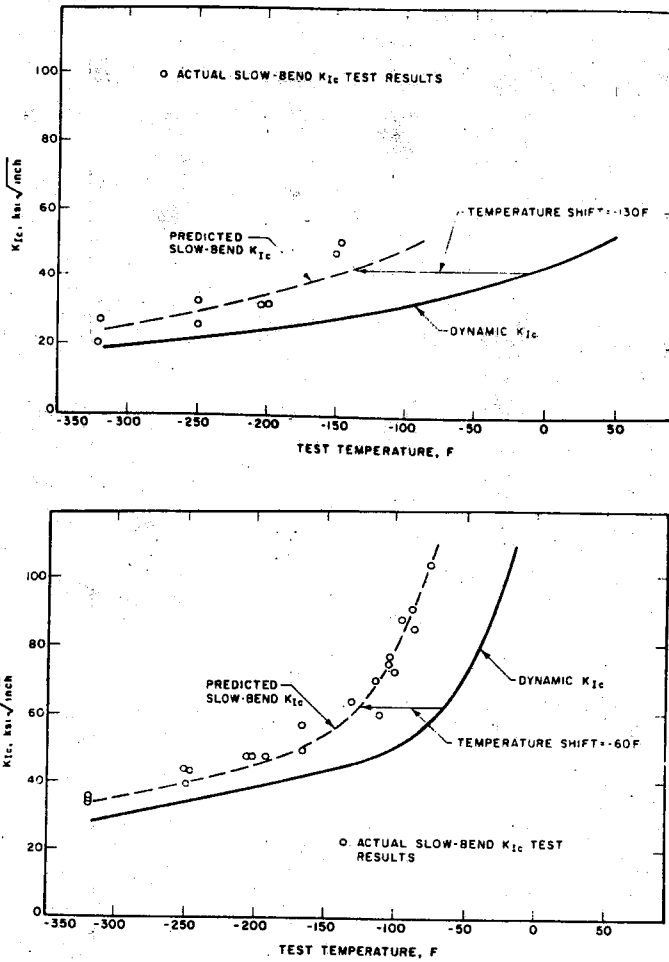


Fig.6.14: Use of CVN test results to predict the effect of loading rate on K_{IC} for (a) A 302-B steel (b) A 517-F steel [2]

is limited to steels having $S_y > 100$ ksi. These higher strength steels not showing marked temperature shift due to strain rate makes it possible to relate impact values to static K_{IC} values.

K_{Id} values can be predicted from CVN impact results in the transition temperature region using the empirical relationship [2]

$$\frac{K_{Id}^2}{E} = 5 \text{ CVN} \tag{6.3a}$$

where E is ksi, K_{Id} in $\text{ksi}\sqrt{\text{in}}$ and Charpy values in ft-lb, or through

$$\frac{K_{Id}^2}{E} = 0.64 \text{ CVN} \quad (6.3b)$$

in units of $\text{MPa}\sqrt{\text{m}}$, MPa, J. To obtain estimates of K_{IC} values the estimated K_{Id} values should be modified according to the rate shift described in eq. 6.1. K_{Id} values are assumed to equal about 20-25 $\text{ksi}\sqrt{\text{in}}$ when CVN energy absorption value is less than 5ft-lb. This procedure is limited to the lower end of the transition curve. As the upper shelf region is approached the upper shelf correlation (eq.6.2) is recommended eventough it was developed primarily for steels with $S_y > 80$ ksi.

The correlations between K_{IC} and CVN values are limited to specific material populations. Roberts and Newton, who examined the accuracy of 15 such relationships concluded that no single correlation could be used with any degree of confidence to encompass all possible test conditions and differences in materials [4]. Furthermore, because of the intrinsic scatter associated with K_{IC} and CVN measurements, the correlations possessed a relatively wide scatter band.

To guide the design of pressure vessels the American Society of Mechanical Engineers has determined a reference toughness versus temperature curve. This reference toughness curve, designated as K_{IR} , is the lower bound of the available K_{IC} , K_{Id} and K_{Ia} values for the pertinent materials (Fig.6.15). The temperatures are specified relative to the NDT temperature. In fact, a reference nil ductility transition temperature RT_{NDT} is defined which is the higher of nil ductility transition temperature (T_{NDT}) and $T_{40} + 60$ °F where T_{40} stands for the temperature at which all Charpy V-notch tests give a lateral expansion more than 40 mils. An alternative requirement for T_{40} can be 35 mils of lateral expansion together with a minimum of 50 ft-lb absorbed energy. Thus the ASME procedure tries to weed out nontypical materials such as those which might have low transition temperature but abnormally low energy absorption on the upper shelf.

The drop weight test to determine the NDT temperature is interpreted in terms of LEFM by Irwin and Pellini, separately. The relationship between dynamic yield strength S_{yd} and K_{Id} resulting from these studies is:

$$K_{Id} = (\text{Factor}) \times S_{yd} \quad (6.4)$$

where the factor varies from 0.634 to 0.78. When the lower bound curve of ASME is checked against this analytical relationship the value of K_{IR} at NDT is 0.55 of the dynamic yield of the steels tested. The resulting curve (Fig.6.15), therefore, represents a very conservative assumption as to

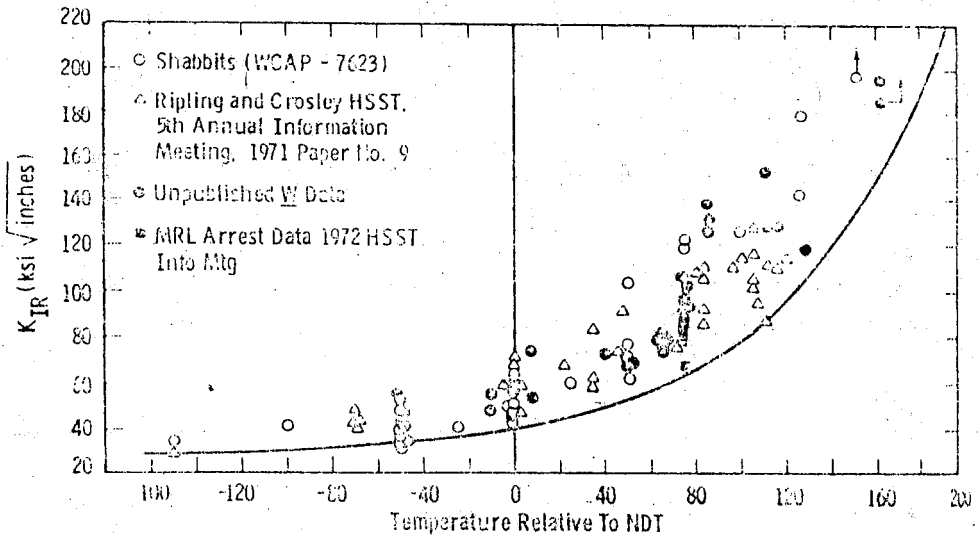


Fig.6.15: Reference stress intensity factor K_{IR} used in pressure vessel code of ASME [6]

the critical stress intensity vs. temperature properties of materials with yield strengths $S_y < 345$ MPa (50 ksi). Only K_{Id} and K_{Ia} data are shown in Fig.6.15 because K_{Ic} values are invariably much higher, so they do not affect the lower bound. The analytical approximation to this lower bound curve is:

$$K_{IR} - 26.777 = 1.223 \exp \{0.0145 [T - RT_{NDT} + 160]\} \quad (6.5a)$$

where K_{IR} is in $\text{ksi} \sqrt{\text{in}}$ and temperature in $^{\circ}\text{F}$, or

$$K_{IR} - 29.45 = 1.345 \exp \{0.261 [T - RT_{NDT} + 89]\} \quad (6.5b)$$

where K_{IR} is in $\text{MPa} \sqrt{\text{m}}$ and temperature in $^{\circ}\text{C}$.

The K_{IR} curve of pressure vessel code was conceived as a lower bound

toughness value in 1972. Since then, both rapid initiation toughness (K_{Id}) and arrest toughness (K_{Ia}) values have been found to fall slightly below K_{IR} near the lower shelf. Besides, the K_{IR} curve does not have a statistical meaning. A practical lower bound curve must have a predefined low probability that the fracture toughness of the steel can lie below the curve. To define such a lower bound, a functional relationship must first be found which describes the change in the mean fracture toughness with temperature. Then from an examination of the distribution of the data about the mean, the lower bound can be defined for any specified probability. Efforts have been concentrated on improving the crack arrest technology in the last decade since the average slope of K_{Ia} data is found to be smaller than that of K_{Id} data as the test temperature is raised within the ductile/brittle transition region.

ASTM has formed a Task Group to develop a standard test procedure for measuring crack arrest toughness and a multinational cooperative test program has been conducted to examine candidate procedures. Compact crack arrest (CCA) specimen loaded through a transverse wedge is expected to be the standard specimen. The specimen dimensions and the loading set-up are shown in Fig.6.16 and 6.17, respectively.

The experimental procedure can be outlined as follows [7] :

- 1- Displacement is measured between knife edges across the crack mouth at $0.25W$ from the center of the loading hole. The knife edges are attached by screws to the specimen.

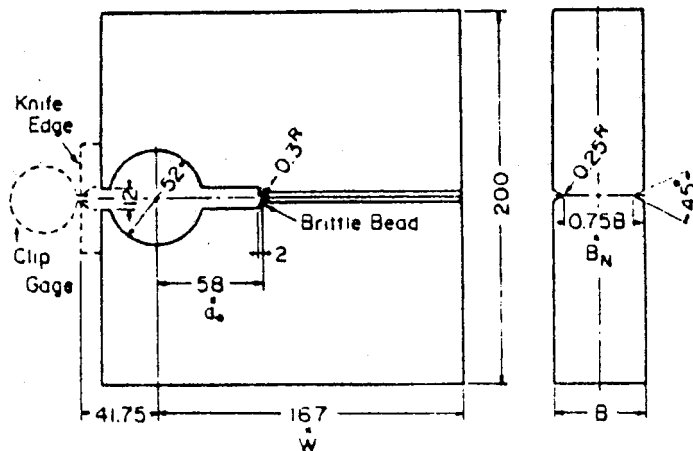


Fig.6.16: Geometry of compact crack arrest specimen

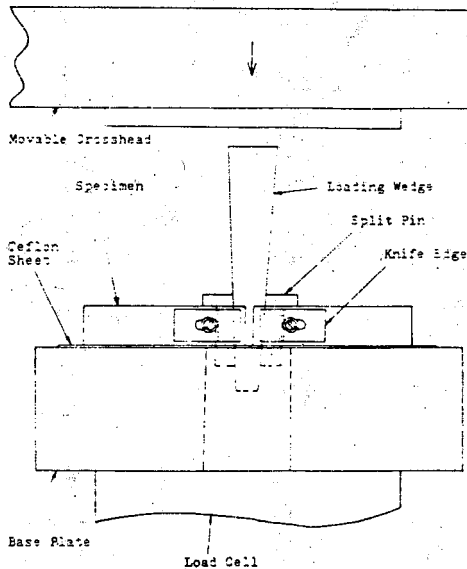


Fig.6.17: Test specimen loading arrangement

- 2- Each specimen is loaded in a universal testing machine at a cross-head speed of 5 mm/min.
 - 3- To reduce friction, a high pressure lubricant is applied to the loading surfaces and a thin (0.1mm) Teflon sheet is placed between the specimen and the base plate (Fig.6.17).
 - 4- Load is applied monotonically until crack propagation and is removed immediately following crack arrest. Displacements at crack initiation and arrest are obtained from autographic load-displacement records (Fig.6.18).
 - 5- Before the wedge is extracted the crack front should be marked to determine the distance of the crack jump. This can be achieved either by heat tinting or by introducing ink into the crack and baking the set to dry the ink completely. Upon reloading the specimen is broken and the measurements are taken.
- The stress intensity factor is calculated from the equation provided by Crosley et.al.

$$K_{Ia} = E \Delta_f \sqrt{\frac{B}{B_N W}} f\left(\frac{a_f}{W}\right) \quad (6.6)$$

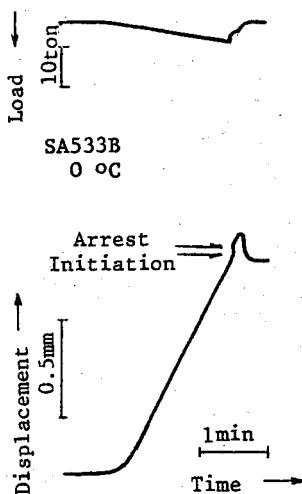


Fig.6.18: Typical record of displacement and load vs. time for compact test

$$\text{where } f(\alpha) = \frac{2.2434 (1.7164 - 0.9\alpha + \alpha^2) \sqrt{1-\alpha}}{(9.85 - 0.17\alpha + 11.0\alpha^2)}$$

The crack opening displacement Δ_f is the arrest displacement, a_f is the crack length at arrest. Using the crack opening displacement at crack initiation Δ_o instead of Δ_f and initial crack length a_o for a_f in eq.6.6 will yield the stress intensity factor at crack initiation, which was called K_Q in chapter five (In crack arrest studies this initiation toughness is commonly denoted by K_o).

The specimen size used in cooperative test program was 200x200x50mm. Lower CCA size criteria are suggested by Rosenfield et.al. These are given by [8].

$$\left. \begin{aligned} 2H > 1.0 (K_Q/S_{ys})^2 \\ B > 4/\pi (K_Q/S_{yd})^2 \end{aligned} \right\} \quad (6.7)$$

where S_{ys} and S_{yd} stand for static and dynamic yield strength, respectively.

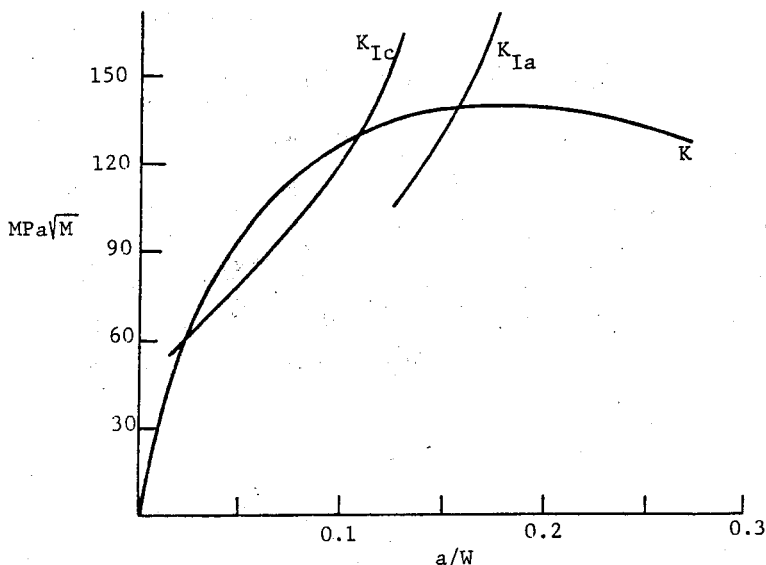
References:

- 1- ———, "PVRC Recommendations on Toughness Requirements for Ferritic Materials, PVRC Ad Hoc Task Group on Toughness Requirements, Welding Research Council Bulletin 175, 1972, also available in Pressure Vessels and Piping: Design and Analysis, Vol.3 pp.140-163 ASME
- 2- Rolfe, S.T. and Barsom, J.M. "Fracture and Fatigue Control in Structures" Prentice Hall, Inc. New Jersey 1977
- 3- Barsom, J.M. and Rolfe, S.T. "Correlations Between K_{IC} and Charpy V-Notch Test Results in the Transition Temperature Range" ASTM STP 466, Amer.Soc.for Testing and Materials, 1970 pp.281-302
- 4- Hertzberg, R.W. "Deformation and Fracture Mechanics of Engineering Materials" second ed. John Wiley and Sons, Inc., New York, 1983
- 5- Pellini, W.S. and Puzak, P.P. "Practical Considerations in Applying Laboratory Fracture Test Criteria to the Fracture-Safe Design of Pressure Vessels" Journal of Engineering for Power, 1964; also available in Pressure Vessels and Piping: Design and Analysis, Vol.3 pp.124-139, ASME, New York 1976
- 6- ———, ASME Boiler and Pressure Vessel Code 1977, Sec.III. Division I and sec.XI Division I
- 7- Lin, C. and Hoagland, R.G. "Crack Arrest Behavior of a High Strength Aluminum Alloy" ASTM STP 868, Amer.Soc. for Testing and Materials, 1985 pp.467-489
- 8- Rosenfield, A.R., Mincer, P.N., Marschall, C.W. and Markworth, A.J. "Recent Advances in Crack Arrest Technology" ASTM STP 833, Amer.Soc. for Testing and Materials, 1984, pp.149-164.

Problems

1- A variety of different specimen types are used by Ripling and Crosley (Eng. Fracture Mechanics, Vol.23 No.1 pp.21-33, 1986) to check the invariance of K_{Ia} . CCA and tapered DCB specimens provided arrest data through the measurement of the arrested crack length and the imposed loading. SEN specimens, however, acted as "go/no go" gages. That is, the crack at the brittle weld either ran completely through the specimen or arrested at the end of the weld when it ran into the base plate. Discuss the suitability of the SEN specimen for K_{Ia} estimation.

2- To check the possibility of a thermal shock occurring in a nuclear reactor pressure vessel tests have been conducted on large cylinders about 1 m. in diameter, with walls 150mm thick. They were first flawed and then subjected to a thermal shock. The K value through the wall, at the time when the crack "popped", was calculated by using the temperature gradient to first calculate the stresses through the wall from which the K values were calculated. In addition to the driving force K, using K_{Ic} and K_{Ia} values it was possible to estimate the crack advance. Determine this amount through the figure given below.



7. ELASTIC PLASTIC FRACTURE MECHANICS

Linear elastic fracture mechanics breaks down when high toughness materials are used. A simple-minded but restricted approach for such materials is that of chapter 6, the transition temperature approach. To have quantitative predictions, elastic-plastic analysis of cracked bodies is necessary. A single parameter characterization of elastic-plastic fracture, analogous to LEFM, is aimed at. Fracture analysis in the plastic regime has, however, a number of complications not present in the elastic case. Foremost are the inherent nonlinearities in the material deformation and large geometry changes together with the fact that flaws will propagate in a stable manner prior to final fracture. Hence, a plastic fracture methodology must explicitly treat crack initiation and the subsequent stable crack growth to the onset of the ultimate unstable crack propagation. These aspects are covered in this and the subsequent chapter eight, respectively.

Figure 7.1 depicts the possible levels of plastic deformation in a cracked body. As the plastic enclaves at the crack tip become comparable to other linear dimensions in the body the small scale yielding approximation of LEFM ceases to apply and EPFM range starts. EPFM may extend to cover general yield conditions of figure 7.1 c and d. A schematic diagram illustrating the various approaches to fracture is given in figure 7.2. It is to be noted that components likely to reach gross or general yield even if analyzed satisfactorily by fracture mechanics, must be also checked against plastic collapse by an appropriate design procedure.

The two elastic-plastic fracture mechanics concepts that have received most attention are the J contour integral and the crack opening displacement.

7.1 THE J-INTEGRAL

The J-Integral proposed by Rice [1] forms the basis of fracture

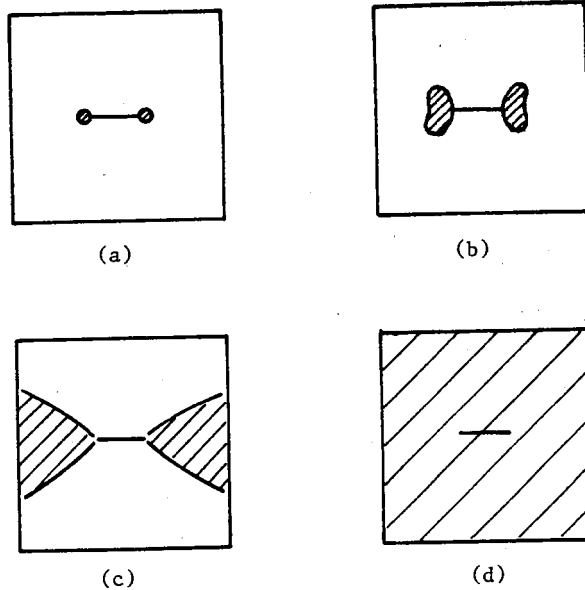


Fig.7.1- (a) small scale yielding state (b) net section stress approaches yield (c) net section stress exceeds yield (d) gross section stress exceeds yield

predictions beyond the linear elastic range. It is an extension of LEFM, relating the crack size to applied stress, in the presence of large scale yielding and an elegant alternative to obtain K_{IC} values from subsize specimens.

The J-Integral is defined as a line integral in the two dimensional strain field of a nonlinear elastic material:

$$J = \int_{\Gamma} (w \, dy - t_i \frac{\partial u_i}{\partial x} \, dS) \quad , \quad (i = 1,2) \quad (7-1)$$

where w = strain energy density defined by $w(\epsilon_{ij}) = \int_0^{\epsilon_{ij}} \sigma_{pq} \, d\epsilon_{pq}$

p = path of the integral shown in Fig.7.3

t_i = traction on the path Γ

u_i = displacement in the direction of t_i

dS = increment of distance along the path

n = the outward unit normal to the path Γ

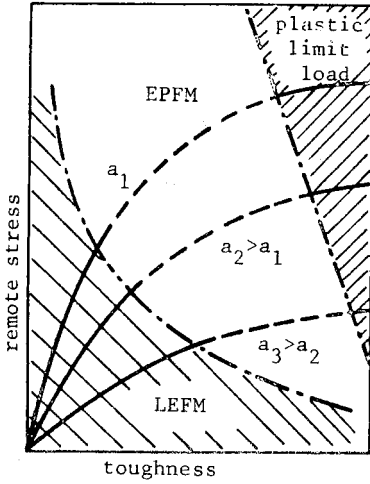


Fig.7.2- Fracture Mechanics Methods

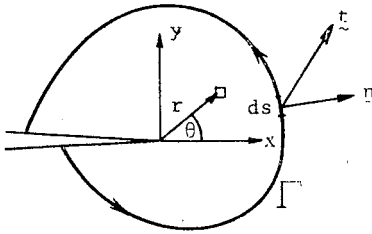


Fig.7.3- The integration path with respect to crack tip geometry.

7.1.1 Path Independence: J-Integral is path independent. To see that its value is identically zero for closed paths not containing singular points, consider eq.7.1 around a closed contour

$$\begin{aligned}
 I &= \oint (w \, dy - t_i \frac{\partial u_i}{\partial x} \, dS) \\
 &= \oint (w \, n_x - \sigma_{ij} \, n_j \, u_{i,x}) \, dS \tag{7-2}
 \end{aligned}$$

since $t_i = \sigma_{ij} \, n_j$ and $n_x \, dS = dy, n_y \, dS = -dx$. This last expression can be written in long-hand notation

$$I = \oint (w - \sigma_x \frac{\partial u}{\partial x} - \tau_{xy} \frac{\partial v}{\partial x}) \, dy + (\tau_{xy} \frac{\partial u}{\partial x} + \sigma_y \frac{\partial v}{\partial x}) \, dx \tag{7-3}$$

where $u = u_1$, $v = u_2$. It is easier, however, to use the indicial notation in the proof. Thus, using eq.7.2 and the divergence theorem, the contour integral can be converted to a surface integral

$$I = \int_{\hat{A}} \frac{\partial w}{\partial x} dA - \int_{\hat{A}} (\sigma_{ij} u_{i,x})_{,j} dA \quad (7-4)$$

where \hat{A} denotes the area inside the closed path. Since

$$\begin{aligned} dw &= \sigma_{ij} d\epsilon_{ij} \\ \frac{\partial w}{\partial x} &= \sigma_{ij} \frac{\partial \epsilon_{ij}}{\partial x} \end{aligned} \quad (7-5)$$

and

$$(\sigma_{ij} u_{i,x})_{,j} = \sigma_{ij,j} u_{i,x} + \sigma_{ij} \epsilon_{ij,x} \quad (7-6)$$

eq. 7.4 becomes

$$I = \int_{\hat{A}} \left(\sigma_{ij} \frac{\partial \epsilon_{ij}}{\partial x} - \sigma_{ij,j} \frac{\partial u_i}{\partial x} - \sigma_{ij} \frac{\partial \epsilon_{ij}}{\partial x} \right) dA$$

which is identically zero due to the equilibrium equation

$$\sigma_{ij,j} = 0$$

yielding

$$I = \oint (w dy - t_i \frac{\partial u_i}{\partial x} ds) = 0 \quad (7-7)$$

Now assume that the closed path is chosen to be composed of paths $\Gamma' + L_1 + \Gamma'' + L_2$ (Fig.7.4). Since the traction vector is zero on the

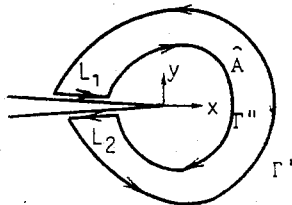


Fig.7.4- The closed path around the crack tip used to prove path independence.

upper and lower crack surfaces and $dy = 0$ along the x -axis, there is no contribution to the contour integral along L_1 and L_2 . Assuming the region between Γ' and Γ'' is simply connected and free of singularities

$$I = J_{\Gamma'} + J_{\Gamma''} = 0$$

Traversing Γ'' in the counterclockwise sense, we obtain

$$J_{\Gamma'} = J_{\Gamma''}$$

Since the choice of Γ' and Γ'' are completely arbitrary, the value of J integral can be calculated through paths ranging from very small ones to large ones coinciding with the outside boundaries of the specimen.

7.1.2 Alternative Definition of J : Another property of J integral is that it relates to energy available to drive the crack just like G of LEFM. To show this, consider the potential energy (PE) of a system with a blunt-ended notch (Fig.7.5) [2].

$$PE(a, \Delta) = \int_{A(a)} w(\epsilon_{ij}) B dA - \int_{S_T} t_i^o u_i B dS \quad (7.8)$$

where $u_i(x_i, a)$ and $\epsilon_{ij}(x_i, a)$ are the equilibrium displacement and strain fields, Δ is the load point displacement and S_T is the portion of boundary (S) where the tractions are specified. The rate of change of potential energy with respect to crack area is

$$\frac{1}{B} \left(\frac{\partial}{\partial a} PE \right)_{\Delta} = \int_A \frac{\partial w}{\partial a} dA + \int_{\Gamma_O} w(-1) n_x dS - \int_{S_T} t_i^o \frac{\partial u_i}{\partial a} dS \quad (7.9)$$

where the first term describes the contribution due to changes in w with respect to crack growth at inside points of A and the second term is due to flux of w across the boundary $\Gamma_1 + \Gamma_O + \Gamma_2$. Since the blunt ended notch translates only in the x -direction and since $\partial x / \partial a = -1$ one obtains $-n_x$ in the second term, and no contribution comes from Γ_1 and Γ_2 . But

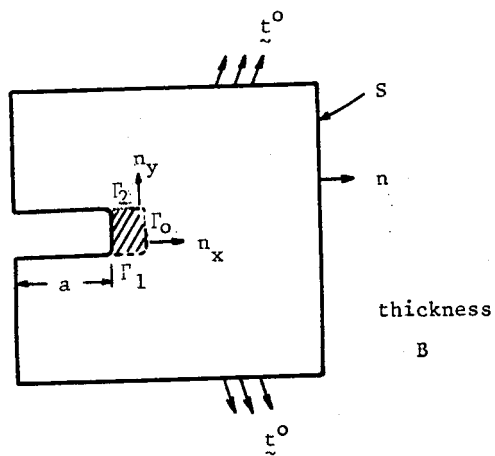


Fig.7.5: A blunt-ended notch configuration

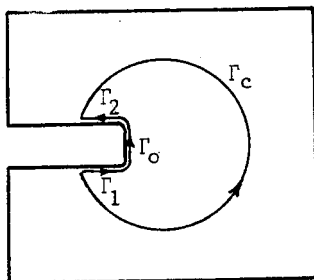


Fig.7.6: Judiciously chosen integration paths

$$\begin{aligned}
 \int_A \frac{\partial w}{\partial a} dA &= \int_A \frac{\partial w}{\partial \epsilon_{ij}} \frac{\partial \epsilon_{ij}}{\partial a} dA \\
 &= \int_A \sigma_{ij} \left(\frac{\partial u_i}{\partial a} \right)_{,j} dA \\
 &= \int_S \sigma_{ij} n_j \frac{\partial u_i}{\partial a} dS \\
 &= \int_S t_i \frac{\partial u_i}{\partial a} dS = \int_{S_T} t_i^o \frac{\partial u_i}{\partial a} dS
 \end{aligned} \tag{7.10}$$

Thus, eq.7.9 becomes

$$-\frac{1}{B} \left(\frac{\partial PE}{\partial a} \right)_{\Delta} = \int_{\Gamma_o} w n_x dS = \int_{\Gamma_o} w dy - t_i \frac{\partial u_i}{\partial x} dS \tag{7.11}$$

Adding the second term to the last integral does not change its value since this term vanishes on Γ_o , the notch surface being traction free. Since the integrand in eq.7.11 identically vanishes on Γ_1 and Γ_2 , we can also perform the integration along $\Gamma_1 + \Gamma_o + \Gamma_2$ without altering its value. Now because of the path independence (Fig.7.6)

$$J_{\Gamma_1 + \Gamma_o + \Gamma_2} = J_{\Gamma_c}$$

Thus

$$-\frac{1}{B} \left(\frac{\partial PE}{\partial a} \right)_{\Delta} = \int_{\Gamma_c} w dy - t_i \frac{\partial u_i}{\partial x} dS \equiv J \tag{7.12}$$

which implies that the J integral amounts to the potential energy difference for two notched bodies differing in geometry by an infinitesimal

amount. The proof given above is for flat surfaced notch with a smooth tip. One would expect the same result to hold in the limiting case of a straight crack in a two-dimensional deformation field. A formal proof of this is given by Rice [3].

It is important to remember that the results regarding the energy connotation of J are strictly true for elastic behavior only. For both linear and nonlinear elastic conditions, J is the energy made available at the crack tip per unit crack extension, da , and it is equivalent to the crack driving force. Therefore

$$J = G = K^2/E' \quad (7-13)$$

where $E' = E$ for plane stress
 $= E/(1-\nu^2)$ for plane strain

7.1.3 Crack Tip Fields: The physical interpretation of J integral in the above section is not valid when large scale plasticity is encountered. In the presence of plasticity w is not strain energy density; energy is dissipated within material elements. Thus, J does not correspond to G , as the available energy for crack extension. Its definition in eq.7.12 remains valid, however.

The general applicability of the J integral comes from viewing the stress and strain fields surrounding the crack tip. Hutchinson [4] and Rice and Rosengren [5] revealed that for stationary cracks in a power hardening material ($\epsilon/\epsilon_0 = \bar{\alpha}(\sigma/\sigma_0)^n$, $1 \leq n < \infty$), the stresses and strains in the vicinity of the crack tip under both small scale yielding and fully plastic conditions may be represented by

$$\begin{aligned} \sigma_{ij} &= \sigma_0 \left(\frac{J}{r \sigma_0 \epsilon_0} \right)^{1/n+1} \tilde{f}_{ij}(\theta, n) + \dots \\ \epsilon_{ij} &= \epsilon_0 \left(\frac{J}{r \sigma_0 \epsilon_0} \right)^{n/n+1} \tilde{g}_{ij}(\theta, n) + \dots \end{aligned} \quad (7-14)$$

which poses a perfect analogy to LEFM as presented in Fig.7.7. In these equations, J is the J integral defined by eq.7.1, σ_0 and ϵ_0 are the effective yield (or flow) stress and the associated elastic strain, respectively, r is the radial distance from the crack tip and \tilde{f}_{ij} and

σ_{ij} are dimensionless functions of the circumferential position θ and the

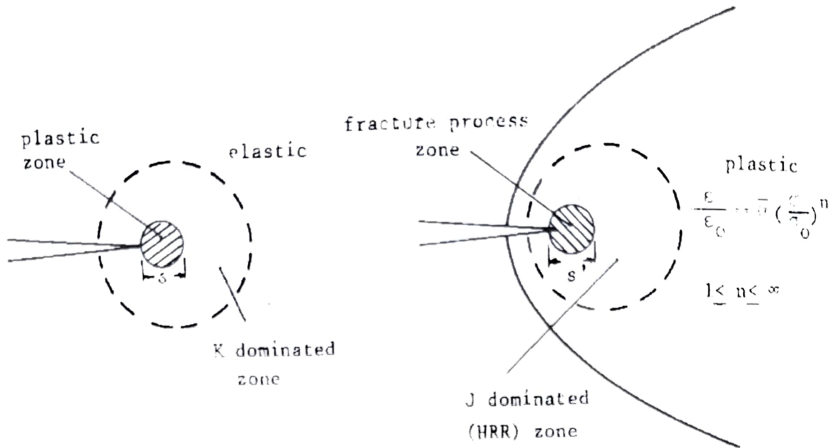


Fig.7.7: Analogy between crack tip zones in elastic and in elastic-plastic conditions.

hardening exponent n , dependent upon plane stress/plane strain conditions. The equations 7.14 are first terms in a series expansion describing near-tip fields and are known as the Hutchinson-Rice-Rosengren (HRR) singularities or fields and J is the HRR field parameter. J reflects the intensity of the elastic-plastic field surrounding the crack tip in spite of the severely deformed fracture process zone s' just as K reflecting the intensity of the surrounding elastic field for the LEFM case in spite of the small plastic zone s (Fig.7.7) [6]. Thus, J integral is the natural candidate for characterizing fracture.

7.1.4. Limitations: There are two aspects that need to be examined closely for the applicability of J integral [7]. First, deformation theory of plasticity — i.e. nonlinearly elastic material — must be an adequate model of the small-strain behavior of real elastic-plastic materials under the monotonic loads being considered. Second, the regions in which finite strain effects are important and in which the microscopic processes occur must each be contained well within the region of the small-strain solution dominated by the HRR-fields — a condition called J dominance.

The first condition is the classical debate of the physically appropriate incremental theory versus the simple-to-use deformation theory of plasticity. Any solution based on deformation (total strain)

theory of plasticity coincides exactly with a solution to the flow (incremental) theory of plasticity if proportional loading occurs everywhere. That is, if no unloading takes place and the stress and strain ratios are held constant. The singular fields (eq.7.14) by themselves satisfy this condition exactly. In other words, the crack tip singularity fields are also solution to the flow theory equations, and J as it appears in eq.7.14 could serve as the amplitude of the singular fields, independent of its line integral definition in eq.7.1 [7]. While the full solution for a body characterized by power hardening law will not generally satisfy proportional loading exactly, most problems with a single, monotonically applied load do come sufficiently close to meeting proportionality to justify use of deformation theory. Many investigators ([8,9] for example) have demonstrated that the line integral defined in eq.7.1 is substantially path independent for numerical solutions of incrementally plastic materials conforming to flow theory, even though its strict path independence is tied to its deformation theory definition. Moreover, the J values themselves are accurately approximated by the corresponding deformation theory solutions. It is fair to say that the use of deformation theory solutions to stationary crack problems for monotonic loading is generally accepted for the purpose of determining J .

The requirements for J -dominance are more complicated. Consider plane strain, mode I problems. The crack tip opening displacement δ_t provides a measure of the size of the zone in which finite strains are important. Finite element studies based on finite strain incremental plasticity formulation [8,10] have been performed for the plane strain small scale yielding problem. For distances from the tip that are greater than 2 or 3 times δ_t , the deviations from small strain theory become unimportant.

Let R denote the "radius" of the zone of dominance of the HRR fields, i.e. the characteristic size of the region in which the HRR fields provide a good approximation to the complete small-strain deformation theory solution. As depicted in Fig.7.8, one condition for J -dominance is

$$R > 3\delta_t \quad (7.15)$$

A second condition is that R be greater than the fracture process zone in which the microscopic separation processes occur. The predominant ductile fracture mechanism is void nucleation, growth and coalescence.

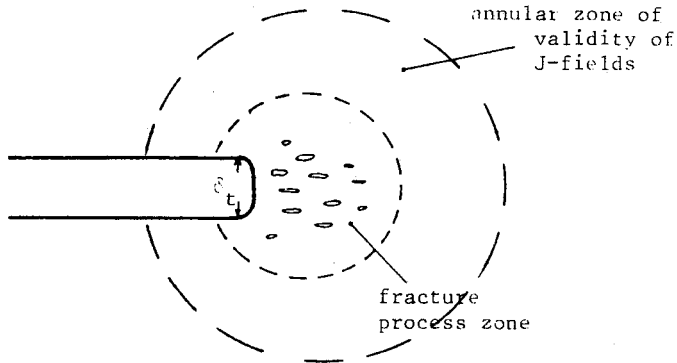


Fig.7.8: Schematic of neartip behavior under J-dominance conditions [7]

Since hole growth is itself a finite strain process, the fracture process zone for this mechanism is roughly comparable to the zone of finite strains, and therefore eq.7.15 again serves to ensure J-dominance. If failure due to shear localization intervenes, or if it actually precipitates hole nucleation and growth, then the fracture process zone may be somewhat larger than $3\delta_t$. When the separation process is cleavage, the size of the fracture process zone appears to be set by the grain size in many materials with the zone extending from 2 to 10 grain diameters from the tip. This sets a constraint on R for J dominance under cleavage conditions which usually renders eq.7.15 superfluous.

The relation of the characteristic size R of the zone of dominance of the HRR fields to the linear dimensions of the body depends strongly on geometry and hardening. The geometry dependence is especially strong for low hardening materials. The mathematical character of the equations governing behavior near the crack tip changes in the limit $n \rightarrow \infty$, corresponding to perfect plasticity. For finite n the equations are elliptic and HRR fields do represent near-tip stress and strains. In the perfect plasticity limit the governing equations are hyperbolic and there no longer exists a unique near-tip solution independent of specimen geometry [11]. Hence, some strainhardening must exist to have a single parameter approach. Certain configurations have approximately the same near-tip fields in perfect plasticity as those obtained by letting $n \rightarrow \infty$ in eq.7.14. Important examples are the small-scale yielding problem itself and the fully plastic bend or compact (tension) configurations (Fig.7.9a) and

the double edge notched configuration (Fig.7.9b) in-plane strain. The triaxiality is high (normal stress σ_y reaching $2.5 \sigma_0$ and $3\sigma_0$, respectively)

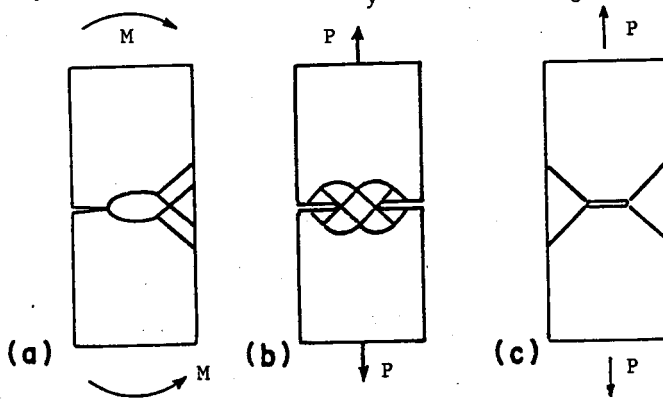


Fig.7.9: Slip line field for (a) edge-cracked bend configuration SE(B), (b) double edge cracked tension configuration, DE(T) (c) center-cracked tension configuration M(T).

in the ligaments which is also the case in HRR-fields. Some configurations have completely different fields in perfectly plastic materials as compared to HRR-fields with $n \rightarrow \infty$. Center cracked strip (Fig.7.9c) in plane strain conditions pulled to full yield in tension develops intense shear bands at 45° from the tensile direction and the triaxiality ahead of the tip is low ($\sigma_y = 2/\sqrt{3} \sigma_0$) [12].

In view of the above facts it is not unusual to expect that HRR-fields will dominate in a larger area in bend configurations than in center cracked tensile strips, for finite n . A graphic illustration of the variation of the relative size of the region dominated by the HRR singularity with the level of plastic deformation, material hardening properties and specimen configuration is, indeed, given in figure 7.10. Numerical studies [13,14] suggest that

$$\begin{array}{ll}
 R \approx 7\% \text{ of } b & \text{for bend configurations,} \\
 & \text{for any } n \\
 & (7.16) \\
 R \approx 1\% \text{ of } b & \text{for center-cracked tensile} \\
 & \text{strip, for } n=10
 \end{array}$$

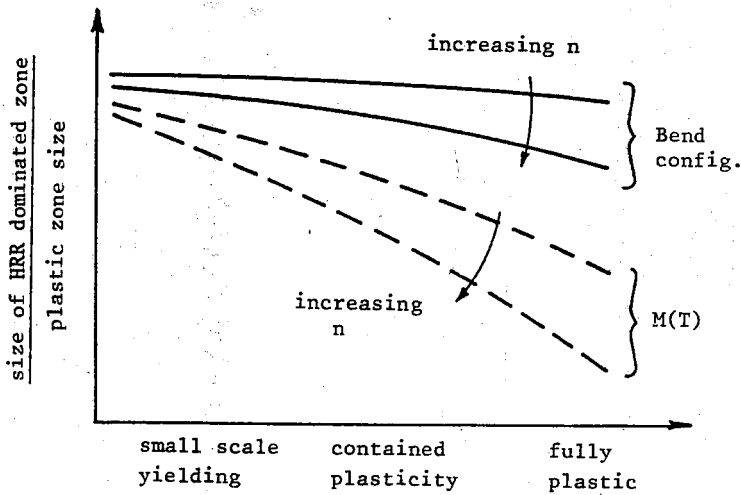


Fig.7.10: Relative size of region dominated by HRR singularity

when the plastic zone reached across the entire uncracked ligament b . As discussed above, the zone of dominance becomes vanishingly small as $n \rightarrow \infty$ in center cracked tensile configuration.

Geometric conditions for J-dominance result from eq.7.15 and eq.7.16:

$$b > \frac{300}{7} \delta_t \quad \text{for bend specimen} \quad (7.17)$$

$$b > 300 \delta_t \quad \text{for center cracked strip}$$

The HRR fields indicate that the opening of the crack faces varies at $r \rightarrow 0$ as $r^{1/1+n}$. A widely accepted operational definition of the crack tip opening displacement δ_t is the opening distance between the intercept of two 45° lines drawn back from the tip with the deformed profile (Fig.7.11). The result is [15]

$$\delta_t = d_n \frac{J}{\sigma_o} \quad (7.18)$$

where d_n is a proportionality factor dependent upon yield strain and work hardening exponent n . It varies weakly with ϵ_o/E and quite significantly with n (Fig.7.12). Examination of Fig.7.12a reveals that for

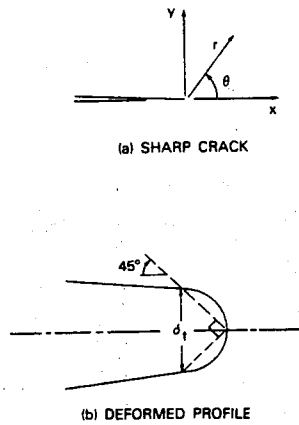


Fig.7.11: Sharp crack and deformed crack profile illustrating the operational definition of δ_t [15]

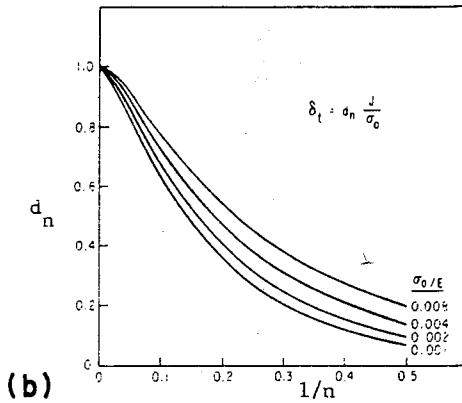
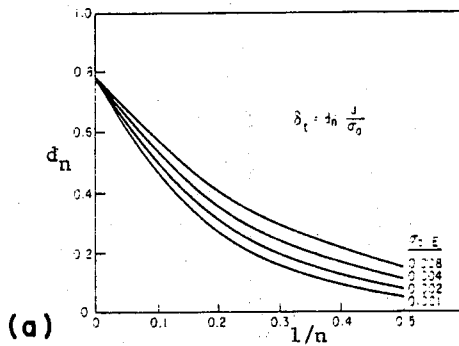


Fig.7.12: Variation of d_n with n and σ_0/E for (a) plane strain. (b) plane stress [15]

low-to-moderate hardening, $d_n \approx 0.65$. Thus, geometric conditions for J-dominance in plane strain (eq.7.17) become

$$b > 25 J/\sigma_0 \text{ bend configuration} \quad (7.19a)$$

$$b > 200 J/\sigma_0 \text{ center cracked tensile strip} \quad (7.19b)$$

Analogous studies in plane stress have not been made. It is possible that the configuration-dependence under fully plastic conditions will not be as strong as in plane strain, primarily because the perfectly plastic limit solutions do not display as wide a variation at least as far as the stresses are concerned.

7.2 DETERMINATION OF J INTEGRAL

7.2.1 Direct Integration: For simple geometry and loadings the contour integral definition, that is eq.7.1 or the long-hand version of it (cf. eq.7.3)

$$J = \int_{\Gamma} w \, dy - \left(\sigma_x \frac{\partial u}{\partial x} + \tau_{xy} \frac{\partial v}{\partial x} \right) dy + \left(\tau_{xy} \frac{\partial u}{\partial x} + \sigma_y \frac{\partial v}{\partial x} \right) dx \quad (7.20)$$

can be directly applied to obtain the J-value as a function of the loading. The infinite strip of height h containing a semi infinite notch (Fig.7.13) is the classical case discussed by Rice [1]. The crack is assumed to extend under fixed displacement conditions. Thus, the y directional displacement v is constant, whereas the x -directional displacement u is zero along the clamped boundaries. Along the top and bottom portions of Γ , $dy=0$, $\partial u/\partial x = \partial v/\partial x = 0$. At $x=+\infty$, $\sigma_x = \sigma_y = \tau_{xy} = w = 0$ and $\partial u/\partial x = \partial v/\partial x = 0$ since there is no deformation but just rigid body motion at that end. The only contribution to J comes from the portion of Γ at $x=-\infty$. Since there exists a uniform stress distribution, $\partial u/\partial x = \partial v/\partial x = 0$, $\tau_{xy} = 0$. Thus

$$J = w_{\infty} h$$

For pure power law hardening materials of the type $\sigma = \sigma_0 (\epsilon/\epsilon_0)^m$

$$w_{\infty} = \int_0^{\epsilon} \sigma d\epsilon = \sigma_0 \frac{\epsilon^{m+1}}{(m+1)\epsilon_0^m}$$

which implies

$$J = \frac{\sigma_0}{(m+1)\epsilon_0^m} h \epsilon^{m+1} \quad (7.21)$$

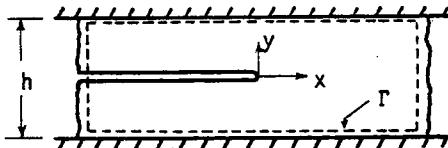


Fig.7.13: Infinite strip containing a semi-infinite notch

7.2.2 The Potential Energy Route: As shown in eq.7.12, the alternative definition of J integral is the potential energy difference for two bodies differing in geometry by an infinitesimal amount. For a nonlinear elastic system, the available energy (i.e. work done in going from crack of size a to $a+da$ minus the change in strain energy) is the cross-hatched region in figure. 7.14. This area has no obvious association with

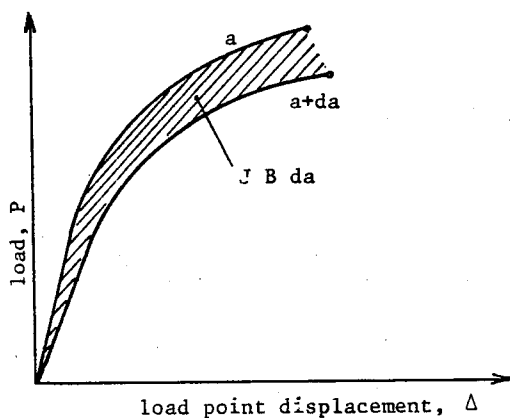


Fig.7.14- Graphical Interpretation of J-Integral

energy release for elastic-plastic solids, it simply defines J. Independent of the machine stiffness (i.e. dead load or fixed displacement conditions) this area corresponds to $J B da$. In other words,

$$J = - \frac{1}{B} \int \frac{\partial \mathcal{E}}{\partial a} P(\Delta', a) d\Delta' = \frac{1}{B} \int \frac{P}{\partial a} \Delta(P', a) dP' \quad (7.22)$$

The fundamental approach to J-integral determination is the Begley and Landes [16] procedure. It is an experimental, multispecimen method based on the alternate definition of J (eq.7.12). A series of identical specimens is used with slightly differing crack lengths $a_1 > a_2 > a_3 \dots$ (Fig.7.15a).

A load (P) vs. load point deflection (Δ) trace is obtained for each specimen (Fig.15b). The value of J is independent of machine stiffness; hence, fixed displacement readings are adopted for simplicity. The area under the load versus deflection trace for each specimen up to an arbitrary deflection Δ_1 is the potential energy (PE) for that specimen. Repeating this for a series of deflections Δ_2, Δ_3 etc. enables one to plot potential

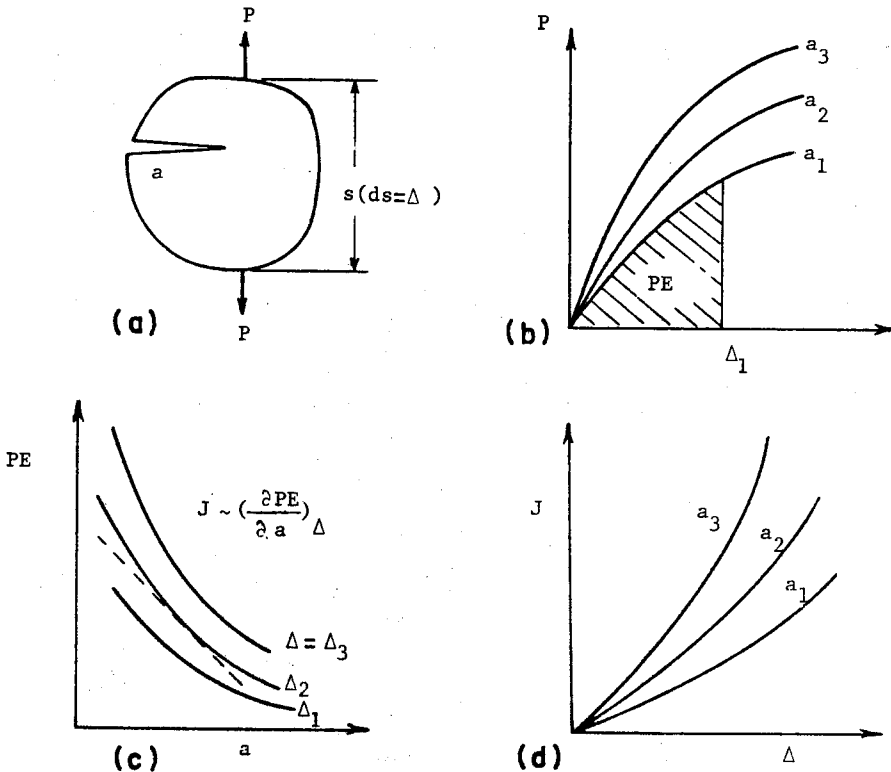


Fig.7.15: Schematic steps in a compliance J determination

energy as a function of crack size (Fig.7.15c) the slope of which gives J vs. Δ curves with crack size being the parameter (Fig.7.15d). The final plot is termed J calibration curve for the particular geometry and loading. The major advantage of this compliance J calibration is that it is suitable to any geometry. While possessing the advantage of generality it is tedious and expensive in both time and material since it usually requires 4-6 specimens.

7.2.2.1 Deeply Notched Bend Configurations: A significant advance in J integral estimation is provided by Rice-Paris-Merkle analysis [17] which allows the calculation of J from a single $P-\Delta$ record for different configurations where the uncracked remaining ligament (b) is small compared to any other planar dimension. In particular, for deeply notched specimens in plane strain bending — such as deeply notched three point bend or compact (tension) specimens — J is shown to be twice of the work of deformation divided by the ligament area (Fig.7.16)

$$J = \frac{2A}{Bb} \quad (7.23)$$

where

$$A = \int_0^{\theta} M d\theta \quad \text{or} \quad \int_0^{\Delta} P d\Delta$$

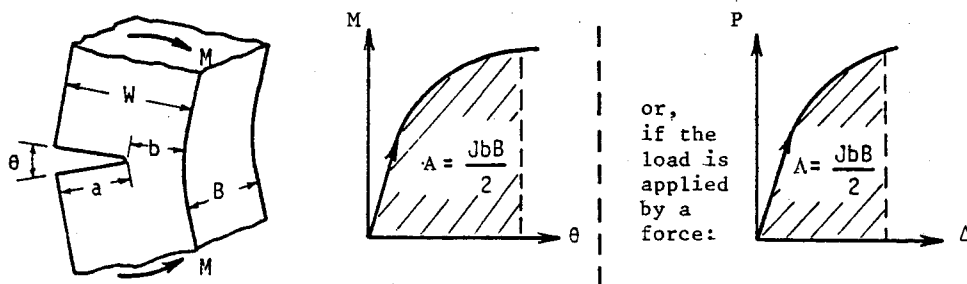


Fig.7.16: Determination of J from single load-displacement diagram for deeply cracked bend specimen

The original derivation of Rice et.al. excludes the energy absorbed due to the crack in the calculation of A in eq.7.23. Srawley [18], however, showed that better correlation exists if total displacement is used. Retention of the unnotched beam deflection is also supported by Chipperfield [19] and Landes et.al. [20].

An extension to eq.7.23 is provided by Merkle and Corten [21] by considering the combined loading that exists on the net section in a compact specimen. For compact specimens with $0.5 < a/W < 0.7$, eq.7.23 underestimates the applied J value by 10-15%. Thus a correction is introduced through

$$J = \alpha_1 \frac{2A}{Bb} + \alpha_2 \frac{2P\Delta}{Bb} \quad (7.24)$$

where Δ and P are the final load point displacement and the final load,

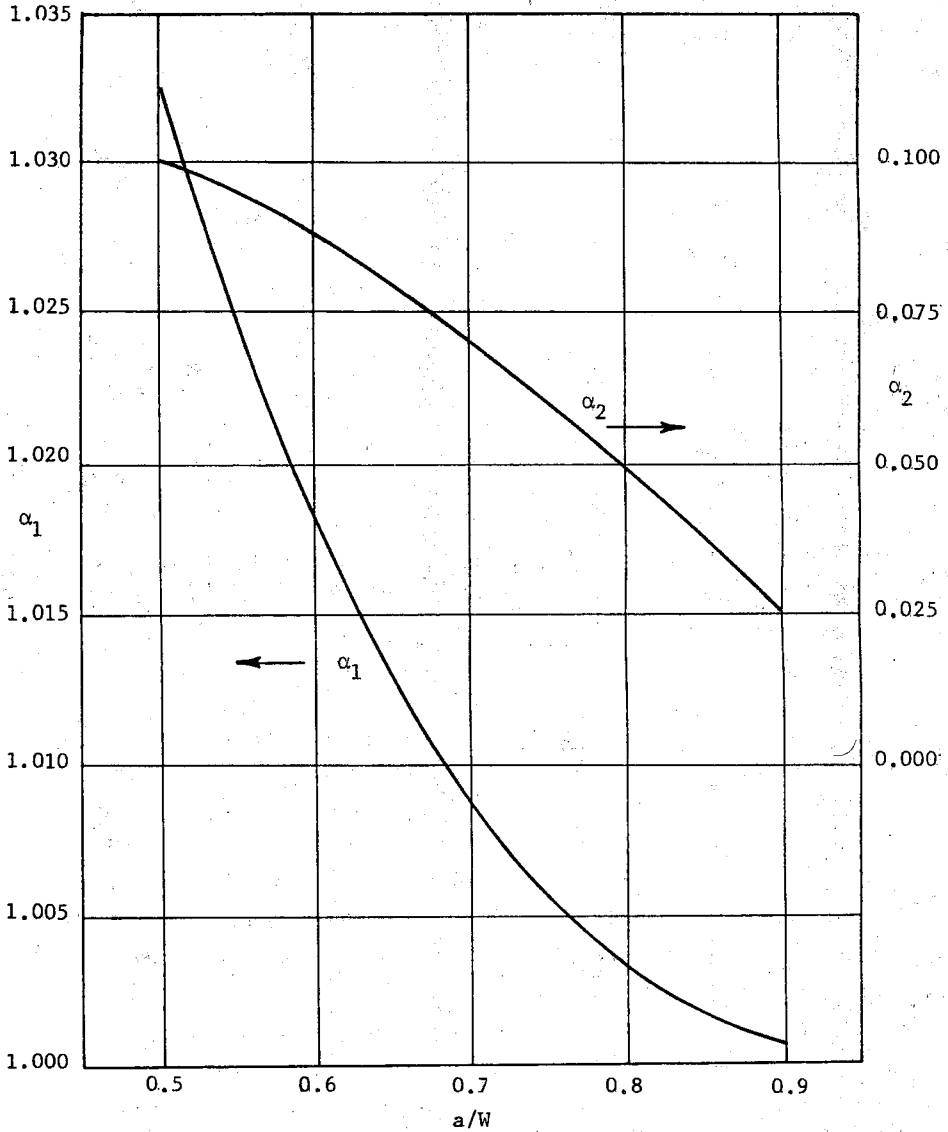


Fig.7.17: Variation of the coefficients α_1 and α_2 with normalized crack size

respectively and α_1 and α_2 are coefficients plotted in figure 7.17. A polynomial can also be fitted to α_1 and α_2 curves [20] :

$$\alpha_1 = 1.222468 - 0.637295(a/W) + 0.614937(a/W)^2 - 0.200797(a/W)^3$$

$$\alpha_2 = -0.006771 + 0.595163(a/W) - 0.940241(a/W)^2 + 0.353779(a/W)^3$$

A simplification to eq.7.24 can be made if it is assumed that the complementary energy is much smaller in amplitude than the total energy (i.e. $P\Delta \approx A$). Landes, Walker and Clarke [20] arrived thus to the simple expression for J:

$$J = (\alpha_1 + \alpha_2) \frac{2A}{Bb} \quad (7.25a)$$

$$J = \left(\frac{1+\alpha}{1+\alpha^2} \right) \frac{2A}{Bb} \quad (7.25b)$$

where $\alpha = 2 \left[(a/b)^2 + (a/b) + 1/2 \right]^{1/2} - 2(a/b+1/2)$ in terms of the remaining ligament, or

$$\alpha = \left\{ \sqrt{2(a/W)^2 + 2} - (1+a/W) \right\} / (1-a/W) \text{ in terms of the width.}$$

The values of α and $(1+\alpha/1+\alpha^2)$ are plotted against a/W ratios in figure 7.18. This approach of Landes et.al. is not only simple but it also gives excellent agreement with the J obtained through the multispecimen technique since it eliminates the slight overestimation present in the Merkle and Corten analysis. Clarke and Landes [22] rewrote this last expression as

$$J = \eta A / Bb \quad (7.25c)$$

where $\eta = 2 + 0.522 b/W$.

For the three-point bend specimen there is no tensile component of load and eq.7.23 directly applies.

7.2.2.2 Tensile Configurations: The extreme situation of tensile loading only (double edge notched plates in tension, DE(T), shown in figure 7.19a and center cracked panel in tension, M(T), shown in figure 7.19b) is also

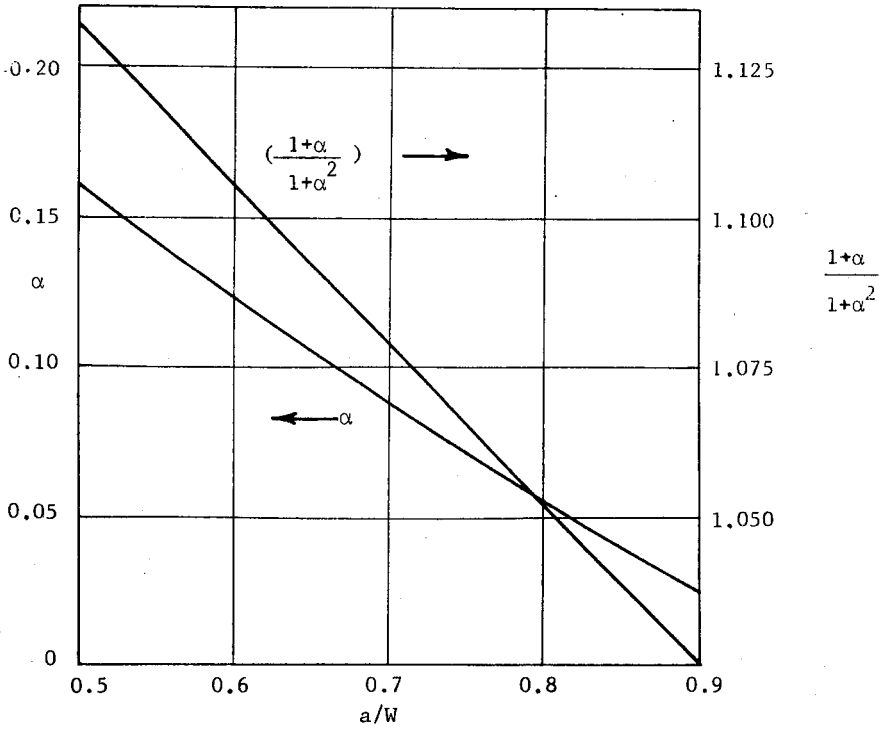


Fig.7.18: Variation of the coefficient of eq.7.25b with crack length.

analyzed by Rice et.al. [17]. J is determined by adding elastic and plastic components, the elastic component being G, calculated from the applied load and crack length just as if there were no plasticity.

$$J = G + \frac{2}{Bb} \left\{ \int_0^{\Delta p_1} P d\Delta_{p1} - \frac{1}{2} P \Delta_{p1} \right\} \quad (7.26)$$

The bracket in eq.7.26 corresponds to the area A between the load versus load point displacement curve and the secant offset line to the displacement of interest. This area is shown in figure 7.20.

7.2.2.3 Improvements proposed by Ernst: Ernst [23] presented a unified solution to bending plus tension situations which includes eq.7.25b and 7.26 as special cases and mainly addressed loadings where the tensile component becomes dominant. Compact specimen with $a/W < 0.5$ or the single edge notched specimen subject to tensile pin loading, SE(T), are such loadings.

$$J = G + \frac{\gamma + \beta}{b} \int_0^{\Delta_{p1}} P d\Delta_{p1} - \beta \frac{P\Delta_{p1}}{b} \quad (7.27)$$

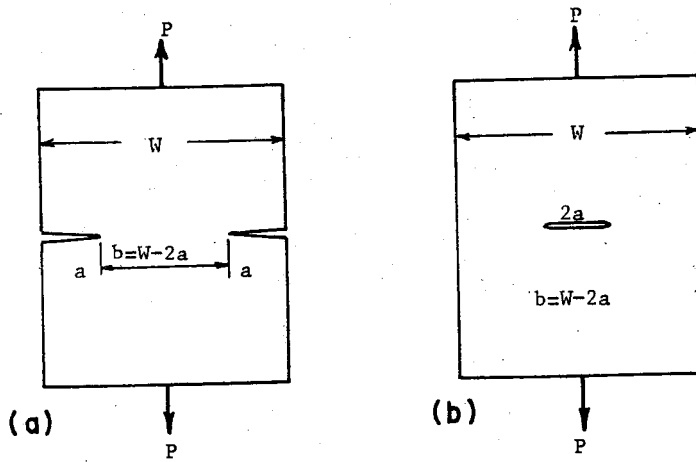


Fig.7.19: Tension specimens (a) DE(T) (b) M(T)

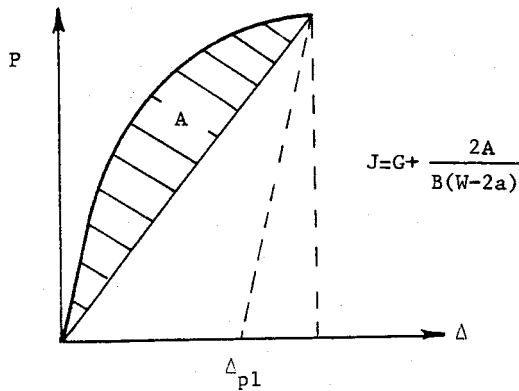


Fig.7.20: Description of the graphical evaluation of J from $P-\Delta$ records

$$\text{where } \gamma = \left[\frac{2(1+\alpha)(1+x)}{1+\alpha^2} + \alpha(1-x) \right] \left[\frac{1}{(1+x)+\alpha(1-x)} \right]$$

$$\beta = \frac{\alpha}{\alpha + \left(\frac{1+x}{1-x} \right)}$$

α = as defined above in eq.7.25

x = the dimensionless coordinate of the crack tip taking the load line-crack line intersection as origin

= a/W for compact specimen, $2a/W-1$ for SE(T)

Values of γ, β as functions of a/W are given in table 7.1 and figure 7.21

Table 7.1: Coefficients which are used in eq.7.27 [23]

x	$(a/W)_{SE(T)}$	$(a/W)_{C(T)}$	γ	β
-1.0	0.00	...	1.000	1.000
-0.9	0.05	...	1.055	0.947
-0.8	0.10	...	1.122	0.890
-0.7	0.15	...	1.201	0.826
-0.6	0.20	...	1.294	0.758
-0.5	0.25	...	1.400	0.684
-0.4	0.30	...	1.517	0.606
-0.3	0.35	...	1.643	0.526
-0.2	0.40	...	1.769	0.445
-0.1	0.45	...	1.891	0.367
0.0	0.50	0.0	2.000	0.293
0.1	0.55	0.1	2.089	0.226
0.2	0.60	0.2	2.154	0.168
0.3	0.65	0.3	2.193	0.119
0.4	0.70	0.4	2.207	0.081
0.5	0.75	0.5	2.200	0.051
0.6	0.80	0.6	2.177	0.030
0.7	0.85	0.7	2.141	0.015
0.8	0.90	0.8	2.097	0.006
0.9	0.95	0.9	2.050	0.001
1.0	1.00	1.0	2.000	0.000

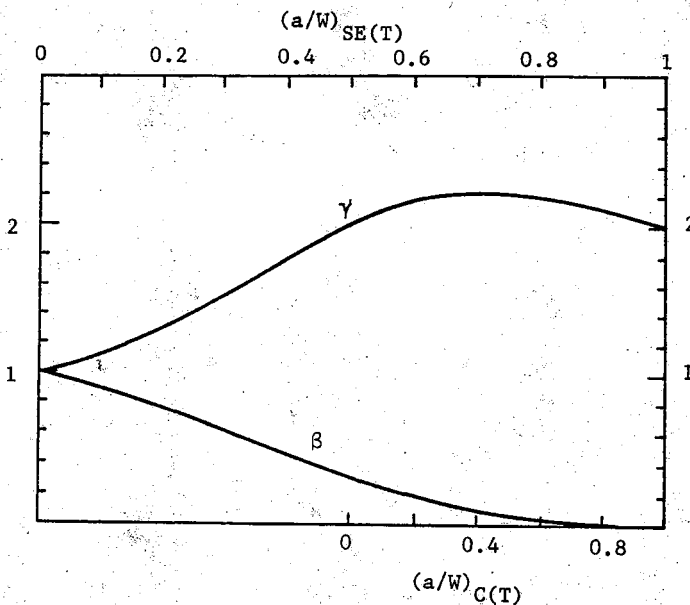


Fig.7.21: Plastic factors β and γ versus the crack length for SE(T) and C(T) geometries [23]

The amount of crack extension allowable in a J_{IC} test is relatively small. However, the value of J corrected for crack growth can be calculated for bend configurations. Ernst et.al. [24] showed that

$$J_{i+1} = \left(J_i + \frac{\eta_i}{Bb_i} A_{i,i+1} \right) \left(1 - \frac{\gamma_i}{b_i} (a_{i+1} - a_i) \right) \quad (7.28)$$

where the subscripts i or $i+1$ indicate functions evaluated at that step. The term $A_{i,i+1}$ refers to the area enclosed by the actual test record and lines of constant displacement Δ_i and Δ_{i+1} . Here

$$\gamma_i = \begin{cases} 1+0.76 b_i/W & \text{for compact specimen} \\ 1 & \text{for three point bend specimen} \end{cases}$$

$$\eta_i = \begin{cases} 2+0.522 b_i/W & \text{or the equivalent expressions given in} \\ & \text{in eq.7.25 for compact specimen} \\ 2 & \text{for three point bend specimen} \end{cases}$$

For the first step, $\Delta = 0$, $J = 0$. If, up to a certain point $j+1$, no crack growth has occurred, eq.7.28 reduces to

$$J_{j+1} = J_j + \frac{\eta_j}{b_j} A_{j,j+1}$$

$$= \frac{\eta}{b_0} \int_0^{\Delta} P d\Delta$$

which coincides with eq.7.25 (or eq.7.23 for three point bend specimen). Thus, eq.7.28 is completely general and can be used for the whole test record, starting from the origin [24].

7.2.3. The Superposition Technique: Another class of solutions is obtained by joining elastic and fully plastic J values to approximate elastic-plastic behavior. Bucci et.al [25] used the relationship between J and the area between load-deflection records of cracked bodies differing only in crack length by the amount da . They simulated the $P-\Delta$ records by using known compliance functions for the linear range and the slip line field predictions for the limit (collapse) load. In figure 22a, the elastic contribution to J is simply the first triangular area. This may be computed from LEFM solutions and is given by

$$J_{e1} = G = K^2(1-\nu^2)/E$$

where K is evaluated at the limit load P_L . The plastic contribution to J is represented by the rectangular area and is given by

$$J_{p1} = \frac{dP_L}{Bda} (\Delta - \Delta_{e1})$$

Hence the total J is

$$J = J_{e1} + J_{p1} = G + \frac{dP_L}{Bda} (\Delta - \Delta_{e1})$$

This procedure has been refined by Bucci et.al [25] by introducing a plastic zone correction which smooths the transition from elastic to fully plastic loading (Fig.7.22b). If J is plotted against the applied

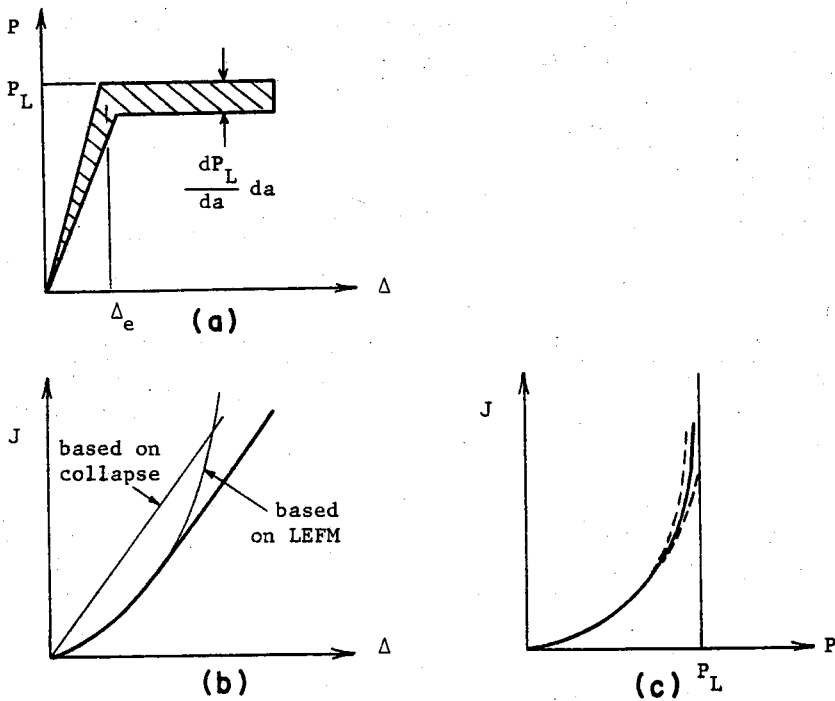


Fig.7.22: Estimating J from approximations of load-deflection records

load, P , a curve similar to that of figure 7.22c is obtained. The applied J becomes unbounded at the limit load. A small error in the estimated limit load can lead to gross errors in the estimated J . For fully plastic situations estimates of J vs. Δ are clearly subject to much less error than estimates of J vs. P .

Shih [26], Shih and Hutchinson [27] and Shih et.al. [28] developed a method for estimating J which enables a compendium of solutions to be constructed in a similar manner to the compendia at present available for K solutions. This is achieved by evaluating J from two terms

$$J = J_{el} + J_{pl}$$

where J_{pl} is the fully plastic solution for a pure power hardening material of the type

$$\epsilon/\epsilon_0 = \bar{\alpha}(\sigma/\sigma_0)^n$$

As Ilyushin showed many years ago, a solution to the boundary value problem, based on the deformation theory of plasticity, involving a single load or displacement parameter has the property that all stress quantities are linearly proportional to the applied load P , and all strain and displacement quantities are proportional to P^n . A consequence of this, as noted by Goldman and Hutchinson [29], is that similar to linear elastic crack problems there exist scaling laws for various fracture parameters, such as the J integral and COD, associated with the nonlinear problem also. In other words, dependence of fracture parameters on load can be separated from its dependence on geometric and material variables as

$$J_{p1} = \bar{\alpha}\epsilon_0\sigma_0 \left\{ \text{function of } \frac{a}{W} \text{ and } n \right\} \left[P/P_0 \right]^{n+1} \quad (7.29)$$

Where P_0 is a reference load, proportional to $Bb\sigma_0$ (coinciding with the limit load for the rigid-perfectly plastic case, $n \rightarrow \infty$). Consequently, it is feasible to tabulate the solutions for J (and other parameters of interest such as δ or Δ) as functions of crack depth and strain hardening exponent n . Such solutions have been developed for a variety of crack configurations [30].

For compact specimens fully plastic solutions can be tabulated in the following form [30]:

$$\begin{aligned} J_{p1} &= \bar{\alpha}\epsilon_0\sigma_0 b h_1\left(\frac{a}{W}, n\right) \left[P/P_0 \right]^{n+1} \\ \Delta_{p1} &= \bar{\alpha}\epsilon_0 a h_3\left(\frac{a}{W}, n\right) \left[P/P_0 \right]^n \\ \delta_{p1} &= \bar{\alpha}\epsilon_0 a h_2\left(\frac{a}{W}, n\right) \left[P/P_0 \right]^n \end{aligned} \quad (7.30)$$

where Δ is the load point displacement, δ is the crack mouth opening displacement, b is the uncracked ligament. The dimensionless functions h_1, h_2, h_3 are contained in tables 7.2 and 7.3. The limit load expressions for use in eq.7.30 are given as

$$P_0 = 1.455 \alpha b B \sigma_0 \quad (7.31)$$

for plane strain, and as

Table 7.2: Plane Strain h-Functions for C(T) [30].

	n=1	n=2	n=3	n=5	n=7	n=10	n=13	n=16	n=20	
$a/W = \frac{1}{4}$	h_1	2.23	2.05	1.78	1.48	1.33	1.26	1.25	1.32	1.57
	h_2	17.9	12.5	11.7	10.8	10.5	10.7	11.5	12.6	14.6
	h_3	9.85	8.51	8.17	7.77	7.71	7.92	8.52	9.31	10.9
$a/W = \frac{3}{8}$	h_1	2.15	1.72	1.39	0.970	0.693	0.443	0.276	0.176	0.098
	h_2	12.6	8.18	6.52	4.32	2.97	1.79	1.10	0.686	0.370
	h_3	7.94	5.76	4.64	3.10	2.14	1.29	0.793	0.494	0.266
$a/W = \frac{1}{2}$	h_1	1.94	1.51	1.24	0.919	0.685	0.461	0.314	0.216	0.312
	h_2	9.33	5.85	4.30	2.75	1.91	1.20	0.788	0.530	0.317
	h_3	6.41	4.27	3.16	2.02	1.41	0.888	0.585	0.393	0.236
$a/W = \frac{5}{8}$	h_1	1.76	1.45	1.24	0.974	0.752	0.602	0.459	0.347	0.248
	h_2	7.61	4.57	3.42	2.36	1.81	1.32	0.983	0.749	0.485
	h_3	5.52	3.43	2.58	1.79	1.37	1.00	0.746	0.568	0.368
$a/W = \frac{3}{4}$	h_1	1.71	1.42	1.26	1.033	0.864	0.717	0.575	0.448	0.345
	h_2	6.37	3.95	3.18	2.34	1.88	1.44	1.12	0.887	0.665
	h_3	4.86	3.05	2.46	1.81	1.45	1.11	0.869	0.686	0.514
$a/W \rightarrow 1$	h_1	1.57	1.45	1.35	1.18	1.08	0.950	0.850	0.730	0.630
	h_2	5.39	3.74	3.09	2.43	2.12	1.80	1.57	1.33	1.14
	h_3	4.31	2.99	2.47	1.95	1.79	1.44	1.26	1.07	0.909

Table 7.3: Plane Stress h-Functions for C(T) [30].

	n=1	n=2	n=3	n=5	n=7	n=10	n=13	n=16	n=20	
$a/W = \frac{1}{2}$	h_1	1.61	1.46	1.28	1.06	0.903	0.729	0.601	0.511	0.395
	h_2	17.6	12.0	10.7	8.74	7.32	5.74	4.63	3.75	2.92
	h_3	9.67	8.00	7.21	5.94	5.00	3.95	3.19	2.59	2.023
$a/W = \frac{3}{8}$	h_1	1.55	1.25	1.05	0.801	0.647	0.484	0.377	0.284	0.220
	h_2	12.4	8.20	6.54	4.56	3.45	2.44	1.83	1.36	1.02
	h_3	7.80	5.73	4.62	3.25	2.48	1.77	1.33	0.990	0.746
$a/W = \frac{1}{2}$	h_1	1.40	1.08	0.901	0.686	0.558	0.436	0.356	0.298	0.238
	h_2	9.16	5.67	4.21	2.80	2.12	1.57	1.25	1.03	0.814
	h_3	6.29	4.15	3.11	2.09	1.59	1.18	0.938	0.774	0.614
$a/W = \frac{5}{8}$	h_1	1.27	1.03	0.875	0.695	0.593	0.494	0.423	0.370	0.310
	h_2	7.47	4.48	3.35	2.37	1.92	1.54	1.29	1.12	0.928
	h_3	5.42	3.38	2.54	1.80	1.47	1.18	0.988	0.853	0.710
$a/W = \frac{3}{4}$	h_1	1.23	0.997	0.833	0.683	0.598	0.506	0.431	0.373	0.314
	h_2	6.25	3.78	2.89	2.14	1.78	1.44	1.20	1.03	0.857
	h_3	4.77	2.92	2.24	1.66	1.38	1.12	0.936	0.800	0.666
$a/W \rightarrow 1$	h_1	1.13	1.01	0.775	0.680	0.650	0.620	0.490	0.470	0.420
	h_2	5.29	3.54	2.41	1.91	1.73	1.59	1.23	1.17	1.03
	h_3	4.23	2.83	1.93	1.52	1.39	1.27	0.985	0.933	0.824

$$P_0 = 1.071 \alpha b B \sigma_0$$

(7.32)

for plane stress, where α is defined in eq.7.25 and plotted in figure 7.18.

The fully plastic solution is only applicable when the cracked configuration has completely yielded and the elastic strains are negligible throughout the body. At the other extreme, small scale yielding will occur for P small compared to P_0 and LEFM is applicable. Similar to Bucci's approach, Shih [28] proposed to bridge the gap between the two extremes by introducing an effective crack length

$$a_e = a + \phi r_y \quad (7.33)$$

$$\text{where } r_y = \frac{1}{\beta\pi} \left(\frac{n-1}{n+1} \right) \left(\frac{K}{\sigma_0} \right)^2 \quad \text{and} \quad \phi = \frac{1}{1+(P/P_0)^2}$$

Thus,

$$\begin{aligned} J &= J_{e1}(a_e) + J_{p1}(a,n) \\ \Delta &= \Delta_{e1}(a_e) + \Delta_{p1}(a,n) \\ \delta &= \delta_{e1}(a_e) + \delta_{p1}(a,n) \end{aligned} \quad (7.34)$$

become the operational expressions. The length r_y is based on Irwin's idea of a plastically adjusted crack length, but modified to account for strain hardening. For plane stress β equals 2, and for plane strain 6. To simplify the calculation of r_y , K is based upon the crack length a .

Fully plastic solutions of common geometries other than the compact specimen are given in the Appendix.

7.3 EVALUATION OF J_{IC}

Stable crack growth precedes failure in high toughness metallic materials. The value of J at initiation of crack growth is considered the critical value (J_{IC}) in direct analogy to K_{IC} . It is evaluated using the standard specimens of three point bend and compact tension. The procedure is described in detail in ASTM standard E813-81. It is extremely difficult to pinpoint the onset of growth, thus backwards extrapolation is utilized to find the initiation point indirectly. J values for a series of crack extensions Δa are plotted to form the beginning of the resistance curve of the material^x; extrapolation to zero crack advance yields the initiation value of J . Prior to actual separation at the crack tip, a crack tip

^xUse of J -integral for minor amounts of crack growth is well justified and discussed in the subsequent chapter in some detail.

blunting or stretch zone formation occurs. This is an apparent crack growth (Fig.7.23) and can be expressed in terms of the crack tip opening and the material flow properties [31]. Thus, the intersection of the resistance curve with the crack blunting line corresponds to the true J_{IC} .

The strength σ_0 , used in the blunting line expressions is sometimes the 0.2% offset tensile yield strength; other times it is the average of this value and the ultimate tensile strength. For high work-hardening materials, however, the blunting line is even steeper. The crack blunting line, for example, for 316 stainless steel is reported [32] to be

$$J = 3.8\sigma_0\Delta a \quad (7.35)$$

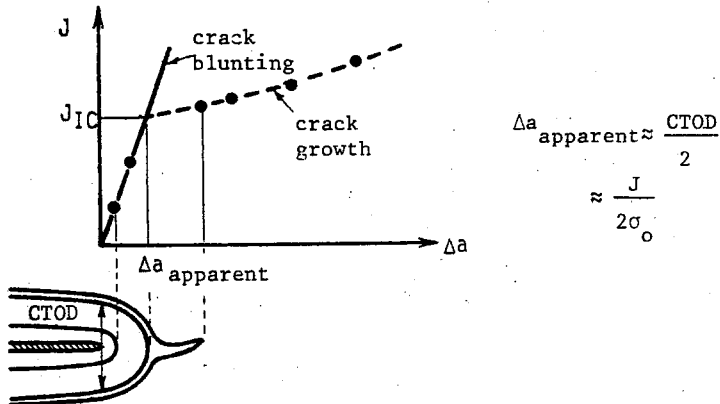


Fig.7.23: Schematic of backward extrapolation to find J_{IC}

7.3.1 Experimental Details: The specimens used in J_{IC} testing are limited by $0.50 < a_0/W < 0.75$ condition. Side grooving is optional. Fatigue precracking procedure and the specimen grips are as in LEFM based K_{IC} testing [33]. J values are determined from load-load point displacement ($P-\Delta$) records using eq.7.25a, b or c, with $B = B(\text{net})$ for side grooved specimens. Crack extension may be taken into consideration through eq.7.28.

The data points generated are required to obey the condition

$$B, b > 15 J/\sigma_0$$

or else they are disqualified for subsequent use. At least four data points are used to characterize the early portion of the resistance curve through a linear regression line. Absolute limits on crack extension are set by parallel offsets from the blunting line as illustrated in figure

7.24. By restricting both the data to fall within these two lines (approximately 1.5mm apart) and the specimens to conform to the size criterion (eq.7.19a),

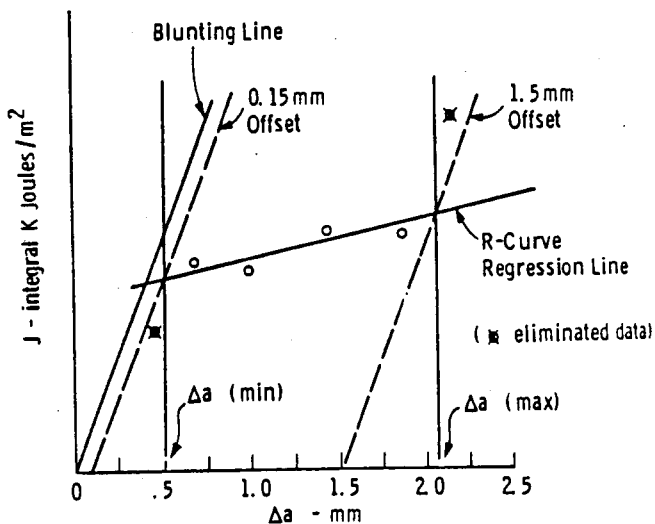


Fig.7.24: Data elimination in the regression analysis

the maximum amount of crack extension allowed for most materials during the test will be approximately 6% of the remaining ligament. It has been shown by Shih et.al. [34] that, for crack extensions up to 6% of b , the value of J is accurately predicted by J estimation procedures discussed above.

Just like in plane strain fracture toughness testing, it is not clear whether the J_{IC} value found is valid until the conditions

$$B \text{ (or) } B_{net} > 25 J_{IC}/\sigma_o$$

$$b > 25 J_{IC}/\sigma_o$$

and

$$dJ/da \leq \sigma_o$$

are met. Thus it is customary to designate the candidate value as J_Q until the above stated checks are completed.

7.3.2 Estimation of crack growth: The major problem in J_{IC} evaluation is the difficulty of assessing crack extension, Δa , correctly. Two methods have gained popularity. These are the multiple specimen heat-tint method and the single specimen unloading compliances method.

The Multi-specimen method: In this approach crack front is marked after completion of each test. Heat tinting is the common way. Heating the specimen to 300°C for 10 minutes per 25mm. of thickness will discolor the existing fracture surface for most steels. For other materials, that do not discolor readily, fatigue cycling to extend the crack will adequately mark the crack extension. After the specimen is chilled and, pulled apart, Δa is determined by the average of 9 readings taken across the crack front from one surface to the other.

The Unloading Compliance Method: The above procedure is both tedious and very expensive since it requires numerous specimens. Another technique suggested by Paris has been developed by Clarke et.al. [35] which enables J_{IC} to be determined from multiple loadings of a single sample. After the sample is loaded to a certain load and displacement level, the load is reduced by approximately 10% (Fig.7.25). Unloading slopes tend to be linear, independent of prior plastic deformation developed on loading. Thus, by measuring the specimen compliance during this slight unloading period, the crack length corresponding to this compliance value can be defined.

To obtain sufficient sensitivity it may be necessary to amplify the unloading slopes (Fig.7.26). The present practice for J_{IC} determination (E813-81) is based on determining the value of J_{IC} within a scatter band of 10%. In keeping within this scatter band, it is found that for the unloading compliance procedure to determine J_{IC} accurately, it is necessary to predict the final amount of crack extension within 15% of the heat-tint value. The amount of accuracy and reliability in unloading compliance method is intimately related to the amount of care taken in the test procedure. Pin friction, clip gage linearity and specimen alignment all go, hand in hand in the development of reliable data [36,37]. The crack size change of interest is often-times small relative to the overall specimen dimensions. Hence changes in slope will also be small and it is necessary to adjust instrumentation accuracy requirements to this fact. To illustrate it, table 7.4 lists various standard sizes of compact specimens and the change in compliance that 0.13mm. of stable crack growth would represent. It is immediately obvious that extra ordinary precision in unloading compliance practice is needed for the larger specimens.

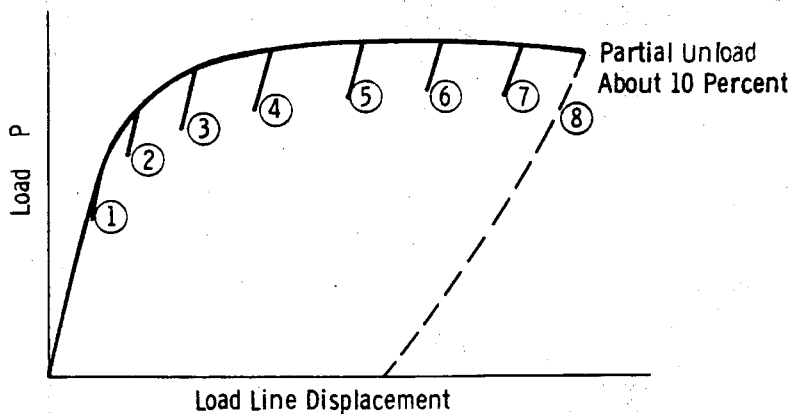


Fig. 7.25: Schematic test record with partial unloading slopes
ASTM E813

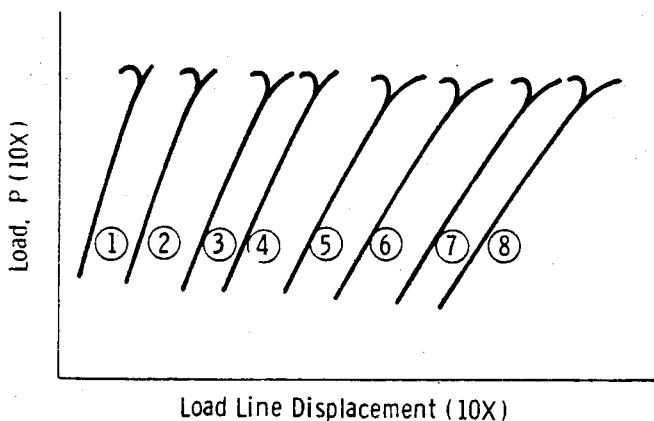


Fig. 7.26: Schematic of amplified unloading slopes [ASTME813]

Table 7.4: Compliance change for 0.127mm of crack growth, assuming
 $a_0/W = 0.5$ [38]

size	a_0, mm	crack size change, %	compliance $\Delta C/C_0, \%$
1T	25.4	0.5	1.2
2T	50.8	0.25	0.6
4T	101.6	0.12	0.3
10T	254	0.05	0.13

Compliance information for several specimens have been calculated and published by various authors [39-41]. For compact specimens, Saxena and Hudak [39] gives the load line compliance, C_{LL} , in terms of normalized crack length as

$$EBC_{LL} = \frac{16}{(1-a/W)^2} - \frac{24}{(1-a/W)} - 4.51 \ln \left(1 - \frac{a}{W}\right) + 18.71 \quad (7.36)$$

and the normalized crack length in terms of the load line compliance as

$$a/W = 1.000196 - 4.06319 U_{LL} + 11.242 U_{LL}^2 - 106.043 U_{LL}^3 + 464.335 U_{LL}^4 - 650.677 U_{LL}^5 \quad (7.37)$$

where

$$U_{LL} = \frac{1}{\sqrt{E B_e C_{LL} + 1}}$$

The effect of reduced thickness of side grooved compact specimen is introduced [41] through

$$B_e = B - \frac{(B-B_{net})^2}{B} \quad (7.38)$$

Kapp et.al [40] present a similar expression for the compact specimen,

$$EBC_{LL} = \frac{31.6}{(1-a/W)^2} \left[0.0334 + 0.875 (a/W) - 1.003 (a/W)^2 + 0.5694 (a/W)^3 \right] \quad (7.39)$$

where $E' = E$ for plane stress and $E' = E/(1-\nu^2)$ for plane strain. The load line compliance expressions given above as well as the crack mouth compliances for compact specimens have been plotted in figure 7.27 for convenience. Crack mouth-to-load line compliance ratio is roughly 0.7. A better estimate of crack mouth compliance can be made if compact specimen is assumed to rotate as a rigid body around a point lying 0.33b ahead of the crack tip [42].

For three point bend specimens - with displacements measured at the notched edge, i.e. crack mouth - the crack length is given by [41]

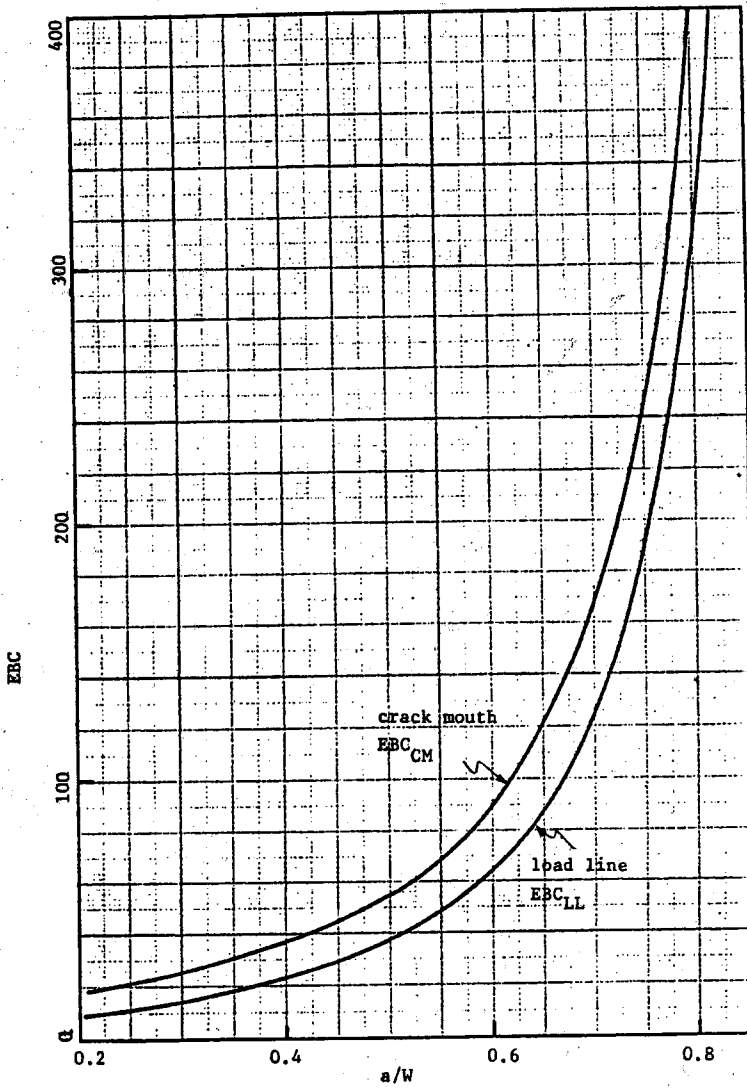


Fig.7.27: Crack mouth and load line compliances of the Compact Specimen, C(T).

$$a/W = 0.998265 - 3.81662 U_x - 1.80596 U_x^2 - 32.3104 U_x^3 - 44.1566 U_x^4 - 52.6788 U_x^5 \quad (7.40)$$

where

$$U_x = \frac{1}{\sqrt{\frac{E_b W C_{CM}}{S/4} + 1}}$$

and W = width of the bend specimen

S = span of the bend specimen

B_e = as given in eq.7.38

Kapp et.al. present the crack mouth compliance of the three point bend specimen

$$E'BC_{CM} = \frac{3.95(S/W) (a/W)}{(1-a/W)^2} \left[2.21-6.57(a/W)+17.86(a/W)^2 \right. \\ \left. - 26.55(a/W)^3 +19.91(a/W)^4 -5.86(a/W)^5 \right] \quad (7.41)$$

and the load line compliance of the three point bend specimen

$$E'BC_{LL} = (S/W)^2 \left[\frac{S/W}{4} + \frac{(a/W)^2}{(1-a/W)^2} (8.887-33.90(a/W) \right. \\ \left. + 68.48(a/W)^2 -68.06(a/W)^3+25.58(a/W)^4 \right] \quad (7.42)$$

The compliance information for three point bend specimen is combined in figure 7.28. Further information regarding Wedge Opening Loading specimen, Center-Cracked Panel, Disk-Shaped Compact specimen and Arc-Shaped Tension specimen is contained in references [39,40].

While the compliance calibration equations cited/plotted above are used to determine the difference in crack lengths, absolute values of crack length can be erroneously predicted due to the use of incorrect elastic modulus values. It is easier to predict crack growth using differential compliances [41] given by

$$da_i = \frac{b_i}{2} \left[\frac{C_i - C_{i-1}}{C_{i-1}} \right] g(a_i/W) \quad (7.43)$$

$$\text{where } g(a/W) = -7.3341 +51.151 a/W - 128.32(a/W)^2 \\ +162.17 (a/W)^3 -103.33 (a/W)^4 +26.667 (a/W)^5$$

for compact specimens, and by,

$$da_i = \frac{b_i}{2} \left[\frac{C_i - C_{i-1}}{C_{i-1}} \right] \quad (7.44)$$

for three point bend specimen with span-to-width ratio of four. McCabe

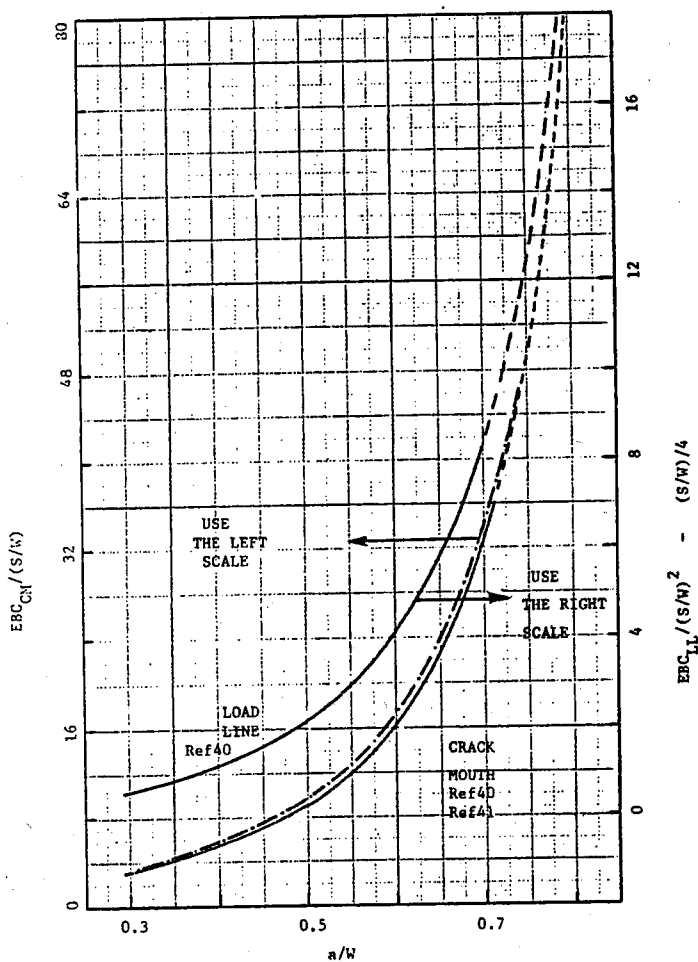


Fig.7.28: Crack mouth and load line compliances of the three point bend specimen, SE(B).

and Landes [43] report better correlation using fixed ligament size b_0 in eq.7.43 and recommend, for compact specimens

$$da_i = \frac{b_0}{2} \left[\frac{C_i - C_{i-1}}{C_{i-1}} \right] \left(\frac{1 + \gamma^2}{1 + \gamma} \right) \quad (7.45)$$

where γ is defined in eq.7.25 using a_{i-1} .

When compact specimen tests result in large displacements, it is necessary to account for rotational effects of the specimen. Both the

load point and the displacement point rotate around the stress reversal point in the remaining ligament of the specimen. The corrected compliance for rotational effects (Δ_c/P_c) is given in the following in terms of measured compliance (Δ_m/P_m) and the specimen dimensions

$$\frac{\Delta_c}{P_c} = \frac{\Delta_m}{P_m} \left[\frac{1}{(1-X/Z)(1-Y/Z)} \right] \quad (7.46)$$

where

$$X = \frac{2\Delta_m H + \Delta_m^2}{2Z}$$

$$Y = \frac{2\Delta_m D + \Delta_m^2}{2Z}$$

and H,D,Z are as shown in figure 7.29.

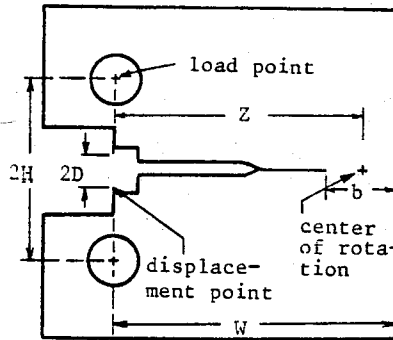


Fig.7.29: Schematic of Compact Specimen with points for large rotation correction [38]

Another alternative to crack length measurements is the so called Key curve method [44]. This method is based on the idea that load-displacement behavior can be separated into material and geometry variables. For bend configurations, the following describes a relationship of the acting variables

$$\frac{P}{S} = \frac{b^3}{W} g\left(\frac{a}{W}\right) F\left(\frac{2a}{W}\right) \quad (7.47)$$

where $g(a/W) = \exp(0.522 b/W)$ for compact specimens, and $g(a/W) = 1$ for three point bend specimens -- representing a weak dependence on (a/W) .

If the $P-\Delta$ relation obtained from a specimen with blunt notch and ligament b_0 fits a power law

$$f\left(\frac{\Delta_{pl}}{W}\right) = k \left(\frac{\Delta_{pl}}{W}\right)^n$$

by appropriate choice of k and n , the current crack length -- in specimens with extending cracks -- can be calculated from eq.7.47 as

$$b = \left[\frac{(P/B) W^{n+1}}{\Delta_{pl}^n g k} \right]^{1/2}$$

Available data is not sufficient yet to judge about the success of this procedure.

7.3.3 The Significance of J_{IC} : J_{IC} signifies the initiation of crack growth for metallic materials. It applies specifically to geometries that contain notches and flaws and that are sharpened with fatigue cracks.

In the field of research and development, J_{IC} can be used to evaluate materials in terms that can be significant to design. The value of J_{IC} may be used as a ductile fracture toughness criterion to evaluate the effects of metallurgical variables, heat treatments and weldments.

If for a specific structure of interest an elastic-plastic analysis is available which describes J as a function of the loading parameter and crack size, then the critical value of load or the crack size can be determined by comparing the applied J versus J_{IC} , in cases where onset of slow stable crack growth, as opposed to maximum failure load, constitutes a design limitation. In particular for cracks emanating from notches, LEFM will not be much of a help since due to the stress concentration effect of notches large scale plastic deformation will take place at nominal stresses much below yield.

The most common use of J_{IC} is to develop toughness values of materials on specimens which are too small to comply with the size requirements of E399-81 for valid K_{IC} toughness measurements. In general, a smaller specimen will allow considerable plasticity to develop prior to crack propagation. While this invalidates the small scale plasticity

requirements of K_{IC} testing, the J-integral can be utilized to calculate J_{IC} . The value of J_{IC} , which may be measured on a small specimen can be related to the value of K_{IC} by the expression

$$J_{IC} = \frac{K_{IC}^2(1-\nu^2)}{E} \quad (7.48)$$

where E is the elastic modulus and ν the Poisson's ratio. The comparison in eq.7.48 assumes that the measurement point for both J_{IC} and K_{IC} be taken identically. However, J_{IC} is measured at the beginning of cracking whereas for stable cracking K_{IC} is taken at the 2% crack extension point. This difference in measurement point results in a J_{IC} value which is often lower than the corresponding K_{IC} as related through eq.7.48. Therefore, J_{IC} very often provides a conservative lower bound estimate for K_{IC} when stable cracking occurs during the fracture process (Fig.7.30).

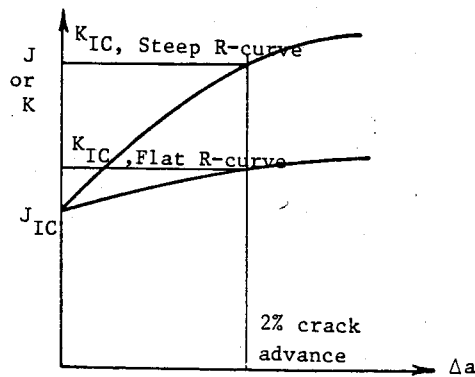


Fig.7.30: Schematic of R-curve showing the differences between the J_{IC} and K_{IC} measurement point.

7.3.4 Examples of J_{IC} Results: J_{IC} tests have been successfully conducted on a number of metal alloy systems. Some of the results will be presented here as taken mostly from reference [45].

Ferritic steels provide a good illustration of the use of the J_{IC} test since these alloys have a transition from a low toughness brittle fracture mode at low temperatures to a high toughness ductile fracture mode at higher temperatures. This is illustrated in figure 7.31 for an ASTM A217 2.25 Cr-1 Mo cast steel where fracture toughness is plotted as a function of test temperatures [46]. In the low temperature brittle

fracture regime, fracture toughness can be measured by linear elastic techniques. In the transition range as toughness increases, the size of the K_{IC} specimen must also increase. At some point, the specimen size necessary for a K_{IC} test becomes prohibitively large. At this point, the

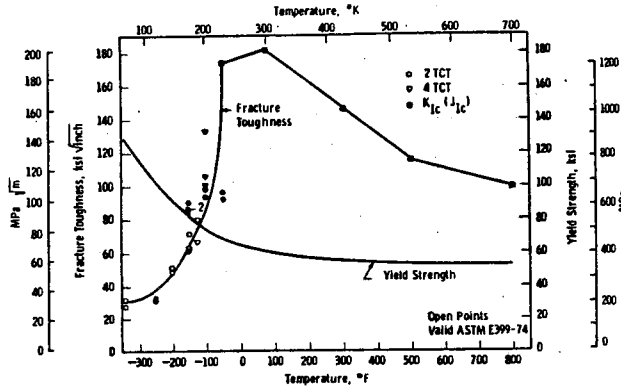


Fig.7.31: Temperature dependence of fracture toughness and yield strength for A217 2.25Cr-1 Mo cast steel [46]

J_{IC} test can be used to measure toughness with a small specimen. As the test temperature is increased and the fracture mode becomes purely ductile, a maximum "upper shelf" toughness value is reached. Toughness then decreases with increasing temperatures.

Resistance curves for two steels, an AISI 403 modified 12Cr stainless rotor steel and an ASTM A470 Cr-Mo-V rotor steel, which are used to determine J_{IC} values in the ductile fracture regime are shown in figures 7.32 and 7.33. The curves of toughness versus test temperature are shown

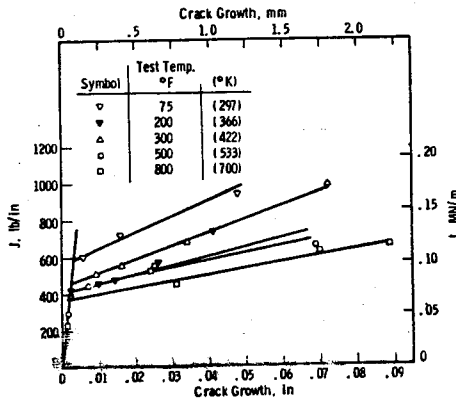


Fig.7.32: J-resistance curves for 403 modified 12 Cr stainless steel [46].

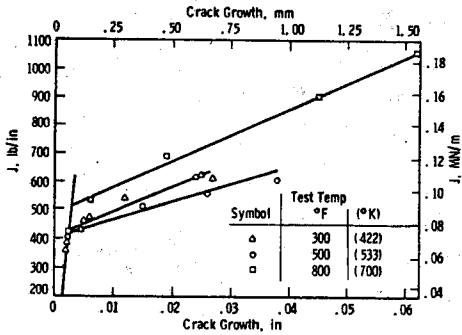


Fig.7.33: J-resistance curves for A470 rotor steel [46]

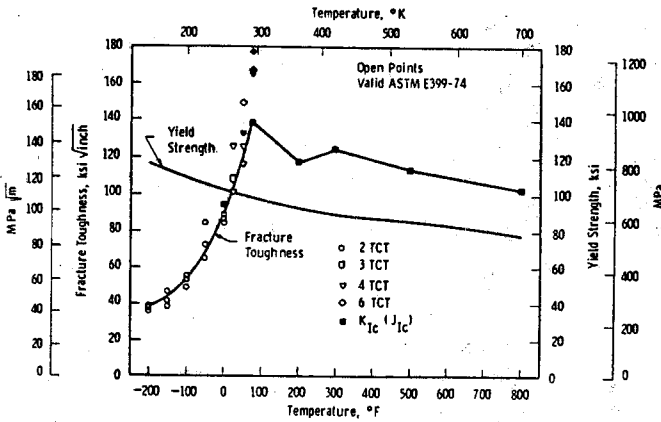


Fig.7.34: Temperature dependence of fracture toughness and yield strength for 403 modified 12 Cr stainless steel [46]

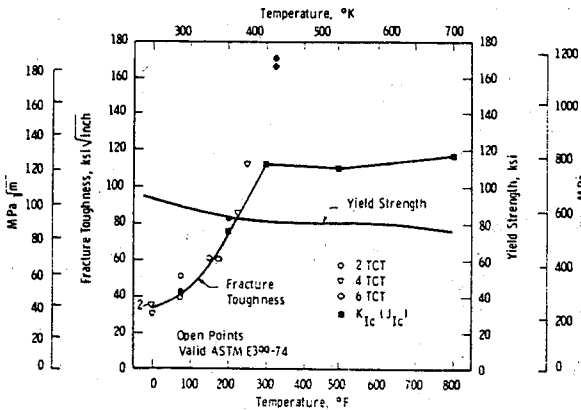


Fig.7.35: Temperature dependence of fracture toughness and yield strength for A470 rotor steel [46]

in figures 7.34 and 7.35 for these two steels. Resistance curves for a 2024-T351 aluminum alloy are shown in figure 7.36. J_{IC} values have been determined for three different specimen thicknesses at two crack lengths and found to be reasonably consistent [47]. Similar data for 7005-T6351 Aluminum alloy are shown in figure 7.37.

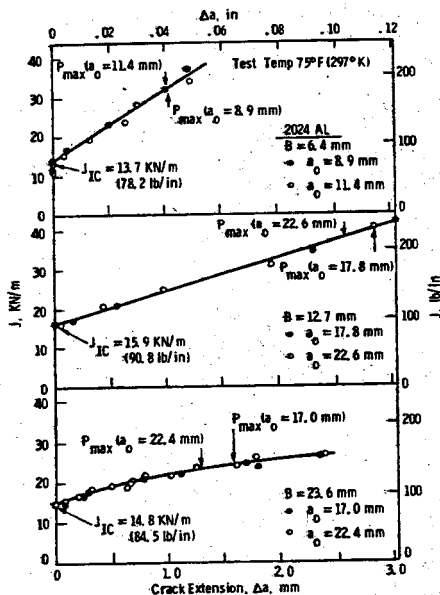


Fig. 7.36: J resistance curves for 2024-T351 Al alloy [47]

J_{IC} values can be determined from a single specimen when crack advance occurs by a brittle unstable mechanism, such as steels fracturing by a cleavage mode. For this case J_{IC} can be measured at the point of maximum load. Care must be taken to ensure that no stable crack growth occurred before the instability point. This can be done by several methods, the easiest being by visual examination of the fracture surface. If the instability point was the point of first crack advance, the fracture surface will show a negligible region of ductile fracture between the fatigue crack area and the cleavage fracture area. For such cleavage modes, J_{IC} and K_{IC} values closely agree (Fig. 7.38).

In the ductile "upper shelf" regime of fracture for steels a comparison is difficult since valid K_{IC} tests generally require very large specimens and such data are not often available. A comparison of K_{IC} with J_{IC} is given for an ASTM A 471 Ni-Cr-Mo-V rotor in figure 7.39.

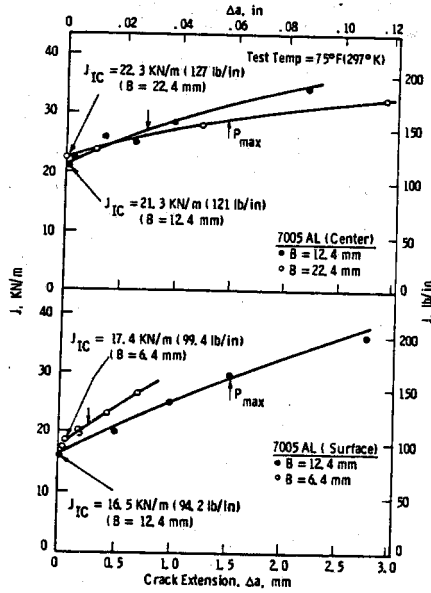


Fig.7.37: J resistance curves for 7075-T6351 aluminum alloy [47]

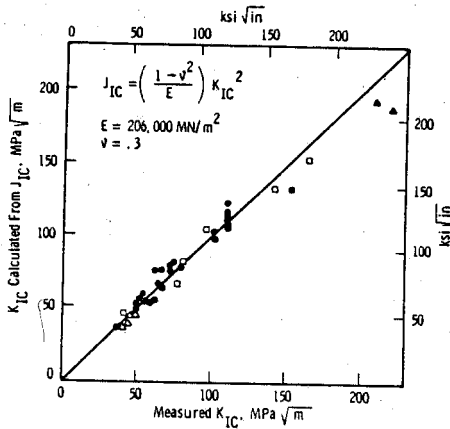


Fig.7.38: Correlation between K_{IC} values calculated from J_{IC} and actual K_{IC} values [45]

Fracture toughness from 1 inch thick compact specimens is determined by the J_{IC} method and converted to K_{IC} to compare with toughness values

from valid K_{IC} tests on 8 inch thick compact specimens. As would be expected (cf. Fig. 7.30) the J_{IC} values are lower than the K_{IC} values.

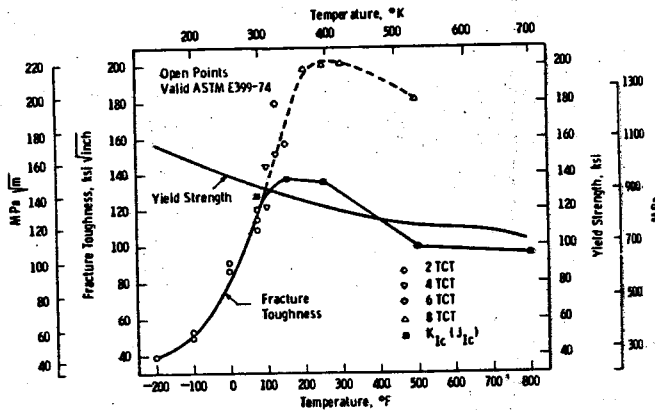


Fig. 7.39: Temperature dependence of fracture toughness and yield strength for A 471 Ni-Cr-Mo-V rotor steel [46]

7.4 THE CRACK OPENING DISPLACEMENT

It has been discussed that under conditions of general yield plastic flow is no longer contained and the plastic zone spreads through the entire cracked section (Fig. 7.1). Particularly for negligible strain hardening, the nominal stress hardly increases after general yield and fracture condition may be expressed as occurrence of a sufficiently large strain, rather than stress [48]. A measure of the plastic strain at the crack tip is the crack opening displacement, CoD or δ . Thus,

$$\delta = \delta_c$$

could be used as a fracture criterion. For small scale yielding behavior, this is indeed the case. Irwin's approach (Fig. 7.40a) defines the crack opening displacement through the elastic solution (eq. 2.28) at $\theta = \pi$ and $r = r_y$, yielding

$$\delta = \frac{4}{\pi} \frac{G}{S_y} \quad (7.49)$$

for plane stress. This can be extended to plane strain as well, getting

$(4/\pi) G/\sqrt{3}S_y$. Dugdale's approach (Fig.7.40b) makes use of the crack face

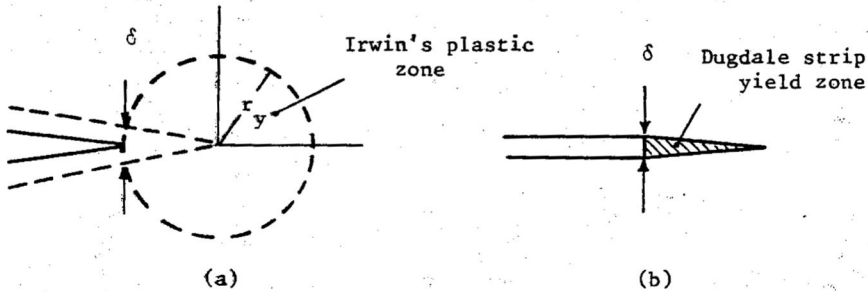


Fig.7.40: Schematic CoD definitions in small scale yielding
(a) based on Irwin's plastic zone (b) based on Dugdale strip yield zone

displacements worked out by Goodier and Field [49], leading to

$$\delta = \frac{8}{\pi} \frac{a S_y}{E} \ln \sec\left(\frac{\pi}{2} \frac{\sigma}{S_y}\right)$$

$$\approx \frac{8}{\pi} \frac{a S_y}{E} \left[\frac{1}{2} \left(\frac{\pi}{2} \frac{\sigma}{S_y}\right)^2 + \frac{1}{12} \left(\frac{\pi}{2} \frac{\sigma}{S_y}\right)^4 + \dots \right]$$

which reduces for $\sigma \ll S_y$ to

$$\delta = \frac{\sigma^2 a \pi}{E S_y} = \frac{G}{S_y} \quad (7.50)$$

Intuitive arguments would also lead to similar solutions. Opening up a crack by a distance δ against a yield stress S_y in plane stress probably requires an energy $G = \delta S_y$.

It is not universally accepted yet that fracture may always be predicted by $\delta = \delta_c$. So far, only England standardized CoD tests^x. Main work has been towards obtaining valid K_{IC} data from δ_{IC} . That is, obtaining material constants using small laboratory specimens. The other issue, namely that of using $\delta = \delta_c$ for fracture predictions in high toughness materials, has received less attention. The CoD design curve approach, as founded by Wells and evolved mainly by Dawes [50,51] is based upon empirical

^x ASTM has a preliminary draft (1985)

correlations currently. It is formulated as

$$\frac{\delta_c}{2\pi e_y a_{\max}} = \begin{cases} (e/e_y)^2 & \frac{e}{e_y} < .5 \\ (e/e_y) - 0.25 & \frac{e}{e_y} > .5 \end{cases} \quad (7.51)$$

where e is the local applied strain that would exist in the vicinity of the crack if the crack were absent, $e_y = S_y/E$ is the yield strain, δ_c is the critical COD, and a_{\max} is a conservative estimate of the critical flaw size.

The major advantage of the CoD approach is that it is not limited to linear elastic materials. There is no conceptual constraint on extending to fracture predictions beyond yield. Ambiguities, however, exist in the definition and it is difficult to measure COD. An unambiguous, operational definition is the one given in figure 7.11 defining it at the tip through two 45° lines. It is usually worthwhile to distinguish between the crack opening displacement at a general location and the crack tip opening displacement and the designation δ_t (CTOD) is preferred at times to emphasize the difference.

To reduce the uncertainties in measurement British Standards recommend, for three point bend specimens, CTOD evaluation through crack mouth opening displacement, as depicted in figure 7.41. Experiments show that

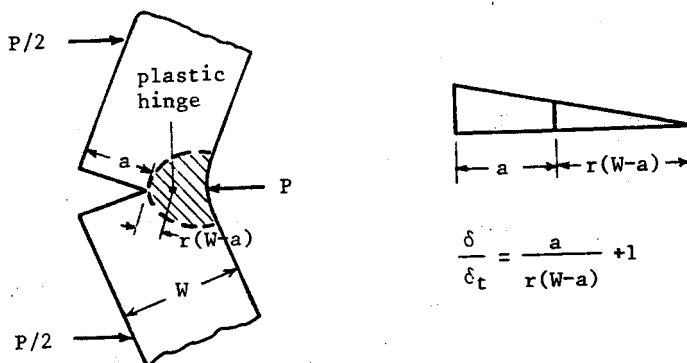


Fig.7.41: Relation between crack tip opening displacement and crack mouth opening displacement for bend geometries

the rotational factor r increases during loading from almost zero (for elastic with only contained plastic flow at the crack tip) to a more-or-less

constant value of 1/3 (for fully plastic ligaments) (Fig.7.42). In fact, the new version of the British Standard as well as the ASTM draft simplify

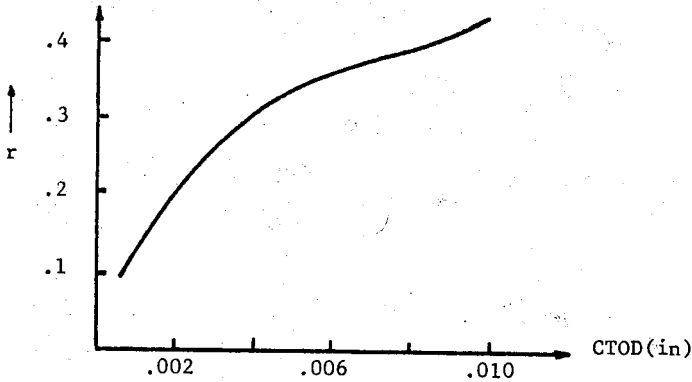


Fig.7.42: Variation of r for a variety of materials [53]

the procedure and specify that the crack tip opening displacement should be calculated using the relationship [52]

$$\delta_t = \frac{K^2}{2\sigma_o E'} + \frac{\delta}{1+2.5\left(\frac{a+z}{W-a}\right)} \quad (7.52)$$

where z represents the knife edge thickness and δ the crack mouth opening at the knife edges.

REFERENCES

1- Rice, J.R., "A Path-Independent Integral and the Approximate Analysis of Strain Concentration by Notches and Cracks" *Journal of Applied Mechanics*, Transaction ASME, 35, (1968) pp.379-386

2- Hutchinson, J.W. "A Course on Nonlinear Fracture Mechanics" Tech.Univ. of Denmark (1979)

3- Rice, J.R. "Mathematical Analysis in the Mechanics of Fracture" in *Fracture: An Advanced Treatise*, Vol.2. H.Liebowitz, Ed.Academic Press, New York, (1968) p.211

4- Hutchinson, J.W., "Singular Behavior at the End of A Tensile Crack in a Hardening Material" Journal of the Mechanics and Physics Solids, 16, (1968) pp.13-31

5- Rice, J.R., and Rosengren, G.F., "Plane-Strain Deformation Near a Crack Tip in a Power-Law Hardening Material" Journal of the Mechanics and Physics of Solids, 16, (1968), pp 1-12

6- Paris, P.C., "Fracture Mechanics in the Elastic-Plastic Regime" ASTM STP 631, Amer.Soc.for Testing and Materials (1977), pp.3-27.

7- Hutchinson, J.W., "Fundamentals of the Phenomenological Theory of Nonlinear Fracture Mechanics" Journal of Applied Mechanics, Transactions ASME, 50 (1983), pp.1042-1051

8- Mc Meeking, R.M., "Finite Deformation Analysis of Crack Tip Opening in Elastic-Plastic Materials and Implications for Fracture Initiation" Journal of the Mechanics and Physics of Solids, 25 (1977) pp.357-381

9- Parks, D.M., Proceedings of the Second International Conference on Numerical Methods in Fracture Mechanics, Swansea, U.K(1980)

10- Rice, J.R., Mc Meeking, R.M., Parks, D.M., and Sorensen, E.P., "Recent Finite Element Studies in Plasticity and Fracture Mechanics" Computer Methods in Applied Mechanics and Engineering, 17/18, (1979) pp.411-442

11- Mc Clintock, F.A. "Plasticity Aspects of Fracture" in Fracture: An Advanced Treatise, Vol.3 Liebowitz, H. ed., Academic Press, New York, (1971), pp.47-225.

12- Ritchie, R.O., "Why Ductile Fracture Mechanics" Journal of Engineering Materials and Technology, Transaction ASME, 105, (1983) pp.1-7

13- Shih, C.F. and German, M.D., "Requirements for a One Parameter Characterization of Crack Tip Fields by the HRR Singularity" International Journal of Fracture, 17 (1981) p.27

- 14- Mc Meeking, R.M., and Parks, D.M., "On Criteria for J-Dominance of Crack Tip Fields in Large Scale Yielding" ASTM STP 668, Amer.Soc. for Testing and Materials (1979) pp.175-194
- 15- Shih, C.F., "Relationships Between the J-Integral and the Crack Opening Displacement For Stationary and Extending Cracks" Journal of the Mechanics and Physics of Solids, 29(1981) pp.305-326
- 16- Begley, J.A., and Landes, J.D., "The J-Integral as a Fracture Criterion" ASTM STP 514, Amer.Soc. for Testing and Materials, (1972) pp.1-23
- 17- Rice, J.R., Paris, P.C., and Merkle, J.G. "Some Further Results of J-Integral Analysis and Estimates" ASTM STP 536, Amer.Soc. for Testing and Materials (1973), pp.231-245
- 18- Srawlay, J.E., "On the Relation of J_I to Work Done Per Unit Un-cracked Area: Total or Component due to Crack" International Journal of Fracture, 12 (1976) pp.470-474
- 19- Chipperfield, C.G. "A Summary and Comparison of J Estimation Procedures" Journal of Testing and Evaluation, JTEVA,6, (1978), pp.253-259
- 20- Landes, J.D., Walker, H., and Clarke, G.A., "Evaluation of Estimation Procedures Used in J-Integral Testing" ASTM STP 668, Amer. Soc. for Testing and Materials (1979) pp.266-287
- 21- Merkle, J.G. and Corten, H.T., "A J-Integral Analysis For the Compact Specimen, Considering Axial Force as Well as Bending Effects" Journal of Pressure Vessel Technology, Transactions ASME, 96, (1974) pp.286-292
- 22- Clarke, G.A. and Landes, J.D., Journal of Testing and Evaluation, JTEVA, 7(1979) pp.264-269
- 23- Ernst, H.A., "Unified Solution for J Ranging Continuously from Pure Bending to Pure Tension" ASTM STP 791, Amer.Soc. for Testing and Materials (1983) pp.1-499-519

24- Ernst, H.A., Paris, P.C., and Landes, J.D. "Estimations on J-Integral and Tearing Modulus T from a Single Specimen Test Record" ASTM STP 743, Amer.Soc. for Testing and Materials (1981) pp.476-502

25- Bucci, R.J., Paris, P.C., Landes, J.D. and Rice, J.R. "J-Integral Estimation Procedures" ASTM STP 514, Amer.Soc. for Testing and Materials, (1972), pp.40-69

26- Shih, C.F. "J-Integral Estimates for Strain Hardening Materials in Antiplane Shear Using Fully Plastic Solution" ASTM STP 590, Amer. Soc. for Testing and Materials (1976), pp.3-26

27- Shih, C.F. and Hutchinson, J.W., "Fully Plastic Solutions and Large Scale Yielding Estimates for Plane Stress Crack Problems" Journal of Engineering Materials and Technology, Transactions ASME, 98, (1976) pp. 289-295

28- Shih, C.F., German, M.D., and Kumar, V., "An Engineering Approach For Examining Crack Growth and Stability in Flawed Structures" International Journal of Pressure Vessel and Piping, 9, (1981) pp.159-196

29-Goldman, N.L. and Hutchinson, J.W. "Fully Plastic Crack Problems: The center cracked strip under plane strain" International Journal of Solids and Structures, 11(1975),pp.575-591

30- Kumar, V., German, M.D., and Shih, C.F., "An Engineering Approach for Elastic-Plastic Fracture Analysis" GE Report to EPRI, RP 1237-1 (1981)

31- Rice, J.R., "Elastic Plastic Fracture Mechanics" AMD-Voll9: The Mechanics of Fracture, Amer.Soc.Mech.Eng. (1976) pp.23-53

32- Davies, P.H., "An Elastic-Plastic Fracture Mechanics Study of Crack Initiation in 316 Stainless Steel" ASTM STP 803, Amer.Soc. for Testing and Materials (1983) pp.II-611-631

- 33- Clarke, G.A., Andrews, W.R., Begley, J.A., Donald, J.K., Embley, G.T., Landes, J.D., McCabe, D.E., Underwood, J.H., "A Procedure for the Determination of Ductile Fracture Toughness Values Using J Integral Techniques" Journal of Testing and Evaluation, JTEVA, 7 (1979), pp.49-56.
- 34- Shih, C.F. de Lorenzi, H.G., German, M.D., Andrews, W.R., VanStone, R.H., Wilkinson, J.P.D., "Methodology for Plastic Fracture", GE Sixth Quarterly Report to EPRI, RP 601-2, (1978).
- 35- Clarke, G.A., Andrews, W.R., Paris, P.C., and Schmidt, D.W. "Single Specimen Tests for J_{IC} Determination" ASTM STP 590, Amer.Soc. for Testing and Materials (1976), pp.27-42.
- 36- Clarke, G.A. "Single Specimen Tests for J_{IC} Determination-Revisited" ASTM STP 743, Amer.Soc. for Testing and Materials, (1981) pp.553-575.
- 37- Hewitt, R.L., "Accuracy and Precision of Crack Length Measurements Using a Compliance Technique" Journal of Testing and Evaluation, JTEVA, 11 (1983), pp.150-155.
- 38- Clarke, G.A. and Landes, J.D. "Toughness Testing of Materials by J-Integral Techniques" Toughness Characterization and Specifications for HSLA and Structural Steels Ed. by P.L. Manganon, Jr. The Metallurgical Society of AIME (1979), pp.108-111.
- 39- Saxena, A. and Hudak, S.J. Jr "Review and Extension of Compliance Information for Common Crack Growth Specimens" International Journal of Fracture, 14(1978), pp.453-468.
- 40- Kapp, J.A. Leger, G.S. and Gross, B., "Wide-Range Displacement Expressions for Standard Fracture Mechanics Specimens" ASTM STP 868 (1985) pp.13-21.
- 41- Albrecht, P., Andrews, W.R., Gudas, J.P., Joyce, J.A., Loss, F.J., McCabe, D.E., Schmidt, D.W., and Van Der Sluys, W.A., "Tentative Test Procedure For Determining the Plane Strain J_I -R Curve" Journal of Testing and Evaluation, JTEVA, 10 (1982), pp.245-251.

42- Landes, J.D. "J Calculation From Front Face Displacement Measurement on a Compact Specimen" International Journal of Fracture, 16(1980), pp.183-186.

43- McCabe, D.E. and Landes, J.D. " J_R -Curve Testing of Large Compact Specimens" ASTM STP 803, Amer.Soc.for Testing and Materials(1983) pp.II. 353-371.

44- Joyce, J.A., Ernst, H., and Paris, P.C., "ASTM STP 700, Amer.Soc. for Testing and Materials (1979), pp.222-236.

45- Landes, J.D. and Begley, J.A. "Experimental Methods for Elastic-Plastic and Post Yield Fracture Toughness Measurements" in Post Yield Fracture Mechanics, Latzko, D.G.H. Ed., Applied Science Publishers, London (1979) pp.211-254.

46- Logsdon, W.A, and Begley, J.A. "Upper Shelf Temperature Dependence of Fracture Toughness For Four Low to Intermediate Strength Ferritic Steels" Engineering Fracture Mechanics, 9(1977) pp.461-470.

47- Griffis, C.A. and Yoder, G.R., "Initial Crack Extension in Two Intermediate Strength Aluminum Alloys" Journal of Engineering Materials and Technology, Transactions ASME, 98(1976), pp.152-158.

48- Wells, A.A. "Application of Fracture Mechanics at and Beyond General Yielding" British Welding Journal, 10 (1963), pp.563-570.

49- Goodier, J.N. and Field, F.A. Fracture of Solids, D.C.Drucker and J.J.Gilman, Wiley, New York (1963) pp.103-118.

50- Dawes, M.G. "Fracture Control in High Yield Strength Weldments" Welding Journal Research Supplement, 53 (1974) pp.369s-379s.

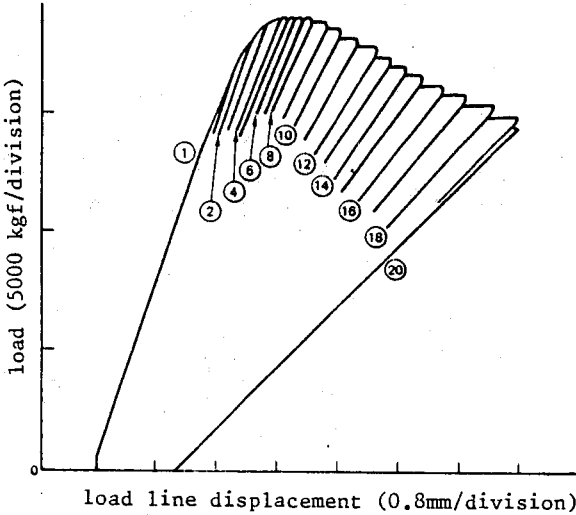
51- Harrison, J.D., Dawes, M.G., Archer, G.L., Kamath, M.S. "The COD Approach and Its Application to Welded Structures" ASTM STP 668, Amer.Soc. for Testing and Materials (1979) pp.606-631.

52- Dawes, M.G. "Elastic Plastic Fracture Toughness Based on the COD and J-Contour Integral Concepts" ASTM STP 668, Amer.Soc.for Testing and Materials (1979), pp.307-333.

53- Broek, D. Elementary Engineering Fracture Mechanics, Noordhoff Leyden, Holland (1974) p.219.

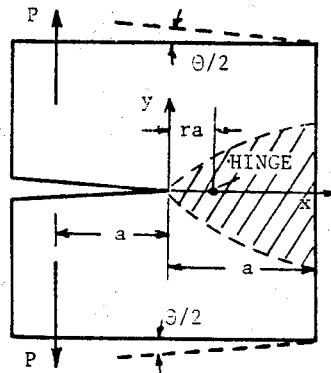
Problems:

1- Using the test record of a 25mm thick steel standard compact tension specimen supplied below, obtain the J versus a curve.



Answer: $J(\text{kg/mm}) = 100 \ 200 \ 250$
 $a(\text{min}) = 30 \ 34 \ 36$

2- Assuming that a compact tension specimen hinges about an axis by angle θ , calculate the J-Integral value for "rigid-perfectly plastic" material by using the line integral definition and choosing Γ to coincide with the specimen outer boundaries.



Answer: $J = P\theta/B + S_y(1-r)a^2$

3- As an extension of the Key-Curve Method Landes(Int.J.Fracture 36, 1988, pp.R9-R20) developed an alternate, more direct expression for determining J from experimental test records. The method assumes that the relationship between load, displacement and crack length can be represented by known functions:

$$P = \frac{b^2}{W} B g\left(\frac{b}{W}\right) H(\Delta p l / W)$$

In cases where the experimental results of $P/\frac{b^2}{W} B g$ versus $\Delta p l / W$ fit a power law, i.e.

$$H = h_0 (\Delta p l / W)^{1/n}$$

the plastic component of J can be integrated directly to give

$$J_{pl} = \frac{\eta^2 \Delta p l}{B b} \left(\frac{n}{n+1}\right)$$

where η is described through eq.7-25c for compact specimens. This last expression accounts for slow stable crack growth and is presented as a substitute for eq.7.28. Using the load-displacement plot of problem 1, you are asked to estimate J at station No.18, based on this direct procedure and assuming $n \approx 5$.

Answer: 275 kgf/mm

8. FURTHER TOPICS OF EPFM

8.1 CRACK GROWTH AND INSTABILITY

J_{IC} characterizes the onset of growth. Instability-true limit of load carrying capacity-occurs usually much later. The substantial stable crack growth in high toughness materials before unstable fracture may lead to unnecessarily high margin of safety when design is based on J_{IC} .

In certain structural materials, high strength steel for example, there appears to be two distinct possibilities for instability. The first is the cleavage instability which is normally attributed to a local material instability on a microscopic scale (such as inclusion spacing). The second type of instability is associated with the global conditions in a component and loading arrangement providing the driving force to cause continuous crack extension by a "tearing" mechanism. Cleavage is associated with very flat fracture on crystalline planes whereas tearing is normally associated with dimpled rupture mechanism on a microscopic level.

Moreover, in testing compact specimens to produce J integral resistance curves, cleavage is associated with a sudden instability where the crack jumps ahead, severing the test piece almost instantaneously. At low temperatures, just above transition, steady tearing commences first, followed after some amount of stable tearing by the sudden cleavage instability. At yet higher temperatures, much more extensive stable tearing occurs prior to cleavage, if the sudden cleavage occurs at all (Fig.8.1). In fcc metals, typically aluminum alloys, cleavage is absent altogether. We address here to the problem of upper-shelf toughness behavior.

8.1.1 Theoretical Justification for the Use of J Integral: Initially the J resistance (J_R) curve was used only as a means of better determining J_{IC} by using the curve to extrapolate back to $\Delta a = 0$. But it soon became clear that the J_R curve could be regarded as a material based curve, in the sense that the K_R curve is in small scale yielding, at least under

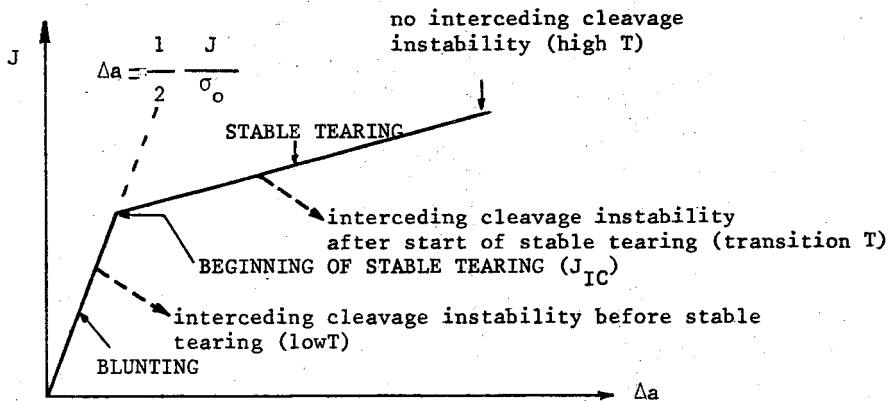


Fig.8.1: J integral resistance curve and interceding cleavage instability

certain restrictions, discussed below.

The near tip stress and strain fields for nonstationary flaw are far more complex than the stationary crack. Crack growth involves elastic unloading and nonproportional plastic loading, both of which are poorly described by deformation theory on which J is based. However, if the region of elastic unloading and nonproportional loading are embedded within the HRR-field of radius R and controlled by this field, crack growth may be described through J. The argument relies on the fact that many metals sustain only very small amounts of crack growth relative to other dimensions for overall deformations well beyond initiation of growth. In a typical tough, intermediate-strength steel, the amount of crack advance associated with a doubling of J above J_{IC} may be as little as 1 or 2 mm [1].

Since the wake of elastic unloading and the region of distinctly nonproportional plastic loading (Fig.8.2) will be of the order of Δa in length, one condition for J-controlled crack growth is [2]

$$\Delta a \ll R \quad (8.1)$$

where R denotes the characteristic radius of the HRR zone.

The second condition is obtained by examining the strain increments determined from deformation theory under a simultaneous increase in J and crack lengths [2]. The crack lies along the x-axis and is assumed

to advance by an amount da in the x direction. For deformation theory, the strain field (eq.7.14)

$$\epsilon_{ij} \sim J^{n/n+1} r^{-n/n+1} \tilde{g}_{ij}(\theta)$$

continues to hold in the presence of growth with r and θ centered at the current tip location. The strain increments are

$$d\epsilon_{ij} \sim \frac{n}{n+1} J^{-1/n+1} dJ r^{-n/n+1} \tilde{g}_{ij}(\theta) - J^{n/n+1} \frac{\partial}{\partial x} [r^{-n/n+1} \tilde{g}_{ij}(\theta)] da$$

Since

$$\frac{\partial}{\partial x} = \frac{\partial r}{\partial x} \frac{\partial}{\partial r} + \frac{\partial \theta}{\partial x} \frac{\partial}{\partial \theta} = \cos\theta \frac{\partial}{\partial r} - \frac{\sin\theta}{r} \frac{\partial}{\partial \theta}$$

the above equation becomes

$$d\epsilon_{ij} \sim J^{n/n+1} r^{-n/n+1} \left[\frac{n}{n+1} \frac{dJ}{J} \tilde{g}_{ij} + \frac{da}{r} \beta_{ij} \right] \quad (8.2)$$

where $\tilde{\beta}_{ij}(\theta) = \frac{n}{n+1} \cos\theta \tilde{g}_{ij} + \sin\theta \frac{\partial}{\partial \theta} \tilde{g}_{ij}$. The first term in the bracket in eq.8.2 corresponds to a proportional loading increment (i.e. $d\epsilon_{ij} \sim \epsilon_{ij}$), while the second term is not proportional. Since \tilde{g}_{ij} and $\tilde{\beta}_{ij}$ are of comparable magnitude, the first term in the bracket will overwhelm the second term if

$$\frac{da}{r} \ll \frac{dJ}{J} \quad (8.3)$$

This condition can be written as

$$D \equiv \frac{J}{dJ/da} \ll r \quad (8.4)$$

The second condition is therefore

$$D \equiv \frac{J}{dJ/da} \ll R \quad (8.5)$$

since this ensures that there exists an annular region, as shown in figure 8.2, $D \ll r \ll R$, in which nearly proportional loading holds and in which

the J-fields control, or dominate, the actual behavior.

For a fully yielded configuration R will be some fraction of the uncracked ligament b (e.q. 7.16). This implies

$$b \gg D$$

or introducing a nondimensional parameter

$$\omega \equiv \frac{b}{D} = \frac{b}{J} \frac{dJ}{da} \gg 1 \quad (8.6)$$

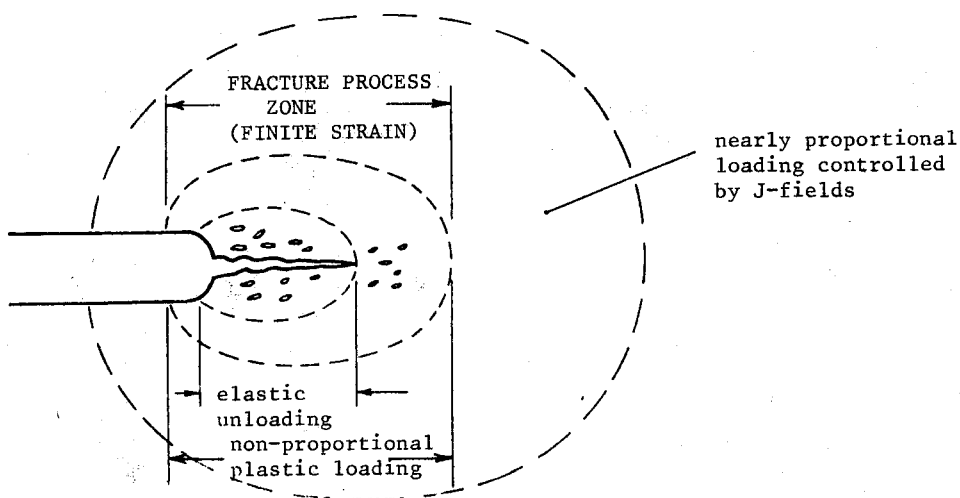


Fig.8.2: Schematic of near tip behavior under J controlled growth conditions [1]

For the bend configuration with $R \approx 0.07 b$, the above condition becomes

$$\omega > 14$$

which is somewhat too restrictive on the face of tests on bend and compact specimens. Hutchinson [1] suggests $\omega > 5$ to 7 is more realistic. The conditions for the onset of growth

$$b_o > 25 J/\sigma_o \quad \text{or} \quad M_b \equiv b_o \sigma_o / J > 25 \quad (8.7)$$

and

$$B_{Net} > 25 J/\sigma_o \quad \text{or} \quad M_B \equiv B_{Net} \sigma_o/J > 25 \quad (8.8)$$

are still required for J-dominance.

Experimental data support the characterization of some amount of crack growth by J_R curves [3]. These curves appear to be independent of specimen size and extent of plastic deformation if plane strain conditions prevail in the crack tip region and certain other requirements are met. Numerical calculations by Shih [4] indicate that for specimens subjected to remote bending, the path independence of J is observed for growth up to 6% of the original uncracked ligament ($\Delta a < 0.06 b_o$). Using a typical 25mm thick compact specimen only the first 1.5-2mm of crack extension can be taken as J controlled. If Δa is excessive, J-R curve shows a pronounced dependence on geometry. In such cases, a resistance curve must be determined specifically for the geometry of interest [5].

8.1.2 The Modified J: J_M A significant step in developing a geometry independent R-curve came from the work of Ernst [6] in which he suggested a modified J parameter, J_M , which could be used to characterize the R-curve behavior.

The modified J, J_M , is defined as

$$J_M = J - \int_{a_o}^a \frac{\partial(J-G)}{\partial a} \Big|_{\Delta_{pl}} da \quad (8.9)$$

where J = current value of the deformation theory based J-integral

G = linear elastic energy release rate ($G = K^2/E = J_{el}$)

Δ_{pl} = plastic part of the load point displacement ($\Delta_{pl} = \Delta - \Delta_{el}$)

At first Ernst had produced equations that were specific to certain geometries and the following equation for the compact specimen is perhaps best known.

$$J_M = J + \int_{a_o}^a \frac{1+0.76 b/W}{b} J_{pl} da \quad (8-10)$$

where J_{pl} = plastic component of deformation theory J

b = current value of the remaining ligament.

Recently, more detailed studies have led to an equation for modified J that is simpler, yet generalized to encompass all geometries [7]

$$J_M = G + \int_0^{\Delta_{pl}} \frac{\eta_{pl}}{\beta b} P d\Delta_{pl} \quad (8.11)$$

where the plastic eta, updated for crack growth, is a function of geometry and material work hardening via Ramberg-Osgood n values. The equations to determine plastic eta (η_{pl}) are presented for various geometries in table 8.1, using the fully plastic solutions of J tabulated in Shih's Handbook [8]

Typically modified J and deformation theory J are nearly equal in value in compact specimens up to about 10% of slow stable crack growth. Hence, for geometries with large ligaments or for materials that suffer only small relative slow stable growth there is complete interchangeability between modified J and deformation theory J based R-Curves. For small compact specimens with correspondingly small remaining ligaments, however, R curves differ considerably when J_M or J is used. For example, experiments on 1/2" Compact Specimens reveal that J_R values depart from data of large specimens after only 0.05 inch(1.27mm) of crack growth (Fig.8.3)

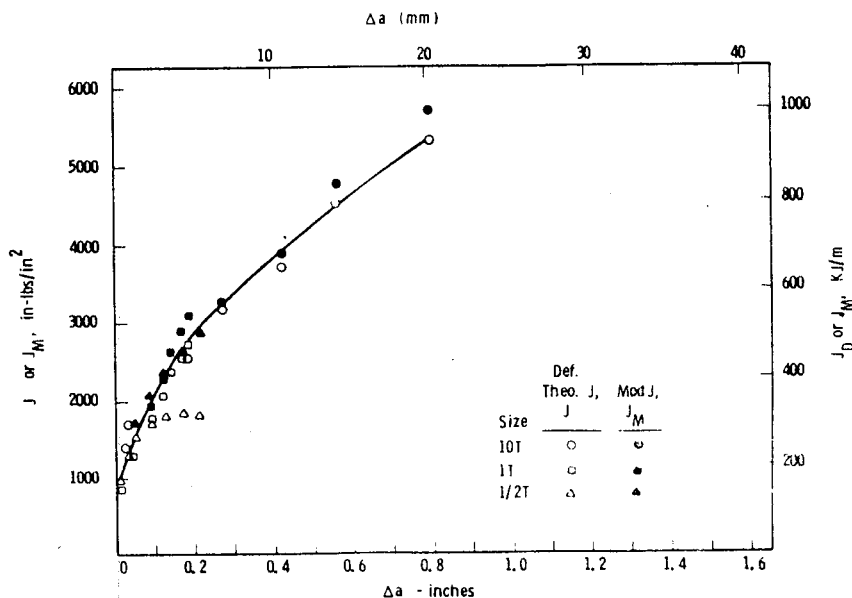


Fig.8.3: R-curve using J and J_M for three sizes of compact specimen 20% side groove [9]

Table 8.1: Summary of Δ_{p1} solutions to be used in eq.8-11

Specimen type	η_{p1} expression*	Numerical Examples			
		a/W=.50		a/W=.625	
		n=5	n=10	n=5	n=10
C(T) plane stress	$0.934 \left(\frac{1}{\alpha}\right) \left(\frac{b}{a}\right) (N+1) \frac{h_1}{h_3}$	2.27	2.34	2.28	2.27
C(T) plane strain	$0.687 \left(\frac{1}{\alpha}\right) \left(\frac{b}{a}\right) (N+1) \frac{h_1}{h_3}$	2.31	2.42	2.39	2.40
M(T)(or CCP) plane stress	$(N+1) \frac{b}{W} \frac{h_1}{h_3}$.920	.907	.832	.872
M(T)(or CCP) plane strain	$0.866(N+1) \frac{h_1}{h_3} \frac{b}{W}$.806	.910	.795	.854
DE(T)(or DEN) plane stress	$0.866(N+1) \frac{h_1}{h_3}$.779	.797	.751	.868
DE(T)(or DEN) plane strain	$\frac{(N+1)}{0.36W/b+0.91} \frac{h_1}{h_3}$.641	.534	.563	.546
SE(T)(or SEN) plane stress	$0.933 \frac{1}{\alpha} \frac{b}{W} (N+1) \frac{h_1}{h_3}$	2.27	2.29	2.39	2.35
SE(T)(or SEN) plane strain	$0.687 \frac{1}{\alpha} \frac{b}{W} (N+1) \frac{h_1}{h_3}$	2.21	2.29	2.36	2.34
SE(B)(or BEND) $\frac{S}{W}=4$, plane stress	$0.933 \frac{S}{a} (N+1) \frac{h_1}{h_3}$	1.95	1.90	1.98	1.92
SE(B) (or BEND) $\frac{S}{W}=4$, plane strain	$0.687 \frac{S}{a} (N+1) \frac{h_1}{h_3}$	1.89	1.85	1.93	1.89

* $\alpha' = \{1+(a/b)^2\}^{1/2} - a/b$; $\alpha =$ as given in eq.7.25

S = span ; h_1 and h_3 as given in Shih's Handbook [8] ; N = 1/n ;

8.1.3 J-R Curve: The Resistance curve represents a locus of equilibrium conditions where the crack will remain stable if the loading is stopped, and where the applied crack driving force is equal to the crack growth resistance of the material [10]. In order to justify the use of R-curve in design or for instability analysis its independence from initial crack size and/or plan view size and loading mode should be investigated. Limited amount of experiments indicate, indeed, to this independence.

Side grooving seems to be necessary to induce plane strain constraint. It is advocated in J-R testing for two principal reasons: (1) The crack front curvature which develops when side grooves are not used is usually accompanied by lack of agreement between the crack size from partial-unloading compliance and the crack size from a nine point average obtained by heat tinting and optical measurements. (2) The lagging regions of a curved-crack front tend to elevate the slope of the J-R curve [11]. It is not known in detail how much the side groove depth, root radius, flank angle affect the R-curve. Available data is mostly on Compact specimens, but no systematic differences can be observed. Convenience dictates 45° included angle with a tip radius of 0.5mm ± 0.25mm. 20% side grooves (10% on each face) are reported to lower the average slope of the R curve by 20-40 percent [12,13].

In side-grooved specimens or thicker specimens, the extending crack front remains straight and the fracture surfaces are macroscopically flat. Correspondingly, the J_R curves appear to approach a limiting lower bound curve with increasing specimen dimensions. Typically

$$\frac{b}{R_{Net}} < 1 \quad (8.12)$$

seems to be a sufficient constraint for specimens of the same geometry. Figure 8.3 indicates that specimen size does not affect R-curve if sufficient constraint, such as eq.8.12, is introduced.

When different loading modes are compared, creating equal specimen ligament dimensions may not develop equal constraint in all cases. It is well known that the remaining ligament requirements for J controlled deformation in tension are about one order of magnitude larger than in bend. It is not clear yet how to manage "equal constraint" in different loading modes.

In the case of thin plates in plane stress, initial crack size or the panel width does not affect the R-curve [7]. The dominant loading on the remaining ligament (tension/bending) is also ineffective. In single edge notched specimens subject to remote tension, the loading in the remaining ligament changes from pure tension to pure bending as the crack length changes from zero to panel width. Figure 8.4 illustrates the independence of the R curve from the loading mode by varying the bend stress-to-tension stress ratio from 9/1 to 1/1 by geometry changes.

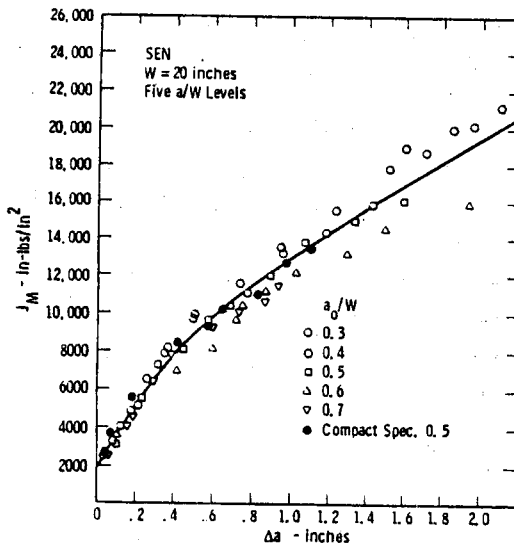


Fig.8.4: R-Curve for 20 inches wide SE(T) specimens [7]

J_R -curve data from tests with center cracked panels are generally higher than the corresponding data from similar sized compact specimens or single edge notched specimens (Fig.8.5). With increasing panel dimensions, the slope of the J_R data decreases and the R-curves seem to approach the plane strain curves from the compact specimens. This apparent loading mode dependence is specific to center cracked panel geometry. Center cracked panel is not representative of tensile loading. Because of its unique slip line deformation characteristics (cf. Fig.7.9) it generates inflated toughness values. Another geometry reflecting pure tensile loading is the double edge notched panel in tension. The R curve results of DE(T) specimens are in complete agreement with other specimen types (Fig.8.6) which support the idea that R curves are invariant provided

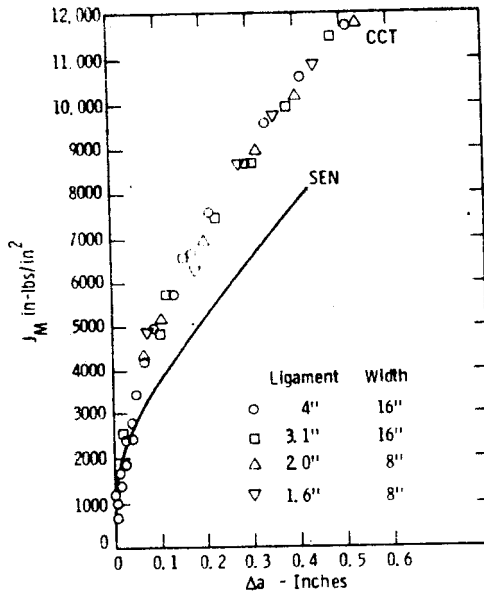


Fig.8.5: R-Curve for center cracked tension specimen as compared to that of single edge notched specimen [7]

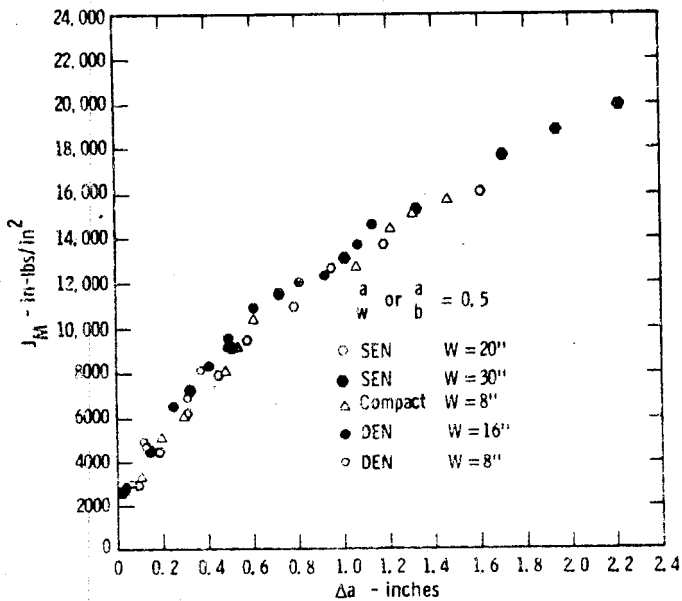


Fig.8.6: R curve data for three specimen types [7]

J_M is used and M(T) geometry excluded.

8.1.4 Instability: Once the existence of J_R -curve is justified (i.e. that there exists indeed a J controlled crack growth regime), the question centers on at which point of this R curve unstable crack propagation will intervene. The applied J is a function of load P (or displacement Δ) and the current crack length a

$$\left. \begin{array}{l} J = J(P, a) \\ \text{or } J = J(\Delta, a) \end{array} \right\} \equiv J_{\text{applied}} \quad (8.13)$$

whereas the resistance curve is a material property and a function of crack extension Δa , only.

$$J_R = J_R(\Delta a) \equiv J_{\text{material}} \quad (8.14)$$

At the point of instability

$$J_{\text{applied}} = J_{\text{material}} \quad (8.15)$$

$$\text{and } \frac{d}{da} J_{\text{applied}} = \frac{d}{d \Delta a} J_{\text{material}} \quad (8.16)$$

That is, up to the instability point any sufficiently small accidental advance of the crack due to some disturbance will result in a J value that falls below that required for continued advance. Unstable propagation results when applied J increment exceeds the incremental increase in resistance. If one regards crack length change, da , as a displacement, J_{applied} takes on the connotation of a generalized force and J_{material} may be regarded as the material resistance to that force [14]. Consequently, eq.8.15 is a statement of equilibrium with respect to crack extension and eq.8.16 is the stability criterion. It is a generalization of Irwin's resistance curve approach for small scale yielding (Fig.5.30).

Crack growth instability depends on the total system of which the component containing the crack may be a single member. To observe this, it is worthwhile to examine the expressions closer. The rate of change of the applied J in eq.8.16 is with the total displacement, $-T$, held fixed (or with other similar conditions specified). Thus, it can be written as

$$\frac{dJ_{\text{applied}}}{da} = \left(\frac{\partial J_{\text{applied}}}{\partial \Delta} \right)_a \left[\frac{\partial \Delta}{\partial a} \right]_{\Delta_T} + \left(\frac{\partial J_{\text{applied}}}{\partial a} \right)_{\Delta} \quad (8.17)$$

or

$$\frac{dJ_{\text{applied}}}{da} = \left(\frac{\partial J_{\text{applied}}}{\partial P} \right)_a \left[\frac{\partial P}{\partial a} \right]_{\Delta_T} + \left(\frac{\partial J_{\text{applied}}}{\partial a} \right)_P \quad (8.18)$$

Specifically,

$$\Delta_T = \Delta + C_M P = \text{constant} \quad (8.19)$$

where C_M is the compliance of the structure, thought as a spring in series with the specimen. Taking $\Delta = \Delta(P, a)$ implies

$$d\Delta_T = \left(\frac{\partial \Delta}{\partial P} \right)_a dP + \left(\frac{\partial \Delta}{\partial a} \right)_P da + C_M dP = 0$$

$$\left(\frac{\partial P}{\partial a} \right)_{\Delta_T} = \frac{-(\partial \Delta / \partial a)_P}{C_M + \left(\frac{\partial \Delta}{\partial P} \right)_a} \quad (8.20)$$

Or taking $P = P(\Delta, a)$

$$d\Delta_T = d\Delta + C_M \left[\left(\frac{\partial P}{\partial \Delta} \right)_a d\Delta + \left(\frac{\partial P}{\partial a} \right)_{\Delta} da \right] = 0$$

$$\left(\frac{\partial \Delta}{\partial a} \right)_{\Delta_T} = \frac{-C_M (\partial P / \partial a)_{\Delta}}{C_M \left(\frac{\partial P}{\partial \Delta} \right)_a + 1} \quad (8.21)$$

Equations 8.20 and 8.21 substituted into eq.8.18 and 8.17 express explicitly the dependence of instability on system(machine) compliance. Different approaches to the application of eq.8.16 have been proposed. These are discussed in the following:

(i) Tearing Modulus Criterion: Paris et.al. [15] defined, for convenience, the tearing modulus T as

$$T_{\text{applied}} = \frac{E}{\sigma_0^2} \left(\frac{dJ_{\text{applied}}}{da} \right) \quad (8.22)$$

and

$$T_{\text{material}} = \frac{E}{\sigma_0^2} \left(\frac{dJ_{\text{material}}}{d\Delta a} \right) \tag{8.23}$$

where E is elastic modulus and σ_0 the flow stress. Then the stability criterion, eq.8.16, may be expressed in nondimensional terms by

$$T_{\text{applied}} \begin{matrix} < \\ = \\ > \end{matrix} T_{\text{material}} \quad \begin{matrix} \text{stable} \\ \text{indifferent} \\ \text{unstable} \end{matrix} \tag{8.24}$$

T_{material} is formed from the slope of the J_R curve at a given level of J. Thus,

$$T_{\text{material}} = T_{\text{material}}(J)$$

Making use of eq.8.13,

$$T_{\text{applied}} = T_{\text{applied}}(J, a)$$

Thus, both T_{applied} and T_{material} may be thought of as functions of J, where increasing J is viewed as the variable indicating increasing load or deformation applied to the body. A crack stability diagram in the form of J as a function of T plot is shown to be useful in demonstrating safe levels of loading(applied J) by comparison with the material J_R curve, reduced on to the same diagram. As shown in figure 8.7, J versus T_{material} curves all reflect concave upward behavior, T_{material} decreasing monotonically with J. It remains to determine the $T_{\text{applied}}(J)$ curve to

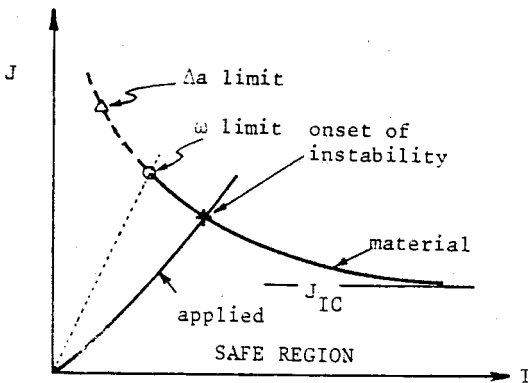


Fig.8.7: Tearing Instability for stable crack growth

locate the intersection of the two curves which uniquely indicates the onset of instability. In certain cases like the deeply cracked compact specimen in a rigid testing machine, T_{applied} is negative and crack growth is always stable (i.e. T_{applied} curve is to the left of the ordinate).

J versus T diagram turns out to be more meaningful than eq.8.24 since T_{material} as well as T_{applied} are not constant. In most of early work, including the original paper of Paris [15], T_{material} values are based on the early (straight) portion of the J_R curve. Joyce et.al [16] suggest that taking a least squares slope of J_R -curve over an extended crack growth range (between 0.15mm and 5mm) gives better results. Nevertheless, T_{material} values at a point of the J_R curve (usually from the early portion of the resistance curve) are well suited for comparative purposes; $T > 100$ implies a high degree of stability against tearing for all crack configurations whereas $T < 10$ almost guarantees tearing instability in some configurations — such as double edge cracked panel — as soon as J_{IC} and limit load are reached [15]. Pipe fracture experiments [17,18] represent an important step forward in the assessment of structures using tearing modulus concept.

The validity of J versus T format is limited by the conditions of J-controlled growth, eq.8.1 and 8.6. Thus, the lower of

$$\Delta a \ll b$$

and

$$\frac{J_{\text{material}}}{T_{\text{material}}} = \frac{J \sigma_0^2}{E(dJ/da)} = \frac{\sigma_0^2 b}{E \omega}$$

with the smallest acceptable ω will be an upper bound to valid J- T_{material} curve (Fig.8.7).

The use of tearing modulus concept certainly does not bypass the need to evaluate J as a function of both load and crack size, which is the major difficulty in stability analysis. Also the limited geometry dependence of the J_R -curve is carried over to tearing modulus; compact tension is reported to give a lower bound value of T_{material} [19]. A drawback of J vs. T plot is that it does not readily reveal how much increase in load or crack size it takes to reach the instability point. In geometries and

stress fields where J_{applied} is sensitive to crack size, small changes in crack size—which may be within the uncertainty range—could shift the conditions from $T_{\text{applied}} < T_{\text{material}}$ to $T_{\text{applied}} > T_{\text{material}}$.

R-curves plotted with J_M are not subject to the same limitations imposed on the traditional deformation J-R curve representation. Compact specimen data plotted on J-T and J_M-T_M format are shown in figure 8.8 for comparison. The advantage of the modified J is evident as all data points fall into one curve when J_M and T_M are used.

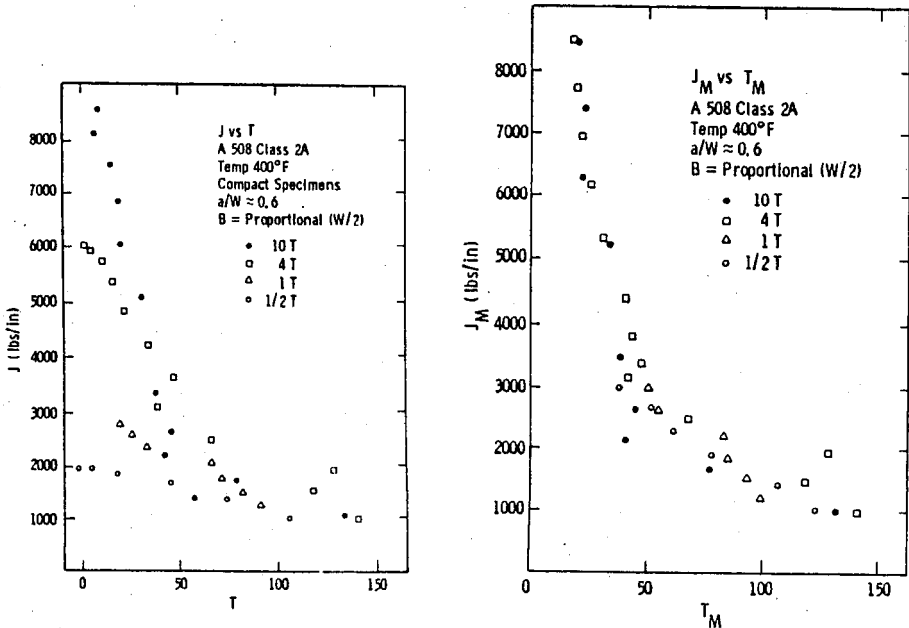


Fig.8.8: Test Results of A508 Class 2 steel at 400°F converted into (a) J versus T (b) J_M versus T_M plots [10]

Ernst [20] approached the instability condition from a different point of view, as well. Analyzing the load-load point displacement record of a structure he showed that instability condition

$$T_{\text{applied}} \geq T_{\text{material}}$$

is equivalent to

$$-\frac{dP}{d\Delta} \geq K_M \quad (8.25)$$

where K_M is the stiffness of the machine ($= C_M^{-1}$) i.e. of the spring in series with the structure/specimen. This relation of eq(8.25) is well known from literature on the common tension test.

(ii) EPRI Estimation Scheme: Shih et.al. [3] use the original format of J_R vs. a to estimate the point of instability. They promote the finite element method based procedure to determine $J = J(P, a)$ which is discussed in Sec.7.2.3, and plot J_{applied} , which they call the crack driving force, for several values of loading. In figure 8.9, the crack driving forces for two limiting situations are depicted. The solid lines correspond to the variation of the driving forces with crack length with the load held fixed (i.e. $C_M = \infty$) while the dashed lines are driving forces with the load line displacements Δ held fixed (i.e. $C_M = 0$).

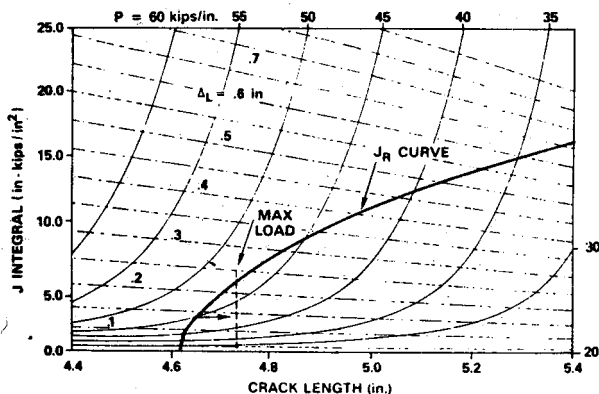


Fig.8.9: A typical J integral crack driving force diagram for A533B steel [3]

Such diagrams are useful for estimating the load carrying capacity and the deformation behavior of the structure. In the analyses of the extent of stable crack extension and the onset of instability, it is only necessary to construct one set of crack driving force diagrams corresponding to the actual loading applied by the system. For example, figure 8.10 shows the crack driving force diagram for an A533B 4T compact specimen subject to fixed grip loading (i.e. $C_M = 0$ or $\Delta = \Delta_T$). The experimentally

determined J_R -curve is superimposed on the diagram at an initial crack length of 4.615 in. Crack growth in this configuration will clearly be stable since the driving force decreases with increase of crack length while the J_R curve rises rapidly with crack growth. In other words, the instability condition posed by eq.8.16 or eq.8.24 cannot be met in this configuration. This can be observed by sliding the J_R -curve along the crack length axis to correspond to different initial crack sizes.

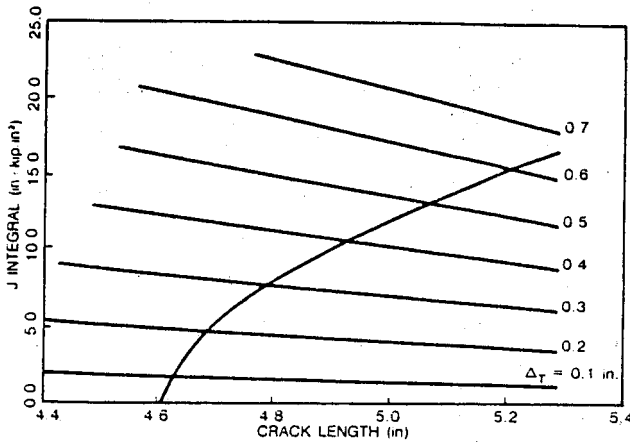


Fig 8.10: Crack driving force diagram for fixed grips [3]

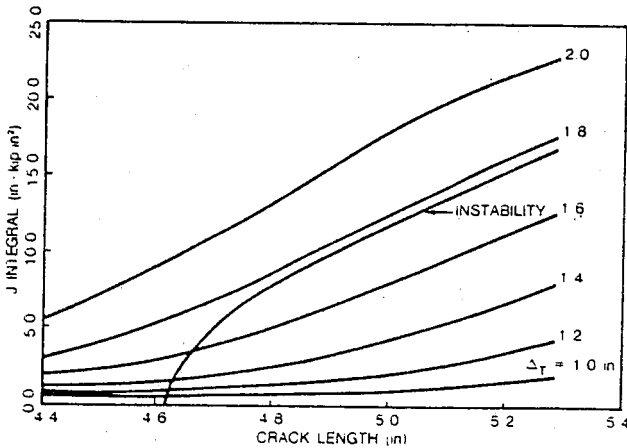


Fig.8.11: Crack driving force diagram for soft load system,
 $EBC_M = 1000$ [3]

The crack driving force in a soft loading system ($EBC_M=1000$) acting on the compact specimen is displayed in figure 8.11. The driving force corresponds to total displacement $\Delta_T (= \Delta + C_M P)$ held fixed and the value of Δ_T is indicated. From this diagram, it is clear that a 4T A533B compact specimen with an initial crack length of 4.615 in. will withstand about 0.4 in. of stable growth, reaching a J value of about 12 000 in-lb/in². The applied load at instability is about 42 000 lbs per unit thickness.

The crack driving force diagram for an infinitely soft system (i.e. $C_M = \infty$ or dead load system) is shown in figure 8.12. For the dead load situation, the crack will grow stably for about 0.12 in, instability occurring at an applied load per unit thickness of 47 000 lb/in and a J value of 6000 in-lb/in².

The three examples illustrate that the extent of stable growth is strongly dependent on the loading system and the material properties. The

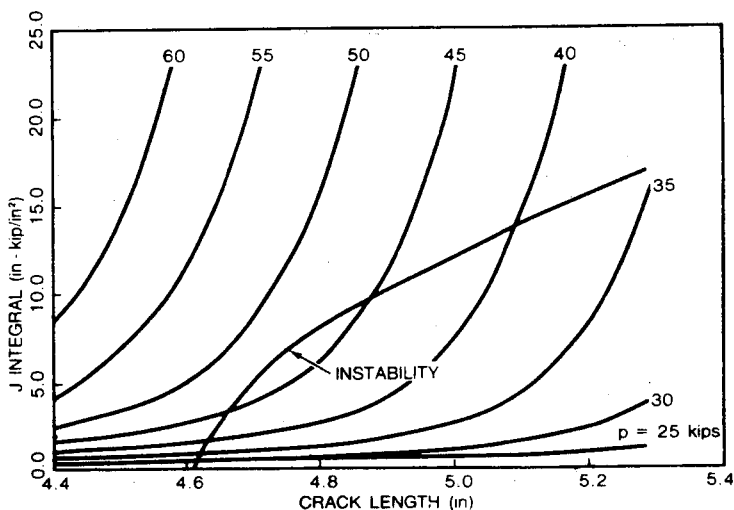


Fig.8.12: Crack driving force diagram for dead load system, the applied load values being indicated in the figure [3]

amount of stable growth decreases with increasing compliance; the values of J, T and the applied load at instability also depend on the compliance of the loading system. The EPRI scheme (crack driving force diagram) is really a procedure to obtain a graphical solution to crack growth stability as posed by eq.8.16 and eq.8.24.

8.1.5 The Crack Tip Opening Angle: Just as the initiation of crack growth can be characterized by a critical value of the crack tip opening displacement δ_t , the subsequent resistance to crack extension may be expressed through a δ_t - Resistance Curve. Using the definition of figure 7.11, δ_t and J were shown to be interrelated through

$$\delta_t = d_n \frac{J}{\sigma_o} \quad (7.18)$$

where d_n is a function of the material properties and is plotted in figure 7-12. Furthermore, the tearing modulus based upon δ_t can be defined as

$$T_\delta = \frac{E}{\sigma_o} \frac{d\delta_t}{da} = \frac{nd_n}{n+1} T \quad (8.26)$$

and used for instability predictions just as the tearing modulus based on J. If the conditions of J controlled crack growth are satisfied (eq.8.1, 8.6) then J and CTOD (or T and T_δ) approaches are equivalent. J-dominance and J-control, however, are limited to small amounts of crack growth. The modified J, J_M is introduced to avoid this limitation. Another possibility to analyze extended crack growth seems to be the crack tip opening angle, CTOA, which is the local slope of the crack faces near the crack tip. A similar concept is the average crack opening angle (COA) which is the ratio of the crack opening displacement at the site of the initial crack tip to the current crack extension. While the critical value of the COA can be measured, it is difficult to see how its value has any direct connection with the fracture process [5].

CTOA exhibits a constant resistance value after an initial transient which makes it highly attractive when large amounts of crack growth must be considered [5, 21, 22]. Both finite element calculations and direct experimental evidence on aluminum and steel [23] have confirmed that CTOA is essentially constant after a certain transitional period (Fig. 8.13). The major disadvantage is that its experimental determination is difficult and the theoretical basis is not sufficiently well developed yet.

One attractive possibility is a two-criteria method. The J criterion would apply to initiation and a small amount of crack growth, with the CTOA criterion being used for extended amounts of growth. A key calculation is performed by Battelle Columbus Laboratories to predict the

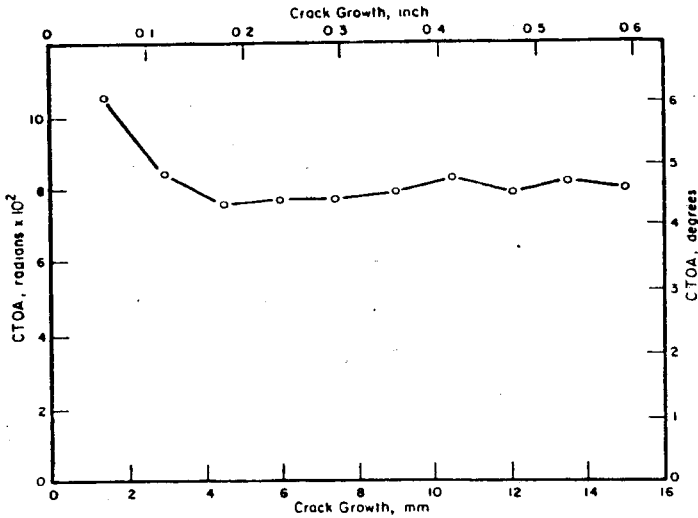


Fig.8.13: Crack-tip opening angle resistance curve generated from a Battelle CT specimen [23]

load-crack growth behavior in a wide center-cracked panel of 2219-T87 aluminum using several criteria determined from CT test results. The results are shown in figure 8.14. The combined J/CTOA approach is clearly the most accurate.

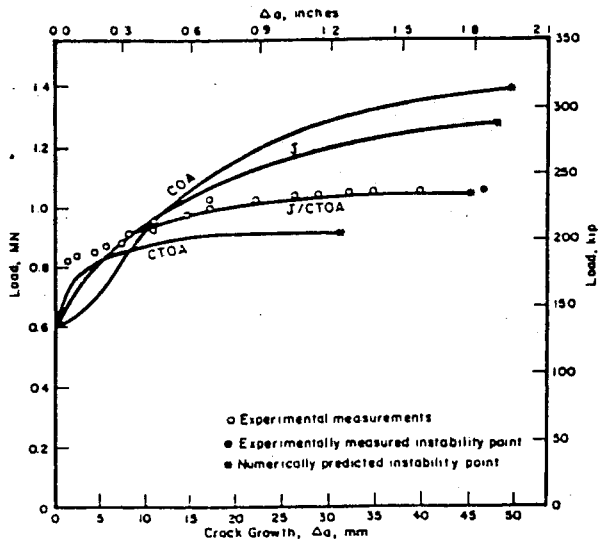


Fig.8.14: Critical comparison of fracture criteria [23]

In the combined J/CTOA approach, the deformation theory J Resistance curve is used for initiation and some amount of stable crack growth with an internally computed CTOA-value used thereafter. Thus, full advantage of the R-curve approach is taken without suffering from its restriction to small amounts of crack growth. It also uses the observed constancy of CTOA while avoiding the complications of the initial transient in this parameter. Yet, because the critical CTOA to be used for extensive growth is one that is calculated during the early stages of crack growth, the combined parameter approach does not require any further experimental measurements. The numerical calculations, however, need finite element routines and are sensitive to the near-tip element type and size.

8.2 The Failure Assessment Diagram

Both the J_{IC} based initiation and the J_R based instability evaluations for ductile fracture are quite sophisticated techniques. A simpler engineering procedure has been developed to assess the integrity of typical structures in industry, namely the Failure Assessment Diagram approach.

The underlying principle of the failure assessment diagram is two-criteria approach of Dowling and Townley, which states that structures will fail by either of two mechanisms - linear elastic (brittle) fracture or plastic collapse (Fig.7.2). These two mechanisms are connected by a transition curve which allows one to go directly from LEFM behavior to plastic instability.

8.2.1 The R-6 Failure Diagram: The transition curve that the British Central Electricity Generating Board (CEGB) adopted is based upon the Dugdale strip yield model. The "safety/failure" plane is defined by normalized stress intensity factor

$$K_r = K_I / K_C \quad (8.27)$$

and the normalized applied stress

$$S_r = \sigma / \sigma_1 \quad (8.28)$$

where K_C is the fracture toughness and σ_1 is the plastic collapse stress based on flow stress σ_0 . The failure assessment line (a failure envelope) for elastic-perfectly plastic center cracked infinite plates (known as R-6 curve of CEGB, and shown in figure 8.15) is obtained from the COD concept of sec.7.4. Crack initiation condition

$$\delta_t = \delta_{tc}$$

is cast by Harrison, Luxmoore and Milne [24] into the form

$$K_r = S_r \left[\frac{8}{\pi^2} \ln \sec\left(\frac{1}{2}S_r\right) \right]^{-1/2} \quad (8.29)$$

If the coordinates corresponding to a particular stress level and flaw size (the assessment point) lies on or outside of this failure assessment line, crack growth will initiate; if the point is inside this curve, the structure is safe from the initiation of crack growth. Increased loading is represented by a ray from the origin with the equation

$$K_r/S_r = \text{constant.}$$

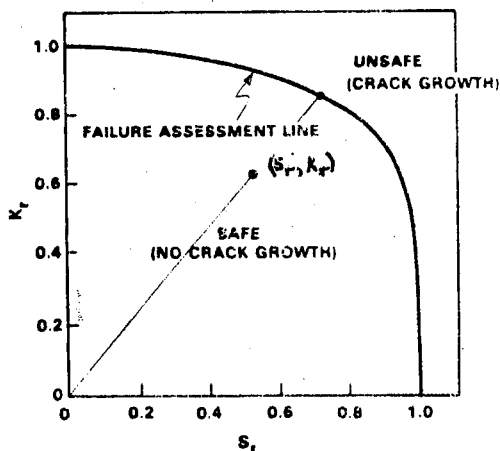


Fig.8.15: R-6 failure assessment Diagram

The position of any point along this loading line (S_r, K_r) relative to failure assessment curve gives the margin of that point with respect to initiation. This procedure works well for cleavage fracture as well as ductile fracture, up to the point of crack initiation [25], in spite of its limitations. Major shortcomings are:

- 1- The strip yielding plastic zone may be an unrealistic physical representation of real plastic zones
- 2- The model is derived only for infinite plate geometry and should not, therefore, be applied to real physical geometries of complex shape.

It should be remembered, however, that the CEBG procedure is developed to solve practical problems with all their concomitant uncertainties. Theoretical rigor is sacrificed for practical convenience, and good results are achieved on ferritic structures. Stainless steels with their high

strain hardening capacity need modified procedures. For materials with a high capacity for strain hardening, use of a flow stress criterion together with the R-6 diagram can be nonconservative at stress levels close to general yield. This may be avoided either by using a yield stress criterion or by using an assessment line which incorporates strain hardening effects. The yield stress criterion is the simplest to apply, requiring no adjustment of the assessment line, but it may be highly pessimistic.

8.2.2 Deformation Plasticity Based Failure Diagram: The deficiencies of the CEBG failure assessment procedure can be reduced by expressing K_r in terms of the J-integral, and using the estimation scheme of Shih et.al. (based on Ilyushin's principle) discussed in sec.7.2.3. The crack initiation condition

$$J = J_{IC} \quad (8.30)$$

can be cast into the form

$$\sqrt{\frac{J_{e1}}{J}} = \sqrt{\frac{J_{e1}}{J_{IC}}} \quad (8.31)$$

Parallel to R-6 curve approach, the right-hand side of this expression is

$$\sqrt{\frac{J_{e1}}{J_{IC}}} = \sqrt{J_r} = K_r \quad (8.32)$$

whereas the left-hand side can be expanded using

$$\begin{aligned} J &= J_{e1} + J_{p1} = \hat{J}(a_e) \left(\frac{P}{P_0}\right)^2 + \hat{J}(a,n) \left(\frac{P}{P_0}\right)^{n+1} \\ &= \hat{J}(a_e) S_r^2 + \hat{J}(a,n) S_r^{n+1} \end{aligned}$$

where \hat{J} are functions independent of load, reflecting the geometry and strain hardening. Note that

$$S_r = \frac{\sigma}{\sigma_1} = \frac{P}{P_0} \quad (8.33)$$

is kept the same as in R-6 procedure. Now eq.8.30 or its equivalent eq. 8.31 can be expressed as

$$f(S_r) = K_r \quad (8.34)$$

where

$$f(S_r) = \left\{ \frac{\hat{J}(a_e) S_r^2}{\hat{J}(a_e) S_r^2 + \hat{J}(a, n) S_r^{n+1}} \right\}^{1/2}$$

Eq.8.34 represents the locus of the failure points satisfying condition $J = J_{IC}$, and is referred to as the deformation plasticity based failure assessment curve [26-28]. R-6 curve is just a special case of the above relationship. For strain hardening materials, these failure assessment curves do not intersect the abscissa at unity but approach the abscissa asymptotically (Fig.8.16). Any applied loading being a ray from the

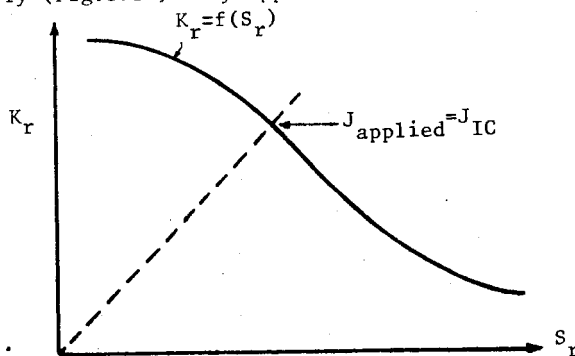


Fig.8.16. Schematic of failure assessment diagram based on deformation plasticity (initiation only) origin, reaches the crack initiation point when $J_{\text{applied}} = J_{IC}$, i.e. when the two curves in figure 8.16 intersect. To avoid the physically unacceptable asymptotic behavior observed in Fig 8.16, Bloom has introduced a cut-off based upon the plastic collapse stress calculated using the ultimate tensile strength.

In figure 8-17 the failure assessment curve is depicted for a center cracked panel in plane strain for different values of the hardening exponent. As the hardening exponent increases (strain hardening decreases) these failure curves move closer to the R-6 curve. Materials which strain harden and eventually reach a saturation stress σ_s can be represented by

[27]

$$\frac{\epsilon}{\epsilon_0} = \frac{\sigma}{\sigma_0} + \alpha \left(\frac{\sigma}{\sigma_0}\right)^n + \beta \left(\frac{\sigma}{\sigma_0}\right)^m \quad (8.35)$$

where α and β are material constants and $m/n \gg 1$. The failure diagram for such models (Fig.8.18) approach that of R-6.

In principle, new assessment curves should be generated for each specific α , n and crack and/or geometry. But, Bloom illustrated that by choosing the limit loads P_0 judiciously, failure assessment curves for a wide range of specimen geometries may be squeezed in a tight band slightly above the R-6 curve for $S_r < 1.1$ (Fig.8.19). Beyond $S_r = 1.1$ in the fully plastic region, the R-6 curve is, however, overly conservative

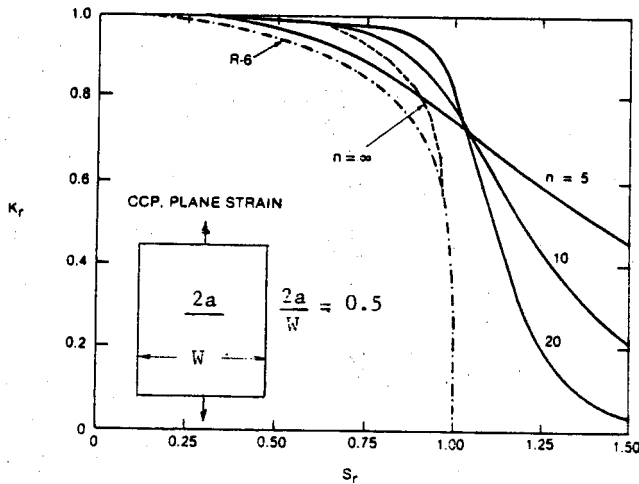


Fig.8.17: Typical failure assessment curves for power hardening materials [27]

since it does not account for the strain hardening behavior of the pressure vessel steel. The center-cracked plate failure curve could be used as a conservative basis for an engineering approach to failure assessment diagrams for pressure vessel steels.

The failure assessment procedure can be extended to account for stable crack growth (ductile tearing) beyond initiation. In this case $J_R (\equiv J_{\text{material}})$, the experimentally measured J resistance curve plotted

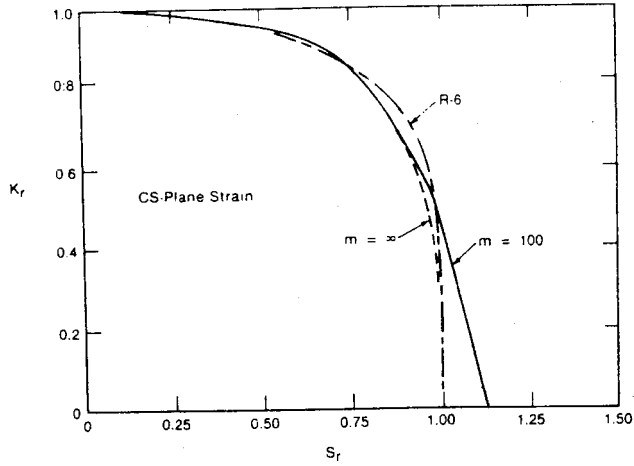


Fig.8.18: Failure curve for a material with a saturation stress which is 33% higher than the yield. Compact specimen, $n = 10$, $a/W = 0.5$ [27]

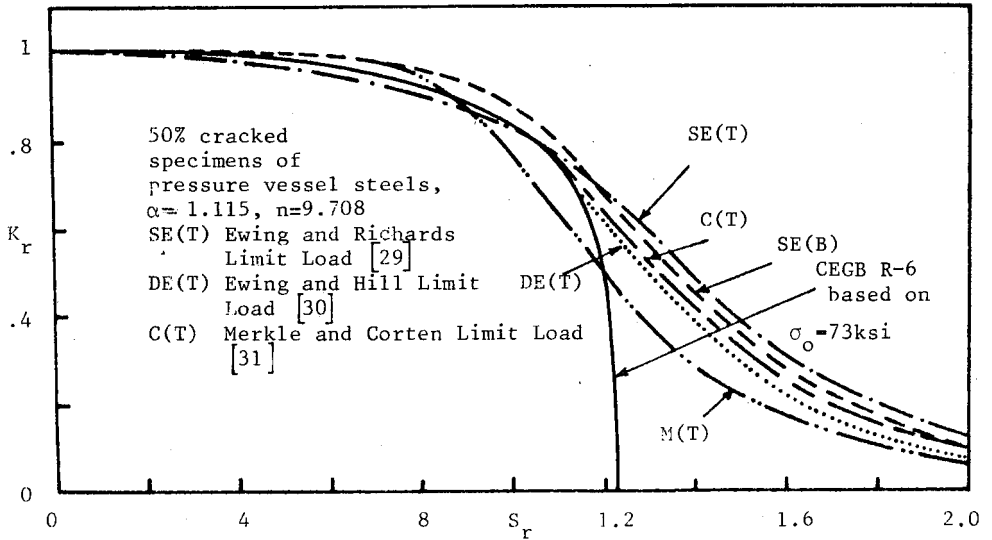


Fig.8.19: Comparison of various specimen configurations in terms of failure assessment diagrams [26]

as a function of slow stable crack growth, Δa) replaces J_{IC} and

$$K_R = \sqrt{\frac{J_{elastic}(a+\Delta a)}{J_R(\Delta a)}} = \sqrt{J_R}$$

$$S_R = \frac{\sigma}{\sigma_1(a+\Delta a)}$$
(8.36)

are used to represent the loading (assessment) point. The failure envelope (eq.8.34) is now the locus of points satisfying

$$J = J_R$$

To satisfy

$$\frac{dJ}{da} = \frac{dJ}{d\Delta a}$$

condition also, the path that the assessment point takes at loads P_x, P_y, P_z should be considered (Fig.8.20). This path is dictated by the R-curve of the material. The unique load level that develops tangency with the

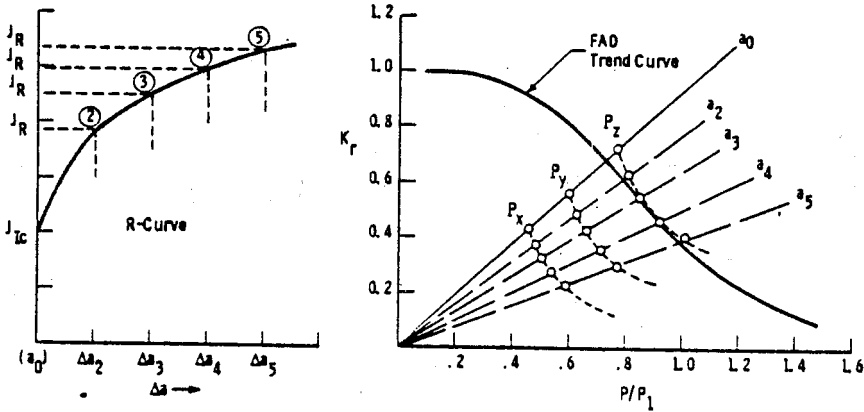


Fig.8.20: R-Curve modified FAD procedure for prediction of instability load. Trial values of P [32]

failure envelope (P_z in this case) is the load that will result in crack

instability. The factor of safety, which is the ratio between the instability load and the design load is again based on a simple linear dimension ratio except that it is made at the crack size for tangency (between a_3 and a_4 in figure 8.20).

Crack length-to-width (a/W) ratio dependence is weak in failure assessment curves, as shown in figure 8.21. In the analysis of small amounts of crack growth a failure curve based on a_0 may be sufficient. Thus, the application procedure of the failure assessment diagram including stable crack growth can be outlined as follows:

1- Failure curve is constructed based on initial crack length a_0 .

2- For the given crack configuration and a_0 , K is computed.

This value is normalized by J_{IC} or K_{IC} to obtain K_R . The stress ratio S_R is obtained by normalizing the applied load by the collapse load for the crack configuration being examined.

3- The point S_R, K_R is placed on the failure plane. If the point falls on or beyond the failure curve, the crack in the structure will initiate.

4- To evaluate the load carrying capacity of the structure further, the crack is incremented by an amount Δa . The collapse load is recomputed using $a_0 + \Delta a$. K is also recalculated and normalized by K_R (or J_R) corresponding to crack growth Δa , which is directly obtained from the resistance

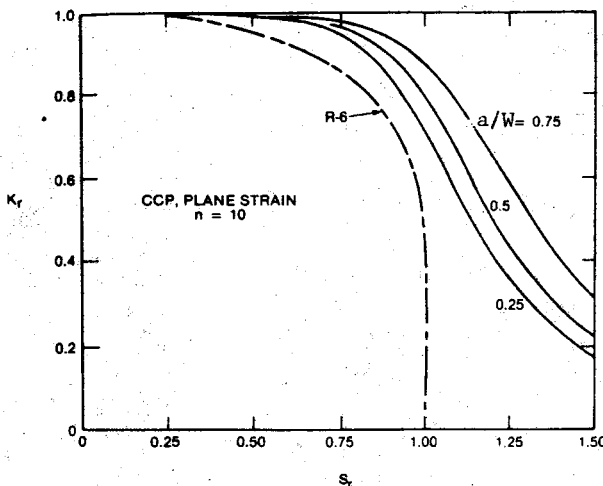


Fig.8.21: Failure diagrams for various a/W ratios [27]

curve for the material.

5- The updated (assessment) point S_r, K_r is again placed on the failure plane. Steps 4 and 5 are replaced until the assessment point falls on (and becomes tangent to) the failure curve.

The failure assessment diagram is an alternative presentation of certain information obtainable from the R-curve approach of sec.8.1.4. It is essentially a replotting scheme. But FAD curves are not a modified method of representing R-curves; they do not contain information on material toughness as a function of crack growth.

Experimental support to failure assessment diagram approach is provided through the guidance of ASTM E24.06.02 task group. Comparison of data with the derived failure curve is very satisfactory for both 2024-T351 aluminum and 304 stainless steel compact tension specimens (Fig.8-22,23).

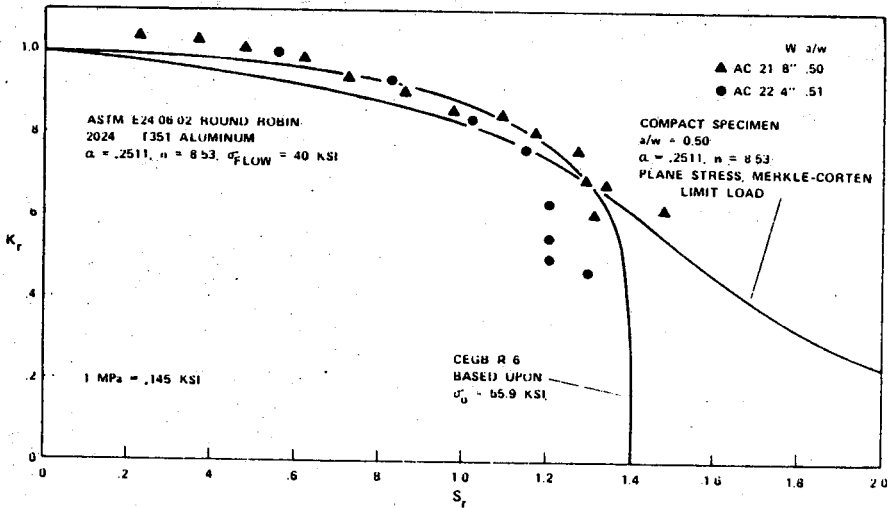


Fig.8.22: Failure Assessment of ASTM round robin Al-alloy specimens [28].

Although the failure assessment diagram offers a simplified procedure for a quick first evaluation of the safety margin of flawed structures subjected to load controlled boundary conditions, the procedure becomes more complex for displacement controlled systems [27].

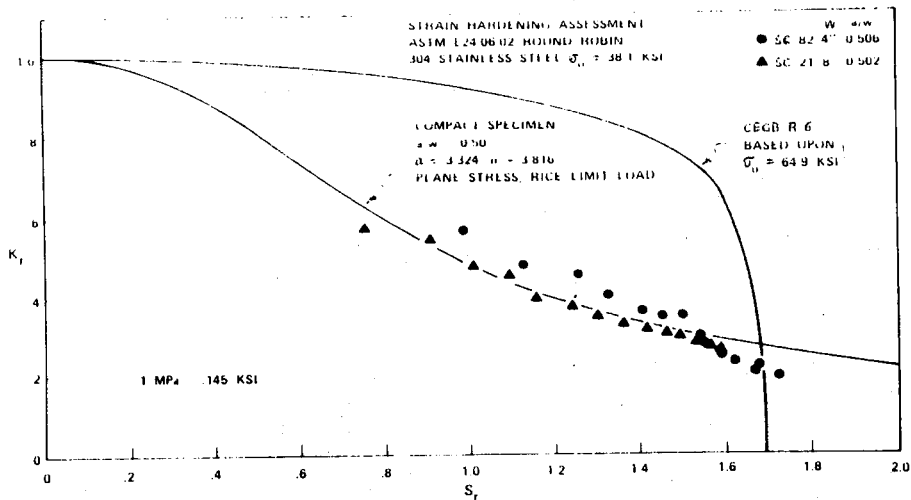


Fig.8.23: Failure assessment of ASTM round robin stainless steel specimens [28]

References

- 1- Hutchinson, J.W., "Fundamentals of the Phenomenological Theory of Nonlinear Fracture Mechanics" Journal of Applied Mechanics, Transactions ASME, 50 (1983), pp.1042-1051.
- 2- Hutchinson, J.W. and Paris, P.C., "Stability Analysis of J-Controlled Crack Growth" ASTM STP 668, Amer.Soc. for Testing and Materials, (1979), pp.37-64.
- 3- Shih, C.F., German, M.D., and Kumar, V., "An Engineering Approach For Examining Crack Growth and Stability in Flawed Structures" International Journal of Pressure Vessel and Piping, 9, (1981) pp.159-196.
- 4- Shih, C.F. German, M.D., Wilkinson, J.P.D. "Methodology for Plastic Fracture" Quarterly Review by General Electric Company for EPRI, RP 601-2 (1979).

5- Kanninen, M.F., Popelar, C.H., Broek, D., "A Critical Survey On the Application of Plastic Fracture Mechanics to Nuclear Pressure Vessels and Piping" Nuclear Engineering and Design, 67(1981) pp.27-55.

6- Ernst, H.A. "Material Resistance and Instability Beyond J Controlled Crack Growth" ASTM STP 803, Amer.Soc.for Testing and Materials (1983) pp.I.191-213.

7- Landes J.D., McCabe, D.E., Ernst, H.A., "Elastic Methodology to Establish R-Curves and Instability Criteria" Final Report, RP 1238-2 (1985). Westinghouse R and D Center.

8- Kumar, V., German, M.D., and Shih, C.F., "An Engineering Approach for Elastic-Plastic Fracture Analysis" GE Report to EPRI, RP 1237-1 (1981)

9- McCabe, D.E. and Landes, J.D. "J_R-Curve Testing of Large Compact Specimens" ASTM STP 803, Amer.Soc.for Testing and Materials (1983) pp.II.353-371.

10- Ernst, H.A. Landes, J.D. "Elastic-Plastic Fracture Mechanics Methodology Using the Modified J, J_M, Resistance Curve Approach" Journal of Pressure Vessel Technology, Transactions ASME, 108 (1986), pp.50-56.

11- Irwin, G.R. "Side Grooves" NUREG Report 0744, Appendix E1 (1982).

12- Loss, F.J. "Effect of Side Grooves on the R Curve: An Experimental Viewpoint" NUREG Report 0744, Appendix E11, (1982).

13- Davis, D.A., Vassilaros, M.G. and Gudas, J.P. "Specimen Geometry and Extended Crack Growth Effects on J_I-R Curve Characteristics for HY-130 and ASTM A533B Steels" ASTM STP 803, Amer.Soc.for Testing and Materials (1983), pp.II.582-610.

14- Paris, P.C. and Johnson, R.E., "A Method of Application of Elastic Plastic Fracture Mechanics to Nuclear Vessel Analysis" ASTM STP 803, Amer.Soc. for Testing and Materials (1983). pp.II-5-40

15- Paris, P.C., Tada, H., Zahoor, A., Ernst, H., "The Theory of Instability of the Tearing Mode of Elastic-Plastic Crack Growth" ASTM STP 668, Amer.Soc. for Testing and Materials (1979), pp.5-36.

16- Joyce, J.A., Vassilaros, M.G., "An Experimental Evaluation of Tearing Instability Using the Compact Specimen "ASTM STP 743, Amer.Soc. for Testing and Materials (1981), pp.525-542.

17- Zahoor, A., and Kanninen, M.F., "A Plastic Fracture Mechanics Prediction of Fracture Instability in a Circumferentially Cracked Pipe in Bending- Part 1: J Integral Analysis" Journal of Pressure Vessel Technology, Transactions ASME, 103(1981), pp.352-358.

18- Wilkowski, G.M., Zahoor, A., and Kanninen, M.F., "A Plastic Fracture Mechanics Prediction of Fracture Instability in A Circumferentially Cracked Pipe in Bending - Part II: Experimental Verification on a Type 304 Stainless Steel Pipe" Journal of Pressure Vessel Technology, Transaction ASME, 103 (1981), pp. 359-365.

19- Kaiser, and Carlsson, A.J. "Studies of Different Criteria for Crack Growth Instability in Ductile Materials" ASTM STP 803, Amer.Soc. for Testing and Materials (1983) pp. II-58-79.

20- Ernst, H.A., "Some Salient Features of the Tearing Instability Theory" ASTM STP 803, Amer.Soc. for Testing and Materials (1983), pp.II-133-155.

21- Marston, T.U., Jones, R.L., Kanninen, M.F. and Mowbray, D.F. "Development of a Plastic Fracture Methodology for Nuclear Systems" ASTM STP 803, Amer.Soc. for Testing and Materials, (1983), pp.II.115-132.

22- Kanninen, M.F. and Popelar, C.H. Advanced Fracture Mechanics Oxford University Press, New York (1985).

23- Kanninen, M.F., Hahn, G.T., Broek, D., Stonesifer, R.B., Marschall, C.W., Abousayed, I.S. and Zahoor, A "Development of a Plastic Fracture Methodology" Battelle's Columbus Laboratories Report RP 601-1, EPRI NP 1734 (1981).

- 24- Harrison, R.P., Loosemore, K., and Milne, I. "Assessment of the Integrity of Structures Containing Defects" CEGB Report R/H/R6 (1976).
- 25- Chell, G.G. and Milne, I., "Ductile Tearing Instability Analysis: A Comparison of Available Techniques" ASTM STP 803, Amer.Soc. for Testing and Materials (1983), pp.II-179-205.
- 26- Bloom, J.M., "A Procedure for the Assessment of the Structural Integrity of Nuclear Pressure Vessels" Journal of Pressure Vessel Technology, Transactions ASME, 105 (1983) pp.28-34.
- 27- Shih, C.F., Kumar, V., and German, M.D., "Studies on the Failure Assessment Diagram Using the Estimation Method and J-Controlled Crack Growth Approach" ASTM STP 803, Amer.Soc. for Testing and Materials (1983), pp.II-239-261.
- 28- Bloom, J.M. "Validation of a Deformation Plasticity Failure Assessment Diagram Approach to Flaw Evaluation" ASTM STP 803, Amer. Soc. for Testing and Materials (1983) pp.II-206-238.
- 29- Ewing, D.J.F. and Richards, C.E. "The Yield-Point Loads of Singly- Notched Pin Loaded Tensile Strips" Journal of the Mechanics and Physics of Solids, 22, (1974), pp. 27-36.
- 30- Ewing, D.J.F and Hill. R. "The Plastic Constraint of V-notched Tension Bars" Journal of the Mechanics and Physics of Solids, 15, (1967) pp.115.
- 31- Merkle, J.G. and Corten, H.T. "A J-Integral Analysis for the Compact Specimen, Considering Axial Force as Well as Bending Effects" Journal of Pressure Vessel Technology, Transactions ASME, 96(1974) pp.286-292.
- 32- Mc Cabe, D.E., Ernst, H.A. and Landes, J.D. "A Viewpoint on the Failure Assessment Diagram" 9th Semiannual Report, RP 1238-2, Westinghouse (1984).

Problems:

1- ASTM developed the E561 practice for use on high strength sheet material. It may be possible to extend its usage to more ductile structural grades of materials, as long as the component is stressed below net section yield. In the following you are asked to perform an instability analysis using the K_R curve concept for 7075-T651 Al-panel.

An interesting specimen developed to simulate the crack propagation in a stiffened panel is the so-called three-hole crack tension (THT) specimen. It is a panel subject to tensile loading with three circular holes and a crack emanating from one of the holes. The stress intensity factor is given by Newman [STP 896, 1985, p.64]:

$$K = \frac{P}{WB} \sqrt{\pi a} F$$

where

$$F = \sum_{i=1}^4 \sum_{j=1}^2 \frac{A_{ij} (1-a/b)^{-1/2}}{(1+a/r)^{i-1} \left\{ (y_0/x_0)^2 + (a/x_0 - 1)^2 \right\}^{\frac{j-1}{2}}} \quad (8.37)$$

$$A_{11} = 2.02, A_{12} = -9.17, A_{21} = -62.37, A_{22} = 287.72, A_{31} = 1025.8$$

$$A_{32} = -2845.1, A_{41} = -8270.6, A_{42} = 11927.3$$

and $r = 12.7 \text{ mm}$ (0.5 in), $b = 165 \text{ mm}$ (6.5 in), $X_0 = 63.5 \text{ mm}$ (2.5 in)

$y_0 = 50.8 \text{ mm}$ (2 in). The specimen proportions and the variation of $K/(P/WB)$ with a/W , for $W = 254 \text{ mm}$, is plotted in Fig. 8.24.

Estimate the load level at instability for a 254 mm wide, 12.7 mm thick THT panel containing a crack of 25 mm long, if K_R curve for 7075-T651 Aluminum is as given below, in Fig. 8.25.

Answer: $P = 675 \text{ kN}$

2- Using the load-displacement plot of problem 7-1, estimate J_M at station No. 18 assuming $n \approx 5$ and plane strain.

Answer: $J_M = 292 \text{ kg/mm}$

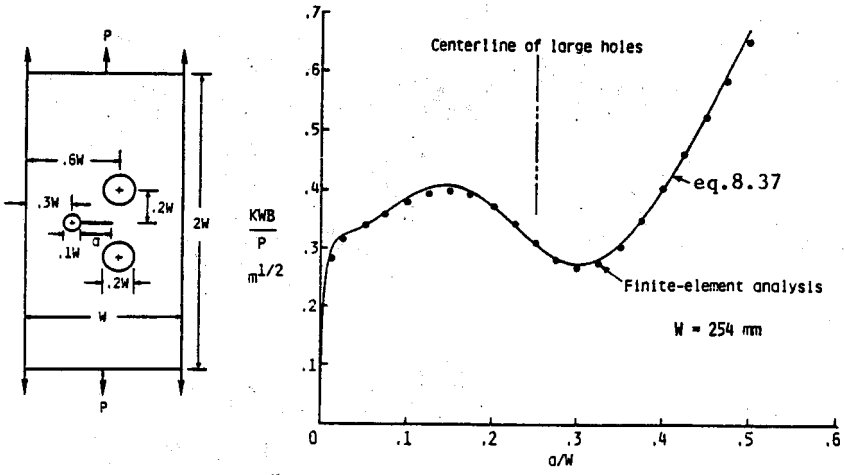


Fig.8.24

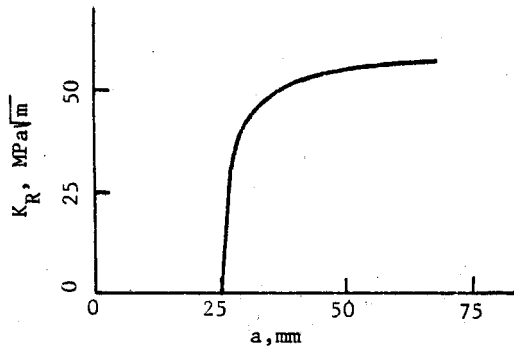


Fig.8.25

9. FATIGUE CRACK PROPAGATION UNDER CONSTANT AMPLITUDE LOADING

9.1 INTRODUCTION

Fatigue failure in engineering materials consists of three phases: initiation, propagation and final failure. The interphase between initiation and propagation is hard to define. Thus, the usual approach has been to assume one phase as dominating and study it alone. The traditional assumption, typical in machine design, of a defect free part regards the failure process as one of the crack initiation. This is an accurate and logically sound concept in small, carefully prepared components such as shafts or springs. However, in large structures and welded parts it is more realistic to assume the presence of a defect and determine how fast it grows. The life of such structures as aircraft, ships, bridges and off-shore drilling platforms are governed by the propagation of defects. This roughly represent the two different philosophies of design.

In safe-life approach parts are designed for a finite service life during which no significant damage will occur. No defects are assumed to be present in the new structure and no inspections are required during the design life. After reaching the life limit the part is retired from service.

In damage tolerance design an initial, rather large flaw is assumed to exist in the structure from Day 1- when it leaves the factory. In-service damage and damage that may occur during maintenance is also taken into account in evaluating the structure. The idea is to account for the assumed initial defects in such a way that they will not be allowed to go to "critical" during the life of the component. Airframe components, for example, are being designed according to damage tolerance concepts since 1970's. Now, even for engine components, the tendency is to shift to damage tolerance design and lifing procedures.

Components designed on the basis of safe life concept are observed frequently to have appreciable remaining life after being discarded. To avoid such inefficient usage of potential component life, Retirement-for-cause(RFC) lifing policy is instituted. It aims at running components beyond their declared safe-life until quantifiable damage has been

identified and rests on the principles of damage tolerance design philosophy.

In the absence of initial defects some 90% of the fatigue life is spent in the micro-range (Fig.9.1). That is, the fatigue damaging process is largely occurring in a very small volume of the material and it will be highly depending on local conditions. Hence such localized phenomena leads to considerable scatter. Crack propagation, however, depends on bulk properties only and exhibits much less scatter. In general, most of life is consumed during the early stages whether nucleation or macrocrack growth is considered (Fig.9.1). There are, however, certain practical and fundamental difficulties in extending fatigue design codes to include such small cracks. The practical difficulty relates to the NDI sizing limit – cracks being too small to be detected. The fundamental difficulties

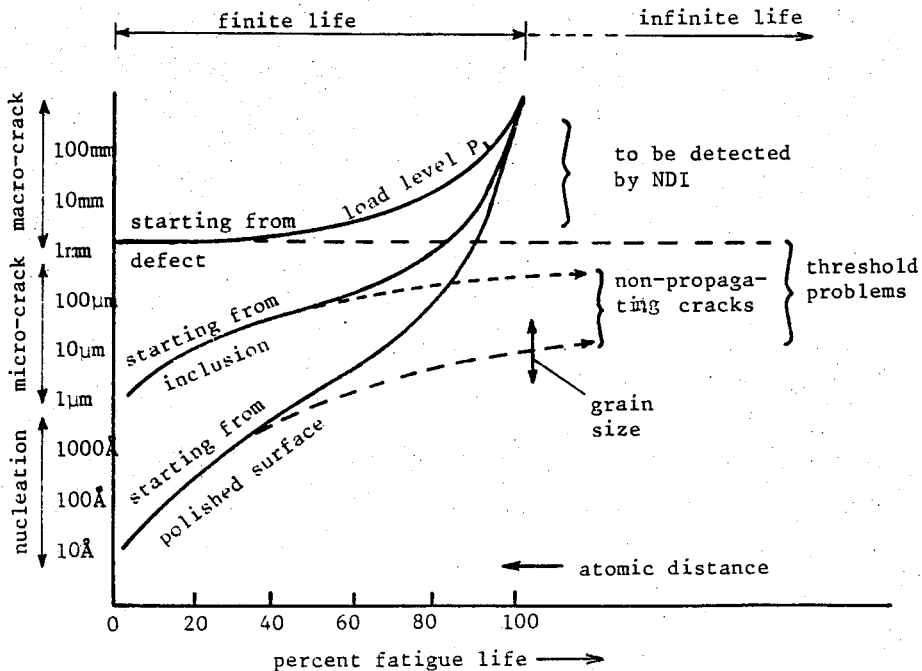


Fig.9.1: Survey of different crack growth cases [1]

arise from anomolous behavior of short cracks. Small cracks may exhibit growth rates several orders of magnitude greater than those of long cracks. Additionally, the restriction of LEFM – that the crack tip plastic

zone size should be much smaller compared to the crack size — is difficult to comply with. Microstructure starts to play a major role at such small sizes.

The fact that small cracks are usually at the vicinity of some stress raiser and engulfed completely within the plastic zone of this stress raiser complicates the issue further. In some cases EPFM should be drawn upon to analyze fatigue crack propagation rather than LEFM. These aspects — that of short crack and plastic crack — will be addressed later in the chapter, after the more common aspects of constant load amplitude situations are covered. Corrosion fatigue is not included, however, in the present chapter.

9.2 GENERAL CHARACTERISTICS

Typical constant amplitude (CA) loading is sketched in figure 9.2. The resulting crack growth rate (da/dN) is strongly dependent on crack length a and the stress range $\Delta\sigma$. The stress intensity factor, being a sufficient parameter to describe the whole stress field at the tip of a crack, is a natural candidate controlling the crack propagation rate. In fact in most engineering applications the nominal loads leading to fatigue failure are small with respect to yield or limit loads such that LEFM rightfully applies. It has been the celebrated experiments of Paris and Erdogan [2] which established the superiority of relations based

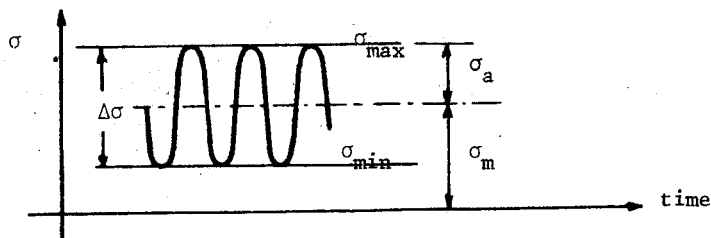


Fig.9.2: Constant load amplitude case and the associated terminology

upon K . They tested center cracked panels of a high strength aluminum alloy. In the first part of the test they applied uniform remote tension such that both the net section stress range and the stress intensity factor range increased as the crack extended. In the second part, the

concentrated load was applied at the crack surfaces. As the crack extended the net section stress again increased but the stress intensity factor decreased this time as Sec.3.2.1 indicates. Experimental results, indeed, showed the crack growth rate reversal anticipated by the sense of the crack length dependent change in stress intensity factor. The crack-line loaded sample exhibited the highest growth rates at the outset of the test when the crack was small, with progressively slower growth rates being monitored with increasing crack length. The opposite was true for the panels under remote tension. Thus, it was concluded that

$$\frac{da}{dN} = f(\Delta K) \quad (9.1)$$

where $\Delta K = K_{\max} - K_{\min}$, using the σ_{\max} and σ_{\min} values respectively. Moreover, Paris & Erdogan choose a power function in eq 9.1 since it fits the experimental data over a large range of ΔK . The relation

$$\frac{da}{dN} = C (\Delta K)^m \quad (9.2)$$

where C and m are taken as material properties, has been known as Paris law in fracture.

In general, three distinct types of behavior occur in fatigue crack propagation. Figure 9.3 displays the sigmoidal shape of the growth rate vs. ΔK curve. Region I is the low ΔK end where the growth rate decreases rapidly with decreasing ΔK and approaches lower limit at ΔK_{th} . Region II is the midrange of crack growth rates where the power law dependence prevails. Region III is the high ΔK end of the curve where K_{\max} approaches K_c and local static modes of fracture start to dominate. No crack propagation is observed below the threshold stress intensity factor range, ΔK_{th} . But this does not have a practical importance since ΔK_{th} for most engineering materials is below 10% of their fracture toughness values, ranging between 3-8 MPa \sqrt{m} for most metals [3]. It is rather uneconomical to design at $\Delta K < \Delta K_{th}$.

The stress intensity factor range used in da/dN vs. ΔK relationship (eq.9.2) is traditionally interpreted as

$$\Delta K = \begin{cases} K_{\max} - K_{\min} & \text{for purely tensile loading} \\ & \text{i.e. } K_{\min} \geq 0 \\ K_{\max} - 0 & \text{for tension-compression} \\ & \text{type of loading, i.e. } K_{\min} < 0 \end{cases} \quad (9.3)$$

Since crack faces will close in compression and no singularity is expected at the tip, it is more logical to ignore the compressive part of the loading and just take the tensile range as damaging. Welded structures are exceptions to this generalization, however. Because of the very high tensile residual stresses in weldments it is customary to use the full value of $K_{\max} - K_{\min}$ even if $K_{\min} < 0$.

If the range of the alternating stress is the most important factor in classical fatigue, its mean value is the next important factor. A similar behavior is observed in fatigue crack propagation (FCP). Tensile mean loading accelerates crack growth. The increase in crack growth rate is particularly pronounced in regions I and III. Mean loading is expressed using the stress ratio $R = \sigma_{\min}/\sigma_{\max} = K_{\min}/K_{\max}$. Majority of tests are done at $R > 0$ since it is difficult to grip specimens without backlash for $R < 0$. Typical trend is sketched in figure 9.4. ΔK_{th} shifts by about 30-50% as R changes from 0 to 0.5.

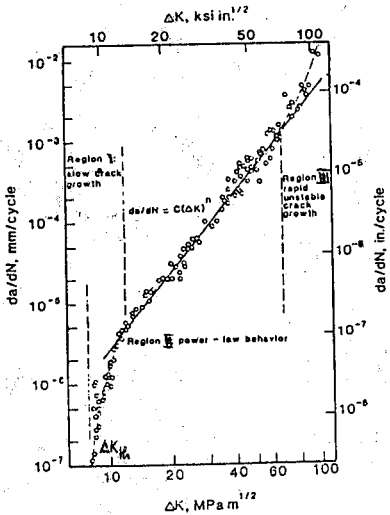


Fig.9.3: Typical fatigue crack propagation behavior (A533B steel)

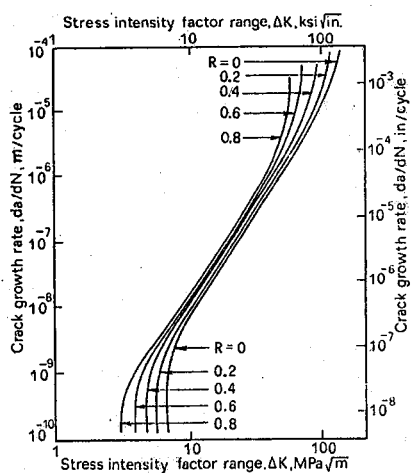


Fig.9.4: Effect of mean load in FCP.

9.2.1 Crack Propagation Laws: Paris equation (eq.9.2) is a simple relation but it is not capable of accounting for mean load effects, for threshold behavior or for accelerated growth near K_c . More sophisticated relations have been proposed to reflect such factors. Forman equation

$$\frac{da}{dN} = \frac{C \Delta K^m}{(1-R)K_c - \Delta K} \quad (9.4)$$

is a popular one and identifies correctly FCP response under combinations of high ΔK and K_{mean} conditions, but it is difficult to apply since K_c is difficult to determine. Forman equation is reported to give good results with Al-alloys and high strength steel but overestimates mild steel behavior. For $R>0$ and for $R<0$ situations appropriate Forman parameters should be determined separately. Major divergence may occur in predictions for CA-loading in the $R<0$ range if the calculation is made with those Forman parameters determined for $R>0$. As a general rule, though, predictions are conservative when " $R>0$ parameters" are used.

The relation proposed by Walker

$$\frac{da}{dN} = C \left[\frac{\Delta K}{(1-R)^n} \right]^m \quad (9.5)$$

exhibits a particularly strong dependence upon R . The value of n should be determined from experimental data along with C and m . $n = 0.5$ is a typical value used in literature.

$$\frac{da}{dN} = C (\Delta K - \Delta K_{\text{th}})^m \quad (9.6)$$

and

$$\frac{da}{dN} = C \left(\frac{\Delta K - \Delta K_{\text{th}}}{K_c - K_{\text{max}}} \right)^m \quad (9.7)$$

are other suggested relations reflecting the departures from power law behavior at high and low ΔK values.

All of the above cited relations are empirical and are not developed considering basic mechanisms of FCP. The differences among them are not

large and none of them has a general applicability. Each one may be found reasonably satisfactory in a limited region or for limited sets of data.

A semi-empirical approach has been the crack closure concept advanced by Elber [4]. He observed that under zero-to-tension loading the crack faces can close on each other even under a tensile applied stress, i.e. before reaching the minimum point in unloading. This was attributable to plastic deformation left behind the advancing fatigue crack. Compliance measurements showed that an effective change in crack length occurred prior to any actual change in crack length. That is, the crack was closed for a portion of the loading cycle and did not open fully until a certain opening K level, K_{op} , was applied (Fig.9.5). As a result, the damaging portion of the cyclic load excursion would be restricted to that part of the load cycle which acted on a fully opened crack. Thus, Elber

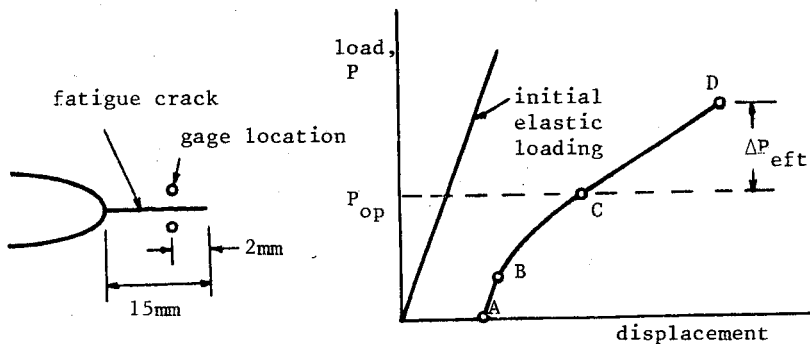


Fig.9.5: Crack Closure observed through compliance. The slope AB is equal to that of the uncracked body, the slope CD is equal to that of the body having a 15mm crack.

defined an effective stress intensity factor range as

$$\Delta K_{eff} = K_{max} - K_{op} \quad (9.8)$$

where K_{op} corresponds to the point at which the crack is fully open. He suggested that existing fatigue crack growth relations could be utilized by simply replacing ΔK by ΔK_{eff} . Paris law, for example, would become

$$\frac{da}{dN} = C (\Delta K_{eff})^m \quad (9.9)$$

Although physically appealing, the concept is difficult to quantify. K_{op} needs to be evaluated for the material and conditions of interest. Elber himself performed a series of constant amplitude tests on Al 2024-T3 to evaluate $\Delta K_{eff}/\Delta K$ ratio, which he denoted by U . Both his findings ($U=U(R)$) and those of others in the field are still disputed and the issue of quantifying the closure remains controversial yet [5,6]. Some of the recent studies are summarized below. Kurihara's work covers a wide range of stress ratios (Fig.9.6) leading to a simple relation for two steels of different yield strength (367 MPa and 723 MPa). The proposals of Elber

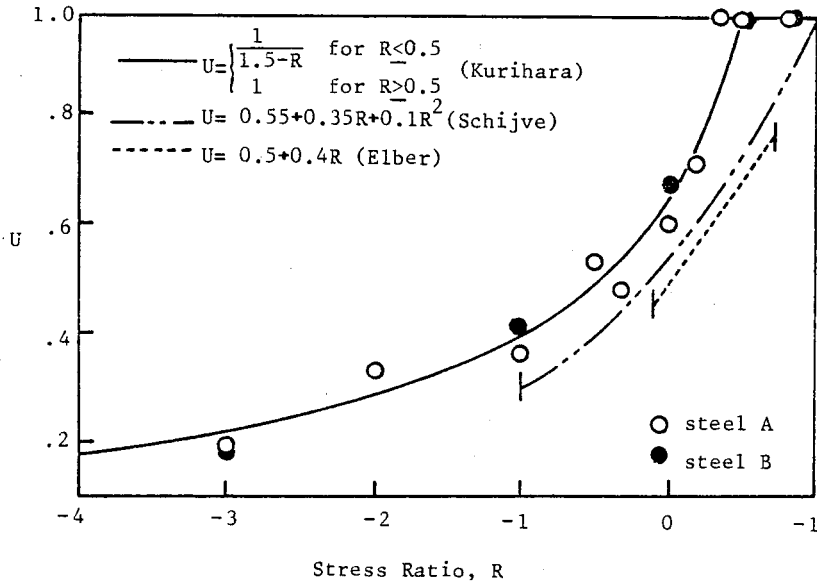


Fig.9.6: Variation of the effective ΔK with R [7].

and Schijve for 2024-T3 Al-alloy are also plotted in figure 9.6. K_{max} dependence of U , raised by Shih and Wei [8], is not investigated in detail. Nevertheless, figure 9.6 points out rightfully to the effect of the compressive portion of the loading. Although cracks close under compression on a macroscale, the crack surfaces near the crack tip yield, thereby lowering the subsequent crack opening stress. If the Kurihara eq. applies, $\Delta K_{eff} = 0.67 K_{max}$ for $R=0$ and $\Delta K_{eff} = 0.80 K_{max}$ for $R=-1$ (Fig.9.7). Hence the compressive portion of a cyclic load may be not negligible at all — as opposed to the simple minded approach of eq.9.3. Data in literature reflects this, particularly for medium strength materials (e.g. 2024-T3 [9,10], 2219-T851 [11], Fig.9.8). For high strength materials, such as 7075-T6 or maraging steel the stress amplitude below zero does not add much to the growth rate.

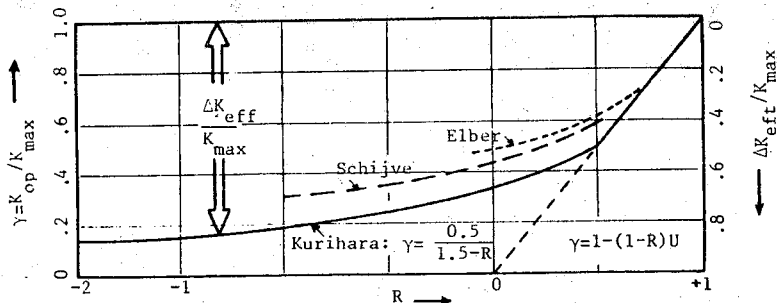
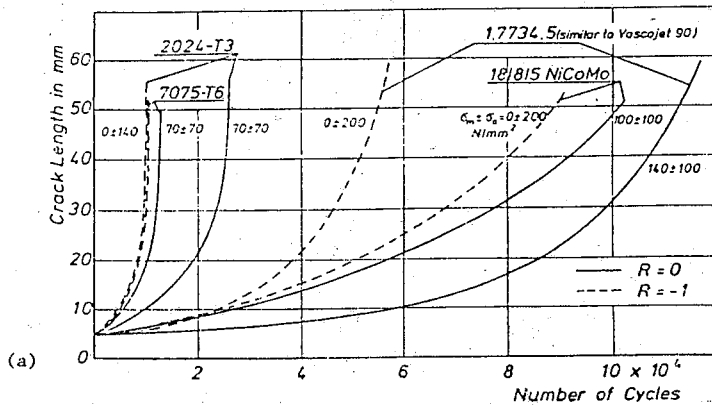
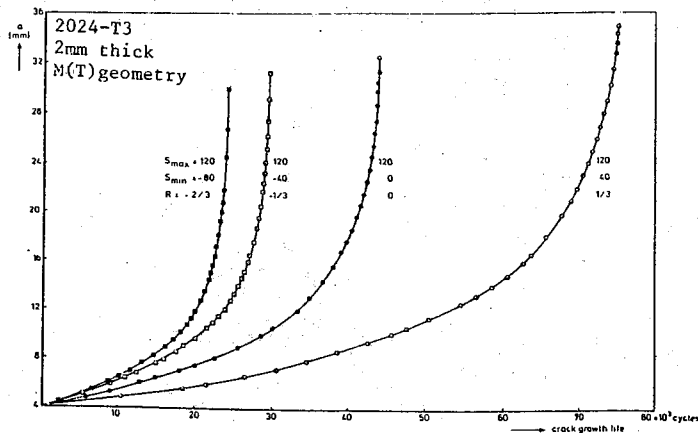


Fig.9.7: Variation of K_{op} and ΔK_{eff} with the stress ratio R , as determined through Kurihara's equation.



(a)



(b)

Fig.9.8: Comparison of growth rates for several R for several materials (a) Ref 9, (b) Ref 10

The crack growth rates for 2024 specimens are plotted in Fig.9.9 as a function of both ΔK and ΔK_{eff} . The use of ΔK_{eff} , calculated through the expression proposed by Schijve (Fig.9.6), eliminates the R-effect and the results merge into one single scatter band. Misawa and

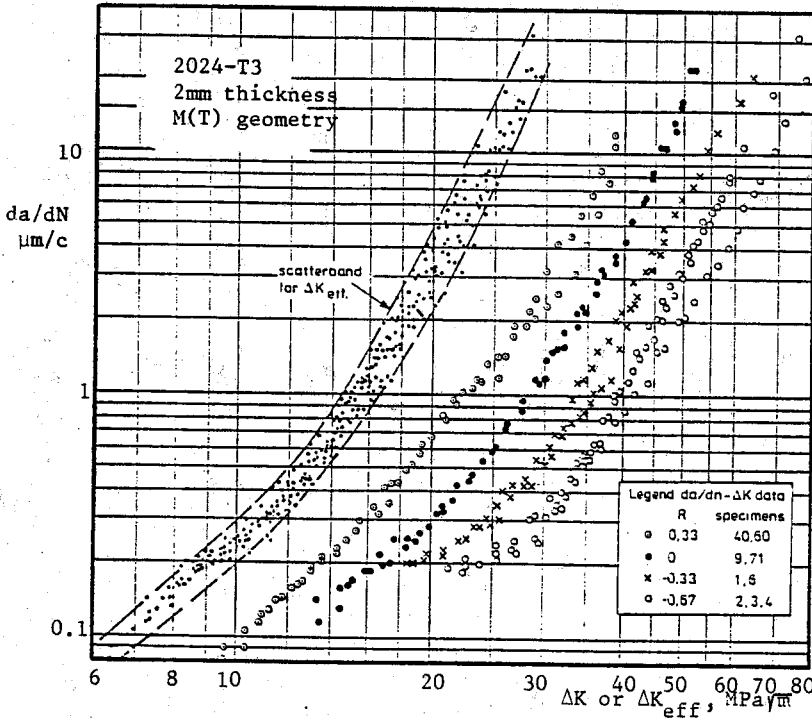


Fig.9.9: The crack growth rate for 9 specimens with the same σ_{max} but different R-values [10]

Schijve [10] also report just a weak trend to higher crack rates for higher σ_{max} values. Their data agree reasonably well with a single relation between da/dN and ΔK_{eff} including cracks growing in shear mode.

The crack growth laws presented above can be integrated to make predictions about the cyclic life between a starting and a final flaw size. A closed form expression may be obtained with Paris law. Others would require numerical procedures. Expressing the stress intensity factor range of interest as

$$\Delta K = Y \Delta \sigma \sqrt{\pi a} \tag{9.10}$$

where $Y = Y(a/W)$ represents the geometrical correction factor, Paris

law becomes

$$\frac{da}{dN} = C (Y \Delta \sigma \sqrt{\pi a})^m$$

or

$$N = \int_{a_i}^{a_f} \frac{da}{C(Y \Delta \sigma \sqrt{\pi a})^m}$$

which (for Y not changing within the limits of integration) will yield

$$N = \frac{2}{(m-2) C Y^m \pi^{m/2} \Delta \sigma^m} \left[\frac{1}{a_i^{m/2}} - \frac{1}{a_f^{m/2}} \right] \quad (9.11)$$

Note that $m \neq 2$ in this integration and a_i and a_f denote the integration limits, namely the initial and final crack sizes. For $a_i \ll a_f$ the computed fatigue life is not sensitive to the final crack length a_f but, instead, is strongly dependent on estimations of the starting crack size a_i . Thus, it becomes crucial to correctly determine a_i , which is the major problem in estimations of life by combining the initiation as well as the propagation phases. The final size a_f , here, could be the critical size based on the fracture toughness of the material or a convenient length to determine the next inspection interval. Limit load criterion may apply in the case of very ductile materials.

9.2.2 Constant Amplitude Testing: The general design data relevant to fatigue crack growth is obtained usually using center cracked panels, M(T). For cycling with $R > 0$, compact specimen C(T) may also be used. In fact round compact specimens, DC(T), appear to be a satisfactory alternative for some product forms. The proportions of the specimens and possible grips are described in the ASTM standard E 647-83. It is worth to repeat here the following aspects.

Particular care must be taken to avoid the unrealistic buckling of crack lips which may occur in thin center cracked panels at high a/W ratios. In actual structures this situation is prevented by the stiffeners; in the test, anti-buckling guides can be used for this purpose. The specimen aspect ratio must be high enough for the stress distribution in the crack plane to be uniform.

Residual stress remaining in the test coupons may lead to unrealistic growth rates. This is particularly true when test specimens are removed from weldments, complex forged or extruded shapes or from metallurgical coupons which have been heat treated without subsequent stress relief [12]. Crack propagation results obtained from nonstress relieved extruded rod is illustrated in figure 9.10. Rapid quenching produces a core of residual tension at the center which leads to rapid growth of the central crack in M(T) specimen, but to slow growth of the edge crack in SE(T) specimen.

Near threshold region will be affected most seriously by the residual stress pattern since the external load levels are low there. To minimize such effects the following guidelines are suggested [12]:

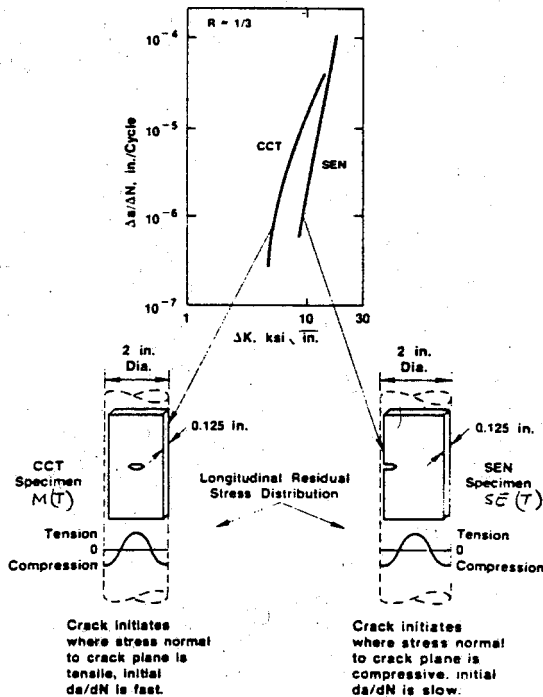


Fig.9.10: Effect of specimen type on FCP rates established from non stress-relieved high strength 7XXX al-alloy [12]

- (1) Excessive crack front curvature or irregular crack growth (that is, out of plane fracture) hints to residual stresses

- (2) When residual stresses are suspect, local displacement measurements made before and after the machining of the crack starter slot indicate the severity of the residual stresses.
- (3) If residual stresses exist normal to the fracture plane (variation in the thickness direction), choose B/W small to minimize residual stress effects .
- (4) If residual stresses exist parallel to fracture plane (varying as you move normal to the fracture plane) select symmetrical specimen configurations (e.g. select M(T) over C(T)).

Residual stresses can be beneficial in precrack formation, in fatigue crack propagation tests as well as in fracture toughness testing. A compressive overload applied before the precracking procedure leads to tensile residual stresses at the notch root which shortens the initiation period of a fatigue crack and leads to a more uniform crack front shape. Underwood and Kapp [13] report a reduction of 34% to 220% by using a compressive overload which is twice of the precracking amplitude.

Although methods for fatigue crack growth rates above 10^{-8} m/cycle are standardized by ASTM, low ΔK testing is not yet part of the standards. To evaluate ΔK_{th} values it is suggested [14] to have larger precracks at the notch roots to avoid the short crack effects and to eliminate any transient effects by gradually decreasing ΔK levels not to introduce any retardation. An operational definition of the fatigue crack growth threshold is suggested as that value of ΔK corresponding to $da/dN = 10^{-10}$ m/cycle.

The raw data of FCP tests are in the form of crack length versus number of cycles. To obtain da/dN values a second order polynomial (parabola) is fitted to sets of 7 (or 9 or 5 or 3) successive data points using least squares method. A fortran program for this evaluation is included in ASTM E 647-83. Polynomial fitting procedure smooths the jerky propagation of cracks and/or small random errors built in the crack length measurement technique.

To evaluate the constants in the crack growth law of interest, a suitable coordinate change is performed so that a straight line plot is obtained. Paris law, for example,

$$\frac{da}{dN} = C (\Delta K)^m \quad (9.2)$$

is converted into

$$\log \frac{da}{dN} = \log C + m \log \Delta K \quad (9.12)$$

whereas the Forman's law

$$\frac{da}{dN} = \frac{C \Delta K^m}{(1-R) K_c - \Delta K} \quad (9.4)$$

is converted into

$$\log \left\{ \left(\frac{da}{dN} \right) [(1-R) K_c - \Delta K] \right\} = \log C + m \log \Delta K \quad (9.13)$$

from which the unknown constants C and m can be determined as slope and intercept. The m value lies typically between 2 and 4. Throop and Miller [15] tabulated values for a number of different metals ranging from 2.3 to 6.7 with a sample average of $m=3.5$. Knott [16] reports that high values of m are obtained in materials of low toughness and in high toughness materials m has a value close to 2.

Fatigue initiation is associated with slip and nucleating cracks lie often at 45° to the loading axis. After a relatively short distance the orientation of the fatigue crack shifts and propagation continues in a direction normal to the loading direction. When the crack grows the size of the plastic zone increases and the plane strain situation which acted at the beginning can shift to plane stress. Plane stress develops when the size of the plastic zone is in the order of the sheet thickness. This causes the fatigue crack to change to single or double shear (Fig.9.11) analogous to the fracture mode transition of a ductile fracture (Sec.4.4). It is expected that more energy is dissipated in plane stress than in plane strain. And the data suggest that crack growth is slower in plane stress than in plane strain at the same stress intensity. In making fatigue crack growth predictions for structural components if the appropriate crack propagation parameters are not available for the thickness in question, the usual procedure is to take the parameters of specimens which are thicker than the component.

As the thickness increases the center portion will experience more constraint and tunneling will result. This crack front curvature reduces the accuracy of optical crack detection techniques. Another aspect

associated with increased thickness is that the chances of having through cracks diminishes as thickness increases. Elliptical or semielliptical flaws have varying stress intensity factor along the front thus the growth rate will vary along the crack front. By the time the flaw becomes a semi-circular one the growth rate will be uniform along the periphery. Extensive tests on part-through cracks revealed that data from compact specimens can be used to predict fatigue crack growth in surface cracked specimens [17].

The well-known striations on a fatigue fracture surface correspond to the cyclic opening and closing of the crack. Attempts have been made to correlate the crack growth rate with the COD. This leads to relations of the form

$$\frac{da}{dN} = C \left(\frac{\Delta K}{E} \right)^2 \quad (9.14)$$

where E is the elastic modulus. It is interesting that data for a large variety of materials fall within one large scatterband when normalized by the elastic moduli. However it is not universal. Also the exponent in eq.(9.14) being 2 differs from that of Paris in most cases and brings another limitation to the practical use of this microscopic approach.

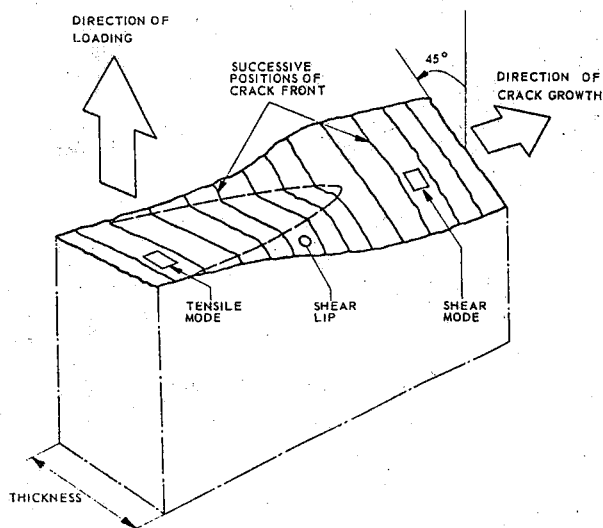


Fig.9.11: Fracture mode transition in fatigue crack growth.

9.3 SHORT CRACK BEHAVIOR

9.3.1 Observed Trends: Crack growth rate of short cracks (typically 0.2mm or less, in isolated instances as large as 1mm) show two anomalous behaviors: considerable scatter about the long crack growth rate data, and an apparent higher than expected growth rate. These have been termed the short crack effect. Generally, data are said to show a short crack effect if they do not correlate when growth rate is plotted against stress intensity factor range, ΔK . Such variation in the growth rate behavior of short and long cracks is illustrated in figure 9.12. Growth rates associated with the short cracks may be up to two orders of magnitude faster

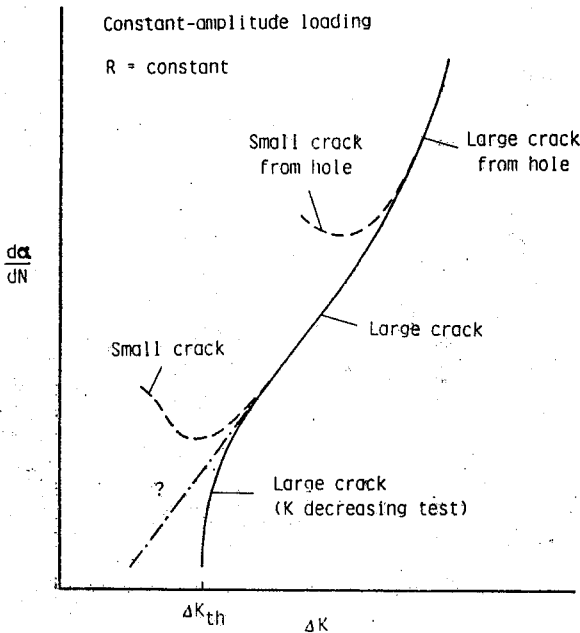


Fig.9.12: Typical fatigue-crack growth rate data for small and large cracks

than those of the long cracks. There is the concern, that since a considerable portion of crack growth life is typically obtained from the growth at small size, an underestimate of growth rate in this region could seriously overestimate service life. Additionally, such accelerated short crack advance may occur at stress intensities well below the so-called fatigue threshold stress intensity range ΔK_{th} , below which long cracks remain dormant or grow at experimentally undetectable rates. ΔK_{th}

values associated with long crack test specimens may, then, lead to non-conservative life estimates of a component that contains very small cracks.

Although conventional fracture mechanics arguments infer that the threshold stress intensity range for a particular material should be independent of crack length, Kitagawa and Takahashi [18] first showed that below a critical crack size, the threshold for short cracks actually decreased with decreasing crack length, where the threshold stress $\Delta\sigma_{th}$ approached that of the smooth bar fatigue limit ΔS_e at very short crack lengths (Fig.9.13). Several workers have shown that this critical crack size below which ΔK_{th} is no longer constant with crack length is dependent upon microstructural and mechanical factors, but from a continuum argument it is approximately given by $\frac{1}{\pi} (\Delta K_{th}^{long\ crack} / \Delta S_e)^2$ where both $\Delta K_{th}^{long\ crack}$ and ΔS_e are corrected for a common load ratio. Values of this dimension, which effectively represent the limiting crack size for valid LEFM analysis, range from typically 1-10 μm in ultrahigh strength materials (i.e. $\sigma_o \sim 200$ MPa) to 0.1-1mm in low strength materials (i.e. $\sigma_o \sim 200$ MPa). Thus, it appears that the threshold condition for long cracks is one of a constant stress intensity whereas the threshold condition for short cracks is one of a constant stress [19]

9.3.2: Difficulties associated with short cracks: In many of the described cases above the key assumptions of LEFM are violated. The concept of similitude implies that equal changes in the value of the stress intensity factor lead to equal amounts of crack advance. But it is conditional; there are several limitations - mechanical as well as metallurgical - for the similitude concept to apply. These are [20] :

- 1, The plastic zone must be small compared to all lengths dimensions and small with respect to the distance over which the first term of the elastic stress field solution is dominant, so that both the size of the plastic zone and the surrounding stress field are adequately described by the stress intensity factor, K. This length limitation certainly includes the thickness since there has to be equal constraint (plane stress/plane strain condition).
- 2, The plastic zones in the wake of the crack must also be equal in as much as they affect the local stress field through closure forces.

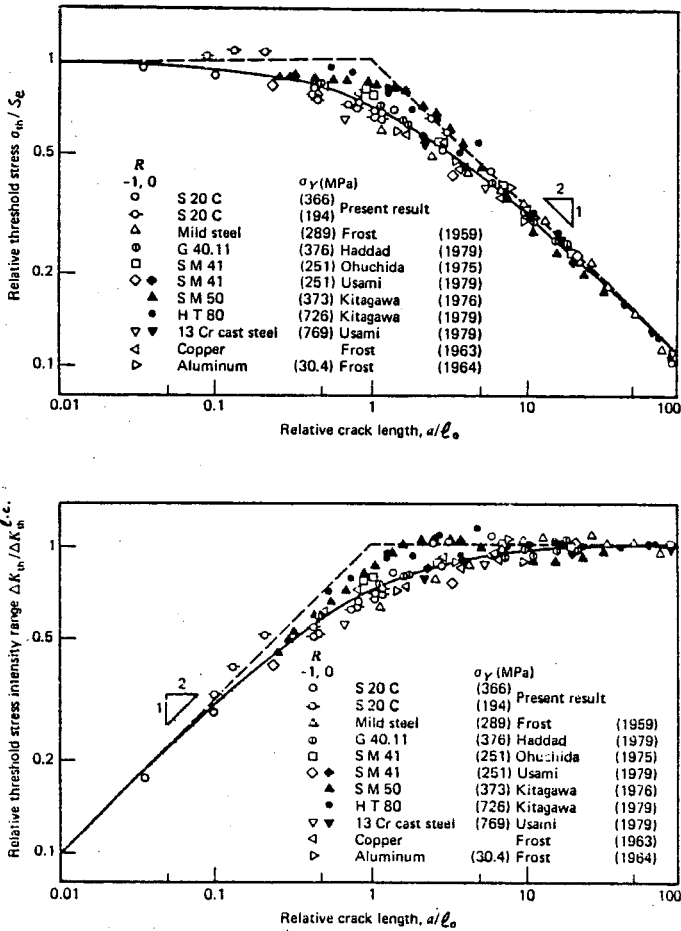


Fig.9.13: Variation of threshold stress normalized with respect to the smooth bar fatigue limit ΔS_e , and threshold stress intensity normalized with respect to the long crack threshold $\Delta K_{th}^{l.c.}$, with crack length normalized with respect to $\xi_0 = 1/\pi(\Delta K_{th}^{l.c.}/\Delta S_e)^2$

- 3, The material should be the same with regard to phase, orientation, dislocation density, particle density etc. for it to respond in a unique manner to mechanically similar conditions.
- 4, Local environments (temperature and chemistry) should be the same. When all of these conditions are satisfied the response of the crack— be it long or short— will be the same. But it is extremely difficult to satisfy all of these conditions for short cracks.

For a given ΔK a smaller crack will require a higher stress. As long as the plastic zone is uniquely related to K , equal K means equal plastic zones. As a consequence the plastic zone to crack size ratio is larger for the small crack, so that the first similitude requirement tends to be jeopardized. For very small cracks the same ΔK requires stresses at or close to yield and the plastic zone becomes undefined. Thus the first requirement is violated. It has been attempted to mend this problem by applying a plastic zone correction, mostly interpreted as a pseudo crack length or as an empirical constant.

El Haddad and co-workers [21] redefined the stress intensity factor by

$$\Delta K = \Delta \sigma \sqrt{\pi(a + \ell_0)}$$

The material dependent constant ℓ_0 — which they called the intrinsic crack length — was estimated from the limiting conditions of crack length where the nominal stress $\Delta \sigma$ approaches the fatigue limit ΔS_e when $a \rightarrow 0$ and

$$\Delta K = \Delta K_{th}^{long\ crack}, \text{ i.e.}$$

$$\ell_0 \approx \frac{1}{\pi} \left(\frac{\Delta K_{th}^{long\ crack}}{\Delta S_e} \right)^2$$

and can be seen to be equivalent to the critical crack size (above which $\Delta K_{th} = \Delta K_{th}^{long\ crack}$) in Fig. 9.13. Although such intrinsic crack length arguments successfully rationalize many apparent anomalies between the growth rate kinetics of long and short cracks limited by LEFM analyses, there is currently no available physical interpretation for the parameter ℓ_0 .

Metallurgical conditions (third similitude condition above) also present difficulties. In the case of cracks with long fronts this condition is satisfied on the average even in multi-phase materials with high crystallographic anisotropy. However, if the crack front is short (e.g. of the order of several grains) this condition will generally be violated. Grain boundaries, inclusions, hard second phases etc. influence heavily micro-cracks whose length will be comparable to the size of these microstructural features. Such cracks are termed microstructurally short cracks. There is now a large body of evidence, for example, that the growth of microstructurally short cracks is impeded by the presence of

grain boundaries by such mechanisms as the blocking of slip bands or containment of the plastic zone within the grain, reorientation and reinitiation of the crack as it traverses the boundary and simply cessation of growth at the boundary. It is possible to translate this condition, then, into a geometrical requirement that the crack be long with respect to metallurgical features.

Crack initiation and early growth is transient. The crack is tending toward a steady state condition, the limit of which is the long crack condition. The mechanism of initiation will control the length the crack must attain before a steady state develops at its tip. Brittle initiation at inclusions localize the process and allow a sharp crack with a well defined tip and a continuous front to form. In contrast, ductile initiation involves extensive flow before a crack is formed, which has usually a poorly defined tip and a discontinuous front. Thus, it will not achieve a steady state as quickly as its brittle counterpart. Brittle initiation tends to form a crack which grows stably from the beginning, with limited flow at the crack tip. In contrast, ductile initiation would initially tend to violate the plastic zone to crack length limitation of LEFM. The short crack influence on life is much smaller in brittle initiations compared to ductile initiations. For cracks growing at inelastically strained notch roots transient behavior continues longer and LEFM based analyses may easily lead to nonconservative errors of more than an order of magnitude on life.

It is also worthwhile to note multiple initiations and branching in ductile initiations which are completely absent in artificially induced flaws. Artificial flaws tend to concentrate deformation and tend to cause a more brittle initiation. Thus, natural cracks are expected to show the short crack effect much more than artificial preflawed samples [20].

Even physically-short cracks - i.e cracks which are long compared to both the scale of microstructure and the scale of local plasticity, yet simply physically small, typically less than 0.5-1mm in length- show growth rates in excess of those of long cracks under nominally identical driving force conditions. Both crack closure and chemical effects are blamed for this anomolous behavior. Threshold ΔK values for short cracks at low mean stresses ($R=0.1$) were found to be 60% smaller than for long cracks, yet at high mean stresses ($R=0.7$) where closure effects are minimal, this difference was not apparent. Thus, at equivalent nominal ΔK levels, physically short flaws may be expected to propagate faster than

corresponding long flaws simply due to larger effective stress intensity ranges at the crack tip.

Parallel to the above arguments, Miller [22] recognized three separate regimes in a Kitagawa-Takahashi diagram (Fig.9-14). The microstructurally short crack regime reflects the recently expressed view that fatigue crack initiation occurs immediately for all practical cases at stress levels above and just below the fatigue limit and that this limit is more accurately defined as one which differentiates between continuous propagation and non-propagation of a crack. d_1, d_2, d_3 represent the microstructural barriers to crack growth existent in a single material. As the stress level is increased a barrier can be overcome and the crack will propagate to the

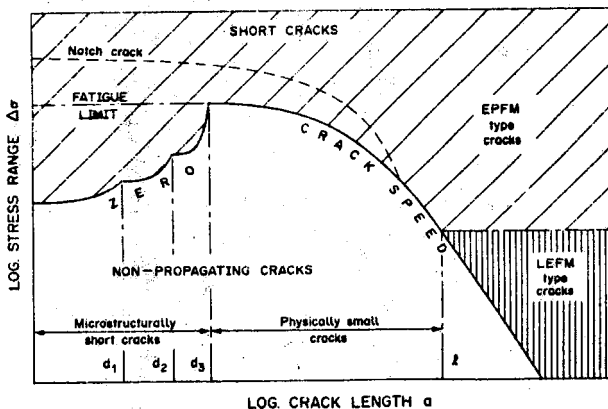


Fig.9.14: The three regimes of short crack behavior [22]

next barrier. The physically short crack regime is bounded at minimum lengths by the MSC zone and at maximum lengths and low stresses by the LEFM zone. The LEFM zone is limited, typically, to $\Delta\sigma$ less than two thirds of cyclic yield. At higher stress range levels up to the upper bound of $2S_u$ cracks will necessarily have to be described by EPFM analyses.

Short cracks are by definition three dimensional cracks where the stress intensity factor solutions are less well established and less amenable to adaptation to fit actual crack front shapes (Fig.9.15). Substantial variation of the local K value along the curved crack front of a three dimensional flaw adds to the complication. It must also be remembered that since cracks originate in shear (stage I), it is not sufficiently accurate to apply Mode I crack opening K solutions until the cracks become

established as stage II cracks.

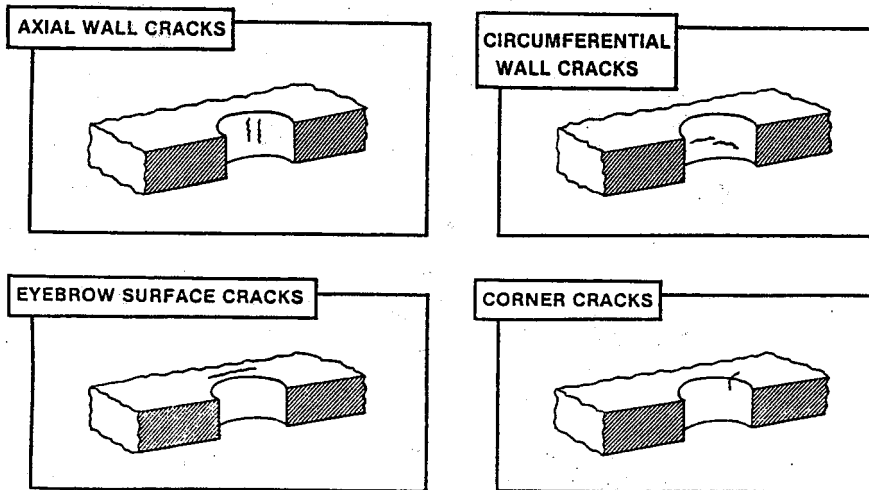


Fig.9.15: Typical short crack types found in fastener holes in a commercial transport aircraft [23]

Uncertainty in the measurement of the crack size, the crack growth increment and the difficulty in locating the tip of a tight crack in a region of significant cyclic plasticity are other sources of error [24]. Both the resolution of the microscope and the fact that sometimes many short cracks grow simultaneously before a dominant crack develops, limit the repetability of measurements severely.

It is clear that the short crack problem is concerned not only with the plastic deformation associated with the crack tip, but with the consequent residual stresses and closure effects. Therefore, any fracture mechanics parameter to be used to describe the phenomenon must necessarily reflect these history-dependent effects. The CTOD, being a direct measure of the crack tip deformation state, that through suitable determination reflects history dependence, appears to be a candidate parameter [25]. As to the calculation of CTOD for conditions under which residual stress and closure effects are expected to be dominant, an entirely satisfactory method does not currently exist. However approximate solutions based on Dugdale model are valuable starting points. More accurate, though costly, estimates of CTOD may be developed using nonlinear finite element models.

9.4 PROPAGATION BEYOND SMALL-SCALE YIELDING

Fatigue crack propagation expressions based on linear elastic fracture mechanics become inaccurate in applications which involve gross plastic deformation prior to fracture. ASTM E647, for example, limits compact specimens to $b > (4/\pi) (K_{\max}/S_y)^2$. Especially if the part fails by reaching limit load, it is certainly not feasible to use the stress intensity factor to determine the crack growth rate. Usually parts are not designed to operate in the high growth regions. However, it is helpful to have some means to estimate these high rates particularly in the post-mortem analysis of service failures. Even if the applied loads are low, cracks initiating at notches will be usually surrounded by large plastic zones due to the stress concentration effect of these notches. An elastic-plastic analysis is necessary until the crack grows out of this yielded zone. Once the crack tip reaches the elastic portion, LEFM can be utilized for growth rate predictions. There is no theoretical basis for using the LEFM approach for cracks within the region of notch plasticity, and when it is used, the predictions do not reflect the experimental results [26,27].

Attempts to analyze fatigue crack propagation in the presence of extensive plastic deformation have been rather limited. They all indicate the significance of the plastic strain range and the current crack length. Correlation of the crack growth with the nominal strain range has been geometry dependent, and evaluation of the strain range at the defect is difficult as a general approach. El Haddad, Smith and Topper [28] circumvent these difficulties by defining a "Strain intensity factor, K_E " and correlate crack propagation rate with K_E . A more rational approach is proposed by Dowling and Begley [29], and Dowling [30] to extend the application of the J-integral to fatigue problems. The J-integral is the plastic analog of K expressing the strain and stress field at the crack-tip — not at the heavily deformed process zone, but outside of it, in the HRR zone. Although the J-integral seems to be a natural candidate to correlate with fatigue crack growth rates, the difficulty in using it for cyclic loading lies in the "deformation plasticity assumption" inherent in its derivation. As discussed in chapter 7 independence of the J-integral has been proved only for deformation plasticity, which does not allow for non-proportional loading.

It is important in discussing fatigue to realize that the path-depen-

dence of the J-integral for cases involving unloading is not proved either. In fact, recent numerical computations support the path-independence of the J-integral as long as the path is chosen outside the intensely deformed process zone (Sec. 7.14). The use of the J-integral in cyclic loading can be adopted in line with the trend in recent years of relaxing the limitations on the use of the J-integral. Paris [31] argued that "crack tip moves ahead during each cycle into relatively virgin material in terms of plastic deformation. Intense deformation being very localized, previous loading and unloading will not be significant in the next cycle compared to the loading which is then being experienced. Thus, as long as a moving crack is considered, it may be possible to neglect past history including unloading in a J-integral analysis".

Most of the experimental work has been performed using the compact geometry. Assuming that the damage is done during loading, the J-integral is evaluated from the loading portion of the cyclic curve. Typical load versus load line displacement curves are shown in Fig.9.16. The lack of symmetry of the hysteresis loop is caused by the occurrence of crack closure at the lower loads. The point of crack closure corresponds to the

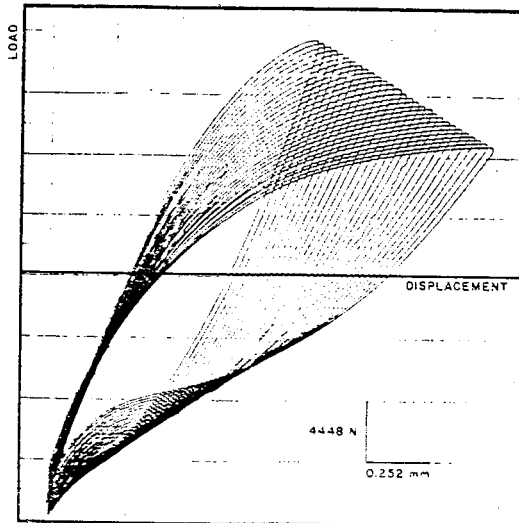


Fig.9.16: Load vs. displacement data for 29 consecutive cycles [33]

inflection point on the unloading portion of the load-displacement record. Since the crack cannot grow unless it is fully open, crack closure may be accounted for by requiring J equal to zero until the crack opening load is attained. This is accomplished by referencing the area under the load displacement curve to the point of crack closure, as shown in Fig.9-17 and using this result in eq.7-25 [29,32,33]. Change in J value due to advancing crack tip may be accounted for through eq.7.28. But the difference

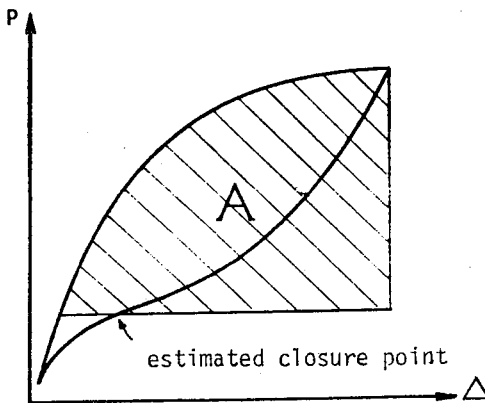


Fig.9.17: Operational definition of cyclic J .

has been found to be negligible provided that the extent of crack extension is less than $250 \mu\text{m}/\text{cycle}$ [34].

Expressing crack growth rates in terms of J -integral range results in a linear relationship on log scales over four orders of magnitude in growth rates. These growth rates fall largely outside of the usually - studied constant growth rate region and coincide with the "accelerated growth" region designated as region III in the well known sigmoidal plot of da/dN vs. ΔK . Propagation rates obtained in A533 B and AISI 1020 specimens at load levels above yielding agree nicely with data obtained under LEFM conditions (Fig.9.18).

The relation of da/dN vs. cyclic J -integral is observed to be independent of the loading conditions; that is, constant amplitude load control experiments are in agreement with constant amplitude displacement control

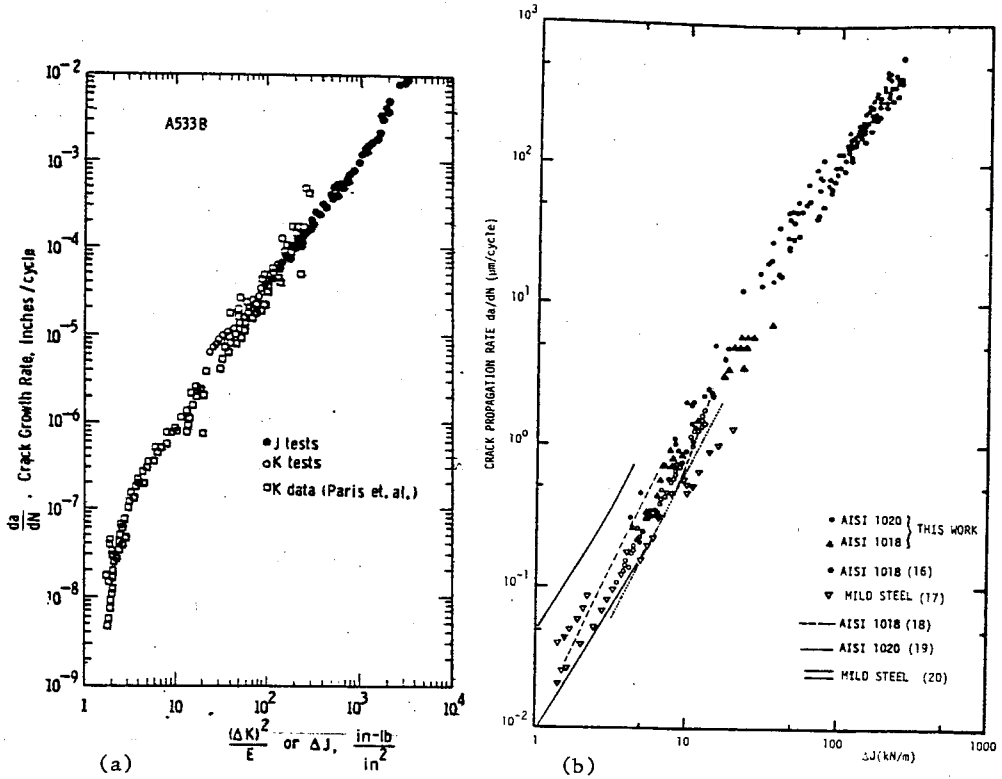


Fig.9.18: Comparison of data obtained through J (solid symbols) and linear elastic route (open symbols) a)Ref.29 b)Ref.33

tests [34]. In addition to compact specimens, center cracked specimens [30], compact type strip specimen [35], smooth axial specimens [36], edge cracked specimens [37] are successfully analyzed using the J-Integral.

References:

- 1- Schijve, J. "Four Lectures on Fatigue Crack Growth" Engineering Fracture Mechanics, Vol.11 pp.167-221 (1979)
- 2- Paris, P.C. and Erdogan, F. "A Critical Analysis of Crack Propagation Laws" Journal of Basic Engineering, Transactions ASME, Series D, Vol 85, 1963, p.528
- 3- Hertzberg, R.W. "Deformation and Fracture Mechanics of Engineering Materials" John Wiley & Sons, 1983
- 4- Elber, W. "The Significance of Fatigue Crack Closure" ASTM STP 486, Amer.Soc.for Testing and Materials, 1971 pp.230-242
- 5- Vecchio, R.S., Crompton, J.S. and Hertzberg, R.W. "Anomalous Aspects of Crack Closure" Int.J.Fracture (1986) pp.R 29-R33
- 6- Kanninen, M.F. and Popelar, C.H. "Advanced Fracture Mechanics" Oxford University Press, New York, 1985
- 7- Kurihara, M., Katoh, A. and Kawahara, M. "Analysis on Fatigue Crack Growth Rates Under a Wide Range of Stress Ratios" Journal of Pressure Vessel Technology, Vol.108, 1986, pp.209-213
- 8- Shih, T.T. and Wei, R.P. "Discussion" Int.Journal of Fracture, Vol.13, 1977, pp.105-106
- 9- Schütz, W. "Calculation Methods for Fatigue Life and Crack Propagation" AGARDograph No.231, Chapter 4.
- 10- Misawa, H. and Schijve, J. "Fatigue Crack Growth in Al-alloy Sheet Material Under Constant Amplitude and Simplified Flight-Simulation Loading" Delft University of Technology Report LR-381, 1983, The Netherlands
- 11- Chang, J.B., Engle, R.M. and Stolpestad, J. "Fatigue Crack Growth Behavior and Life Predictions for 2219-T851 Aluminum Subjected to Variable-Amplitude Loadings" ASTM STP 743, Amer.Soc. for Testing and Materials, 1981, pp.3-27
- 12- Bucci, R.J. "Effect of Residual Stress on Fatigue Crack Growth Rate Measurement" ASTM STP 743, Amer.Soc.for Testing and Materials, 1981, pp.28-47
- 13- Underwood, J.H. and Kapp, J.A. "Benefits of Overload for Fatigue Cracking at a Notch" ASTM STP 743, Amer.Soc.for Testing and Materials, 1981, pp 48-62
- 14- Bucci, R.J. "Development of a Proposed ASTM Standard Test Method

- for Near Threshold Fatigue Crack Growth Rate Measurements" ASTM STP 738, Amer.Soc. for Testing and Materials, 1981, pp.5-28
- 15- Throop, J.F. and Miller, G.A. "Optimum Fatigue Crack Resistance" ASTM STP 467, 1970, p.154
- 16- Knott, J.F. "Fundamentals of Fracture Mechanics" Butter-worths, London, 1973.
- 17- ———, "Part-Through Crack Fatigue Life Prediction" ASTM STP 687, 1979.
- 18- Kitagawa, H. and Takahashi, S. "Applicability of Fracture Mechanics to very small Cracks or the Cracks in the Early Stage" Proceedings International Conference on the Mechanical Behavior of Materials, ASM, 1976, pp.627-631.
- 19- Ritchie, R.O. and Suresh, S. "Mechanics and Physics of the Growth of Small Cracks" AGARD CP-328, Chapter 1, 1983
- 20- Leis, B. "Discussion of the Short Crack Effect in Airframe Materials and Components" AGARD CP-328, Chapter 16, 1983
- 21- El Haddad, M.H., Smith, K.N. and Topper, T.H. "Fatigue Crack Propagation of Short Cracks" J. of Eng. Materials and Technology, Vol.101 (1979) pp.42-46
- 22- Miller, K.J. "The Behavior of Short Fatigue Cracks and Their Initiation Part II- A General Summary" Fatigue and Fracture of Engineering Materials and Structures, Vol.10 (1987) pp.93-113
- 23- Wood, H.A., Rudd, J.L. and Potter, J.M. "Evaluation of Small Cracks in Airframe Structures" Agard Report R-696 (1983)
- 24- Leis, B.N. and Forte, T.P. "Fatigue Growth of Initially Physically Short Cracks in Notched Aluminum and Steel Plates" ASTM STP 743, Amer.Soc. for Testing and Materials (1981) pp.100-124
- 25- Leis, B.N., Hopper, A.T. and Ahmad, J. "Critical Review of the Fatigue Growth of Short Cracks" Engineering Fracture Mechanics, Vol.23 (1986) pp.883-898
- 26- Broek, D., "The Propagation of Fatigue Cracks Emanating from Holes", NLR TR 72134 U, National Aerospace Laboratory, The Netherlands, 1972
- 27- Usami, S., Kimoto, H., Enomoto, K. and Shida, S., "Low Cycle Fatigue Crack Propagation at a Notch Under Pulsated Load", Fatigue 1979, Proceedings of ICM-3 Extension Seminar on Fatigue, Sheffield, 27-29 August 1979.

- 28- El Haddad, M.H., Smith, K.N. and Topper, T.H., "A Strain Based Intensity Factor Solution for Short Fatigue Cracks Initiating from Notches", Eleventh National Symposium on Fracture Mechanics, June 12-14, 1978, Blacksburg
- 29- Dowling, N.E. and Begley, J.A., "Fatigue Crack Growth During Gross Plasticity and the J-Integral", Am.Soc.Test.Mat.STP 590, pp. 82-103 (1976)
- 30- Dowling, N.E., "Geometry Effects and the J-Integral Approach to Elastic-Plastic Fatigue Crack Growth", Am.Soc.Test.Mat.STP 601, pp.19-32 (1976)
- 31- Paris, P.C., "Fracture Mechanics in the Elastic-Plastic Regime", Am.Soc.Test.Mat.STP 631, pp.3-27, (1977)
- 32- Dowling, N.E. "Fatigue Crack Growth Rate Testing at High Stress Intensities" ASTM STP 631, Amer.Soc. for Testing and Materials, 1977, pp.139-158.
- 33- Vardar, Ö. "Fatigue Crack Propagation Beyond General Yield" Journal of Engineering Materials and Technology, Vol 104, No.3, 1982, pp. 192-199
- 34- Jolles, Mitchell "Effects of Load Gradient on Applicability of a Fatigue Crack Growth Rate-Cyclic J Relation" ASTM STP 868, Amer. Soc. for Testing and Materials, 1985, pp.381-391
- 35- Mowbray, D.F. "Use of a Compact-Type Strip Specimen for Fatigue Crack Growth Rate Testing in the High-Rate Regime" ASTM STP 668, Amer.Soc. for Testing and Materials, 1979, pp.736-752.
- 36- Dowling, N.E. "Crack Growth During Low-Cycle Fatigue of Smooth Axial Specimens" ASTM STP 637, Amer.Soc. for Testing and Materials, 1977, pp.97-121
- 37- Minzhong, Z. and Liu, H.W. "Fatigue Crack Growth Under General Yielding Cyclic-Loading" Journal of Engineering Materials and Technology, Vol.108, 1986, pp.201-205

Problems:

1. Cracks 5cm or larger in length can be revealed by visual check in an aircraft. Considering just the fuselage which experiences a stress of 3200 psi during flight, suggest the inspection interval based on the following information: The material is Al 2024-T351. At room temperature $K_{IC}=22$ ksi in; $S_y = 77$ ksi and $da/dN=3 \cdot 10^{-10} (\Delta K)^3$ in units of inches and ksi. Assume $\Delta K_{th}=1.5$ ksi in .

Answer: 10^7 cycles

2. Consider a cylindrical pressure vessel of 20 "inside diameter and 1" wall thickness, made of 7079-T6 aluminum with a yield strength of 65000 psi and a plane strain fracture toughness of 35000 psi in. Experience shows that internal pressurization leads to crack initiation on the inside surface of the cylinder and such semielliptical cracks have typically $2c/a$ ratio of eight. If this vessel must survive 1000 pressurization cycles from 0 to 4000 psi, estimate a safe initial crack size using the only available information for through cracks in panels: $da/dN = 4 \cdot 10^{-18} (\Delta K)^3$, in units of inches/cycle and psi in.

Answer: $a_i = 0.08"$

3. Crack initiation studies have been conducted on C(T) specimens ($B=11\text{mm}$, $W=45\text{mm}$). By the time a crack advance is noted by optical means on the specimen sides, the test is interrupted, the number of cycles of loading is recorded and the specimen is pulled apart. The tunneled crack growth may be converted into effective "uniform" crack growth. Having the information on Δa_{eff} and N_{observed} , you are asked to extrapolate backwards to find the number of cycles at initiation N_i corresponding to $\Delta a=0$. Assume the large crack growth rate expression for this material

$$\frac{da}{dN} = 1.7 \times 10^{-10} (\Delta K)^{2.68} \quad (\text{in units of MPa m and m/cycle})$$

is valid at such short crack lengths.

a_o (mm)	Δa_{eff} (mm)	N_{obs}	$P_{\text{min}} - P_{\text{max}}$ (kgf)
22.50	0.25	10370	0-220
23.60	1.18	100210	20-240

Answer: $N_i = 6300$ and 86000 cycles

4. Consider the compact specimen with $a_0 = 0.9$ " , $B=1$ " , $W=2$ " . The material in question is A514 steel with constant amplitude crack propagation behavior given by $da/dN = 0.66 \cdot 10^{-8} (\Delta K)^{2.25}$ in inches and ksi in. Further properties are $S_y = 100$ ksi, $K_{IC} = 150$ ksi in, $\Delta K_{th} = 7$ ksi in. What is the crack length after 18 min. of operation at 10 Hz with displacement limits

varying between 0 and +0.012 inches?

Answer: $a=1.4$ "

10. FATIGUE CRACK PROPAGATION UNDER VARIABLE AMPLITUDE LOADING

Fatigue crack propagation under variable amplitude loading has an added complication due to interaction (of damages) of loads of different amplitudes. An overload, for example, imposed on a constant amplitude profile (Fig.10.1) leads to retarded crack growth during the subsequent constant amplitude cycling. Usually this retardation is temporary and the CA-crack growth rate is resumed gradually as the effect of the overload diminishes (Fig.10.1). Due to such tensile or compressive overload effects it is not feasible to make predictions for variable amplitude (VA) loading just using CA-data. In general, the damage increment in a certain load cycle will be a function of the damage done by the preceding load cycles (Fig.10.2).

Constant load amplitude fatigue behavior can be regarded as the "steady state" response of a material to cyclic loading. However, cyclic loading in service usually is comprised of a spectrum of variable amplitude load excursions. FCP behavior under variable amplitude loading conditions

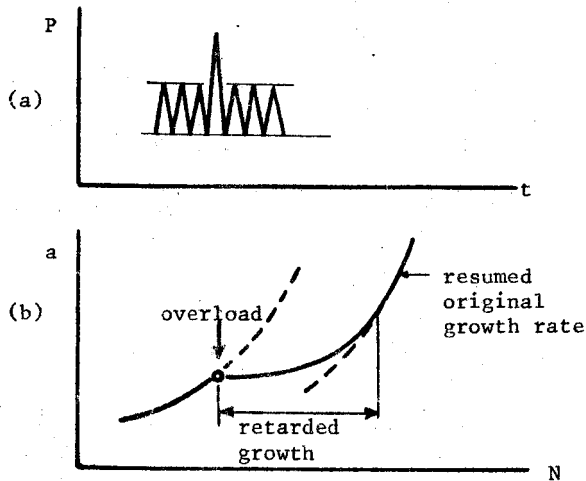


Fig.10-1: (a) Single Overload superposed on a CA-loading (fixed P),
(b) The resulting retardation in crack growth

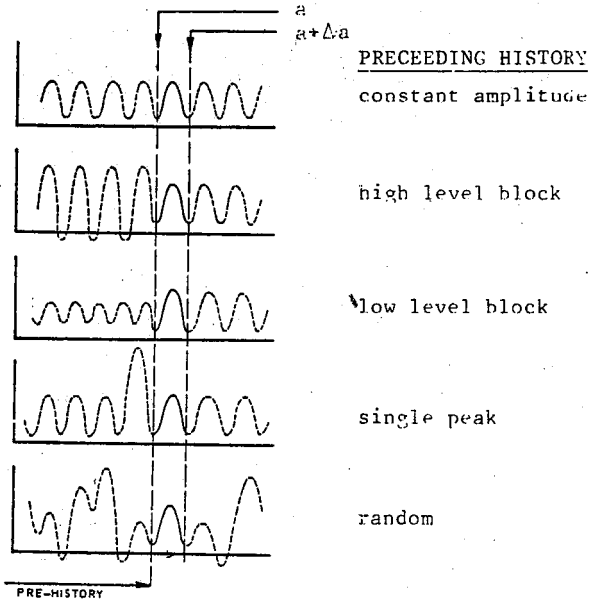


Fig.10.2: History previous to a particular load cycle will dictate the resulting interaction.

includes transient response characteristics not addressed in CA-test. Thus, relative rankings of alloy FCP resistance under spectrum loading can be opposite to rankings obtained from constant load amplitude tests [1].

Several explanations have been proposed as to why retardation occurs. Crack closure model, proposed by Elber, suggests that the effective stress intensity range is disturbed by the overload. Retardation effects associated with low-high and high-low block loading (Fig.10.3), for example, can be explained simply and successfully by the closure concept. During the transition period ΔK_{eff} will differ from the expected value observed under CA-loading and as a result crack growth will be slower (High-low case) or faster (Low-High case). Crack closure and the transitional behavior during step loading also follow from elasto-plastic calculations employing finite element method [2]. Such calculations are fairly expensive but it is highly instructive to know that crack closure considerations can be checked by calculations also [3].

Residual stresses acting at the crack tip are considered as another possibility leading to retarded growth. Nonuniform stress distribution at the crack tip will induce residual compressive stresses upon unloading

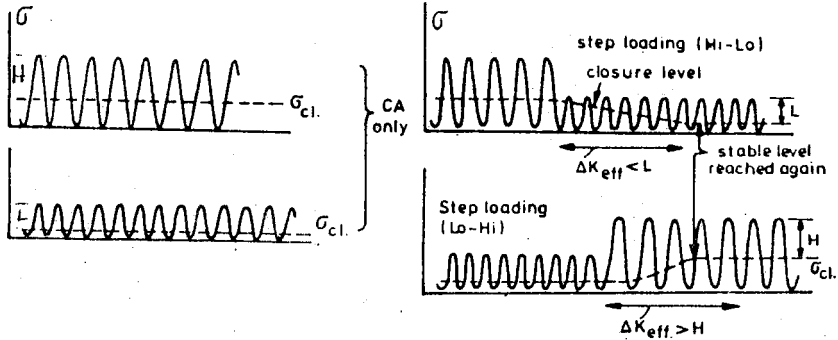


Fig.10.3: Explanation of retardation through closure concept [3]

from a peak load. Single-peak overload, for example, will cause a plastic zone of size

$$r_y^{\text{loading}} = \frac{1}{2\pi} \left(\frac{K_{OL}}{S_y} \right)^2 \tag{10.1}$$

upon loading to a peak stress intensity factor, K_{OL} (Fig.10.4). During unloading a range of $2 S_y$ is available for the material, thus a zone of reversed yielding is created at the tip extending by

$$r_y^{\text{unloading}} = \frac{1}{2\pi} \left(\frac{\Delta K}{2S_y} \right)^2 \tag{10.2}$$

where ΔK represents the range of the overload. For zero-to-tension loading $K_{OL} = \Delta K$ and it is observed that the size of the reversed plastic zone is about 1/4 of the monotonic one. In a region larger than the reversed zone but smaller than the monotonic zone, compressive residual stresses act (Fig.10.4) which tend to close the crack tip. Thus, it is reasonable to expect slower growth rates as the crack tip is enclosed in this compressive field.

Since the material within the reversed plastic zone experiences cyclic straining it might be expected that cyclic strain hardening or softening would result, depending on the starting condition of the material. This has been borne out by microhardness measurements made by Bathias and Pelloux near the tip of a fatigue crack. Extensive softening or hardening within this reversed plastic zone may lead to changes

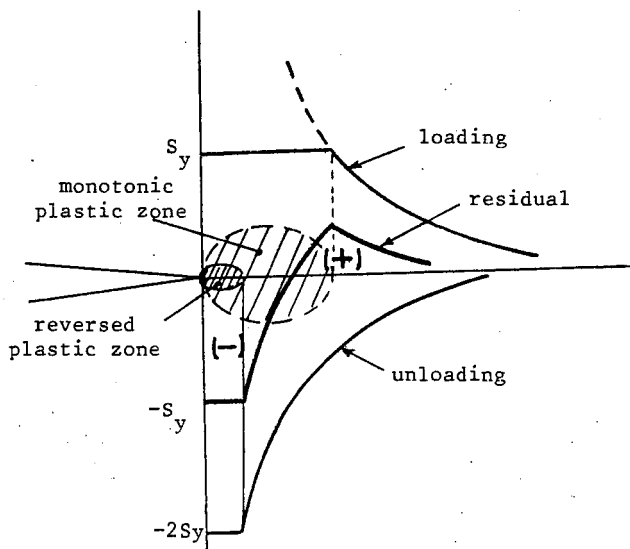


Fig.10.4: Stress pattern at the tip upon a cycle of loading and unloading

in FCP rates which may be another explanation of load interactions.

Crack tip blunting due to high loads is also suspected for leading to retardation. Since the blunted crack would represent a less severe crack tip state, following cycles would be less damaging and the crack growth rate should decrease. The drawback of this model is that it cannot account for the delay in retardation observed after a single overload case.

Another aspect affecting the retardation could be the incompatibility or the mismatch between the load amplitude and the crack front orientation. The low amplitude cycles produce a tensile mode fracture at 90° , whereas the peak loads would produce a shear (45°) fracture. Thus the peak load facing flat fracture surface due to the previous CA-loading will experience a mismatch.

It is difficult to evaluate the relative significance of the various contributions. In general, all or most of them could be operational in a given case.

There is an overwhelming variety of different types of variable-amplitude loading. For an analysis of present knowledge, the various types of loading is classified in a number of groups in table 10.1 [4]

Investigations on overload effects and step loading are usually aimed at increasing the fundamental understanding of the crack growth mechanism under VA-loading. Program loading, random loading or flight simulation studies are more directed towards generating crack growth prediction models and checking their success. The details of the various types of VA-loading will be covered in the following subsections.

Table 10.1: Types of variable amplitude loading with main variables [4]

OVERLOADS	{	single overload repeated overloads blocks of overloads magnitude of overloads (including R) sequence in overloads
STEP LOADING	{	sequence of steps (hi-lo or lo-hi) magnitude of steps (including R)
PROGRAMMED BLOCK LOADING	{	sequence of amplitudes size of blocks distribution function of amplitudes
RANDOM LOADING	{	spectral density function (narrow band, broad band) crest factor (clipping ratio) irregularity factor
FLIGHT-SIMULATION LOADING	{	distribution function of load cycles sequences of flights sequence of loads in flight maximum load in the test

10.1 SINGLE OVERLOADS

Single overload is the primitive building-block of the variable amplitude loading and represents the simplest situation involving retardation. Thus, the response of the material to single overload must be understood well enough for more versatile modeling of random load fatigue.

A large number of single tensile overload experiments have been reported in literature but the issue is complex and no general concensus exists as to the parameters controlling retardation. Excellent studies have been done [5-11] most of which attack different aspects of retardation phenomena. It is difficult to combine the loose ends and to get a coherent picture. The subject deserves more attention and needs "systematic investigation" of

prospective variables as almost all researchers agree upon.

Single tensile overload experiments have been conducted either under fixed load range (Fig.10.1) or under fixed ΔK (Fig.10.5). Symbols associated with such tests are included in figure 10.5. There is an initial

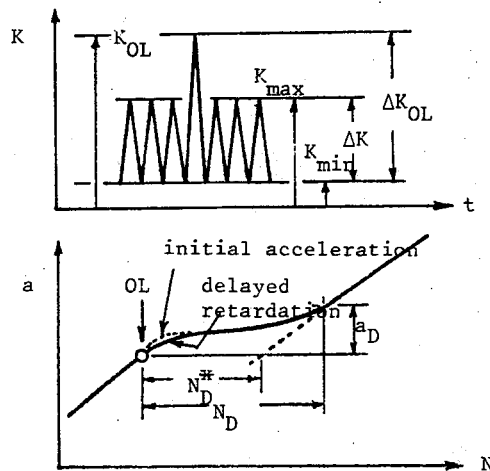


Fig.10.5: A typical single overload case and the resulting retarded growth (fixed ΔK)

acceleration observed in some cases right after the overload. Retardation is not immediate even if acceleration does not take place. The original rate continues over a small distance and the retardation is a "delayed" one. In rare occasions, there is no delay and minimum growth rate occurs immediately following the overload. If the overload is strong enough, crack arrest or abnormally low growth rate is obtained. This crack arrest depends on the material and the stress ratio, R , but typically lies around $K_{OL}/K_{max} = 2.5$

General agreement exists on the following features of single tensile overloading:

- (1) The magnitude of an overload is the most effective factor controlling the length of retardation. Different measures of overload severity have been used in literature. K_{OL}/K_{max} ratio [8,12,13] $\Delta K_{OL}/\Delta K$ [14] and $K_{OL}/\Delta K$ [15,16] are among them. K_{OL}/K_{max} seems to be the most suitable which will be denoted by overload ratio, OLR, here. The results in the open literature, typically, fit an exponential relation of the form

$$N_D^* = b e^{(axOLR)} \quad (10.3)$$

where N_D^* is used to express retardation rather than N_D (Fig.10.5) just for convenience. N_D^* or N_D , by itself, does not have an absolute meaning, however, because of the wide variation in the constant amplitude propagation rates. Normalization with respect to number of cycles at which the crack would travel through the overload effected zone at the overload unaffected rate (i.e. at CA-propagation rate) might enable one to merge data of different alloys or of different R [17] (Fig.10.6).

- (2) Materials with lower yield strength display more retardation at the same load levels, which implies the role of the overload induced plastic deformation.
- (3) Retardation increases as section thickness decreases. Schijve [4] reports for 2024-T3 Al-alloy, for example, doubling of retardation as sheet thickness changed from 10mm to 2mm at $OLR = 1.33$ and $R = 0.67$. For 7075-T6 aluminum a similar trend is reported by Shih and Wei [6] at $OLR = 2$ and $R = 0$. Comparable results on steel are reproduced in figure 10.7

Some of the issues still remain controversial. A group of researchers report that retardation increases with increased base loading range, ΔK , for a given overload ratio, K_{OL}/K_{max} and for a stress ratio R approximately equal to zero. Most of the results relate to aluminum-alloys [6,17,18,19]. Another group observed that retardation decreases with increased base loading range, for similar conditions. Most of the latter results relate to titanium-alloys and steel [5,8,20] but also to an aluminum alloy [15]. This is a puzzling point reflecting the characteristic difficulties of single overloading.

Confusion also exists as to the effect of the R -ratio. Bathias and Vancon [14] report that retardation decreases when R ratio is increased. The data of Bernard et.al [8] on steel and Thomas [15] on aluminum alloy indicate, however, that retardation increases with R ratio, overload ratio held fixed. For negative R , retardation is drastically reduced as R becomes more negative [10]. R value can be increased by keeping K constant but shifting both K_{max} and K_{min} or by keeping K_{max} constant and changing just K_{min} . Hence it may be somewhat misleading just to quote R -effect without reporting the details of the overloading conditions that

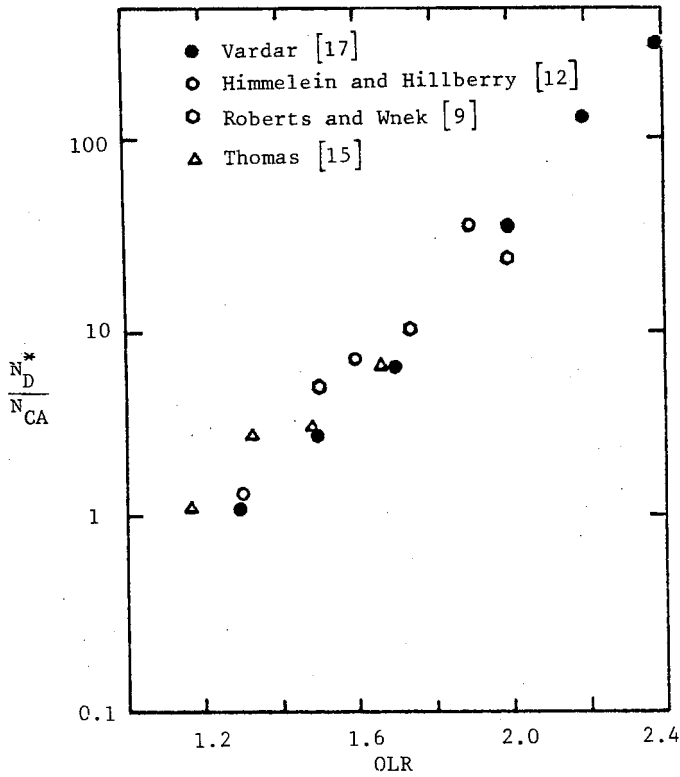


Fig.10.6: Comparison of some published data on the effect of overload ratio on retardation [17] .

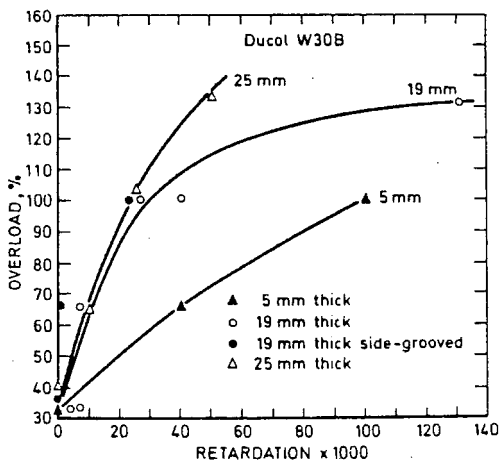


Fig.10.7: Effect of overload level on retardation in Ducol W30B steel specimens of various thicknesses [8]

are compared.

Bretz et.al. [1] and Bucci et.al [21] studied the behavior of 7XXX alloys in simple overload experiments and identified two retardation mechanisms: the overload plasticity leading to increased crack closure and local cracking at second phase particles during high tensile overloads. The first mechanism is the classical hypothesis and it is yield strength dependent. The second mechanism causes part of the crack tip stress intensity to be distributed among local fractures reducing the driving force for crack extension. Thus, it leads to lower fatigue crack growth rates during subsequent CA-cycles. First mechanism dominates when overload plastic strains are too small to cause appreciable secondary cracking at constituents. Local cracking mechanism is expected to be more effective at high ΔK and K_{OL} values. At extreme values of ΔK and K_{OL} (approaching alloy K_{IC}) cracking may even increase the FCP rate. Controversial behavior related to R-ratio or ΔK -range pointed out above may well be due to the interplay of different mechanisms at different load levels.

Retardation is commonly associated with the plastic zone created by the overload and it is assumed to continue as long as the crack tip lies within this overload plastic zone. Hence many investigators have compared the retardation zone size, called a_D in figure 10.4, with the Irwin (or Dugdale) plastic zone size, $2r_y^{OL}$. Some report favorable correlation [7,9,14,22] others [8,20] note poor agreement between the calculated plastic zone size and the observed retardation zone size. The fact that increased frequency affects the number of cycles of retardation but not the retardation zone size, a_D , [14] complicates the issue further.

There is large scatter in published data involving single overloads. Mills and Hertzberg [23] caution that experimental errors which may have little effect on constant amplitude FCP, can significantly alter retardation behavior. It is probable that this unusual scatter disguised certain features of single overloading, even misled researchers in arriving at certain conclusions.

If the single tensile overload is followed immediately by a compressive overload, the retardation - which is expected due to the tensile overload - is partially eliminated. It is related to the compressive overload wiping out the residual stress patterns of the tensile overload. The growth rate, then, is close to CA-case [4,24] (Fig. 10.8).

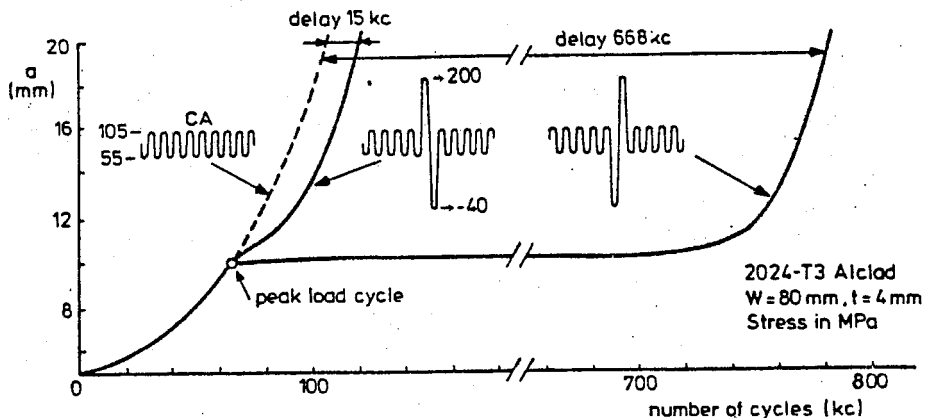


Fig.10.8: Highly different crack growth retardations caused by a single peak load cycle with max \rightarrow min and min \rightarrow max sequence [25]

Compressive overload becomes less effective when separated from tensile overload. Mills and Hertzberg [23] report that a separation of one-fourth of the overload effected zone of a single peak overload case, i.e. $a_D/4$, renders the compressive overload ineffective.

If the compressive overload precedes the tensile overload it is not effective as far as macrocrack growth is concerned since crack faces close in compression and no singularity occurs at the tip. Thus the tensile overload acts alone and retards the crack growth (Fig.10.8). Chang [24] reports this case to be very similar to single overload results. However, if initiation at a notch root or a small crack at the root of a notch is considered, the compressive load is effective since it leads to tensile residual stresses at the root of the notch.

10.2 INTERMITTENT OVERLOADS

When single tensile overloads are applied periodically the resulting retardation depends on the interaction between these overloads. If these overloads are far away from each other they act as isolated events. Mills and Hertzberg [23] report the minimum distance for no interaction to be $3 a_D$, i.e. three times of the overload effected zone of a single peak overload case. For closer overloads the retardation per overload increases.

The maximum retardation is claimed to occur when the second overload is applied at $a_D/4$ [23] or when the crack advance between overloads is less than $0.18 r_y^{OL}$ [19,1]. In materials exhibiting delayed retardation it is also possible that periodic overloads produce less retardation than single overloads [26]. Fleck reports [27] acceleration for very closely spaced overloads (Fig.10.9).

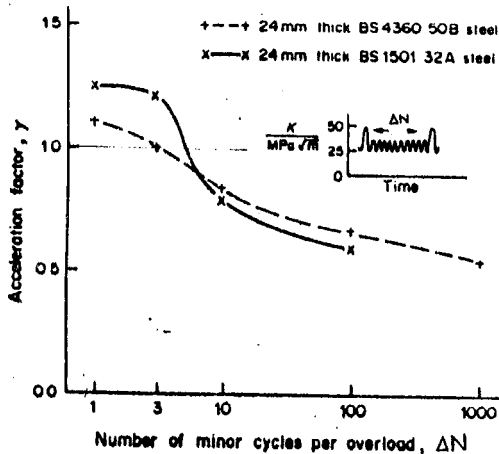


Fig.10.9: Acceleration effect of periodic overloads. γ is the ratio of the measured rate per block to predicted rate by a linear summation of the CA-behavior [27]

Periodic overloads can be expressed in several ways. One neat way [21] is to define an occurrence ratio (OCR) as $\Delta N_{OL} / \Delta N$ where ΔN represents the number of CA cycles between overloads and ΔN_{OL} is the number of overload cycles. Thus, OLR and OCR need to be specified for the simplest spectrum.

The counterpart of periodic overloads is periodic underloads. Periodic underloads—even if they are not compressive—lead to accelerated growth [27,28]. Closer underloads create more acceleration than remote underloads (Fig.10.10). In the terminology of aeronautical fatigue, life is shorter as there are more Ground-to-Air Cycles (GTAC). The increase in growth rate must be associated with the induced residual stresses and not with frequently applied cycles with larger amplitudes. Otherwise the level of ground stress would be important. Fig.10.10a indicates that there is no systematic effect of ground stress S_g . In the case of initiation governed geometries

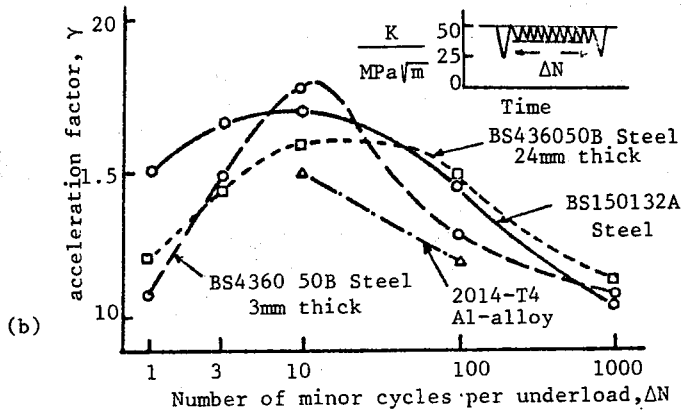
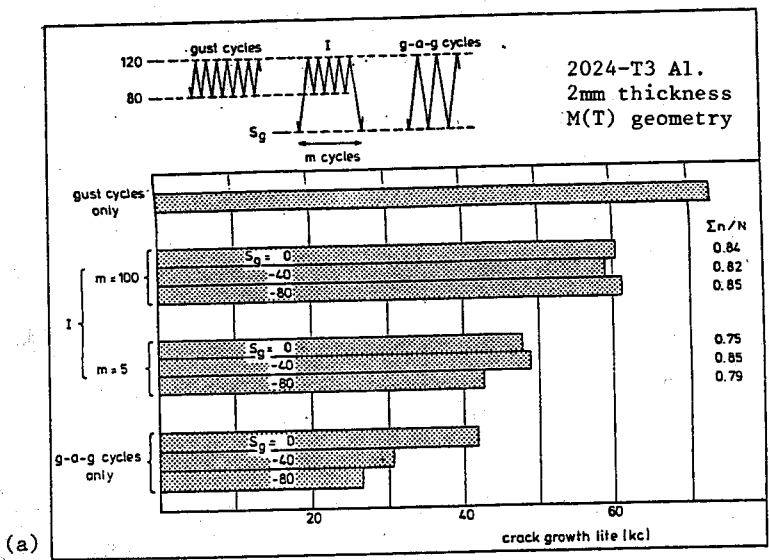


Fig.10.10: Acceleration effect due to periodic underloads
 (a) Ref. [28] (b) Ref [27], γ same as in Fig.10.9.

(such as notched plates), however, life is shorter if the minimum load in the GTAC is going farther down into compression (Table 10.2). It should also be added that conflicting results about underloads do exist. The acceleration due to underloads may be quite small [29] or may be even negative, i.e. underloads may lead to slight retardations instead of accelerations [30].

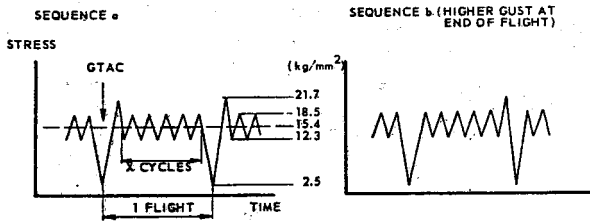
Table 10.2: The effect of minimum stress of GTAC on fatigue life of elliptically notched ($K_t=4$) plates - data of Naumann, Imig and Illg as reported by Schijve [31].

MATERIAL	LOAD SPECTRUM	S_{MIN} in GTAC kgf/mm ²	LIFE flights
7075-T6	Severe gust	0	2699
	spectrum	-7.0	1334
T ₁ -8A1-1Mo-1V	Fairly	0	> 52000
	severe spectrum	-10.5	16600
	representative	-21.1	8500
	of a supersonic transport		

Tension-Compression overloads are mentioned to be much more damaging than compression-tension overloads in the previous subsection. If these overloads are applied periodically the damage apparently depends on ΔN . For large ΔN , there is no interaction and tension-compression sequence leads to much faster growth. Misawa and Schijve [28] report, however, very much the same behavior for periodic compression-tension or tension-compression overloads for $N=4$ as well as for $N=99$. They explain the surprising results by noting that the overload plastic zones are overlapping at low ΔN leading to a stationary retardation for max/min. or min/max. cases. No systematic study is available on the effect of ΔN in macro-crack propagation. But for initiation governed riveted lap joints there is the data of Barrois which qualitatively agrees with the results of Misawa and Schijve (Fig.10.11).

An interesting application of periodic underloads (compressive overloads) is presented by Yu and Ritchie [32]. Cracks arrested at threshold (ΔK_{th}) cycling can be propagated through the application of periodic compression cycles. The amount of crack advance before re-arrest depends on the intensity of the overload (Fig.10.12). Among Al-alloys, 2090-T8E41 seems to respond most to compressive overloads compared to 2124-T351, 7150-T651 and 7150-T751.

Block or program loads may be simple step overloads (as shown in Fig.10.3), periodically repeating simple blocks of fixed amplitude



SPECIMEN : RIVETED LAP JOINT, 2 ROWS OF 5 RIVETS, 2024 - T3 MATERIAL

CYCLES PER FLIGHT (X)		5	10	49	99	999
LIFE	CYCLES : a	19 740	30 380	58 400	59 850	125 800
	b	22 400	28 350	51 500	55 431	84 600
FLIGHTS :	a	3 290	2 762	1 168	598	126
	b	3 733	2 577	1 010	554	85
$\Sigma n / N$	a	0.53	0.51	0.44	0.37	0.63
	b	0.60	0.48	0.38	0.34	0.42

ALL DATA ARE THE MEAN OF THREE TESTS
 FOR GUSTS ONLY N = 205300 CYCLES. FOR GTAC ONLY ($S_{max} = 21.7$ AND $S_{min} = 2.5$ kg/mm²)
 N = 7360 CYCLES
 RESULTS REPORTED BY BARROIS

Fig.10.11: The effect of Ground-to-Air Cycles on the fatigue life in riveted joints [31]

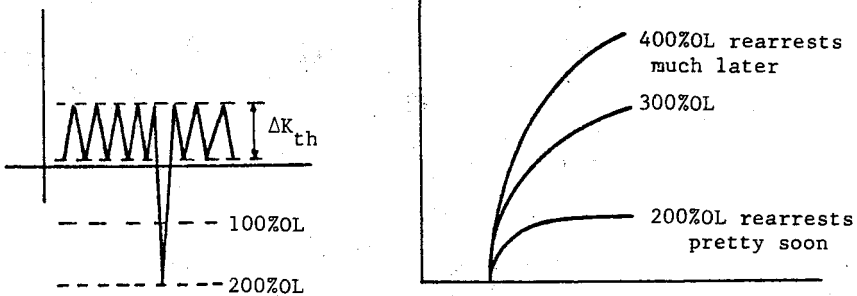


Fig.10.12: Crack growth promoted through compressive overloads [32]

(Fig.10.13a) or sequence programmed blocks(Fig.10.13b). The features of periodic single overloads are carried over to block overloading. There are no general rules, but isolated pieces of information are available. As the number of overload cycles in simple blocks (N_1 in fig.10.13a) increases the resulting retardation increases. Interaction is maximized (i.e. maximum retardation is achieved) at a certain value of N_2 , diminishing as the overload blocks separate further [23]. Low-High-Low program (Fig.10.13b) leads to lower growth rate in the descending part than in the ascending part [4].

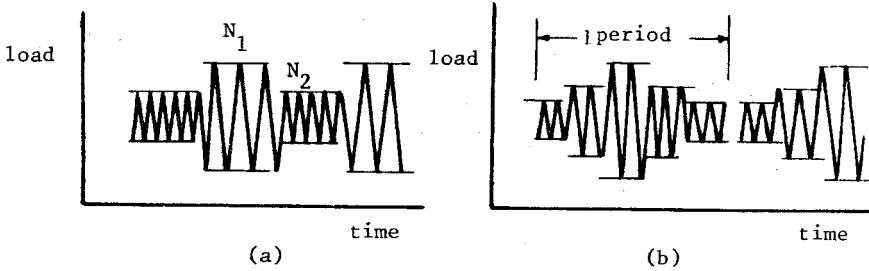


Fig.10.13: Typical block loads: (a) periodic simple blocks
(b) program loading with Lo-Hi-Lo sequence

It is also reported [33] that block loading below threshold levels may influence the crack growth behavior. Application of fatigue underloads with stress intensity ranges below the threshold (ΔK_{th}) can result in significant transient retardations in initial growth rates when cycling is subsequently resumed at base line levels above the threshold (Fig.10.14). The magnitudes of the retardations are found to be dependent on the base-line stress intensity ΔK and underload stress intensity ΔK_u .

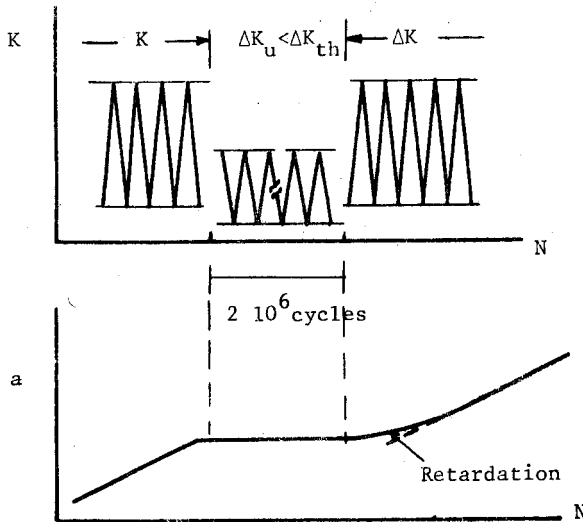


Fig.10.14: A schematic illustration of the loading sequence leading to retardation ($R=0.05$ throughout) [33]

10.3 RANDOM LOADING

Any observed data representing a physical phenomenon can be broadly classified as being either deterministic, if they can be described by an explicit mathematical relationship, or random (stochastic), if such a defined relation between magnitude and time is no longer possible. There are many examples of random processes in nature, some of which are gust loads on aircraft, road roughness along different roads, Brownian motion of particles. The main common feature is an indeterminacy in expected behavior of any single record. Knowledge of the past behavior of a single random record by itself does not give any precise indication of its-future action. The best one can do is to make a particular measurement of interest over large collections (ensembles) of records, then average these individual results in different desired ways so as to determine some of the apparent statistical variations.

A random process (or a stochastic process) is defined formally as an ensemble of time functions $\{x_k(t)\}$, $-\infty < t < \infty$, $k=1,2,3,\dots$, such that the ensemble can be characterized through statistical properties. The functions $\{x_k(t)\}$ of a random process may be functions of time t explicitly, or functions of any other single variable which would take the place of time. For example, $\{x_k(t)\}$ might represent road roughness as a function of distance. Consider a particular ensemble of time functions (Fig.10.15). The subscript k is needed to distinguish one record from another. Ensemble average is

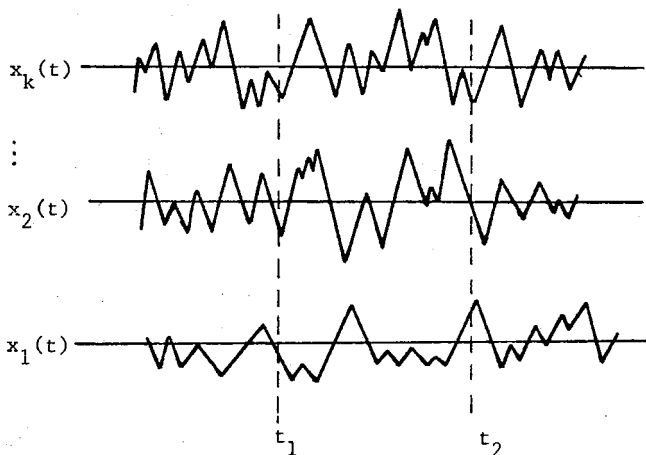


Fig.10.15: A typical ensemble of time functions

the average value of $x_k(t)$ or any function of $x_k(t)$ over the ensemble records at a fixed time t . This is an average over Fig.10.15 in a vertical direction at the point $t=t_1$ and is clearly a function of the particular point t_1 chosen. At a different time $t=t_2$ similar ensemble averages may be calculated and, in general, ensemble averages at t_1 are not related to averages at t_2 . Random processes of this general type are known as nonstationary random processes.

For suitably restricted phenomena, it may happen that averaging over large numbers of different records at time t_1 gives the same answers as at time t_2 , and, in fact, that all statistical quantities associated with the random process are invariant with respect to time translations. Such processes are known as stationary random processes and represent a subclass of nonstationary random processes. If the stationary random process is further restricted so that:

(i) each record of the ensemble is statistically equivalent to every other record;

(ii) ensemble averages over a large number of records at fixed times may be replaced by corresponding time averages on a single representative record of the ensemble;

then such processes are said to be ergodic. In particular, referring to Fig.10.15, averaging in a vertical direction at, say $t=t_1$ over 100 different records must give essentially the same result as averaging a single arbitrarily chosen record $x_k(t)$, k fixed, in a horizontal direction over 100 different values of t .

Typical service loads are random in nature. But it is very difficult to categorize such random processes into stationary, nonstationary or ergodic processes. Particularly if the available time functions are limited, it is impossible. Mostly, it will be assumed that service loads are a mixture of stationary random loads and deterministic loads—such as ground-air-ground transitions. Stationary and ergodic signals are fully described by their probability density function and power spectral density. The former describes the distribution of amplitudes in the signal and the latter describes the frequency content. The overall magnitude of the signal can be characterized by the root mean square (rms) value of the signal. The probability density functions can take many forms such as uniform, triangular or Gaussian (Fig.10.16).

A large variety of physically observed random waveforms can be accu-

rately represented as sample functions selected from Gaussian processes. The Gaussian process has also a number of mathematical features which make analysis relatively simple in many situations which otherwise would present great difficulties. A general mathematical solution for the description of random vibrations does not yet exist; it is only available for Gaussian processes.

A stationary Gaussian process is completely specified by its power spectral density function, and is ergodic provided the power spectral density function is continuous. The power spectral density function, ϕ , should be considered as a density distribution function of the energy in the frequency domain. Some examples of stationary Gaussian random noise and the corresponding power spectral density functions are shown in figure 10.17.

The energy is concentrated in a narrow frequency band in Fig.10.17(a). This narrow band random loading is typical for resonance systems, which predominantly respond at one single resonance frequency if activated by

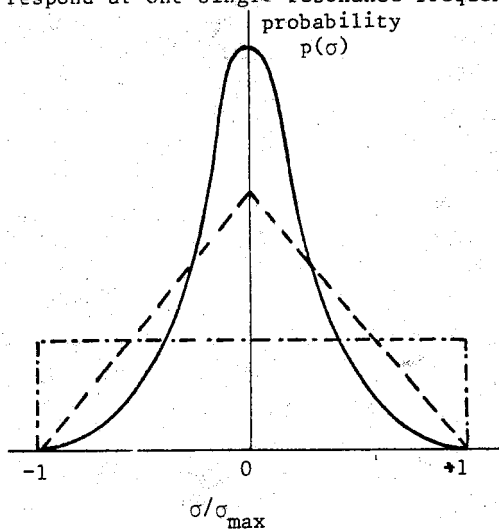


Fig.10.16: Probability density functions: Gaussian(—), triangular (---), uniform (-.-)

some external random process over a broader frequency range. In fig.10.17(c) the spectral density function of the random signal covers a much wider frequency band and the corresponding broad band random loading shows a higher degree of irregularity. White noise is referring to $\Phi(\omega) = \text{constant}$, i.e. the same energy at all frequencies.

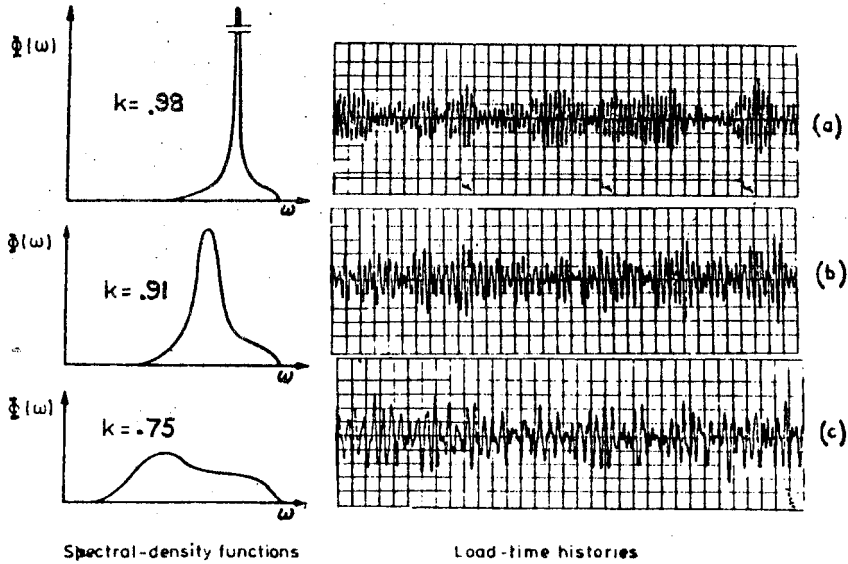


Fig.10.17: Typical random oscillations and their power spectral density functions [3]

Since $\phi(\omega)$ fully characterizes stationary Gaussian random load typical properties can be derived from ϕ . If we consider a stress $\sigma(t)$ varying randomly around a (constant) mean stress σ_m , the root mean square of $\sigma - \sigma_m$ follows from

$$\sigma_{rms} = \left\{ \lim_{T \rightarrow \infty} \frac{1}{T} \int_0^T (\sigma - \sigma_m)^2 dt \right\}^{1/2} = \left\{ \int_0^\infty \phi(\omega) d\omega \right\}^{1/2} \quad (10.4)$$

Characteristic events of a random signal are the peaks and the mean crossings (Fig.10.18). It will be clear that the number of peaks of a random signal will always be larger than the number of mean-crossings, and this will be more so far more irregular signals. This has led to defining an irregularity factor k as the ratio between the number of mean crossings and the number of peaks, with $0 < k < 1$. The relations to $\phi(\omega)$ are given below.

$$\text{Number of mean crossings per sec. (} \rightarrow \text{ and } \leftarrow \text{)} = N_0 = \frac{1}{\pi} \left\{ \frac{\int_0^\infty \omega^2 \phi d\omega}{\int_0^\infty \phi d\omega} \right\}^{1/2} \quad (10.5)$$

$$\text{Number of peaks per sec. (max. and min.)} = N_1 = \frac{1}{\pi} \left\{ \frac{\int_0^{\infty} \omega^4 \phi d\omega}{\int_0^{\infty} \omega^2 \phi d\omega} \right\}^{1/2} \quad (10.6)$$

$$\text{Irregularity factor} = k = \frac{N_0}{N_1} = \left\{ \frac{\int_0^{\infty} \phi d\omega \int_0^{\infty} \omega^4 \phi d\omega}{\left(\int_0^{\infty} \omega^2 \phi d\omega \right)^2} \right\}^{1/2} \quad (10.7)$$

The probability density function of the peak values (i.e. the envelope) can also be derived from ϕ , but it is a fairly complex equation. For narrow band random loading ($k \sim 1$) it reduces to a simple relation known as the Rayleigh distribution. Fig. 10.19 shows the probability density functions, for maxima only. It confirms for narrow band loading that all maxima occur above the mean (σ_{\max} always larger than σ_m), whereas for more irregularly random loading ($k \sim 0.75$) σ_{\max} values below σ_m do occur [3]

The load on a structure in service can be measured for a long period in order to be representative. As a result, the series of maxima and minima will become a very large one and for practical reasons it is then condensed to exceedance curves. An exceedance curve — which is a cumulative distribution function — specifies how often a certain event (e.g. the given peak value, the crossing of a given level or a range of given magnitude) is exceeded (Fig. 10.21 or Fig. 10.29). That is, if level A is exceeded n_1 times and level B is exceeded n_2 times, there will be $n_1 - n_2$ events of a load between levels A and B. These loads will be lower than B, but higher than A. Basically, there are an infinite number of load levels in this range. However, there are only $n_1 - n_2$ occurrences, which means that the number of load levels to be encountered is finite; not every arbitrary load level will be experienced. As a consequence, the spectrum must be approximated by a finite number of levels (as in Figure 10.21). A variety of counting methods have been developed to determine ranges, level crossings etc. But, information on the sequence of load occurrences is lost in such a statistical exceedance description. Investigations on sequence effects have clearly shown their significance. Results of a comparative study on crack growth with random and programmed sequences are summarized in the figure below (Fig. 10.20). Although all sequences were statistically equivalent with respect to load occurrences, the crack growth rates were significantly different. Moreover, the fracture surfaces were also different, even macroscopically. Both the roughness

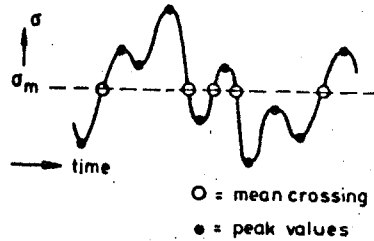


Fig.10.18: Peak and mean crossing values of a random signal

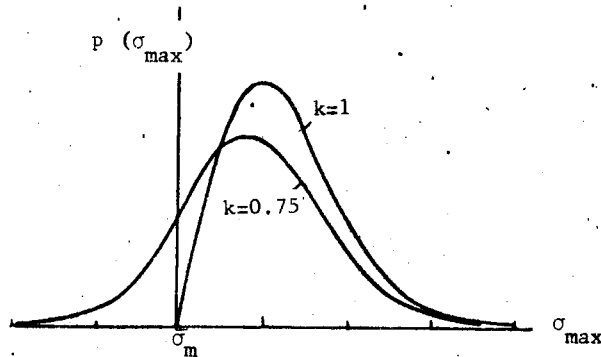


Fig.10.19: Probability density function of the peak values

of the fracture surface and the transition from the tensile mode to the shear mode were different. The conclusion to be drawn here is that complete knowledge about loads in service should include information on load sequences [4] .

10.4. FLIGHT SIMULATION LOADING

Flight simulation loading is a realistic simulation of the load history in service. Flight simulation tests are carried out for various purposes, such as [34] :

- (1) Testing of full scale structures to examine fatigue critical items of the structure
- (2) Tests carried out on specimens to obtain crack growth data to aid the aircraft structural design.
- (3) Comparative tests to study the effects of certain variables, e.g. type of alloy, surface treatment, joint design etc.

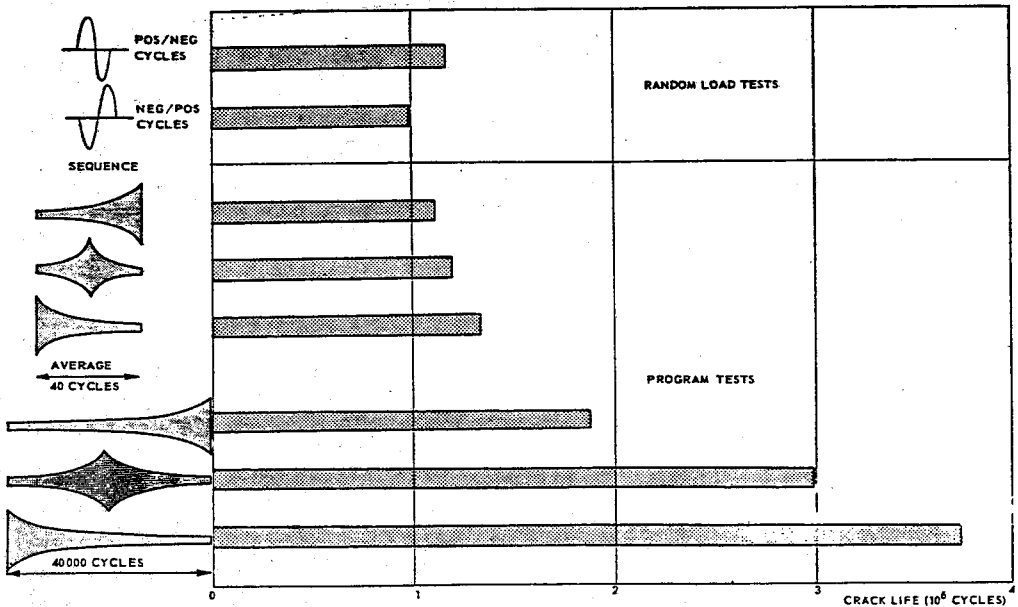


Fig.10.20: Cycles for crack growth from 24mm to 100mm in 2024-T3 alclad sheet specimens [31]

(4) Tests carried out to generate data for checking prediction methods on fatigue life and crack growth.

For the first and second purposes the load spectrum of the relevant aircraft project will be used. For the third and fourth purposes the use of "standard" load sequences has many advantages. Some years ago two standardized load histories were developed for aircraft wings to use in comparative flight simulation testing. The load history TWIST (Transport Wing Standard) is supposed to be representative for the wing tension skin of a transport aircraft. FALSTAFF (Fighter Aircraft Loading Standard For Fatigue) should be typical for the wing root area of a fighter type aircraft. More recently, standardized load histories for helicopter rotor components have been proposed. Helix and Felix represent the loading standards for helicopters with hinged and fixed rotors, respectively. In hinged or articulated rotors the point of maximum bending moment is located at about half rotor radius whereas in fixed or semi-rigid rotors it occurs at the blade root.

The essential requirement for a flight-simulation test is that it

should produce the same fatigue damage accumulation in a much shorter time than the simulated service load history will do at a fully different time scale, that means the same damage after the same number of flights. Because a flight-simulation test should be completed in a relatively short testing time, it has to be an accelerated test. The sequence of load peaks (maxima and minima) can still be representative for the service load history, but the time scale is transformed considerably. Periods without load variations are omitted, small cycles, which are assumed to contribute insignificantly to fatigue are also left out, and loading rates are increased. It is certainly possible that time-dependent influences (e.g. corrosion fatigue) can be more serious in service. But comparative flight-simulation tests at 10 Hz, 1 Hz and 0.1 Hz have shown the same crack rates in 2024-T3 Alclad and 7075-T6 clad material with water vapor as the aggressive element. Present knowledge appears to indicate the constant effect of water vapor on many service conditions as well as on testing in the lab [4]. For more aggressive wet environments the time scale may certainly be significant.

10.4.1 Standard Load Sequences: Some essential points of standardized load sequences used in aircraft industry will be discussed in the following. The discussion is limited to mechanical loading histories. Temperature profiles and humidity cycles used in testing of nonmetallic materials (e.g. fiber reinforced composites) or turbojet engines are not covered here.

FALSTAFF

In order to determine features common to fighter aircraft the loading environment for fighters may be roughly characterized as follows. Loading is primarily due to manoeuvres causing upward bending moments with wing tension skins often being fatigue critical. Usually, the mean flight stress level is relatively low and the ground-air-ground transition is relatively small. Often, the subsequent manoeuvre loads appear in a systematic manner, contrary to the random order which is typical for gust loading.

FALSTAFF is a loading standard considered representative for the load time history in the lower wing skin near the wing root of a fighter aircraft [35]. It represents a block of 200 flights which is the average european annual fighter utilization. The data used was selected from actual loading

data pertaining to five different fighter aircraft types operated by three different air forces. The overall manoeuvre spectrum of the 200 flights is markedly asymmetric (far more positive than negative load increments) with the upper part having a convex shape. Loading spectra derived for different fighters usually have this characteristic shape but differ mainly in severity. From the loading data a stress history was derived such that the final result consisted of a uniquely defined sequence of 17 983 peaks and 17 983 troughs, ranging from 1 to 32 (equidistant discrete levels with 1 corresponding to the lowest trough value and 32 to the highest peak value). Fig.10.21 and table 10.3 describe the details of the spectrum. Ground loads were represented by insertion of two full cycles before and after each set of airborne loads. A sample of the FALSTAFF loading sequence and the distribution of severe flights are given in Fig.10.22 and 10.23. respectively.

FALSTAFF load level units

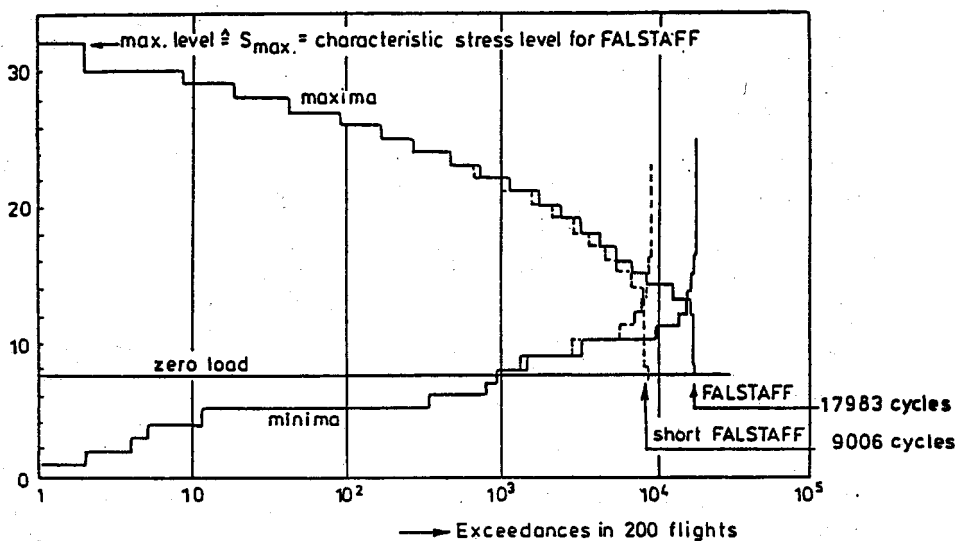


Fig.10.21: Standardized non-symmetrical load spectra for FALSTAFF and short FALSTAFF (see also table 10.3)

In order to save testing time a shorter version of FALSTAFF was proposed, labeled as "short FALSTAFF". It was obtained by omitting small ranges as counted by the rainflow count method. Ranges equal or smaller than three FALSTAFF load level units were omitted (see fig.10.21 and

table 10.3). This reduced the number of load cycles by about 50%, which implies a reduction of the average number of cycles per flight from 90 to 45 cycles.

Table 10.3 Load spectrum for FALSTAFF and short FALSTAFF [35]

level	block of 200 flights			
	FALSTAFF		short FALSTAFF	
	no of peaks	no of throughs	no of peaks	no of throughs
32	2	0	2	0
31	0	0	0	0
30	7	0	7	0
29	10	0	10	0
28	24	0	23	0
27	45	0	44	0
26	76	0	74	0
25	104	1	101	0
24	193	2	183	1
23	233	3	213	1
22	404	4	377	1
21	533	12	484	2
20	640	23	540	3
19	954	37	805	10
18	987	69	803	20
17	1151	135	868	35
16	1282	234	943	85
15	1999	327	1304	143
14	4145	511	1398	228
13	4058	716	218	377
12	493	1445	9	750
11	43	4387	0	1640
10	0	6711	0	2871
9	0	1941	0	1457
8	455	543	445	500
7	155	36	155	36
6	0	508	0	508
5	0	327	0	327
4	0	6	0	6
3	0	1	0	1
2	0	2	0	2
1	0	2	0	2
Σ	17983	17983	9006	9006

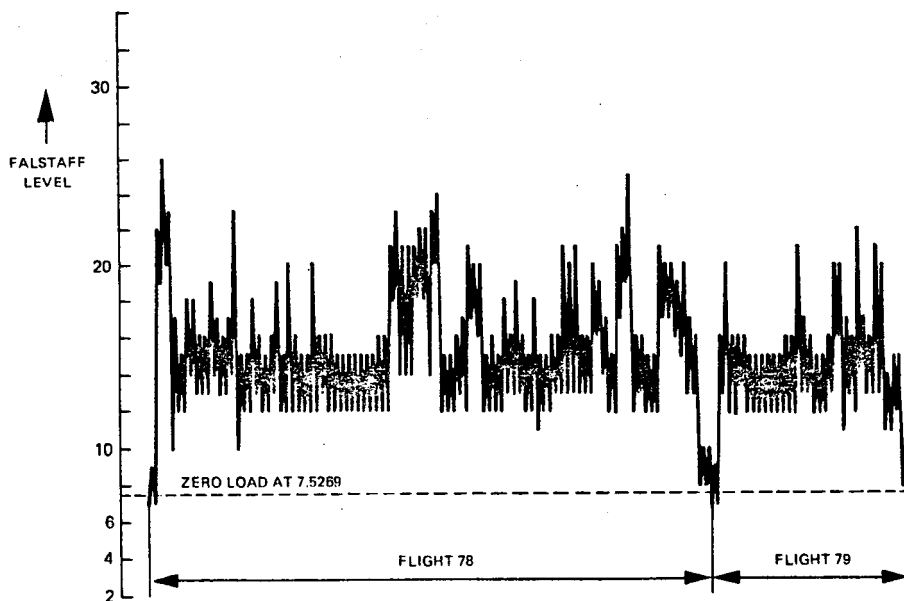


Fig.10.22: Part of FALSTAFF sequence

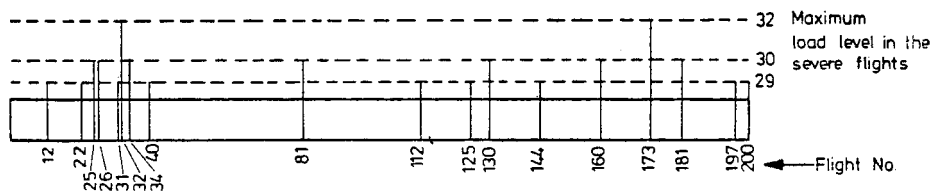


Fig.10.23: Sequence of the severe flights in FALSTAFF

TWIST

The TWIST standard represents the loading environment of lower wing skins of transport aircraft due to gust loading. General features of this type of loading are that the flight load cycles were superimposed on a tensile l-g. flight stress. Taxi load cycles were superimposed on a compressive ground stress giving rise to a pronounced ground-air-ground cycle. Measurements on a variety of transport aircraft showed the sym-

metric gust load spectra with a concave shape. The stepped test load spectrum for 4000 flights is shown in fig.10.24 and table 10.4. All gust loads start from the mean stress in flight, S_{mf} , and return to this stress level. The mean stress in flight is the characteristic stress level of the TWIST load spectrum. All other stress levels are directly related to S_{mf} . Taxi loads are represented by one transition only to a "severe" ground level.

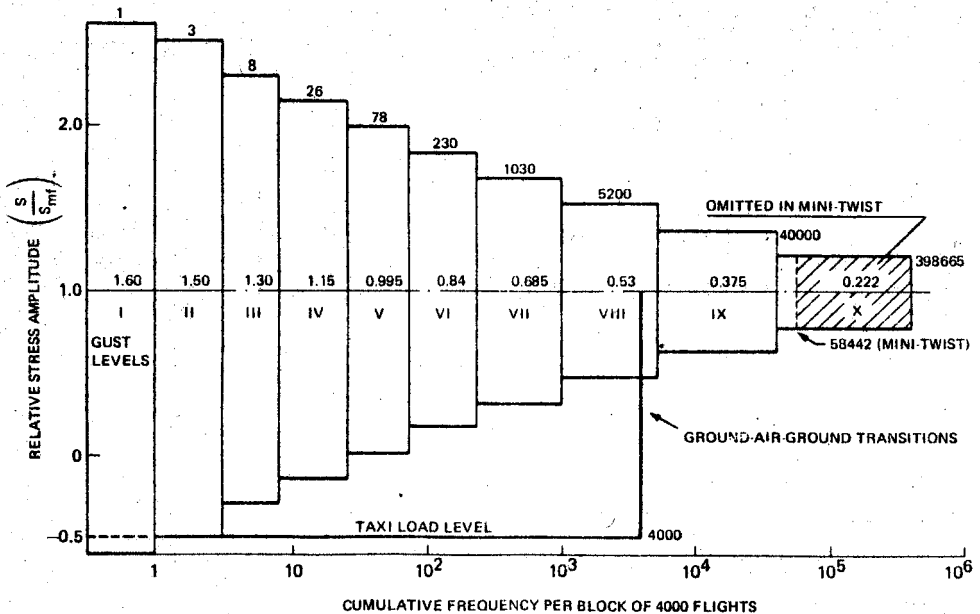


Fig.10.24: The test load spectrum pertaining to TWIST and mini TWIST [36]. A sequence lengths of 4000 flights was thought to be sufficiently large to ignore any sequence effect. The loads were distributed over 10 different flight types varying from very smooth (J-flight) to extremely rough (A-flight), each of them having loading spectra with similar shape but differed in severity. The final TWIST sequence consists of 398 665 gust load cycles plus 4000 ground-air-ground cycles and is uniquely defined by its spectrum content from Fig.10.24 plus a sequence generation algorithm. The average flight length is about 100 cycles per flight. A sample of the TWIST standard is given in Fig.10.25.

Since the number of 100 cycles per flight was sometimes considered as relatively long a shortened version was created, called mini TWIST [36], Omission of most of the cycles of the smallest amplitude (Fig.10.24) resulted in mini TWIST having about 15 cycles per flight which gives

Table 10.4: Load levels, numbers of cycles and flights in one block of 4000 flights according to the TWIST load sequence [36]. Number of cycles for mini TWIST are given in parantheses.

Flight type	Number of flights in one block of 4000 flights	Number and magnitude S_a/S_{mf} of amplitude level										Total number of cycles per flight
		I	II	III	IV	V	VI	VII	VIII	IX	X	
		1.60	1.50	1.30	1.15	0.995	0.84	0.685	0.53	0.375	0.222	
Number of cycles per flight												
A	1	1	1	1	4	8	18	64	112	391 (391)	900 (0)	1500 (600)
B	1		1	1	2	5	11	39	76	366 (385)	899 (0)	1400 (520)
C	3			1	1	2	7	22	61	277 (286)	879 (0)	1250 (380)
D	9				1	1	2	4	44	208 (208)	680 (0)	950 (270)
E	24					1	1	6	24	165 (168)	603 (0)	800 (200)
F	60						1	3	19	115 (107)	512 (0)	650 (130)
G	181							1	7	70 (72)	412 (0)	490 (80)
H	420								1	16 (16)	233 (23)	250 (40)
I	1,090									1 (1)	69 (4)	70 (5)
J	2,211										25 (2)	25 (2)
Total number of cycles per block of 4000 flights		1	2	5	18	52	152	800	4170	34800 (34800)	358665 (18442)	
Cumulative number of load cycles per block of 4000 fl.		1	3	8	26	78	230	1030	5200	40000	398665 (58442)	

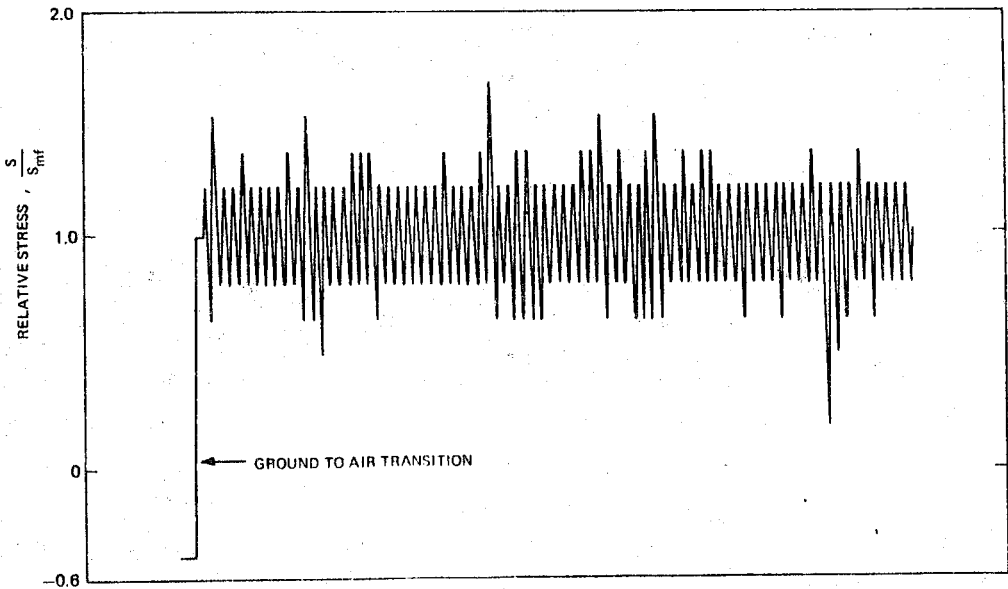


Fig.10.25: A cutout of a "D" flight loading trace within TWIST [37]

much shorter testing times (Fig.10.26).

Helix and Felix

The forces acting on a rotor blade in a helicopter consist of a lift force, a drag-moment and a centrifugal force. In general, each rotor revolution gives one basic load cycle. Normal rotor speeds are in the order of 3 to 7 cps yielding 10 to 25 million cycles per 1000 flights. Thus, the dynamic loading may be characterized by a large number of flight load cycles with relatively small amplitude superimposed on a constant tensile stress due to centrifugal forces. Compared to the rotorspeed the amplitude of these cycles varies slowly so that a sample of a load-time trace has the appearance of a sequence of different blocks representing periods spent in discrete manoeuvres, with each of those blocks containing cycles with relatively constant amplitude. Between the flights pronounced ground-air-ground cycles occur associated with rotor stop and downward bending of the blades under their own weight. Because of

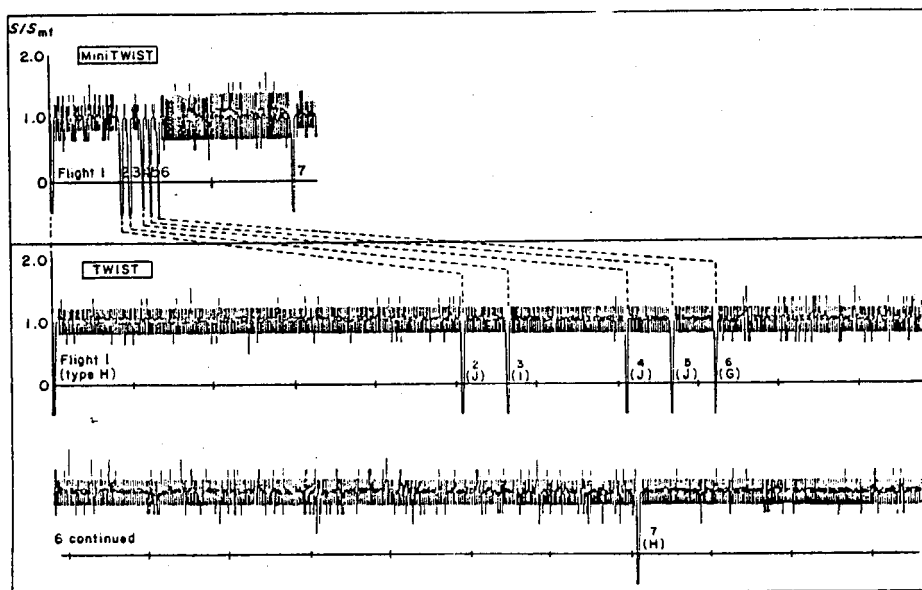


Fig.10.26: Comparison between load histories of TWIST and mini TWIST. The first 6 flights [34] .

the high cycle character of helicopter fatigue it must be expected that a relevant standard must have an extensive sequence length. Helix and Felix, indeed, have more than 2 million cycles representing 140 flights. The positive level cross count of these standards is shown in Fig.10.27 and a sample of the Helix sequence is reproduced in Fig.10.28.

10.4.2. Planning Flight-Simulation Tests: Carrying out a flight-simulation test necessitates decisions on load spectrum, load sequences, truncation of high loads or omission of numerous low-amplitude cycles, etc. In order to weigh the consequences of such choices the available empirical trends should be studied [34] :

Truncation of high loads: In flight simulation tests it is well established that the application of rarely occurring very high loads can decrease the crack growth rate significantly. Truncation of the high loads (reducing

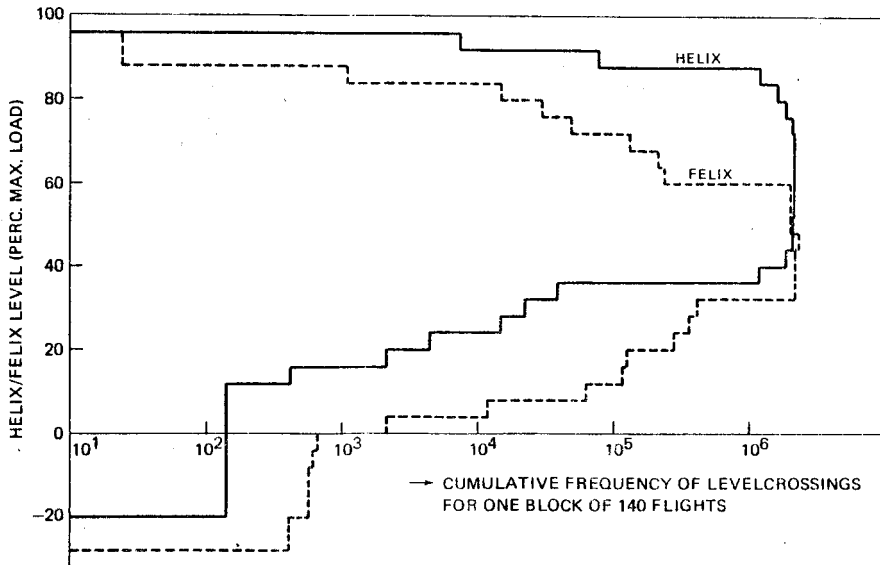


Fig.10.27: Helix/Felix level cross counting [37]

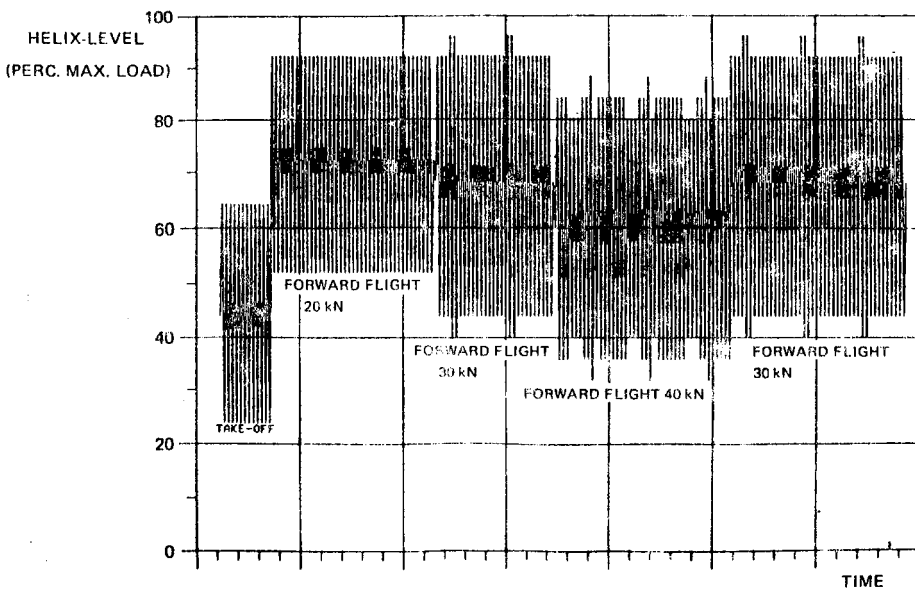


Fig.10.28: Beginning of Helix training-flight (representing 90 seconds flight time) [37]

the amplitude) usually implies a shorter fatigue life and faster crack growth(chopping of the high loads is termed "clipping" by some authors). The effect is larger for crack propagation as compared to crack initiation life.

In notched geometries (initiation governed) the effects of truncating high loads are more significant for gust dominated spectra than for manoeuvre dominated spectra, which is associated with the differences between the shapes of the two types of spectra. Fatigue under a manoeuvre load spectrum is more similar to high-level fatigue. Fatigue under a gust spectrum with rarely occurring high loads is more sensitive to fatigue damage interaction effects, such as caused by truncation of high loads. In macrocrack growth, there is no clear difference between the truncation effects for gust spectra and manoeuvre spectra.

In a full-scale test very high peak loads should be avoided in view of their beneficial effect on fatigue, which could easily lead to unconservatively optimistic results. Since all aircraft of a fleet will not meet those rarely occurring high loads, it is suggested by Schijve and coworkers that the load spectra should be truncated at a load level, which (on the average) will be exceeded, say, 10 times in the aircraft life (Fig.10.29).

Omission of low amplitude cycles: Large reductions of testing time can be obtained by omitting low-amplitude cycles or small load variations (some authors prefer to call this truncation). The time-saving can be significant for a civil transport wing spectrum, but it will be smaller for a fighter wing load spectrum (Fig.10.29). Unfortunately the empirical data suggest that omissions lead to significant increases in life for civil transport (gust) spectrum. The effect is smaller for the manoeuvre spectra. Fatigue under fighter wing spectra being more related to high level fatigue, it can be argued that the contribution of low amplitude cycles in such spectra will be relatively small. Specific correlations cannot be deduced from experiments in view of the large variety of test conditions. As far as the standardized load sequences are concerned, both initiation and propagation lives for MiniTWIST were about twice as long as for TWIST. Differences between FALSTAFF and short FALSTAFF were small or negligible in most test series [34].

The omission of small cycles from a full-scale fatigue test is a

particularly serious problem. In such a test much is to be gained if many cycles can be dropped. However, a structure contains many different notched elements, materials and thicknesses, and as a consequence the effect of omitting small cycles can be different for different components. In addi-

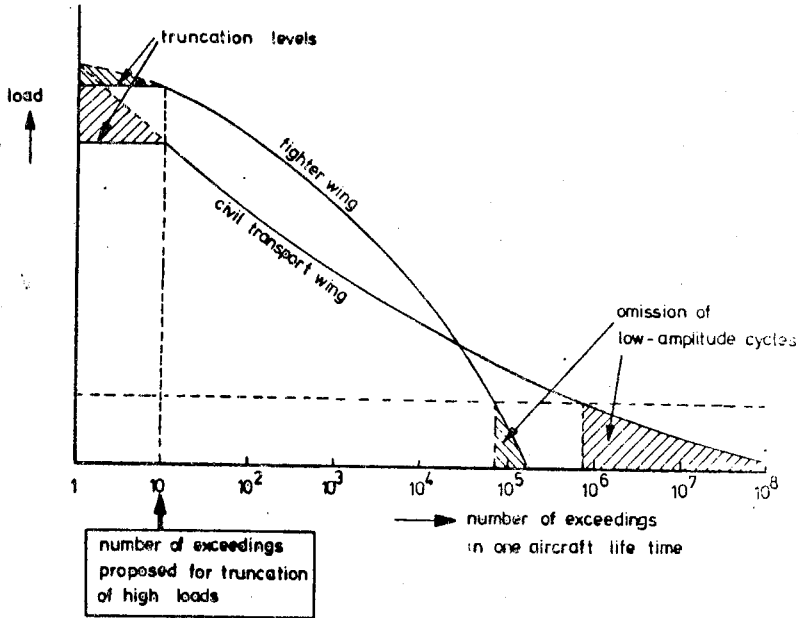


Fig.10.29: Truncation of high loads and omission of low amplitude cycles [34]

tion to that, the stress history can also be different for different components — such as that of the lower and upperskin of a transport aircraft wing. A full scale test should be preferably complemented by flight-simulation tests on specimens to explore the effect of small cycles. The specimens need to be representative for fatigue critical details of the structure (e.g. joints, materials, etc.).

Design stress level: In flight-simulation tests a characteristic design stress level is adapted such that if the design stress level is changed all stress levels of the load spectrum will vary in a linearly proportional way. For TWIST the mean stress in flight (S_{mf}) was adopted, while for FALSTAFF the maximum stress (S_{max}) of the untruncated load spectrum was used.

Higher stress levels are observed to lead to shorter lives for both initiation and propagation cases. Typically

$$\log S = \text{Constant} - \frac{1}{m} \log N \quad (10.8)$$

with m values clustering around 3-6. The m values depend on the category of spectrum, the kind of structural detail and the type of material. Schijve's compilation [34] for Al-alloys is given in table 10-5. Log linear relation does not hold at low fatigue lives and higher m values are obtained at high stress levels. At lives below 10^4 flights m values extend up to 10-13. The scatter is fairly large.

Table 10.5: Median values of slope factor m for Al-alloys [34]

structural detail	load spectra			
	transport wing		fighter wing	
	2XXX	7XXX	2XXX	7XXX
open hole	5	6	5	3.7
double shear joint	5.6	5	-	4.2
single shear joint	4.2-8	4	4.7	4.2
lug	8.3	3.8	4.5	3.5
bonded lap joint	4.7	-	-	-
crack growth (through cracks)	4.7	3	3.3	2.8

Sequence effects: Sequence effects on life (initiation) and crack growth (propagation) appear to be minor provided a randomized sequence of flights or randomized sequence of loads in a given flight is considered. Negative/positive peaks or positive/negative peaks seem to yield the same growth rate in a flight-simulation test [34]. The rather dominant sequence effect of intermittent overloads is no longer significant in flight-simulation tests (Fig.10-30).

The minimum stress of the GAG cycle and clipping of the compression loads:
 The ground-air-ground (GAG) cycle is important for civil transport wing (gust dominated) spectrum. The minimum stress of this cycle has an accelerating effect on fatigue crack initiation as well as propagation. Large amount data indicate that a more severe GAG cycle gives shorter lives. Clipping the negative part of the GAG cycles or clipping the negative part of the flight loads are analogous and lead to larger life, in general. If one compares these results with those of Misawa and Schijve (Fig.10.10a)— where there is no effect of lower S_{ground} on life — one observes that the conclusions of intermittent loading do not coincide with those of flight-simulation loading.

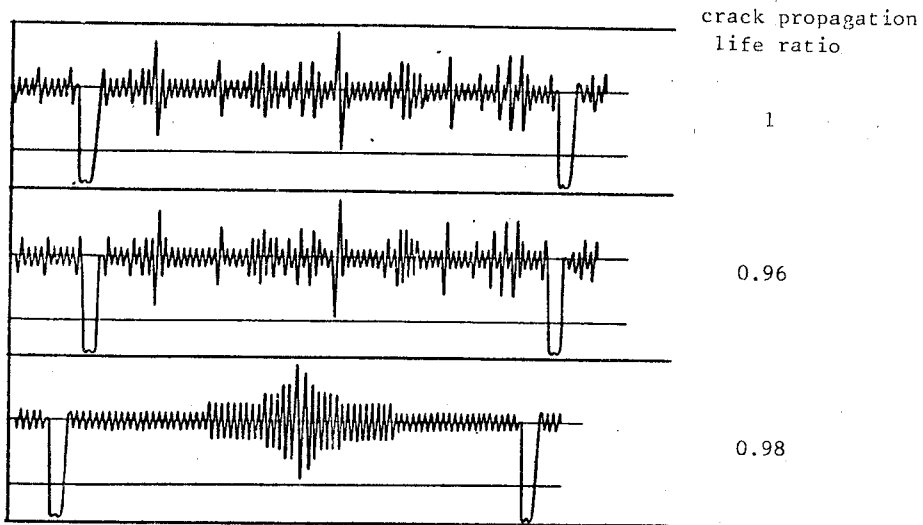


Fig.10.30: The effect of cycle sequence in flight-simulation tests on 2024-T3 and 7075-T6 Al-alloys. The crack life covers propagation from $2a=20\text{mm}$ to complete failure of the sheet ($W=160\text{mm}$) [34]

10.5 PREDICTION MODELS

Service simulation fatigue tests are extremely time-consuming and expensive. The analytical alternative is to develop a prediction model and obtain information on crack growth through numerical computation. In the literature three different categories of prediction models for VA-loading are presented.

(1) Non-interaction models

- (2) Cycle-by-cycle models, including some interaction mechanism
- (3) Empirical models, not employing CA-crack growth data

Some of the approaches are extremely detailed and require long computing times whereas others may be evaluated using a simple calculator. The prediction model is the vital element for reliable and accurate crack growth predictions under VA-loading. However, even if we have a good prediction model, there are still several other problems involved, which will effect the reliability and the accuracy of the predicted crack growth. The significance of these problems can be judged only after a detailed analysis of all steps schematically indicated in Fig.10.31. It is not reasonable to require a high precision of the prediction model if the input data are not accurately known.

The amount of retardation in a given VA-loading depends on the material. Ti 6Al 4V, for example, exhibits nearly two times more retardation than 7075-T351 [38]. Since retardation can reduce ΔK_{eff} to very small values, near threshold fatigue crack growth behavior may contribute significantly to spectrum fatigue performance. Therefore the sensitivity of near-threshold

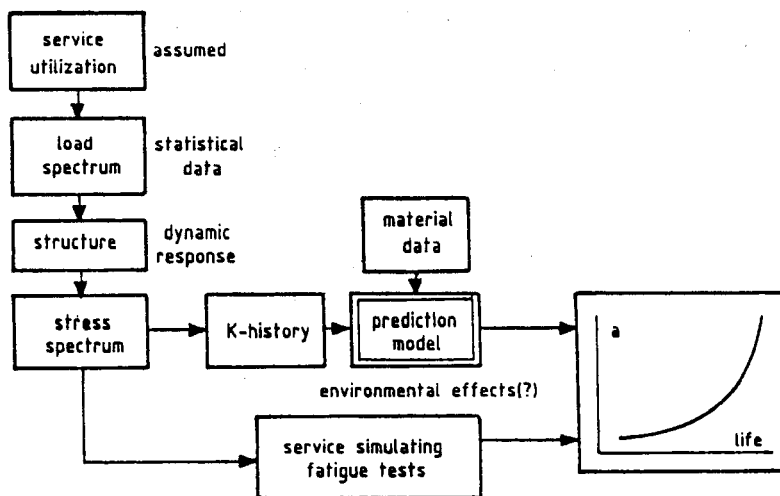


Fig.10.31: Prediction of crack growth in a structure : Survey of the problem

fatigue resistance to alloy microstructure can carry over to FCP under VA-load spectra. It is reasonable, thus, to have some material dependent variables in the prediction models but employing fudge-factors freely limits the applicability of the model.

10.5.1 Non-interaction Models: In the so-called non-interaction concept $\Delta a_i = da/dN$ as observed in CA-tests at the same nominal K-cycle. The value of Δa_i does not depend on crack growth and cyclic loads in previous cycles. Only the present crack length and the present K-cycle are significant. There is no material memory for the past history. That is why it is called non-interaction. Retardations and accelerations do not occur in this concept. Hence predictions on crack growth will be, in general, conservative; but unfortunately, they can easily be over-conservative. Trend predictions on variations of the load spectrum are highly unreliable. For instance, the effect of occasional high loads will be a small reduction on crack growth life, whereas in reality it can lead to most impressive life extensions, due to crack growth retardations. Random loads, in general, lead to retardation rather than acceleration. But there is no guarantee for non-interaction models to be conservative. If there are sufficient underloads in the spectrum (see sec.10.2) the non-interaction model may easily be non-conservative.

10.5.2 Yield zone Models: First generation interaction models try to predict retardation by comparing the overload induced plastic zone with the current plastic zone size. The physical bases are weak, but the models are simple to program and use.

Wheeler model [39] is based on a retardation factor C_p which directly reduces the CA-crack growth rate da/dN .

$$a_n = a_o + \sum_{i=1}^n C_{pi} (da/dN) \quad (10.9)$$

where

$$C_{pi} = \begin{cases} (r_y/r_y^{OL})^m & \text{for } a+r_y < a_p \\ 1 & \text{for } a+r_y > a_p \end{cases}$$

and a_p represents the maximum excursion of elastic-plastic interface. The exponent m is called the shaping exponent and has to be determined empirically from a VA-test. The particular retardation factor chosen by Wheeler satisfies the boundary conditions that it should be bounded between zero and one, and that it should increase from its smallest value immediately after a high load to its maximum value of one at some later time. But the uniqueness of a particular m to one material and/or to one spectrum limits the usefulness of the model in prediction of growth behavior of a particular structure under an entirely different spectrum shape. Typical values of the exponent m as reported by Broek [40] and Schütz [41] are:

$m = 1.8$ for Ti6Al4V

$m = 1.4$ for Al alloys 2024-T3 and 7075-T7351

$m = 0.7$ for maraging steel.

Willenborg Model [42] attempts to model load interaction concept solely based on the CA crack growth rate data. Willenborg assumed that retardation is proportional to a reduction in the maximum applied stress due to residual stresses set up by a preceding overload. An effective ΔK is determined by assuming a form for the residual stress σ_{red} present at the tip and reducing the applied stresses by this amount. Once obtained, this effective ΔK is used in conjunction with constant amplitude growth rate data to determine the increment of crack growth.

To illustrate the mathematical development and the operation of the model, the case of a simple spectrum is considered (Fig.10.32). Following the peak loading σ_1 (max) a plastic zone r_{y1} is created at the tip. The

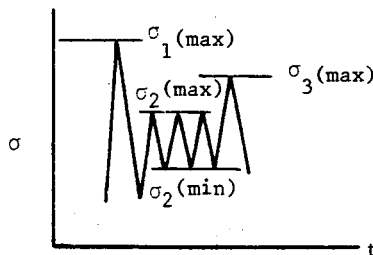


Fig.10.32: A simple spectrum used to explain the development of the Willenborg model

crack continues to grow under cyclic loading $\sigma_2(\max) - \sigma_2(\min)$ within this plastic zone. $\sigma_1(\max)$ being larger than $\sigma_2(\max)$ leads to a retardation, which continues as long as the growth remains within the zone of plasticity caused by $\sigma_1(\max)$. Irwin plastic zone is used in the model in a slightly modified form, giving the extent of the zone (Fig.10.33a) by

$$r_y = \frac{1}{\alpha\pi} (K_1/S_y)^2 \tag{10.10}$$

where $\alpha = 2$ for plane stress and $\alpha = 6$ for plane strain. The step-by-step structure of the model is outlined below for plane stress conditions:

1- Total affected crack length, after $\sigma_1(\max)$ is applied, is denoted by a_p and calculated as (Fig.10.33a)

$$a_p = \frac{K_1^2}{2\pi S_y^2} + a_1 \tag{10.11}$$

2- To determine retardation the applied stress, σ_{app} , necessary for the plastic zone to reach a_p is calculated (Fig.10.33b).

$$r_y = a_p - a_c = \frac{K_{app}^2}{2\pi S_y^2} = \frac{(\sigma_{app}\sqrt{\pi a_c} \beta)^2}{2\pi S_y^2} \tag{10.12}$$

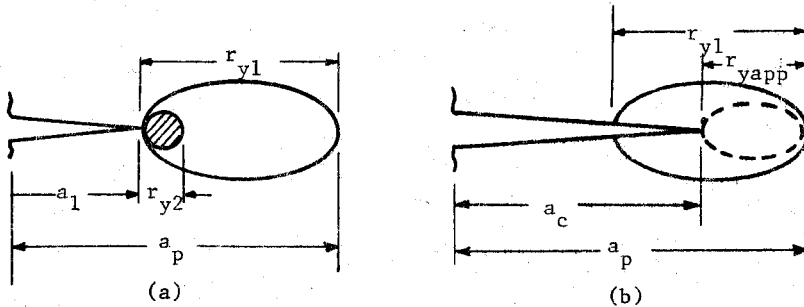


Fig.10.33: (a) Yield zones immediately following the application of σ_2 (b) Yield zone condition for termination of interaction.

Solving for σ_{app} , one obtains

$$\sigma_{app} = \frac{S_y}{\beta} \sqrt{\frac{2(a_p - a_c)}{a_c}} \quad (10.13)$$

where a_c is the current crack length. At the beginning of the second cycle, then, $a_c = a_1$ and eq.10.13 becomes

$$\sigma_{app} = \frac{S_y}{\beta} \sqrt{\frac{2(a_p - a_1)}{a_1}}$$

which is nothing but $\sigma_1(\max)$ itself. Note that σ_{app} is bounded by values $\sigma_{app} = \sigma_1(\max)$ and $\sigma_{app} = 0$ over the increment $a_1 - a_p$ (Fig.10.34). In a physical sense, σ_{app} may be thought of as the effective portion of σ_1 remaining following the application of σ_1 which is capable of causing retardation for stress $\sigma_2 < \sigma_{app}$ at a crack length still within the zone caused by the overload, σ_1 .

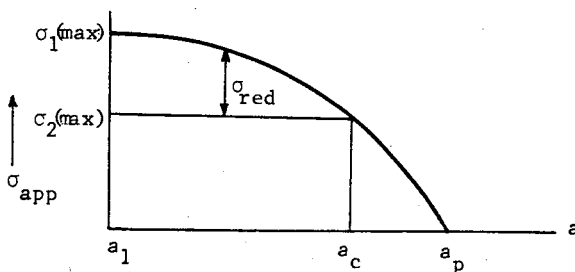


Fig.10.34: Schematic of σ_{app} following overload

- 3- Retardation is assumed to be proportional to the difference of σ_{app} , as defined in eq.10.13, and σ_{max} , the maximum value of stress in a given cycle. This difference is termed "reduction in applied stress, σ_{red} " and signifies the residual stress available to retard the next load cycle. Thus,

$$\sigma_{red} = \sigma_{app} - \sigma_{max} \quad (10.14)$$

which becomes for the second load cycle

$$\sigma_{red} = \sigma_{app} - \sigma_2(\max) = \sigma_1(\max) - \sigma_2(\max)$$

- 4- Both the maximum and the minimum values of the next load cycle are reduced by the amount σ_{red} , yielding

$$(\sigma_{max})_{eff} = \sigma_{max} - \sigma_{red} \quad (10.15)$$

$$(\sigma_{\min})_{\text{eff}} = \sigma_{\min} - \sigma_{\text{red}} \quad (10.16)$$

which become for the second cycle

$$(\sigma_2(\max))_{\text{eff}} = \sigma_2(\max) - \sigma_{\text{red}}$$

$$(\sigma_2(\min))_{\text{eff}} = \sigma_2(\min) - \sigma_{\text{red}}$$

If either of the effective stresses is less than zero, it is set equal to zero.

5- Effective values of R and K are now calculated using eq's. 10.15 and 10.16. The crack growth law is then applied directly, using the effective R and ΔK , to obtain the growth during the interval. At the end of the second cycle we obtain a_2 .

6- The current value a_2 is compared with a_p . Since a_2 is less than a_p , the growth is still retarded (Fig. 10.35). Returning to step 2, the new value of σ_{app} becomes

$$\sigma_{\text{app}} = \frac{S_y}{\beta} \sqrt{\frac{2(a_p - a_2)}{a_2}}$$

which reflects the diminishing σ_{app} as a_c approaches a_p . When σ_{app} equals σ_{max} , σ_{red} is zero and retardation is no longer present.

There are three distinct modes of retardation possible with the Willenborg model.

- (a) Both $\sigma_2(\max)$ and $\sigma_2(\min)$ reduce by the same amount (σ_{red}), keeping $\Delta K_{\text{eff}} = \Delta K$. But R_{eff} being reduced, slight retardation occurs. (Not, if Paris law is used)
- (b) $\sigma_2(\min)$ reduce to negative values so that the resulting $\Delta K_{\text{eff}} < \Delta K$. Both ΔK_{eff} and R_{eff} being reduced— in fact, R_{eff} becomes zero now — retardation occurs.
- (c) $\sigma_2(\min)$ as well as $\sigma_2(\max)$ reduce to negative values so that the resulting $\Delta K_{\text{eff}} = R_{\text{eff}} = 0$. There remains no crack driving force and growth stops. The model predicts arrest at $\sigma_1(\max) / \sigma_2(\max) > 2.0$

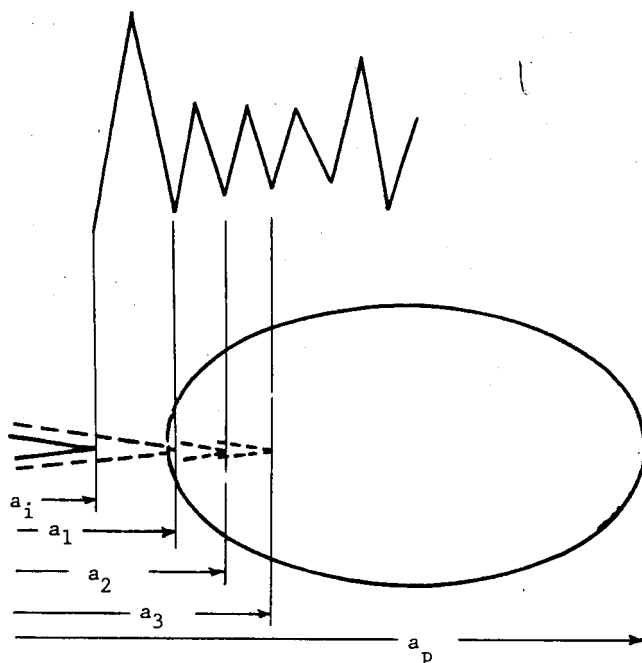


Fig.10.35: Crack tip at different cycles with respect to the overload yield zone

Willenborg model starts from a strange assumption, which implies that the retardation is due to a reduction of K_{\max} instead of a reduction of ΔK_{eff} . This is considered to be physically incorrect [43]. Crack closure in the model is supposed to occur only if $K_{\min} < 0$. From a mechanistic point of view, the Willenborg model does not agree with the present understanding of crack closure. The model ignores all portions of a stress level which are less than zero. On the face of previous discussions, this can be serious when a severe compressive load follows a tensile overload. Another shortcoming stems from the fact that the model treats each overload as a single discrete event. Hence, any cumulative effect of multiple overloads are not accounted for. Delayed retardations and accelerations are not included in the model, either.

In view of limitations, the Willenborg model was modified by Gallagher to the "generalized Willenborg model" [44,45]. Physical arguments were

used for the modifications. Instead of calculating the effective value of the stress, Gallagher modified the stress intensity factor directly. Eq. 10.14 is replaced by

$$K_{red}^W = K_{max}^{OL} \left(1 - \frac{\Delta a}{Z_{OL}}\right)^{1/2} - K_{max} \quad (10.17)$$

where K_{red}^W is the Willenborg residual stress intensity factor, K_{max}^{OL} is the maximum stress intensity for the overload cycle, K_{max} is the maximum stress intensity for the current load cycle, Δa is the crack growth increment between the overload cycle and the current cycle and Z_{OL} is the overload induced plastic zone diameter. In the terminology of Willenborg $Z_{OL} = 2r_y^{OL}$ and K_{red}^W represents — completely analogous to eq.10.14 — the difference between the stress intensity required to produce a current plastic zone equal to $a_p - a_c$ and the current applied stress intensity K_{max} . A further modification was the introduction of a proportionality factor such that

$$K_{red} = \phi K_{red}^W \quad (10.18)$$

The ϕ term adjusts the amount of retardation according to several material parameters through

$$\phi = \frac{1 - \frac{K_{th}}{K_{max}}}{S-1} \quad (10.19)$$

where K_{th} is the threshold maximum stress intensity factor for no fatigue growth at $R=0$ and S is the overload shut-off ratio i.e. OLR at which arrest occurs. The effective quantities become thus

$$(K_{max})_{eff} = K_{max} - K_{red} \quad (10.20)$$

$$(K_{min})_{eff} = K_{min} - K_{red} \quad (10.21)$$

$$R_{eff} = (K_{min})_{eff} / (K_{max})_{eff} \quad (10.22)$$

10.5.3 Crack Closure Models: The occurrence of crack closure at positive (tensile) stresses has been discussed in Sec.9.2 as a probable mechanism

to account for both crack growth retardations and accelerations. Several models have been developed based on closure phenomena. Among those are Bell's model [46], Baudin and Robert's ONERA model [47], DeKoning's CORPUS model [48], and Aliaga's model [49,50]. These models are similar in structure but different mathematically. De Koning's model will be detailed here as a sample closure-based model.

DeKoning assumed that overloads lead to plastic deformations in the wake of the crack tip which he called "humps". These humps are created at the crack length at which the overload is applied and correspond in width to the monotonic plastic zone size. Reversed plasticity due to unloading the spike load, however, reduces the hump width - flattens the hump - somewhat (Fig.10.36). The presence of the hump decreases locally the COD and the crack remains closed for a larger range of the subsequent applied load.

The variation of hump opening stress, S_{op} , with crack advance is

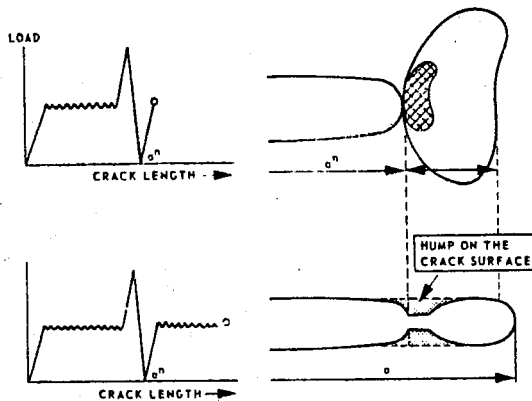


Fig.10.36: Effect of plastic deformation left in the wake of a growing fatigue crack [48]

observed to be a gradual decay. But the model assumes for convenience an "on/off delay switch" behavior described by

$$\left. \begin{aligned}
 S_{op}^n &= g(S_{max}^n, S_{min}^n) && \text{if } a^n < a < a^n + r_y^{OL} \\
 S_{op}^n &= 0 && \text{if } a > a^n + r_y^{OL}
 \end{aligned} \right\} \quad (10.23)$$

i.e. no closure effect remains as soon as the crack has grown through the overload plastic zone. The $g(S_{\max}^n, S_{\min}^n)$ function is an empirical relation obtained in CA-tests similar to the expressions in Fig.9.6 or Fig.9.7. The hump opening stress changes everytime a more severe underload is applied, according to the function g . This effect is illustrated in Fig.10.37. As a result of application of S_{\max}^n a hump n is created. The hump opening stress is determined by the value of the underload $S_{\min,1}^n$. This level is constant provided that the "delay" switch is not set-off. Application of underload $S_{\min,2}^n$ changes this state, however, the new opening level being

$$S_{\text{op}}^n = g(S_{\max}^n, S_{\min,2}^n)$$

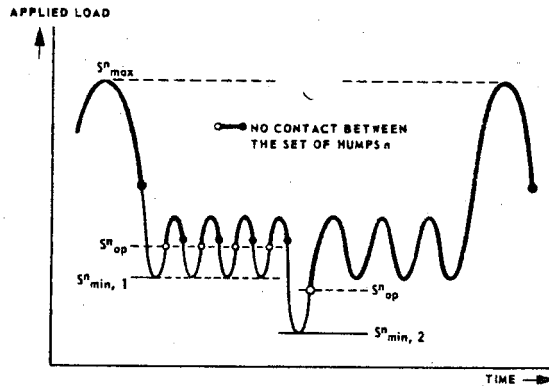


Fig.10.37: Effect of underloads on the hump opening behavior [48].

In a VA-loading there will be a hump associated with each overload and the crack is opened if all humps have lost contact. Thus, the crack opening stress σ_{op} will correspond to the hump that lost contact last

$$\sigma_{\text{op}} = \max(S_{\text{op}}^n) \quad (10.24)$$

This illustrates the limited memory aspect of the model; as a result of application of $S_{\min,2}^n$ the value of $S_{\min,1}^n$ is erased from the memory of the material.

Using the loading sequence presented in Fig.10.38 some other properties of the model are discussed in the following. To indicate parts

of load cycles for which the crack is open and propagation, the load sequence is also plotted versus the crack length. From this sequence it is seen that the first hump is created by application of S^1_{max} and, subsequently, flattened by S^1_{min} .

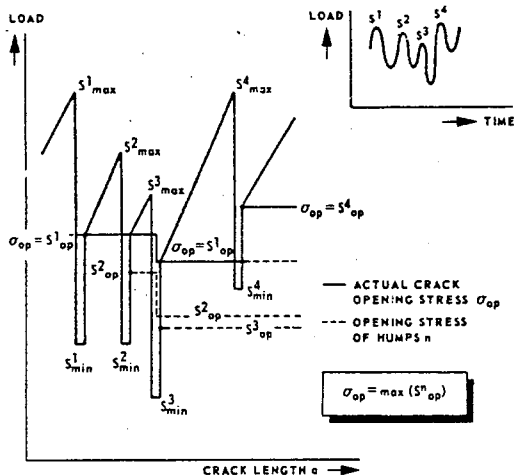


Fig.10.38: Examples of hump and crack opening behavior [48]

The opening stress S^1_{op} of this hump is given by

$$S^1_{op} = g(S^1_{max}, S^1_{min})$$

Then the effective stress range $\Delta\sigma$ for the next cycle is given by

$$\Delta\sigma^1_{eff} = S^2_{max} - S^1_{op}$$

The second hump is created by application of S^2_{max} . This hump has not experienced S^1_{min} , but in the next cycle it is flattened by S^2_{min} . Thus the opening stress of this hump is given by

$$S^2_{op} = g(S^2_{max}, S^2_{min}).$$

The first hump has experienced a minimum stress S^1_{min} . Application of S^2_{min} will not produce a further reduction of this hump provided that $S^2_{min} > S^1_{min}$. Therefore the opening stress of the first hump, denoted by

S_{op}^1 , is the same in the second cycle. According to the definition of the crack opening stress both humps (and also the crack surfaces) break contact if the applied load is greater than S_{op}^1 . It follows that $\sigma_{op} = S_{op}^1$. The effective stress increment in the second cycle is given by

$$\Delta\sigma_{eff}^2 = S_{max}^3 - \sigma_{op} = S_{max}^3 - S_{op}^1$$

A third hump is created by application of S_{max}^3 . The subsequent negative load increment $S_{max}^3 - S_{min}^3$ flattens all three humps because $S_{min}^3 < S_{min}^1$, and $S_{min}^3 < S_{min}^2$. The hump opening stresses for the next positive load increment $S_{max}^4 - S_{min}^3$, are, respectively

$$S_{op}^1 = g(S_{max}^3, S_{min}^3) \quad (\text{update } S_{op}^1)$$

$$S_{op}^2 = g(S_{max}^3, S_{min}^3) \quad (\text{update } S_{op}^2)$$

$$S_{op}^3 = g(S_{max}^3, S_{min}^3)$$

and the crack is fully opened at a level corresponding to the new value of S_{op}^1 , this being the highest opening stress level. It is concluded that the hump created first is still dominant, that is, $\sigma_{op} = S_{op}^1$.

Suppose that the maximum load applied in the next cycle S_{max}^4 is greater than all maximum loads $S_{max}^1, S_{max}^2, S_{max}^3$ applied previously. It will be shown that the hump created by application of S_{max}^4 dominates the effect of humps 1, 2, and 3. Therefore, two subsequent negative load steps will be analyzed. In the first place $S_{min}^4 > S_{min}^3$ gives $S_{op}^4 > S_{op}^1$ and hump 4 becomes dominant. On the other hand, if $S_{min}^4 < S_{min}^3$, then humps 1, 2 and 3 experience a minimum load more severe than the previous minimum S_{min}^3 . For the updated values of the hump opening stress it follows that $S_{op}^4 > S_{op}^1 > S_{op}^2 > S_{op}^3$. It is seen that after application of any negative load increment hump 4 governs the crack opening behavior. In general, it can be concluded that the effect of a previous hump, j , on the crack opening behavior is overruled by application of a more severe maximum load S_{max}^n , that is, $S_{max}^n > S_{max}^j$. In this way application of a relatively high load level erases part of the memory effect.

In the foregoing, it was assumed that a hump can actively influence the crack opening behavior as long as the crack tip is situated in the

plastic zone associated with that hump. It follows that the effect of hump j is also erased permanently if $a \geq a^j + r_y^j$.

10.5.4 Strip Yield Models: Finite Element studies confirm the occurrence of crack closure and the interaction effects associated with closure. But such calculations cannot be made for many cycles to follow crack growth. No closed form solutions for elastic plastic cracked bodies being present the Dugdale (strip yield) model was extended by several workers to arrive at a crack growth model, which leaves plastic deformation in the wake of the crack [51,52].

Newman [51] developed his model for center cracked panel of finite width subject to uniform applied stress. It is composed of three regions as shown in Fig.10.39: (1) A linear elastic region containing a fictitious crack of half length $c + \rho$; (2) a plastic region of length ρ ; and (3) a residual plastic deformation region along the crack surfaces. The physical crack is of half length c . Region I was treated as an elastic continuum, and the crack surface displacements under various loading conditions were obtained from literature and modified for finite plate size. Regions 2 and 3 were composed of rigid-perfectly plastic (l-d) bar elements. The shaded regions in Fig.10.39(a) and (b) indicate material which is in a plastic

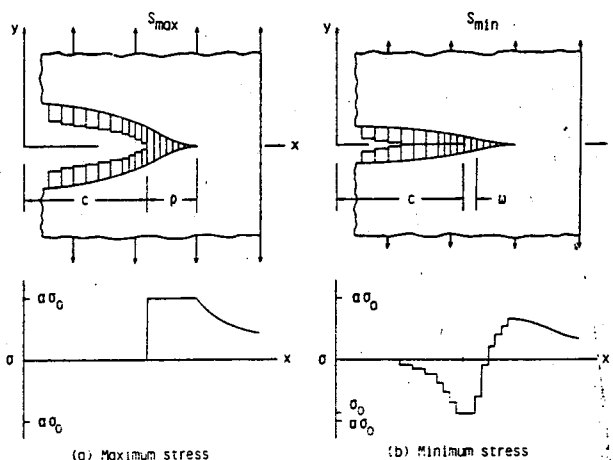


Fig.10.39: Crack surface displacements and stress distributions along crack line as used in Newman model [51]

state. At any applied stress level, the bar elements are either intact (in the plastic zone) or broken (residual plastic deformation). The broken elements carry compressive loads only, and then only if they are in contact. An analytical crack closure model was used to calculate crack closure stresses as a function of crack length and load history. In turn, the crack opening stress was used to calculate the effective stress intensity factor range and consequently the crack growth rates.

Strip yield models do account for delayed retardation after overloads because conceptually they include plastic deformation ahead of the crack tip and building up of plastic deformation in the wake of the crack after some crack growth. But they are quite sophisticated in mathematical structure and take longer computer times.

10.5.5 Empirical Interpolations: If lots of data on crack growth under VA-loading are available it might be hoped that interpolations between existing data can be made for practical problems. In such cases the results of simple tests with overload cycles are of little value. For an aircraft service load spectrum available results of flight-simulation test may be used if the data are relevant to the problem considered. In view of the large number of variables (spectrum shape, stress level, type of material, thickness, geometry) the relevance can be questionable. But, available data can give useful indications, at least, on the order of crack growth rates under flight load histories.

A special case of empirical interpolation is the characteristic K method. The basic idea is that the random variations of the stress in the crack tip zone are fully described by ΔK_{rms} and thus:

$$\frac{da}{dN} = f(\Delta K_{\text{rms}}) \quad (10.25)$$

with $\Delta K_{\text{rms}} = \Delta \sigma_{\text{rms}} \sqrt{\pi a}$. The function f applies to one type of random loading, characterized by its own statistical properties. The relation may depend on the mean stress σ_m . A stress ratio R as defined for CA-loading cannot be defined in the same way for random loading, but the relative severity of the mean stress is given by

$$\gamma = \sigma_m / \sigma_{\text{rms}}$$

and eq.10.25 may be written as

$$\frac{da}{dN} = f(\Delta K_{rms}, \gamma). \quad (10.26)$$

Barsom [53] investigated several steels under variable amplitude random-sequence load fluctuations and concluded that the average fatigue crack growth rates per cycle can be represented by eq.10.25, the functional form f being that of Paris (Eq.9.2). Moreover the average growth rates for the various steels studied under VA-loading were equal to the average growth rates obtained under CA-loading when the ΔK under CA-load fluctuations is equal in magnitude to the ΔK_{rms} of the VA-spectra. The rms-approach cannot be applied, however, to spectra which contain many discrete events such as GAG cycles or rare overloads.

Schijve [3] has extended this idea to crack growth under stationary flight simulation loading by defining

$$K_{FS} = Y \sigma_{char} \sqrt{\pi a} \quad (10.27)$$

where K_{FS} is the characteristic K-value for a specific flight-simulation load history. σ_{char} can be the mean stress in flight (S_{mf}) or the maximum stress of the load spectrum (S_{max}). Because S_{mf} or S_{max} are a kind of a scale factor for the stress history, a unique relation may be expected between the growth rate and K_{FS} .

$$da/dN = f(K_{FS}) \quad (10.28)$$

The early studies reporting unsuccessful correlations are believed to be due to initial transient effects of cracks initiating at notches. Schijve is hopeful [43] that eq.10.28 can account for different geometries and stress levels, if not for different load spectra.

References:

- 1- Bretz, P.E., Vasudevan, A.K., Bucci, R.J. and Malcolm, R.C. " Fatigue Crack Growth Behavior of 7XXX Aluminum Alloys under Simple Variable Amplitude Loading" ASTM STP 833, Amer.Soc.for Testing and Materials, 1984, pp.242-265.

- 2- Newman, J.C. "A Finite Element Analysis of Fatigue Crack Closure" ASTM STP 590, Amer. Soc. for Testing and Materials, 1976 pp.281-301
- 3- Schijve, J. "Four Lectures on Fatigue Crack Growth" Engineering Fracture Mechanics, Vol.11. pp.167-221, 1979.
- 4- Schijve, J. "Observations on the Prediction of Fatigue Crack Growth Propagation Under Variable-Amplitude Loading" ASTM STP 595, Amer. Soc. for Testing and Materials", 1976, pp. 3-23.
- 5- Wei, R.P. and Shih, T.T. "Delay in Fatigue Crack Growth" Int.J. of Fracture, Vol.10, No.1, 1974, pp 77-85.
- 6- Shih, T.T. and Wei, R.P. "Effect of Specimen Thickness on Delay in Fatigue Crack Growth" J. of Testing and Evaluation, Vol.3, No.1, 1975, pp. 46-47.
- 7- Chanani, G.R. "Retardation of Fatigue Crack Growth in 7075 Aluminum" Metals Engineering Quarterly, 1975, pp.40-48
- 8- Bernard, P.J., Lindley, T.C. and Richards, C.E. "The Effect of Single Overloads on Fatigue Crack Propagation in Steels" Metal Science, 1977, pp.390-398
- 9- Roberts, R. and Wnek, K. "Delay Effects in a Pressure Vessel Material 5083-0 Aluminum, J. of Pressure Vessel Technology, Vol.99, 1977, pp.427-431
- 10- Stephens, R.I. Sheets, E.C. and Njus, G.O. "Fatigue Crack Growth and Life Predictions in Man-Ten Steel Subjected to Single and Intermittent Tensile Overloads" ASTM STP 637, Amer.Soc. for Testing and Materials, 1977, pp.176-191.
- 11- Mills, W.J. Hertzberg, R.W. and Roberts, R. "Load Interaction Effects on Fatigue Crack Growth in A514 F Steel Alloy" ASTM STP 637, Amer.Soc.for Testing and Materials, 1977, pp.192-208.
- 12- Himmelein, M.K. and Hillberry, B.M. "Effect of Stress Ratio and Overload Ratio on Fatigue Crack Delay and Arrest Behavior Due to Single Peak Overloads" ASTM STP 590, Amer.Soc.for Testing and Materials, 1976, pp.321-330.
- 13- Arone, R. "Fatigue Crack Growth under Random Overloads Superimposed on Constant-Amplitude Cyclic Loading" Engineering Fracture Mechanics, Vol.24, 1986. pp.223-232.
- 14- Bathias, C. and Vancan, M. "Mechanisms of Overload Effect on Fatigue Crack Propagation in Aluminum Alloys" Engineering Fracture Mechanics, Vol. 10, 1978, pp.409-424

- 15- Thomas, W.M. "The Effect of Single Overloads Upon Fatigue Cracks in 5083-H321 Aluminum" Engineering Fracture Mechanics, Vol.23, 1986, pp.1015-1029.
- 16- Rice, J. "Mechanics of Crack Tip Deformation and Extension by Fatigue" ASTM STP 415, Amer.Soc.for Testing and Materials, 1967, pp.247-311
- 17- Vardar, Ö. "Effect of Single Overload in Fatigue Crack Propagation" Engineering Fracture Mechanics, Vol. 30 1988, pp. 329-335
- 18- von EUW, E.F.J. Hertzberg, R.W. and Roberts, R. "Delay Effects in Fatigue Crack Propagation" ASTM STP 513, Amer.Soc. for Testing and Materials, 1972, pp.230-259.
- 19- Trebules, V.M., Roberts, R. and Hertzberg, R.W. "Effect of Multiple Overloads on Fatigue Crack Propagation in 2024-T3 Aluminum Alloy" ASTM STP 536, Amer. Soc. for Testing and Materials, 1973, pp.115-146
- 20- Lee, E.W. Chakraborty, S.B and Starke, E.A. "The Effect of Overload on the Fatigue Crack Propagation in Metastable Beta Ti-V Alloys" Metallurgical Transactions A, Vol. 15A, 1984, pp.511-517
- 21- Bucci, R.J., Thakker, A.B., Sanders, T.H., Sawtell, R.R. and Staley, J.T. "Ranking 7XXX Aluminum Alloy Fatigue Crack Growth Resistance Under Constant Amplitude and Spectrum Loading" ASTM STP 714, Amer.Soc. for Testing and Materials, 1980, pp.41-78
- 22- Lankford, J. and Davidson, D.L. "Fatigue Crack Tip Plasticity Associated with Overloads and Subsequent Cycling" J. of Engineering Materials and Technology, Vol.98, 1976, pp.17-23
- 23- Mills, W.J. and Hertzberg, R.W. "Load Interaction Effects on Fatigue Crack Propagation in 2024-T3 Aluminum Alloy" Engineering Fracture Mechanics, Vol.8, 1976, pp.657-667
- 24- Chang, J.B. Engle R.M. and Stolpestad, J. "Fatigue Crack Growth Behavior and Life Predictions for 2219-T851 Aluminum Subjected to Variable Amplitude Loadings" ASTM STP 743, Amer.Soc. for Testing and Materials, 1981, pp.3-27.
- 25- Schijve, J. "Fatigue Damage Accumulation and Incompatible Crack Front Orientation" Eng. Fracture Mechanics Vol.6 (1974) pp.245-252
- 26- Morman, K.N. and Dubensky, R.G. "Predicting Fatigue Crack Retardation Under Single and Intermittent Overloading" ASTM STP 601, Amer.Soc. for Testing and Materials, 1976, pp.245-261

- 27- Fleck, N.A. "Fatigue Crack Growth Due to Periodic Underloads and Overloads" Acta Metall. Vol.33 No.7, 1985, pp.1339-1354
- 28- Misawa, H. and Schijve, J. "Fatigue Crack Growth in Al- Alloy Sheet Material Under Constant Amplitude and Simplified Flight- Simulation Loading" Delft University of Technology Report LR-381, The Netherlands.
- 29- Zaiken, E. and Ritchie, R.O. "On the Role of Compression Overloads in Influencing Crack Closure and the Threshold Condition for Fatigue Crack Growth in 7150 Aluminum Alloy" Engineering Fracture Mechanics, Vol.22, 1985, pp.35-48
- 30- Ling, H.R. and Schijve, J. "Fractographic Analysis of Fatigue Crack Growth Under Simple Variable-Amplitude Loading in 2024-T351 Material" Delft University of Technology Report LR-516, 1987, The Netherlands.
- 31- Schijve, J. "The Accumulation of Fatigue Damage in Aircraft Materials and Structures" AGARDograph No.157, 1972.
- 32- Yu, W. and Ritchie, R.O. "Fatigue Crack Propagation in 2090 Aluminum-Lithium Alloy: Effect of Compression Overload Cycles" J. of Engin. Materials and Technology, Transactions of the ASME, Vol 109, 1987, pp.81-85
- 33- Suresh, S. and Ritchie, R.O. "On the Influence of Fatigue Underloads on Cyclic Crack Growth at Low Stress Intensities" Mat.Sci. and Engineering, Vol.51, 1981, pp.61-69.
- 34- Schijve, J. "The Significance of Flight Simulation Fatigue Tests" Delft University of Technology Report LR-466, 1985, The Netherlands.
- 35- —, "FALSTAFF: Description of a Fighter Aircraft Loading Standard For Fatigue Evaluation" Joint International Report of Switzerland, Germany, Netherlands, March 1976.
- 36- Lowak, H., de Jonge, J.B., Franz, J. and Schütz, D. "MINI TWIST: A shortened Version of TWIST" Laboratorium für Betriebsfestigkeit, Report No. T13- 146, 1979, F.R. of Germany.
- 37- ten Have, A.A. "Helix and Felix: Loading Standards for Use in the Fatigue Evaluation of Helicopter Rotor Components" AGARDograph No.292, 1983, pp.249-270
- 38- Geier, W. and Sippel, K.O. "Fatigue Crack Propagation Under Variable Loads" AGARDograph No.257, 1980, Chapter 7.

- 39- Wheeler, O.E. "Spectrum Loading and Crack Growth" J.of Basic Engineering, March 1972, pp.181-186
- 40- Broek, D."Damage Tolerance in Practice" AGARD Lecture Series No. 97, Chapter 11, 1979.
- 41- Schütz,W. "Calculation Methods For Fatigue Life and Crack Propagation" AGARDograph No.231, Chapter 4.
- 42- Willenborg, J., Engle, R.M. and Wood H.A. "A Crack Growth Retardation Model Using an Effective Stress Concept" AFFDL Technical Memorandum-71-1-FBR (1971).
- 43- Schijve,J. "Fatigue Crack Growth Predictions For Variable-Amplitude and Spectrum Loading" Delft University of Technology Report LR-526, 1987, The Netherlands.
- 44- Gallagher, J.P."A Generalized Development of Yield Zone Models" AFFDL-TM-FBR-74-28 (1974).
- 45- Gallagher, J.P. and Hughes, T.F. "Influence of Yield Strength on Overload Affected Fatigue Crack Growth Behavior in 4340 Steel" AFFDL-TR-74-27 (1974).
- 46- Bell,P.D. and Wolfman, A."Mathematical Modeling of Crack Growth Interaction Effects" ASTM STP 595, Amer.Soc. for Testing and Materials, 1976, pp.157-171.
- 47- Baudin, G. and Robert, M. "Crack Growth Model for flight-type Loading" Proc.11th ICAF Symp. Noordwijherhout, 1981.
- 48- De Koning, A.U. "A Simple Crack Closure Model for Prediction of Fatigue Crack Growth Rates Under Variable-Amplitude Loading" ASTM STP 743, Amer.Soc. for Testing and Materials, 1981, pp.63-85.
- 49- Aliaga, D., Davy, A. and Shaff, H. "A Simple Crack Closure Model for Predicting Fatigue Crack Growth Under Flight Simulation Loading" Proc. 13th ICAF Symp. Pisa 1985.
- 50- Aliaga, D., Davy, A. and Schaff,H." A Simple Crack Closure Model for Predicting Fatigue Crack Growth Under Flight Simulation Loading" Int.Symp. on Fatigue Crack Closure, May 1986, Charleston.
- 51- Newman, J.C. "A Crack Closure Model for Predicting Fatigue Crack Growth under Aircraft Spectrum Loading" ASTM STP 748, Amer.Soc. for Testing and Materials, 1981, pp.53-84
- 52- De Koning, A.U. and Liefding,G. "Criteria for Determination of Significant Load Cycles in Variable Amplitude Load Sequences" Int. Symp/ on Fatigue Crack Closure, May 1986, Charleston.
- 53- Rolfe, S.T. and Barsom, J.M. "Fracture and Fatigue Control in Structures" Prentice Hall, Inc. New Jersey, 1977. pp.276-289.

Problems:

1. Experiments on 7075-T6 sheets indicate that

$$\frac{da}{dN} = 6.94 \times 10^{-7} (\Delta K)^{2.93} \quad (\text{in units of MPa}\sqrt{\text{m}} \text{ and mm/c}).$$

Single overload tests on the same material yield that retardation N_D^* can be expressed as

$$N_D^* = 0.0124 \exp(7.22 \times \text{OLR})$$

or a compact tension specimen cycled between $K=1.7$ and $16.7 \text{ MPa}\sqrt{\text{m}}$, estimate the number of cycles for the crack to grow from 33 to 41 mm if a single overload ($K_{OL}=33.3 \text{ MPa}\sqrt{\text{m}}$) is applied at $a=36\text{mm}$.

Answer: 26300 cycles

2. Using the random load sequence supplied below (flight No.123 of FALSTAFF) and a maximum stress of 85 MPa, estimate the amount of crack growth in a center cracked panel with $2a_1=40\text{mm}$, $W=90\text{mm}$. First ignore any interaction, then improve the estimation using RMS and Willenborg models. CA-data is the same as in Prob.1. (Load sequence: 8 5 7 5 17 10 15 11 20 17 20 11 22 11 14 11 17 13 17 10 14 11 21 11 14 10 13 10 13 10 19 15 18 11 16 11 22 8 14 10 14 11 14 10 14 10 13 10 14 11 19 12 19 15 24 10 18 11 14 10 13 10 13 9 14 10 13 6 8 6)

3. Limited tests indicate that maximum interaction between periodic overloads occur when the overloads are applied at $\Delta a \approx 0.25 a_D$ (Sec.10.2). Based on this information estimate the occurrence ratio (OCR) at which maximum retardation will occur as the crack grows from 37mm to 47mm in a C(T) specimen with $W=74\text{mm}$, $B=4.9\text{mm}$. The material is 7075-T6 Alclad, with $S_y = 460 \text{ MPa}\sqrt{\text{m}}$, $P_{OL} = 295\text{kgf}$, $\Delta P = 20-180\text{kgf}$ and CA-growth rate is the same as in Prob.1. Assume $a_D \approx 2r_y^{OL}$ in the absence of single overload data. (Actual tests reveal that $\text{OCR}=1/500$ leads to maximum retardation under prescribed conditions.)

11. TIME DEPENDENT FRACTURE MECHANICS

11.1 INTRODUCTION

Creep crack growth is an important design concern for elevated temperature components and is also important in predicting the residual life of these components which are in service. Thus, there is considerable interest in developing time-dependent fracture mechanics (TDFM) concepts for the creep regime.

Creep damage is often manifested in terms of nucleation of voids or holes at microstructural inhomogeneities which grow and coalesce to form cracks with the final failure occurring by the interlinking of these cracks through the whole cross-section. If the applied stresses in the section are uniform, nucleation of voids and subsequent formation of cracks are also uniformly dispersed. For uniformly stressed specimen, the major part of its life is generally spent on the nucleation and growth of voids with a minor fraction on the growth and interlinking of cracks. An analysis which considers an average strain response to an average applied stress is usually adequate to describe this creep behavior.

Components in service, however, are seldom subjected to uniform stresses. Pre-existing flaws or defects produced during processing or welding will give rise to stress concentrated regions. Non-uniform cross section or eccentric loading will also give rise to stress gradients. Thus, there is some localized creep behavior where failure occurs by the initiation and propagation of a single macroscopic crack. In these cases, the material behavior might be better characterized by fracture mechanics.

There are two competing mechanisms involved in creep crack growth. Crack tip blunting due to creep deformation relaxes the crack tip stress field and tends to retard crack growth. But creep damage leading to

formation of voids and microcracks enhance crack growth as these voids coalesce. Steady state creep crack growth will occur when an equilibrium between these two effects is attained.

Study of the time dependent crack growth behavior in several alloys indicates that the growth occurs either by a brittle mode or by a ductile mode. In the brittle mode, the growth occurs in essentially a continuous manner along grain boundaries. Grain boundary sliding provides a major driving force for this type of growth which generally occurs in high strength materials. While an aggressive environment generally accentuates this process, creep deformation of the matrix may relax the crack tip stress field and retard the growth. Since crack growth occurs rapidly before any extensive creep deformation LEFM can adequately describe this growth. In contrast to this, the ductile mode of crack growth occurs by the nucleation of microcracks ahead of the main crack and their growth and subsequent coalescence with the main crack. Growth of these microcracks occurs predominantly by deformation and results in considerably slower crack growth rates requiring higher stress intensities than for the brittle mode. Non-linear parameters may be required in such instances. In line with these arguments, creep crack growth has been characterized in literature in terms of stress intensity factor K , the net section or reference stress across the uncracked ligament, crack opening displacement and the creep fracture mechanics parameter C^{**} which is the creep equivalent of the J-contour integral. C^{**} , being the most popular parameter, will be studied in some detail.

11.2 STEADY STATE CREEP

For materials in which secondary (steady state) creep dominates, the uniaxial creep law can be written as

$$\dot{\epsilon} = B\sigma^n \quad (11.1)$$

where $\dot{\epsilon}$ is the creep strain rate, σ is the stress and B and n are material constants. The crack tip fields for a stationary crack is given by [1]

$$\left. \begin{aligned} \sigma_{ij} &= \left(\frac{C^*}{Br} \right)^{1/(n+1)} \tilde{f}(\theta, n) \\ \epsilon_{ij} &= \left(\frac{C^*}{Br} \right)^{n/(n+1)} \tilde{g}(\theta, n) \end{aligned} \right\} \quad (11.2)$$

which is in complete analogy to eq.7.14. It follows that C^* is the loading parameter that determines the strength of the crack tip fields in a body undergoing steady state creep. Explicitly, C^* is the path independent integral

$$C^* = \int_{\Gamma} w(\dot{\epsilon}_{ij}) dy - t_i \frac{\partial \dot{u}_i}{\partial x} ds \quad (11.3)$$

in which

$$w(\dot{\epsilon}_{ij}) = \int_0^{\dot{\epsilon}_{ij}} \sigma_{pg} d\dot{\epsilon}_{pg}$$

is the strain energy rate density and the contour Γ is an arbitrary loop enclosing the crack tip and no other defect (Fig.7.3). The proof of the path independence of C^* follows along the same lines as that for path-in dependence of the J-Integral (Sec.7.1.1).

Alternatively, C^* can be expressed as

$$C^* = -\frac{1}{E} \left(\frac{\partial PE}{\partial a} \right) \dot{\Delta} \quad (11.4)$$

where

$$PE = \int_0^{\dot{\Delta}} P d\dot{\Delta}$$

is the rate of work done by the load P acting through the conjugate displacement rate $\dot{\Delta}$.

Examination of eq.(11.2) indicates that when $n=1$, C^* predicts the same stress distribution ahead of a crack tip as K . In the limit as $n \rightarrow \infty$ the singularity at the crack tip disappears and C^* and the net section or reference stress concepts give equivalent stress distributions. The parameter C^* has, therefore, the attractive capability of

encompassing the other parameters as limiting cases.

On first loading, in the absence of plasticity, an elastic stress field will be generated ahead of a crack tip. Subsequently creep deformation will cause stress re-distribution. If cracking commences before this stress redistribution takes place then characterizations of crack growth in terms of K will be expected; whereas, C^* is the appropriate loading parameter for large scale creep deformations at longer times. The transition time from "small-scale creep" to "extensive creep" can be estimated through [2]

$$t_T = \frac{K^2(1-\nu^2)/E}{(n+1)C^*} \quad (11.5)$$

The extensive creep case is completely analogous to the fully plastic state which has been discussed in depth in chapter seven. The size of the zone of C^* dominance is strongly dependent on the relative amount of bending to tension about the ligament. If the load on the ligament is primarily bending, the zone of C^* dominance is a physically significant fraction of the uncracked ligament and the size of the zone does not depend on the creep exponent. If the ligament is subject to primarily stretching, the zone of C^* dominance is substantially smaller and the size of the zone depends strongly on the creep exponent [3].

11.2.1. Creep Tests: Creep crack growth rate testing is performed, typically, either under constant displacement rate or under constant load level.

In constant displacement rate method the tests are conducted under constant ram deflection rate using a servohydraulic test system, which approximately corresponds to constant load-line deflection rate. During the test, specimen load P , load-line deflection Δ , and crack length a are monitored continuously on a strip chart recorder. This method is useful at relatively high crack growth rates, typically above 5 $\mu\text{m/hr}$ [4]. At lower crack growth rates it is not practical since it requires an expensive servohydraulic machine for a long time. Also, under nearly static conditions for long periods of time, the performance of servohydraulic machines can be erratic.

Constant load tests are conducted using deadweight type creep machines which are relatively inexpensive. Hence it is very suitable for obtaining data at $da/dt < 5 \mu\text{m/hr}$. The major disadvantage of the technique is that only data over relatively short crack extensions can be obtained. Since the load is kept constant in time, instability occurs early in life. At higher loads, the amount of crack extension prior to instability can be so small that the technique may become impractical [4]. The deflection rate is obtained through dial gage readings at specific time intervals. Crack growth is monitored mostly using potential drop technique.

11.2.2 Determination of C^* : Parallel to the developments in EPFM, three techniques are available to estimate C^* . These are the multiple specimen graphical method, the fully plastic J-solutions based on EPRI Handbook and a method utilizing the $P-\Delta$ curves directly.

Multiple specimen graphical method is developed by Landes and Begley [5] and is based upon the definition in eq.11.4. First, multiple specimens are subjected to different constant displacement rates. The load and crack length are measured as a function of time as depicted in Fig.11.1. Then, this information is cross plotted to yield the load as a function of the displacement rate for fixed crack lengths (Fig.11.1, step 2). The area under the curves in step 2 is the rate of work done, $\dot{P}\dot{E}$. It is plotted versus crack length in step 3. The slope of the curves in step 3 is then C^* as defined in eq.11.4. C^* can be plotted as a function of displacement rate, step 4, which is the counterpart of the calibration curves in J-determination procedure depicted in Fig.7-15.

If testing is performed under constant load, then the load-point displacement and the crack length are recorded as a function of time (Step 1). For a fixed crack length, the load and the displacement rate are determined from those plots and the procedure is continued through step 2.

To obtain growth rate variation with C^* the data in step one is first converted into crack growth rate vs. crack length plots for various deflection rates and then used in conjunction with C^* vs. $\dot{\Delta}$ plots.

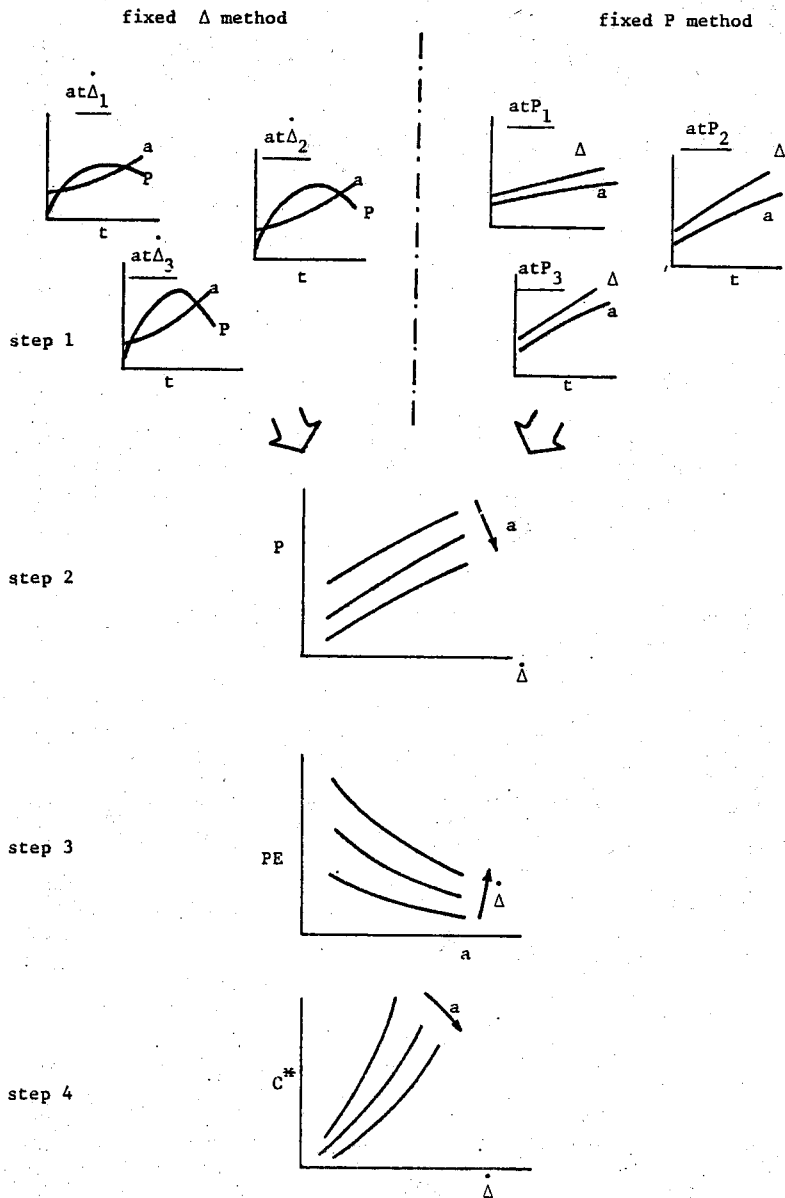


Fig.11.1 Schematic showing the steps involved in determination of C^* from experimental measurements [5].

Analogous to the area technique commonly used to determine J-Integral (Sec.7.2.2), the area under the load-deflection rate curve can be used to estimate C^* . Smith and Webster [6] showed that

$$C^* = \frac{P\dot{\Delta}}{BW} F \quad (11.6)$$

where the nondimensional factor F is obtained from approximate limit analysis techniques, as

$$F \approx \left(\frac{-n}{n+1}\right) \frac{W}{P_{i\text{limit}}} \frac{dP}{da} \text{limit} \quad (11.7)$$

n being the creep exponent used in eq.11.1. This factor F is found to be dependent on specimen geometry and crack length but to be relatively insensitive to the creep stress index n . Using the Merkle Corten limit load solution they arrived at the expression

$$C^* = \frac{P\dot{\Delta}}{Bb} \frac{n}{n+1} \quad (11.8)$$

for C(T) specimen, where

$\eta = 2 \{1.261 - 0.261 (a/W)\} = 2 + 0.522 (b/W)$
is valid for $a/W > 0.4$ [4]. The term $P\dot{\Delta}(n/n+1)$ in eq.11.8 represents the area under the load-deflection rate plot.

Using the Haigh and Richards limit load solution for center cracked plates in tension, Smith and Webster [6] arrived at the expression

$$C^* = \frac{P\dot{\Delta}}{Bb} \frac{n}{n+1} \quad (11.9)$$

which is very close to the earlier analysis of Harper and Ellison [7] giving

$$C^* = \frac{P\dot{\Delta}}{Bb} \frac{n-1}{n+1} \quad (11.10)$$

for both M(T) and DE(T) specimens. The corresponding expression for SE(B) geometry is [6]

$$C^* = \frac{P\dot{\Delta}}{Bb} \frac{2n}{n+1} \quad (11.11)$$

Fully plastic J solutions based on EPRI Handbook are covered in

sec 7.2.3. By analogy, these solutions can also be used to calculate C^* when secondary creep conditions dominate in the entire specimen. The relevant equation for $C(T)$, for example, will be

$$C^* = Bbh_1(a/W, n) \{P/P_0\}^{n+1} \quad (11.12)$$

where B and n are the material constants in eq.11.1, h_1 is the nondimensional function of a/W and n , listed in Table 7.2 or 7.3 and P_0 is the reference load given in eq. 7.31 or 7.32, depending on the plane strain or plane stress conditions.

11.2.3. C^* Based Correlations: For stationary cracks C^* characterizes completely the crack tip conditions. For growing cracks, however, one cannot be sure that the stress and strain fields are controlled by C^* and that the HRR singularity is valid. Hui and Riedel [8] have shown that for growing cracks in creeping material, a new type of singular stress and strain rate field develops which is considerably different from the HRR field. This new singularity is independent of the applied loading and the geometry of the body and is dependent only on the current crack growth rate \dot{a} and material parameters. Consequently, any fracture criterion that involves only a combination of these fields will lead to a crack growth rate that is independent of the applied loading and that is universal for all flawed configurations of the same material. This is contrary to observed behavior. In addition to this, for steady state creep the new singularity is engulfed in a larger zone in which C^* characterizes the stress and strain rate behavior. And for all practical cases, the size of the new singularity zone is much smaller than the crack length or the other pertinent linear dimensions of the component [4]. Thus, the growth rate da/dt is expected to correlate best with C^* . Experimental support to C^* is summarized in the following.

Cr-Mo-V steels which are extensively used in steam turbines have been studied by several investigators. Saxena et.al [4] obtained good correlation between da/dt and C^* over a wide range of C^* values (five orders of magnitude) and crack growth rates (three orders of magnitude). For A470 Class 8 steel at 538°C, the relation reported is

$$\frac{da}{dt} = 10^{-4} (C^*)^{0.67} \quad (11.13)$$

where \dot{a} is in mm/h and C^* is in $J/m^2/h$ (Fig.11.2). For a similar material, 1Cr-Mo-V steel at 565°C Smith and Webster [9] found a parallel offset curve the meantrend of which is included in Fig.11.2. Geometry dependence observed in correlations using stress intensity factor or

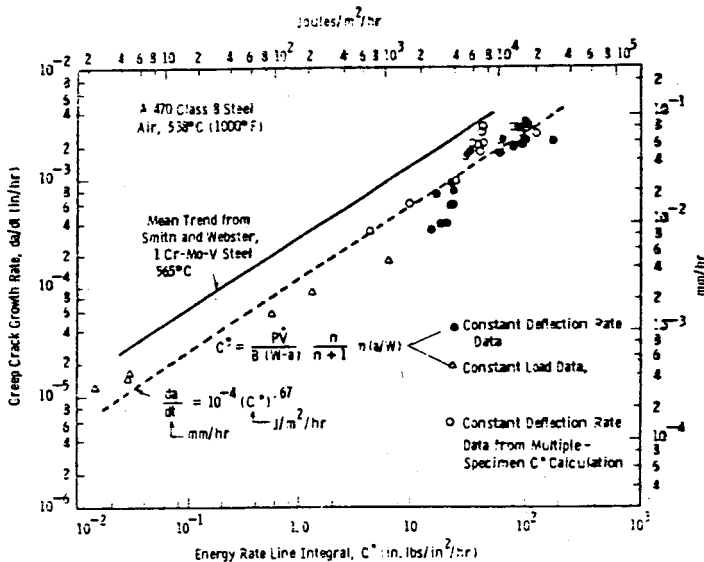


Fig.11.2: Creep crack growth rate as a function of C^* [4]

reference stress is eliminated through the use of C^* . Carbon steels in the temperature range 400–500°C exhibit much less scatter in terms of C^* as compared to net section stress or stress intensity factor [10]. The relationship of da/dt vs. C^* was almost independent on the width of plate specimens, the test temperatures, the testing environments and the fracture mode.

Austenitic stainless steels, being another common material for elevated temperature applications, are also investigated in depth. Tests on type 316 stainless steel at 600–650 °C [10], type 304 at 650 °C [10,11] and type 304 at 594 °C [12,13] show that C^* is superior to others. Considering the wide spectrum of specimen geometries used, all of the data fall in a relatively narrow band with crack growth rates for

a given C^* value varying only by a factor of ten-as opposed to a variation of more than two orders of magnitude for a given K value [14].

In contrast to low alloy steels and austenitic steels, superalloys are generally high strength creep resistant alloys with limited ductility. Thus, If crack growth can occur at low stress intensities then LEFM may be adequate to correlate crack growth rate. The work of Landes and Begley [5] involved both C(T) and M(T) and the authors concluded that C^* parameter is better than K in correlating the data on Discaloy at 649 °C. Tests on Inconel 718 at 538 °C using C(T) specimens [15] and on In 100 at 732 °C using Ring specimens [16], however, do not yield any improvement when analyzed in terms of C^* .

Aluminum alloy RR58 has been studied by Nikbin et.al [17] using several different specimen geometries and crack lengths. They found that growth data for all geometries fall on a narrow band when C^* is used as the load parameter. Based on their analysis C^* appears to correlate the data better than K. Radhakrishnan and Mc Evily [18] performed creep crack growth tests on 6061 in the temperature range 220-320 °C. They again witnessed a superior correlation of C^* over K, but even in terms of C^* they found a systematic variation with load. Dependence on load, certainly, limited the effectiveness of C^* .

Nikbin, Smith and Webster [19] develop a model of creep crack growth and concluded that the universal growth expression

$$\frac{da}{dt} = \frac{3(C^*)^{0.85}}{\epsilon_f^*} \quad (11.14)$$

gives satisfactory fit to existing data in literature. ϵ_f^* in this expression is the creep ductility appropriate to the state of stress local to the crack tip and is usually approximated by the uniaxial creep ductility for plane stress loading, ϵ_f . Crack growth rate \dot{a} is in mm/h, C^* is in MJ/m²/h in eq. 11.14. Based on models of void growth which indicate that ductility can be decreased by a factor of 25 to 80 for the stress state relevant to plane strain situations, Nikbin et.al. chose $\epsilon_f^* \approx \epsilon_f/50$ for plane strain. Thus, crack growth rates about 50 times faster are anticipated at the same value of C^* under plane strain loading

than plane stress. Whether plane stress or plane strain conditions are expected will be dependent upon the test piece dimensions and the creep deformation which accompanies fracture. Low creep ductilities, large sample sizes and the presence of side grooves will favor plane strain situations.

Satisfactory estimates of creep crack propagation rates are obtained in a broad range of materials when eq.11.14 is utilized. The shaded region in the plot of $\dot{a}\epsilon_f$ vs. C^* (Fig.11.3) represents the spread of the experimental results on 2-1/4Cr-Mo steel at 538 °C, Al-alloy RR58 at 150°C, 0.16 C steel at 500°C, 1 CrMoV steel at 538°C, A470 class 8 steel at 538 and 482°C, 316 stainless at 593°C, Inconel X750 at 650°C, 2219-T851 at 148°C and lead at 20°C. It can be seen that the equations

$$\dot{a}\epsilon_f = 3(C^*)^{0.85} \quad (11.15)$$

for plane stress, and

$$\dot{a}\epsilon_f = 150 (C^*)^{0.85} \quad (11.16)$$

for plane strain approximately span the data. Thus, Nikbin et.al propose

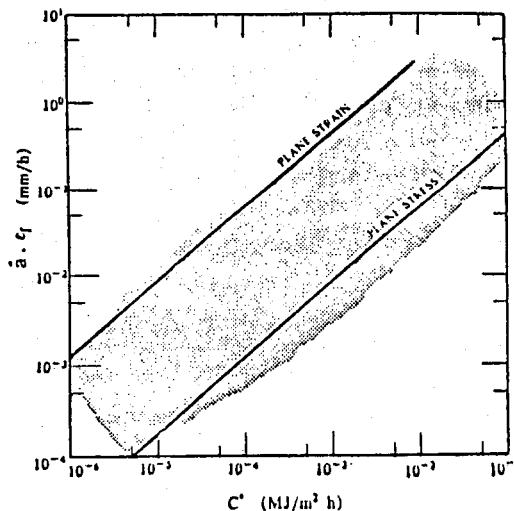


Fig.11.3: Material independent engineering creep crack growth assessment diagram of Nikbin et.al [19].

to use equations 11.15 and 16 as engineering creep crack growth assessment diagram to assess the susceptibility of cracked components to creep failure without further knowledge of material properties. It suggests that regions of low material ductility and high constraint are most likely to be prone to cracking and that heat treatments and fabrication procedures leading to reduced ductilities should be avoided. If, for example, reducing failure strain by a factor of 10 causes, in addition, a change from plane stress to plane strain conditions then propagation rates of over two orders of magnitude faster could be observed in a given circumstance in embrittled regions.

11.2.4. Other Correlations: Saxena, Ernst and Landes [20] partition the load line deflection rate of a cracked component into three parts,

$$\dot{\Delta} = \dot{\Delta}_{e1} + \dot{\Delta}_{p1} + \dot{\Delta}_c \quad (11.17)$$

which correspond to the elastic, plastic and creep deformations, respectively. At constant load, P, it becomes

$$\dot{\Delta} = \dot{a} \left(\frac{\partial \Delta_{e1}}{\partial a} \right)_P + \dot{a} \left(\frac{\partial \Delta_{p1}}{\partial a} \right)_P + \dot{\Delta}_c \quad (11.18)$$

In materials where $\dot{\Delta}_c$ is large compared to the two other terms combined in (11.18), C^{**} is expected to characterize the crack tip conditions and thus da/dt also. On the other hand, they claim that in materials which exhibit high crack growth rates and a high resistance to creep deformation (i.e low deflection rate due to development of creep), J characterizes the growth behavior, rather than C^{**} . Tests on 316 stainless steel at 594°C, indeed, correlate better with J than C^{**} , whereas at 650°C — creep being more dominant— C^{**} proves to be a superior parameter [20]. In fact, if the time independent plastic deformation is negligible in eq.(11.18) compared to the elastic deflection, K may characterize the crack tip condition and da/dt .

If creep deformations occur rapidly crack tip blunting is excessive and the stress concentration is relaxed at a rate faster than the increase of stress due to crack extension. Under these conditions no special significance can be attached to the singular crack-tip fields and the

stresses are essentially homogeneous except in cases where severe bending moments exist. The specimen under such conditions behaves more like a creep rupture specimen. Creep life then could be predicted using net section stress, or more accurately, the reference stress which takes into consideration the presence of a crack in the specimen.

A reference stress is defined for a component as that stress which when applied to a uniaxial specimen will give the same displacement rate. In engineering terms a single stress can be specified for a component under a stress gradient which will predict its deformation behavior relative to uniaxial tests. Williams and Price [21] have shown that the reference stress in a cracked body is equal to the stress at a skeletal point which is a position within the structure where stress is approximately constant for all values of creep index n . Reference stress expressions for different fracture mechanics geometries developed by Williams and Price are reproduced in Table 11.1. Thus the life of a structure containing a flaw can be predicted from conventional creep rupture data.

11.3 TRANSIENT CREEP

Creep crack growth can occur at three different levels of creep deformation. Under small scale yielding, the creep zone size is small in comparison to the crack length and the pertinent dimensions of the body. Under steady state conditions, the creep zone will have penetrated through the cracked body. The transition creep condition represents the intermediate region. The small scale yielding and transition creep regions are under non-steady state (transient) conditions and are characterized by a time-dependent load versus load-line deflection rate behavior. The crack tip stress distribution under non-steady state conditions is a function of time even when the crack is considered stationary.

The problem of creep crack growth under transient conditions is of considerable practical significance to large components which are subjected to stress and temperature gradients. Because these components are designed to resist creep deformation, significant creep deformation is likely to occur during service only in localized regions near crack tips. The material surrounding the crack tip will most likely be under dominantly linear-elastic conditions. This is an ideal situation for crack growth

Table 11.1: Reference Stress for some fracture mechanics specimens [21]

Specimen	Reference Stress
Center Cracked M(T)	$= \frac{P}{Bb} \text{ for crack geometries (that do not include a bending component)}$ $\sigma_{ref} = \sigma_{net}$
Compact tension C(T)	$= \frac{P}{BW} \left\{ 2.02 \frac{(1+a/W)}{(1-a/W)^2} \right\}$
Three point Bend, SE(B)	$= \frac{P}{BW} \left\{ 0.833 \frac{S}{W} \frac{1}{(1-a/W)^2} \right\}$
Four Point Bend	$= \frac{P}{BW} \left\{ 0.67 \frac{S}{W} \frac{1}{(1-a/W)^2} \right\}$
Single Edge Notched SE(T)	$= \frac{1.004}{(1-a/W)^2} \left(\frac{P}{BW} \right) \text{ for } a/W < 0.5$
"	$= 2.007 \left(\frac{a}{W} \right) \frac{P/BW}{(1-a/W)^2} \text{ for } a/W > 0.5$

under non-steady-state conditions to occur..

11.3.1 Growth Rate Correlations: Saxena [22] proposed a crack tip parameter, C_t , for characterizing creep crack growth behavior under non-steady-state creep conditions. C_t is defined as the instantaneous value of the potential energy rate difference between two identically loaded bodies having incrementally differing crack lengths

$$C_t = - \frac{1}{B} \frac{\partial \dot{PE}_t}{\partial a} \quad (11.19)$$

where B is the thickness and $\partial \dot{PE}_t$ is the area between the $P-\dot{\Delta}$ curves for specimens of crack lengths a and $a+da$. To be more specific, consider

several identical pairs of cracked specimens. Within each pair, one specimen has a crack length, a , and the other has an incrementally differing crack length, $a+\Delta a$. The specimens of each pair are loaded to various load levels P_1, P_2, P_3, \dots etc. at elevated temperature, and the load line deflection as a function of time is recorded (Fig.11.4a). The load-line deflection due to creep is Δ . It is assumed that no crack extension occurs

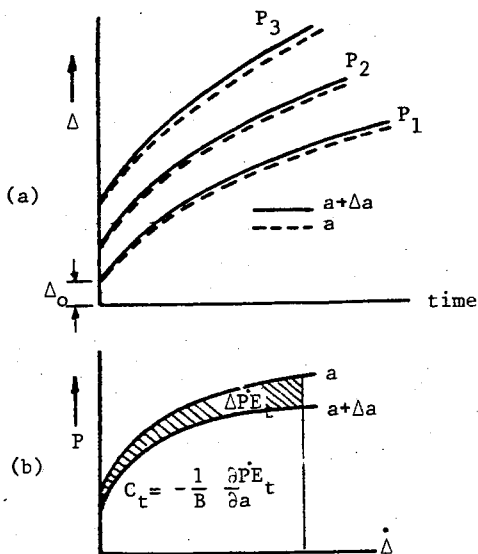


Fig.11.4: (a) Load line deflection as a function of time at various load levels, (b) Definition of C_t parameter [22]

in any of the specimens and the instantaneous response is linear elastic. For small scale creep conditions, characterized by $t/t_T \ll 1$, load versus deflection rate behavior is shown in Fig.11.4(b), at some fixed time t . Several such plots can be generated from the tests by varying time. The area between the $P-\Delta$ curves for specimens of crack length a and $a+\Delta a$ is called ΔPE_t . Physically, ΔPE_t represents the difference in the energy rates supplied to the two cracked bodies with identical creep deformation history as they are loaded to different load or deflection-rate levels.

As $t/t_T \rightarrow \infty$, $C_t = C^*$, by definition of C^* . That is, under extensive

creep conditions, C_t (being the same as C^{**}) characterizes the HRR field. In small scale creep, the C_t parameter does not characterize the crack tip singularity and thus cannot be interpreted in terms of the HRR crack tip field. (Riedel and Rice [23] have shown that the near field intensity is given by

$$\frac{K^2(1-\nu^2)/E}{(n+1)t} \quad (11.20)$$

for small scale creep). But C_t is proportional to the rate of advance of the creep zone under small scale creep conditions and, essentially, well beyond [24]. This is true even when primary creep is added to the constitutive description. Therefore, it is possible that the C_t parameter reflects the accumulation of the history dependent creep damage ahead of the crack tip and is hence a physically viable candidate for characterization of creep crack growth rate in the small scale creep and transition regimes.

A wide range expression for estimating C_t is developed [25] based on load and deflection rate:

$$C_t = \frac{P\dot{\Delta}}{BW} \frac{F'}{F} - C^{**} \left[\frac{F'/F}{\eta} - 1 \right]$$

where $F = K$ calibration factor given by $F = (K/P)BW^{1/2}$

$P =$ applied load

$W =$ width of the specimen

$F' = dF/d(a/W)$

$\dot{\Delta} =$ load line creep deflection rate

$C^{**} =$ analytically calculated value of C^{**}

$\eta =$ calibration factor defined as $C^{**} = \frac{P\dot{\Delta}_{ss}}{BW} \eta(a/W, n)$ with $\dot{\Delta}_{ss}$ being steady state value of $\dot{\Delta}$

Saxena [22] reports excellent correlation between da/dt and C_t values for a range of over five orders of magnitude in C_t and three orders of magnitude in crack growth rates for A 470 Class 8 steel at 538°C. Crack growth data on 2.25 Cr-1 Mo, 1.25Cr-0.5 Mo and 0.5 Cr-0.5 Mo-2.25 V steels available in literature have been reanalyzed and correlated with the C_t parameter [25]. The conclusion is that the

effects of prior service exposure, test temperature and material type on creep crack growth behavior are normalized to a first approximation if the growth rate data are expressed as a function of the C_t parameter.

References:

- 1- Goldman, N.L. and Hutchinson, J.W. "Fully Plastic Crack Problems: The Center Cracked Strip Under Plane Strain" Int.J.of Solids and Structures, Vol.11, 1975, pp.575-591
- 2- Kanninen, M.F. and Popelar, C.H. "Advanced Fracture Mechanics" Oxford University Press, New York, 1985, p.444
- 3- Li, F.Z., Needleman, A. and Shih, C.F. "Characterization of Near Tip Stress and Deformation Fields in Creeping Solids" Int.Journal of Fracture V.36, 1988, pp.163-186.
- 4- Saxena, A., Shih, T.T. and Ernst, H.A. "Wide Range Creep Crack Growth Rate Behavior of A470 Class 8 (Cr-Mo-V) Steel" ASTM STP 833, Amer. Society for Testing and Materials, 1984, pp.516-531.
- 5- Landes, J.D. and Begley, J.A. "A Fracture Mechanics Approach to Creep Crack Growth" ASTM STP 590, Amer.Society for Testing and Materials, 1976, pp.128-148.
- 6- Smith D.J. and Webster, G.A. "Estimates of the C^{**} Parameter for Crack Growth in Creeping Materials" ASTM STP 803, Amer.Society for Testing and Materials, 1983, pp.I-654-674.
- 7- Harper, M.P. and Ellison, E.G. "The Use of the C^{**} Parameter in Predicting Creep Crack Propagation Rates" Journal of Strain Analysis, Vol.12, 1977 pp.167-179.
- 8- Hui, C.Y. and Riedel, H. "The Asymptotic Stress and Strain Field Near the Tip of a Growing Crack Under Creep Conditions" Int.Journal of Fracture, Vol.17, 1981, pp.409-425.
- 9- Smith, D.J. and Webster, G.A. "Characterization of Creep Crack Growth in 1 Per Cent Cr-Mo-V Steel" J.of Strain Analysis, Vol.16, 1981, pp.137-143.

- 10- Taira, S., Ohtani, R. and Kitamura, T. "Application of J-Integral to High Temperature Crack Propagation, Part I: Creep Crack Propagation" J. of Engineering Materials and Technology, Transactions of the ASME, Vol.101, 1979, pp.154-161.
- 11- Koterazawa, R. and Mori, T. "Applicability of Fracture Mechanics Parameters to Crack Propagation Under Creep Conditions" J. of Engineering Materials and Technology, Trans. of the ASME, Vol.99, 1977, pp.298-305.
- 12- Shih, T.T. "A Simplified Test Method For Determining the Low Rate Creep Crack Growth Data" ASTM STP 791 Amer.Soc.for Testing and Materials, 1983, pp.II.232-247.
- 13- Saxena, A. "Evaluation of C^* for the Characterization of Creep Crack Growth Behavior in 304 Stainless Steel" ASTM STP 700, Amer.Society for Testing and Materials, 1980, pp.131-151.
- 14- Sadananda, K. and Shahinian, P. "Creep-Fatigue Crack Growth" in Cavities and Cracks in Creep and Fatigue, J.Gittus Ed., Applied Science Publishers London, 1981, p.154.
- 15- Sadananda, K. and Shahinian, P. "Creep Crack Growth in Alloy 718" Metallurgical Transaction A, V.8, 1977, pp. 439-449.
- 16- Donath, R.C. Nicholas, T. and Fu, L.S. "An Experimental Investigation of Creep Crack Growth in IN 100" ASTM STP 743 Amer.Soc. for Testing and Materials, 1981, pp.186-206.
- 17- Nikbin, K.M., Smith, D.J. and Webster, G.A. "Advances in Life Prediction Methods at Elevated Temperatures" (ed.D.A. Woodford and J.R.Whilehead) Conf.Proc.ASME, 1983, pp.249-258)
- 18- Radhakrishnan, V.M. and Mc Evily, A.J. J. of Engineering Materials and Technology, Transactions ASME vol.102, 1980, pp.200-206.
- 19- Nikbin, K.M., Smith, D.J. and Webster, G.A. "An Engineering Approach to the Prediction of Creep Crack Growth" J. of Engineering Materials and Technology Vol.18,1986, pp.186-191.

- 20- Saxena, A., Ernst, H.A. and Landes, J.D. "Creep Crack Growth Behavior in 316 Stainless Steel at 594°C" Int.Journal of Fracture Vol.23, 1983, pp.245-257.
- 21- Williams, J.A. and Price, A.T. "A Description of Crack Growth From Defects Under Creep Conditions" Journal of Engineering Materials and Technology, Transaction of the ASME Vol.97, 1975, pp.214-222.
- 22- Saxena, A. "Creep Crack Growth Under Non-Steady State Conditions" ASTM STP 905, Amer.Soc.for Testing and Materials, 1986, pp.185-201.
- 23- Riedel, H. and Rice, J.R." Tensile Cracks in Creeping Solids" ASTM STP 700, Amer.Soc. for Testing and Materials, 1980, pp.112-130.
- 24- Leung, C.P., Mc Dowell, D.L. and Saxena, A. "Consideration of Primary Creep at a Stationary Crack Tip: Implications for the C_t Parameter" Int.Journal of Fracture, Vol.36, 1988, pp.275-289.
- 25- Saxena, A., Han, J. and Banerji, K. "Creep Crack Growth Behavior in Power Plant Boiler and Steam Pipe Steels" J. of Pressure Vessel Technology, Transactions ASME, Vol.110, 1988, pp.137-146.

Problems

- 1- One inch thick C(T) specimens ($W=50.8$ mm) machined from A 470, Class 8 steel-forgings are subjected to creep tests at 538°C under constant load conditions. Assume $n=11$ for this material and plot da/dt vs. C^* , using the data provided below.

load kN	Crack length mm	Displ.rate mm/h	Crack ext. mm	Test duration h
35.6	16.69	$5.08 \cdot 10^{-5}$	0.787	2035
26.7	26.34	$2.38 \cdot 10^{-3}$	1.702	760
22.2	26.44	$1.27 \cdot 10^{-3}$	1.346	950
20.0	26.42	$6.6 \cdot 10^{-5}$	1.727	4203
17.8	26.54	$3.81 \cdot 10^{-5}$	1.499	4847
28.9	26.00	$1.09 \cdot 10^{-2}$	0.965	220

Answer: $C^* [J/m^2/h] = 4.87; 230; 102.1; 4.78$
 $2.45; 1130;$
 $10^4 \text{ x} \dot{\Delta} [mm/h] = 3.86; 22.4; 14.2; 4.11$
 $3.09; 43.8;$

- 2- Derivation of the eq.11.8 for C^* assumes implicitly that $\Delta = \text{const} \times P^n$; (thus, the area under the load-deflection rate is expressed as $P \Delta(n/n+1)$).
 Check how well the data in problem 1 obeys such a relationship

APPENDIX

FULLY PLASTIC SOLUTIONS

The superposition technique discussed in Sec.7.2.3 includes fully plastic solutions for compact specimen only. For other common fracture specimens the tabulations of EPRI Handbook (Shih, Ref 7.30) are given below. In general

$$J_{p1} = \bar{\alpha} \epsilon_0 \sigma_0 b \cdot g_1 \left(\frac{a}{W}\right) h_1 \left(\frac{a}{W}, n\right) (P/P_0)^{n+1}$$

$$\Delta_{p1} = \bar{\alpha} \epsilon_0 a \cdot g_3 \left(\frac{a}{W}\right) h_3 \left(\frac{a}{W}, n\right) (P/P_0)^n$$

$$\delta_{p1} = \bar{\alpha} \epsilon_0 a \cdot g_2 \left(\frac{a}{W}\right) h_2 \left(\frac{a}{W}, n\right) (P/P_0)^n$$

where Δ is the load point displacement, δ is the crack mouth opening displacement, b is the uncracked ligament. (The functions g_i are unity for C(T) specimen, as evident from eq.7.30)

Single Edge Notched Specimen, SE(T): The functions h_i are given in table A.1 and A.2. The function $g_1 = a/W$ and $g_2 = g_3 = 1$. The limit load is

$$P_0 = 1.455 \alpha' b B \sigma_0 \quad \text{plane strain}$$

$$P_0 = 1.072 \alpha' b B \sigma_0 \quad \text{plane stress}$$

where $\alpha' = (1 + (a/b)^2)^{1/2} - a/b$.

Double Edge Notched Specimen, DE(T): Based on Fig.7.19 the functions h_i are given in table A.3 and A.4. The functions $g_1 = 1$ and $g_2 = g_3 = W/2a - 1$. The limit load is

$$P_0 = (0.36W + 0.91) B \sigma_0 \quad \text{plane strain}$$

$$P_0 = 2b B \sigma_0 / \sqrt{3} \quad \text{plane stress}$$

Table A.1: Plane Strain h-Functions for a Single Edge Notched Specimen

	n=1	n=2	n=3	n=5	n=7	n=10	n=13	n=16	n=20	
a/W=1/8	h_1	4.95	6.93	8.57	11.5	13.5	16.1	18.1	21.2	
	h_2	5.25	6.47	7.56	9.46	11.1	12.9	14.4	16.8	
	h_3	26.6	25.8	25.2	24.2	23.6	23.2	23.2	23.7	
a/W=1/4	h_1	4.34	4.77	4.64	3.82	3.06	2.17	1.55	1.11	0.712
	h_2	4.76	4.56	4.28	3.39	2.64	1.81	1.25	0.875	0.552
	h_3	10.3	7.64	5.87	3.70	2.48	1.50	0.970	0.654	0.404
a/W=3/8	h_1	3.88	3.25	2.63	1.68	1.06	0.539	0.276	0.142	0.0595
	h_2	4.54	3.49	2.67	1.57	0.946	0.453	0.229	0.116	0.048
	h_3	5.14	2.99	1.90	0.923	0.515	0.240	0.119	0.060	0.0246
a/W=1/2	h_1	3.40	2.30	1.69	0.928	0.514	0.213	0.0902	0.0385	0.0119
	h_2	4.45	2.77	1.89	0.954	0.507	0.204	0.0854	0.0356	0.0110
	h_3	3.15	1.54	0.912	0.417	0.215	0.085	0.0358	0.0147	0.00448
a/W=5/8	h_1	2.86	1.80	1.30	0.697	0.378	0.153	0.0625	0.0256	0.0073
	h_2	4.37	2.44	1.62	0.0806	0.423	0.167	0.0671	0.0272	0.00823
	h_3	2.31	1.08	0.681	0.329	0.171	0.067	0.0268	0.0103	0.00326
a/W=3/4	h_1	2.34	1.61	1.25	0.769	0.477	0.233	0.116	0.059	0.0215
	h_2	4.32	2.52	1.79	1.03	0.619	0.296	0.146	0.0735	0.0267
	h_3	2.02	1.10	0.765	0.435	0.262	0.125	0.0617	0.0312	0.0113
a/W=7/8	h_1	1.91	1.57	1.37	1.10	0.925	0.702			
	h_2	4.29	2.75	2.14	1.55	1.23	0.921			
	h_3	2.01	1.27	0.988	0.713	0.564	0.424			

Table A.2: Plane Stress h-Functions for a Single Edge Notched Specimen

	n=1	n=2	n=3	n=5	n=7	n=10	n=13	n=16	n=20	
a/W=1/8	h_1	3.58	4.55	5.06	5.30	4.96	4.14	3.29	2.60	1.92
	h_2	5.15	5.43	6.05	6.01	5.47	4.46	3.48	2.74	2.02
	h_3	26.1	21.6	18.0	12.7	9.24	5.98	3.94	2.72	2.0
a/W=1/4	h_1	3.14	3.26	2.92	2.12	1.53	0.960	0.615	0.400	0.230
	h_2	4.67	4.30	3.70	2.53	1.76	1.05	0.656	0.419	0.237
	h_3	10.1	6.49	4.36	2.19	1.24	0.630	0.362	0.224	0.123
a/W=3/8	h_1	2.81	2.37	1.94	1.37	1.01	0.677	0.474	0.342	0.226
	h_2	4.47	3.43	2.63	1.69	1.18	0.762	0.524	0.372	0.244
	h_3	5.05	2.65	1.60	0.812	0.525	0.328	0.223	0.157	0.102
a/W=1/2	h_1	2.46	1.67	1.25	0.776	0.510	0.286	0.164	0.0956	0.0469
	h_2	4.37	2.73	1.91	1.09	0.694	0.380	0.216	0.124	0.0607
	h_3	3.10	1.43	0.871	0.461	0.286	0.155	0.083	0.0506	0.0247
a/W=5/8	h_1	2.07	1.41	1.105	0.755	0.551	0.363	0.248	0.172	0.107
	h_2	4.30	2.55	1.84	1.16	0.816	0.523	0.353	0.242	0.150
	h_3	2.27	1.13	0.771	0.478	0.336	0.215	0.146	0.100	0.0616
a/W=3/4	h_1	1.70	1.14	0.910	0.624	0.447	0.280	0.181	0.118	0.0670
	h_2	4.24	2.47	1.81	1.15	0.798	0.490	0.314	0.203	0.115
	h_3	1.98	1.09	0.784	0.494	0.344	0.211	0.136	0.0581	0.0496
a/W=7/8	h_1	1.38	1.11	0.962	0.792	0.677	0.574			
	h_2	4.22	2.68	2.08	1.54	1.27	1.04			
	h_3	1.97	1.25	0.969	0.716	0.591	0.483			

Table A.3: Plane Strain h-Functions for a Double Edge Notched Specimen

		n=1	n=2	n=3	n=5	n=7	n=10	n=13	n=16	n=20
2a/W=1/8	h_1	0.572	0.772	0.922	1.13	1.35	1.61	1.86	2.08	2.44
	h_2	0.732	0.852	0.961	1.14	1.29	1.50	1.70	1.94	2.17
	h_3	0.063	0.126	0.200	0.372	0.571	0.911	1.30	1.74	2.29
2a/W=1/4	h_1	1.10	1.32	1.38	1.65	1.75	1.82	1.86	1.89	1.92
	h_2	1.56	1.63	1.70	1.78	1.80	1.81	1.79	1.78	1.76
	h_3	0.267	0.479	0.698	1.11	1.47	1.92	2.25	2.49	2.73
2a/W=3/8	h_1	1.61	1.83	1.92	1.92	1.84	1.68	1.49	1.32	1.12
	h_2	2.51	2.41	2.35	2.15	1.94	1.68	1.44	1.25	1.05
	h_3	0.637	1.05	1.40	1.87	2.11	2.20	2.09	1.92	1.67
2a/W=1/2	h_1	2.22	2.43	2.48	2.43	2.32	2.12	1.91	1.60	1.51
	h_2	3.73	3.40	3.15	2.71	2.37	2.01	1.72	1.40	1.38
	h_3	1.26	1.92	2.37	2.79	2.85	2.68	2.40	1.99	1.94
2a/W=5/8	h_1	3.16	3.38	3.45	3.42	3.28	3.00	2.54	2.36	2.27
	h_2	5.57	4.76	4.23	3.46	2.97	2.48	2.02	1.82	1.66
	h_3	2.36	3.29	3.74	3.90	3.68	3.23	2.66	2.40	2.19
2a/w=3/4	h_1	5.24	6.29	7.17	8.44	9.46	10.9	11.9	11.3	17.4
	h_2	9.10	7.76	7.14	6.64	6.83	7.48	7.79	7.14	11.1
	h_3	4.73	6.26	7.03	7.63	8.14	9.04	9.40	8.58	13.5
2a/W=7/8	h_1	14.2	24.8	39.0	78.4	140.0	341.0	777.0	1570.0	3820.0
	h_2	20.1	19.4	22.7	36.1	58.9	133.0	294.0	585.0	1400.0
	h_3	12.7	18.2	24.1	40.4	65.8	149.0	327.0	650.0	1560.0

Table A.4: Plane Stress h-Functions for a Double Edge Notched Specimen

		n=1	n=2	n=3	n=5	n=7	n=10	n=13	n=16	n=20
2a/w=1/8	h_1	0.583	0.825	1.02	1.37	1.71	2.24	2.84	3.54	4.62
	h_2	0.853	1.05	1.23	1.55	1.87	2.38	2.96	3.65	4.70
	h_3	0.0729	0.159	0.26	0.504	0.821	1.41	2.18	3.16	4.73
2a/w=1/2	h_1	1.01	1.23	1.36	1.48	1.54	1.58	1.59	1.59	1.59
	h_2	1.73	1.82	1.89	1.92	1.91	1.85	1.80	1.75	1.70
	h_3	0.296	0.537	0.770	1.17	1.49	1.82	2.02	2.12	2.20
2a/W=3/8	h_1	1.29	1.42	1.43	1.34	1.24	1.09	0.970	0.873	0.674
	h_2	2.59	2.39	2.22	1.86	1.59	1.28	1.07	0.922	0.709
	h_3	0.658	1.04	1.30	1.52	1.55	1.41	1.23	1.07	0.830
2a/w=1/2	h_1	1.48	1.47	1.38	1.17	1.01	0.845	0.732	0.625	0.280
	h_2	3.51	2.82	2.34	1.67	1.28	0.944	0.762	0.630	0.232
	h_3	1.18	1.58	1.69	1.56	1.32	1.01	0.809	0.662	0.266
2a/W=5/8	h_1	1.59	1.45	1.29	1.04	0.882	0.737	0.649	0.466	0.0202
	h_2	4.56	3.15	2.32	1.45	1.06	0.790	0.657	0.473	0.0277
	h_3	1.93	2.14	1.95	1.44	1.09	0.809	0.665	0.487	0.0317
2a/w=3/4	h_1	1.65	1.43	1.22	0.979	0.834	0.701	0.630	0.297	
	h_2	5.90	3.37	2.22	1.30	0.966	0.741	0.636	0.312	
	h_3	3.09	2.67	2.06	1.31	0.978	0.747	0.638	0.318	
2a/w=7/8	h_1	1.69	1.43	1.22	0.979	0.845	0.738	0.664	0.614	0.562
	h_2	8.02	3.51	2.14	1.27	0.971	0.775	0.663	0.596	0.535
	h_3	5.07	3.18	2.16	1.30	0.980	0.779	0.665	0.597	0.538

Center Cracked Panel Specimen, M(T): Based on Fig.7.19 the functions h_i are given in table A.5 and A.6. The functions $g_1 = 2a/W$ and $g_2 = g_3 = 1$. The limit load is

$$P_o = 2bB\sigma_o / \sqrt{3} \quad \text{plane strain}$$

$$P = bB\sigma_o \quad \text{plane stress}$$

Three-Point Bend Specimen, SE(B): The functions h_i are given in table A.7 and A.8, for span-to-width ratio (S/W) equal to four. The functions $g_i = 1$. The limit load is

$$P_o = 1.456b^2 B \sigma_o / S \quad \text{plane strain}$$

$$P_o = 1.072b^2 B \sigma_o / S \quad \text{plane stress}$$

Table A.5: Plane Strain h-Functions for a Center-Cracked Panel

	n=1	n=2	n=3	n=5	n=7	n=10	n=13	n=15	n=20	
2a/W=1/8	h_1	2.80	3.61	4.06	4.35	4.33	4.02	3.56	3.06	2.46
	h_2	3.05	3.62	3.91	4.06	3.93	3.54	3.07	2.60	2.06
	h_3	0.303	0.574	0.840	1.30	1.63	1.95	2.03	1.96	1.77
2a/W=1/4	h_1	2.54	3.01	3.21	3.29	3.18	2.92	2.63	2.34	2.03
	h_2	2.68	2.99	3.01	2.85	2.61	2.30	1.97	1.71	1.45
	h_3	0.536	0.911	1.22	1.64	1.84	1.85	1.80	1.64	1.43
2a/W=3/8	h_1	2.34	2.62	2.65	2.51	2.28	1.97	1.71	1.46	1.19
	h_2	2.35	2.39	2.23	1.88	1.58	1.28	1.07	0.890	0.715
	h_3	0.699	1.06	1.28	1.44	1.40	1.23	1.05	0.888	0.719
2a/W=1/2	h_1	2.21	2.29	2.20	1.97	1.76	1.52	1.32	1.16	0.975
	h_2	2.03	1.86	1.60	1.23	1.00	0.799	0.664	0.564	0.469
	h_3	0.803	1.07	1.16	1.10	0.986	0.796	0.665	0.565	0.469
2a/W=5/8	h_1	2.12	1.96	1.76	1.43	1.17	0.863	0.628	0.458	0.300
	h_2	1.71	1.32	1.04	0.707	0.524	0.358	0.250	0.178	0.114
	h_3	0.844	0.937	0.879	0.701	0.522	0.361	0.251	0.178	0.115
2a/W=3/4	h_1	2.07	1.73	1.47	1.11	0.895	0.642	0.461	0.337	0.216
	h_2	1.35	0.857	0.596	0.361	0.254	0.167	0.114	0.0810	0.0511
	h_3	0.805	0.700	0.555	0.359	0.254	0.168	0.114	0.0813	0.0516
2a/W=7/8	h_1	2.08	1.64	1.40	1.14	0.987	0.814	0.688	0.573	0.461
	h_2	0.889	0.428	0.287	0.181	0.139	0.105	0.0837	0.0682	0.0533
	h_3	0.632	0.400	0.291	0.182	0.140	0.106	0.0839	0.0683	0.0535

Table A.6: Plane Stress h-Functions for a Center-Cracked Panel

	n=1	n=2	n=3	n=5	n=7	n=10	n=13	n=16	n=20	
2a/W=1/8	h_1	2.80	3.57	4.01	4.47	4.65	4.62	4.41	4.13	3.72
	h_2	3.53	4.09	4.43	4.74	4.79	4.63	4.33	4.00	3.55
	h_3	0.350	0.661	0.997	1.55	2.05	2.56	2.83	2.95	2.92
2a/W=1/4	h_1	2.54	2.97	3.14	3.20	3.11	2.86	2.65	2.47	2.20
	h_2	3.10	3.29	3.30	3.15	2.93	2.56	2.29	2.08	1.81
	h_3	0.619	1.01	1.35	1.83	2.08	2.19	2.12	2.01	1.79
2a/W=3/8	h_1	2.34	2.53	2.52	2.35	2.17	1.95	1.77	1.61	1.43
	h_2	2.71	2.62	2.41	2.03	1.75	1.47	1.28	1.13	0.988
	h_3	0.807	1.20	1.43	1.59	1.57	1.43	1.27	1.13	0.994
2a/W=1/2	h_1	2.21	2.20	2.06	1.81	1.63	1.43	1.30	1.17	1.00
	h_2	2.34	2.01	1.70	1.30	1.07	0.871	0.757	0.666	0.557
	h_3	0.927	1.19	1.26	1.18	1.04	0.867	0.758	0.668	0.560
2a/W=5/8	h_1	2.12	1.91	1.69	1.41	1.22	1.01	0.853	0.712	0.573
	h_2	1.97	1.46	1.13	0.785	0.617	0.474	0.383	0.313	0.256
	h_3	0.975	1.05	0.970	0.763	0.620	0.478	0.386	0.318	0.273
2a/W=3/4	h_1	2.07	1.71	1.46	1.21	1.08	0.867	0.745	0.646	0.532
	h_2	1.55	0.970	0.685	0.452	0.361	0.262	0.216	0.183	0.148
	h_3	0.929	0.802	0.642	0.450	0.361	0.263	0.216	0.183	0.149
2a/W=7/8	h_1	2.08	1.57	1.31	1.08	0.972	0.862	0.778	0.715	0.630
	h_2	1.03	0.485	0.310	0.196	0.157	0.127	0.109	0.0971	0.0842
	h_3	0.730	0.452	0.313	0.198	0.157	0.127	0.109	0.0973	0.0842

Table A.7: Plane Strain h-Functions for Three-Point Bend Specimen

	n=1	n=2	n=3	n=5	n=7	n=10	n=13	n=16	n=20	
2a/W=1/8	h_1	0.936	0.869	0.805	0.687	0.580	0.437	0.329	0.245	0.165
	h_2	6.97	6.77	6.29	5.29	4.38	3.24	2.40	1.78	1.19
	h_3	3.00	22.1	20.0	15.0	11.7	8.39	6.14	4.54	3.01
2a/W=1/4	h_1	1.20	1.034	0.930	0.762	0.633	0.523	0.396	0.303	0.215
	h_2	5.80	4.67	4.01	3.08	2.45	1.93	1.45	1.09	0.758
	h_3	4.08	9.72	8.36	5.86	4.47	3.42	2.54	1.90	1.32
2a/W=3/8	h_1	1.33	1.15	1.02	0.084	0.695	0.556	0.442	0.360	0.265
	h_2	5.18	3.93	3.20	2.38	1.93	1.47	1.15	0.928	0.684
	h_3	4.51	6.01	5.03	3.74	3.02	2.30	1.80	1.45	1.07
2a/W=1/2	h_1	1.41	1.09	0.922	0.675	0.495	0.331	0.211	0.135	0.0741
	h_2	4.87	3.28	2.53	1.69	1.19	0.773	0.480	0.304	0.165
	h_3	4.69	4.33	3.49	2.35	1.66	1.08	0.669	0.424	0.230
2a/W=5/8	h_1	1.46	1.07	0.896	0.631	0.436	0.255	0.142	0.084	0.0411
	h_2	4.64	2.86	2.16	1.37	0.907	0.518	0.287	0.166	0.0806
	h_3	4.71	3.49	2.70	1.72	1.14	0.652	0.361	0.209	0.102
2a/W=3/4	h_1	1.48	1.15	0.974	0.693	0.500	0.348	0.223	0.140	0.0745
	h_2	4.47	2.75	2.10	1.36	0.936	0.618	0.388	0.239	0.127
	h_3	4.49	3.14	2.40	1.56	1.07	0.704	0.441	0.272	0.144
2a/W=7/8	h_1	1.50	1.35	1.20	1.02	0.855	0.690	0.551	0.440	0.321
	h_2	4.36	2.90	2.31	1.70	1.33	1.00	0.782	0.613	0.459
	h_3	4.15	3.08	2.45	1.81	1.41	1.06	0.828	0.649	0.486

Table A.8: Plane Stress n -Functions for Three-Point Bend Specimen

	$n=1$	$n=2$	$n=3$	$n=5$	$n=7$	$n=10$	$n=13$	$n=16$	$n=20$
$a/W=1/8$	h_1	0.676	0.600	0.548	0.459	0.383	0.297	0.238	0.148
	h_2	6.84	6.30	5.66	4.53	3.64	2.72	1.67	1.26
	h_3	2.95	20.1	14.6	12.2	9.12	6.75	4.09	3.07
$a/W=1/4$	h_1	0.869	0.731	0.629	0.479	0.370	0.246	0.174	0.0593
	h_2	5.69	4.50	3.68	2.61	1.95	1.29	0.897	0.603
	h_3	4.01	8.81	7.19	4.73	3.39	2.20	1.52	1.01
$a/W=3/8$	h_1	0.963	0.797	0.680	0.527	0.418	0.307	0.232	0.174
	h_2	5.09	3.73	2.93	2.07	1.58	1.13	0.841	0.626
	h_3	4.42	5.53	4.48	3.17	2.41	1.73	1.28	0.948
$a/W=1/2$	h_1	1.02	0.767	0.621	0.453	0.324	0.202	0.128	0.0813
	h_2	4.77	3.12	2.32	1.55	1.08	0.655	0.410	0.259
	h_3	4.60	4.09	3.09	2.08	1.44	0.874	0.545	0.344
$a/W=5/8$	h_1	1.05	0.786	0.649	0.494	0.357	0.235	0.173	0.105
	h_2	4.55	2.83	2.12	1.46	1.02	0.656	0.472	0.286
	h_3	4.62	3.43	2.60	1.79	1.26	0.803	0.577	0.349
$a/W=3/4$	h_1	1.07	0.786	0.643	0.474	0.343	0.230	0.167	0.110
	h_2	4.39	2.66	1.97	1.33	0.928	0.601	0.427	0.280
	h_3	4.39	3.01	2.24	1.51	1.05	0.680	0.483	0.316
$a/W=7/8$	h_1	1.086	0.928	0.810	0.646	0.538	0.423	0.332	0.242
	h_2	4.28	2.76	2.16	1.56	1.23	0.922	0.702	0.561
	h_3	4.07	2.93	2.29	1.65	1.30	0.975	0.742	0.592